

---

# **Operational Modal Analysis and Prediction of Remaining Useful Life for Rotating Machinery**

---

A thesis submitted for the degree of  
Doctor of Philosophy by

German Sternharz



College of Engineering, Design and Physical Sciences  
Department of Electronic and Computer Engineering  
Brunel University London



## Declaration of authorship

I, German Sternharz, declare that the work in the dissertation was carried out in accordance with the requirements of the University's Regulations and Code of Practice for Research Degree Programmes and that it has not been submitted for any other academic award. Except where indicated by specific references in the text, the work is the candidate's own work. The work done in collaboration with, or with the assistance of, others, is indicated as such. Any views expressed in the dissertation are those of the author.

Signature: \_\_\_\_\_

Date: 26/09/2022



## Abstract

The significance of rotating machinery spans areas from household items to vital industry sectors, such as aerospace, automotive, railway, sea transport, resource extraction, and manufacturing. Hence, our technologised society depends on efficient and reliable operation of rotating machinery. To contribute to this aim, this thesis leverages measurable quantities during its operation for structural-mechanical evaluation employing Operational Modal Analysis (OMA) and the prediction of Remaining Useful Life (RUL).

Modal parameters determined by OMA are central for the design, test, and validation of rotating machinery. This thesis introduces the first open parametric simulation dataset of rotating machinery during an acceleration run. As there is a lack of similar open datasets suitable for OMA, it lays a foundation for improved reproducibility and comparability of future research.

Based on this, the Averaged Order-Based Modal Analysis (AOBMA) method is developed. The novel addition of scaling and weighted averaging of individual machine orders in AOBMA alleviates the analysis effort of the existing Order-Based Modal Analysis (OBMA) method by providing a unified set of modal parameters with higher accuracy. As such, AOBMA showed a lower mean absolute relative error of 0.03 for damping ratio estimations across compared modes while OBMA provided an error value of 0.32 depending on the processed order. At excitation with high harmonic contributions, AOBMA also resulted in the highest number of accurately identified modes among the compared methods. At a harmonic ratio of 0.8, for example, AOBMA identified an average of 11.9 modes per estimation, while OBMA and baseline OMA followed with 9.5 and 9 modes, respectively. Moreover, it is the first study, which systematically evaluates the impact of excitation conditions on the compared methods and finds an advantage of OBMA and AOBMA over traditional OMA regarding mode shape estimation accuracy.

While OMA can be used to evaluate significant structural changes, Machine Learning (ML) methods have seen substantially greater success in condition monitoring, including RUL prediction. However, as these methods often require large amounts of time and cost-intensive training data, a novel data-efficient RUL prediction methodology is introduced, taking advantage of distinct healthy and faulty condition data. When the number of training sequences from an open dataset is reduced to 5%, an average prediction Root Mean Square Error (RMSE) of 24.9 operation cycles is achieved, outperforming the baseline method with an RMSE of 28.1. Motivated by environmental considerations, the impact of data reduction on the training duration of several method variants is quantified. When the full training set is utilised, the most resource-saving variant of the proposed approach achieves an average training duration of 8.9% compared to the baseline method.



## Acknowledgements

Firstly, I want to thank my family, and foremost my parents, for their unconditional support throughout my studies.

I also want to express my gratitude to my principal supervisor Prof. Tatiana Kalganova, for giving me the opportunity and encouragement to pursue a PhD, and second supervisor Dr. Cristinel Mares for additional consultation and expertise.

I would like to also thank Moritz Meyeringh for his support and industry-oriented insights, which provided the initial spark for the direction of this thesis.





# Contents

<b>Abstract .....</b>	<b>i</b>
<b>Acknowledgements.....</b>	<b>iii</b>
<b>Contents.....</b>	<b>v</b>
<b>List of Figures .....</b>	<b>ix</b>
<b>List of Tables .....</b>	<b>xiv</b>
<b>Nomenclature .....</b>	<b>xvi</b>
Operators .....	xvi
Symbols.....	xvi
Abbreviations.....	xviii
<b>1 Introduction.....</b>	<b>1</b>
1.1 Wider scope and relevance of the research area .....	1
1.1.1 Operational Modal Analysis (OMA) .....	1
1.1.2 Condition monitoring .....	3
1.2 Original contributions of this work.....	4
1.3 List of publications.....	6
1.3.1 Published .....	6
1.3.2 Submitted for publication.....	6
1.4 Structure and outline of the thesis .....	7
<b>2 State of the art in existing research.....</b>	<b>11</b>
2.1 Operational Modal Analysis (OMA) in the presence of harmonic excitation from rotating machinery .....	11
2.1.1 Methods not specifically adapted for input harmonics.....	11
2.1.2 Methods for identification of harmonics .....	14
2.1.3 Methods for reduction of harmonics from the signal .....	15
2.1.4 OMA methods with explicit consideration of harmonics .....	18
2.1.5 OMA methods with implicit consideration of harmonics .....	18

2.1.6	Summary.....	20
2.2	Order-Based Modal Analysis (OBMA) for transient operation runs .....	21
2.2.1	Comparisons of solely operational run-up conditions .....	22
2.2.2	Comparisons of operational run-up and operational stationary conditions .....	23
2.2.3	Comparisons of operational run-up and experimental/numerical response.....	24
2.2.4	Discussion.....	26
2.2.5	Summary.....	27
2.3	Rotating machinery datasets for OBMA and condition monitoring .....	29
2.3.1	Existing open datasets from rotating machinery vibration.....	30
2.3.2	Summary.....	32
2.4	Condition monitoring of rotating machinery .....	33
2.4.1	Modal parameter-based condition monitoring.....	34
2.4.2	Machine learning-based Remaining Useful Life (RUL) prediction.....	36
2.4.3	Summary.....	40
2.5	Conclusions .....	40
<b>3</b>	<b>Theoretical background and terminology.....</b>	<b>43</b>
3.1	Fundamental dynamic system equation .....	43
3.1.1	Eigenvalue problem .....	44
3.1.2	Newmark- $\beta$ method for implicit time integration.....	45
3.2	Modal identification (EMA and OMA).....	47
3.2.1	Relation between the transfer function and modal parameters .....	48
3.2.2	Assumptions and limitations of OMA.....	50
3.2.3	Modal Assurance Criterion (MAC) and extended pole-weighted variants (MACX, MACXP) .....	54
3.2.4	Order tracking with the Time Variant Discrete Fourier Transform (TVDFFT) .....	55
3.2.5	Order-Based Modal Analysis (OBMA).....	58
3.3	Advanced data modelling for general applications.....	60
3.3.1	Linear Least Squares (LS) regression .....	60
3.3.2	Mahalanobis Distance (MD) .....	61
3.3.3	Support Vector Regression (SVR).....	61

---

3.3.4	Long Short-Term Memory (LSTM) Neural Network .....	62
3.4	Conclusions .....	64
<b>4</b>	<b>Open simulation dataset for OMA and vibration analysis of rotating machinery during acceleration .....</b>	<b>66</b>
4.1	Model definition .....	67
4.2	Varied parameters of the forced response.....	71
4.2.1	Harmonic amplitude ratio .....	71
4.2.2	Duration and acceleration rate .....	72
4.2.3	Measurement noise.....	73
4.3	Characteristics of input and output spectra resulting from order excitation .....	75
4.4	Accuracy of the simulation response .....	77
4.5	Conclusions .....	81
<b>5</b>	<b>Introduction of Averaged Order-Based Modal Analysis (AOBMA) and performance assessment of OMA methods during transient order excitation .....</b>	<b>83</b>
5.1	Introduction and motivation .....	83
5.2	Overview and development of relevant theory.....	85
5.2.1	Overview of compared OMA methods.....	85
5.2.2	Order scaling and averaging in the AOBMA method .....	87
5.2.3	Implementation and application of AOBMA .....	92
5.3	Methodology .....	96
5.3.1	Parametric simulation study .....	96
5.3.2	Operational run-up of a turbofan casing .....	98
5.4	Results and discussion.....	99
5.4.1	Comparative performance assessment of OMA, OBMA and AOBMA .....	99
5.4.2	Operational run-up of a turbofan casing .....	110
5.5	Conclusions .....	114
<b>6</b>	<b>Data-efficient estimation of Remaining Useful Life (RUL) for machinery with a limited number of run-to-failure training sequences .....</b>	<b>117</b>
6.1	Proposed methodology for data-efficient RUL prediction.....	119
6.1.1	Machine condition deviation .....	120

---

6.1.2	Health Index (HI) calculation .....	122
6.1.3	Remaining Useful Life (RUL) prediction .....	123
6.2	Application to simulated turbofan engine degradation data.....	126
6.2.1	Model training .....	128
6.2.2	Health Index (HI) calculation .....	132
6.2.3	RUL prediction results .....	134
6.3	Application to vibration data of bearing degradation .....	142
6.4	Conclusions .....	147
<b>7</b>	<b>Conclusions and future work.....</b>	<b>150</b>
7.1	Conclusions .....	150
7.2	Recommendations for future work.....	152
	<b>References.....</b>	<b>153</b>
	<b>Appendix A OMA case study of an aluminium plate under harmonic excitation ....</b>	<b>172</b>
	<b>Appendix B Polyreference Least Squares Complex Frequency Domain (pLSCF) method for OMA .....</b>	<b>175</b>
	<b>Appendix C Least Squares Frequency Domain (LSFD) method for the determination of mode shapes and residues .....</b>	<b>184</b>
	<b>Appendix D Supplementary dataset information.....</b>	<b>188</b>

# List of Figures

Figure 1-1: Relationship between input $X$ and output $Y$ as a function of frequency $\omega$ - broadband excitation with flat spectrum (top), excitation with input harmonics (bottom)	2
Figure 1-2: Graphical structure and flow of the thesis .....	7
Figure 1-3: Graphical structure and summary of the thesis core chapters .....	10
Figure 3-1: Main components of EMA and OMA methods and their different variants .....	47
Figure 3-2: Exemplary Campbell diagram, illustrating harmonic fan blade excitation due to rotation orders [162] .....	53
Figure 3-3: Schematic architecture of an LSTM cell [21].....	62
Figure 3-4: Schematic architecture of an AE model [21].....	63
Figure 3-5: Relation between structural quantities (blocks) through forward (right-pointing arrows) and inverse (left-pointing arrows) problems in structural dynamics [2] .....	64
Figure 4-1: Definition of the geometry and element types of the simulated dynamic structure .....	67
Figure 4-2: Linear auto spectra of the model response from all DOFs to random excitation .	70
Figure 4-3: Spectra and spectrograms of the model response at DOF 1X with harmonic ratios $h_{rat}$ of a) 0.0; b) 0.6; c) 1.0 .....	72
Figure 4-4: Approximate proportionality factors for eigenfrequency estimation errors from spectra of order $l=1$ over run-up durations $T$ ; comparing the implemented logarithmic scaling of $T$ to linear spacing .....	73
Figure 4-5: Spectra and spectrograms of the model response at DOF 1X with harmonic ratios $h_{rat}=0.6$ and noise ratios $n_{rat}$ of a) 0.0%; b) 0.5%; c) 16%.....	74
Figure 4-6: Acceleration output spectrum of the simulated structure at node 1 (see Figure 4-1), X direction, harmonic ratio 0.8.....	75
Figure 4-7: Force input spectrum (top) and spectrogram (bottom) of the simulated structure .....	75
Figure 4-8: PSD estimations for increasing number of averaged blocks with 70% overlap in Welch's method, red vertical lines mark the calculated end-of-order frequencies .....	76
Figure 4-9: Individual extracted response orders .....	77
Figure 4-10: Overlaid spectra of the response simulated with three different integration schemes at a simulation step frequency $f_{s,sim}=752\text{Hz}$ , leading to numerical softening with resonances shifted to lower frequencies; red vertical lines indicate system eigenfrequencies from the eigensolution .....	78

Figure 4-11: Period elongation error (responsible for numerical softening) as a function of simulation step frequency $f_{s,sim}$ relative to the response frequency $f_{max}$ .....	79
Figure 4-12: Overlaid spectra of the response simulated with the Newmark- $\beta$ and HHT methods at a simulation step frequency of 5kHz; as desired, the resonance peaks match the red vertical lines, which indicate system eigenfrequencies from the eigensolution .....	81
Figure 5-1: Processing steps of the compared methods OMA, OBMA and AOBMA .....	86
Figure 5-2: Procedural diagram of AOBMA; additional steps covered in Subchapter 5.2.3: * <sup>1</sup> prior to Eq. (5.7), interpolation of tracked orders to common frequency values; * <sup>2</sup> prior to Eq. (5.9), smoothing (e.g. moving average) due to order spectrum distortions .....	88
Figure 5-3: Averaged difference functions of subsequent orders based on order output acceleration (left) and order input force (right) .....	93
Figure 5-4: Trend functions from each order $l$ to the highest order $o=8$ .....	94
Figure 5-5: Individual order magnitudes before scaling (light lines) and after scaling (bold lines) .....	94
Figure 5-6: Individual order magnitudes before scaling (light lines) and after scaling (bold lines) around the first resonance .....	95
Figure 5-7: Resulting response signal after order scaling and averaging with AOBMA .....	95
Figure 5-8: Positions of accelerometers at the instrumented fan casing .....	98
Figure 5-9: Count of simulation runs with a matched estimation of the reference mode. For OBMA results, the individual source orders (1, 3, 5, 8) are specified in brackets. ....	100
Figure 5-10: Average count of matched (left) and unmatched (right) modes per single simulation run .....	101
Figure 5-11: Relative eigenfrequency errors $(f_{est} - f_{ref})/f_{ref}$ Of matched mode estimations by different methods for individual harmonic ratios, where $f_{est}$ and $f_{ref}$ are the estimated and reference eigenfrequencies, respectively .....	102
Figure 5-12: Relative eigenfrequency errors of matched mode estimations by different methods (for the legend refer to Figure 5-13) .....	103
Figure 5-13: Relative damping ratio errors $(\xi_{est} - \xi_{ref})/\xi_{ref}$ Of matched mode estimations by different methods, where $\xi_{est}$ and $\xi_{ref}$ are the estimated and reference damping ratios, respectively .....	103
Figure 5-14: MACX values of matched mode estimations by different methods .....	105
Figure 5-15: Overlaid deflections of mode 12 estimated at harmonic ratio 0.8 by OMA (left) and AOBMA (right), dashed lines show the undeflected state, red arrow follows the trace of the central node (left) .....	105

Figure 5-16: MPC of mode shape estimations by different methods for individual harmonic ratios .....	106
Figure 5-17: Count of simulation runs with a matched mode estimation by AOBMA and Post-AOBMA .....	107
Figure 5-18: Relative eigenfrequency errors of mode estimations by OBMA(8), AOBMA, Post-AOBMA (for the legend refer to Figure 5-20).....	107
Figure 5-19: Relative damping ratio errors of mode estimations by OBMA(8), AOBMA, Post-AOBMA (for the legend refer to Figure 5-20).....	107
Figure 5-20: MACX values of mode estimations by OBMA(8), AOBMA, Post-AOBMA.....	108
Figure 5-21: Count of simulation runs with a matched mode, 25 Hz analysis bandwidth (for the legend refer to Figure 5-22) .....	109
Figure 5-22: MACX values of matched mode estimations, 25 Hz analysis bandwidth .....	109
Figure 5-23: Relative eigenfrequency errors of matched mode estimations, 25 Hz analysis bandwidth (for the legend refer to Figure 5-22).....	109
Figure 5-24: Relative damping ratio errors of matched mode estimations, 25 Hz analysis bandwidth (for the legend refer to Figure 5-22).....	109
Figure 5-25: Acceleration spectrum (top) and spectrogram (bottom) from operational run-up data.....	110
Figure 5-26: Acceleration magnitude spectrum from scaled and averaged orders (AOBMA) .....	111
Figure 5-27: Eigenfrequency differences $(f_{est} - f_{OMA})/f_{OMA}$ relative to OMA results.....	112
Figure 5-28: Damping ratio differences $(\xi_{est} - \xi_{OMA})/\xi_{OMA}$ relative to OMA results.....	112
Figure 5-29: MACX values between mode shape results from OMA and the specified methods .....	112
Figure 5-30: Mean eigenfrequency differences relative to OMA results .....	113
Figure 5-31: Mean damping ratio differences relative to OMA results.....	113
Figure 5-32: Mean MACX values between mode shape results from OMA and the specified methods .....	113
Figure 5-33: Mean MPC values of mode shape results from all methods .....	113
Figure 5-34: Overlaid deflections of mode 1 estimated by OMA, OBMA(1), AOBMA.....	113
Figure 5-35: Overlaid deflections of mode 15 estimated by OMA, OBMA(4), AOBMA.....	113
Figure 6-1: Overview graphic of the proposed RUL prediction method.....	119
Figure 6-2. Quadratic polynomial fit for RUL prediction on an MD-based HI sequence calculated from a C-MAPSS FD001 training sequence at current cycle 140, leading to a predicted failure cycle overestimation by 58 cycles .....	124

Figure 6-3. Quadratic polynomial fit for RUL prediction on an MD-based HI sequence calculated from a C-MAPSS FD001 training sequence at current cycle 160, reducing the predicted failure cycle overestimation to 27 cycles .....	124
Figure 6-4. Data points of 5 complete C-MAPSS FD001 training sequences and resulting SVR plane for RUL prediction .....	125
Figure 6-5: Correlation matrix of C-MAPSS FD001 training dataset features, constant features displayed in white .....	128
Figure 6-6: MD-based GA optimisation of 5 best scoring feature subset candidates per generation, C-MAPSS FD001 training data .....	128
Figure 6-7: Progression of raw feature 13 and MD (combining features 13, 15, 19) for 7 complete C-MAPSS FD001 training sequences .....	129
Figure 6-8: Usage of optimised hyperparameters between implemented methods.....	130
Figure 6-9: Used NN structures: AE condition deviation model (left); LSTM RUL prediction model (right).....	131
Figure 6-10: Overlaid MD-based health deviation $d_h$ and fault deviation $d_f$ for an exemplary run-to-failure sequence .....	132
Figure 6-11: HI resulting from MD-based health and fault deviations in Figure 6-10 after scaling and rolling average.....	132
Figure 6-12: AE reconstruction for healthy condition data of feature 13.....	133
Figure 6-13: AE reconstruction for faulty condition data of feature 13.....	133
Figure 6-14: Overlaid AE-based health deviation $d_h$ and fault deviation $d_f$ for an exemplary run-to-failure sequence .....	134
Figure 6-15: HI resulting from AE-based health and fault deviations in Figure 6-14 after scaling and rolling average.....	134
Figure 6-16: MD-SVR predictions of RUL based on 20 training sequences for 5 validation sequences (i.e., engines) .....	135
Figure 6-17: AE-SVR predictions of RUL based on 20 training sequences for 5 validation sequences (i.e., engines) .....	135
Figure 6-18: Prediction performance on the C-MAPSS FD001 test dataset over 30 runs per each box and whisker (RMSE, lower is better) of MD-QPoly, MD-SVR, AE-SVR, LSTM, MD-LSTM (* $p < 0.05$ , ** $p < 0.01$ ) .....	136
Figure 6-19: Average training durations over 30 runs per each data point of compared methods (C-MAPSS FD001), relative to LSTM (baseline) at full training set size of 100%.....	138
Figure 6-20: Prediction performance on the C-MAPSS FD002 test dataset over 30 runs per each box and whisker (RMSE, lower is better) of LSTM and MD-LSTM (** $p < 0.01$ ) ...	139



---

Figure 6-21: Prediction performance on the C-MAPSS FD003 test dataset over 30 runs per each box and whisker (RMSE, lower is better) of LSTM and MD-LSTM (* $p < 0.05$ , ** $p < 0.01$ ).....	140
Figure 6-22: Prediction performance on the C-MAPSS FD004 test dataset over 30 runs per each box and whisker (RMSE, lower is better) of LSTM and MD-LSTM (** $p < 0.01$ ) ...	140
Figure 6-23: Correlation matrix of FEMTO training dataset features, constant features displayed in white.....	144
Figure 6-24: MD-based GA optimisation of 5 best scoring feature subset candidates per generation, FEMTO training data .....	144
Figure 6-25: Progression of raw feature 4 and MD (combining features 4, 7, 8, 9, 12) for 6 complete training sequences.....	145
Figure 6-26: Prediction performance on the FEMTO test dataset over 30 runs per each box and whisker (RMSE, lower is better) of LSTM, MD-LSTM (** $p < 0.01$ ) .....	146
Figure A-1: Experimental setup of the instrumented plate [46] (a), stabilization diagram of the plate by the ITD OMA method (b).....	172
Figure A-2: Eigenfrequencies (top) and damping ratios (bottom) of the plate estimated by 6 different OMA methods .....	173
Figure B-1: Stabilisation diagrams of pLSCF implementations with real-valued (left) and complex-valued (right) polynomial coefficients (unstable poles: ·, stabilised frequency: *, stabilised frequency and damping: ●, target frequencies: red vertical lines) .....	182

## List of Tables

Table 2-1: Qualitative comparison of OMA and preprocessing methods at different operating conditions; - ... - - - : limited to no applicability; + ... + + + : suitable to preferred applicability .....	20
Table 2-2: Categories of OBMA case studies in existing literature.....	22
Table 2-3: Estimation errors of different OBMA orders from a car mock-up study [59] (modified from original representation to show minimum/maximum relative errors) .....	25
Table 2-4: Qualitative comparison of OBMA and general OMA at different operating conditions.....	28
Table 2-5: Summary of open datasets with vibration data of rotating machinery.....	30
Table 3-1: Different formulations of the instantaneous phase $\varphi$ for the complex sinusoidal function $e^{j\varphi}$ .....	57
Table 4-1: Simulation parameters.....	67
Table 4-2: Reference values for eigenfrequencies and damping ratios of the simulated structure .....	68
Table 4-3: Complex reference mode shapes of the simulated structure .....	69
Table 4-4: Simulated values and combinations of parameters initially provided in the extendable dataset.....	71
Table 4-5: Integration parameters and characteristics of the Newmark- $\beta$ configurations as the constant acceleration method and linear acceleration method .....	79
Table 5-1: Stabilisation criteria for modal identification .....	97
Table 5-2: Tolerance criteria for matched mode estimations .....	98
Table 5-3: Mode shape deflections from modes 3, 5, 7, 9, 11 – numerical reference and estimations by OMA and AOBMA at harmonic ratio 0.8 .....	104
Table 6-1: Implemented and compared RUL prediction methods .....	120
Table 6-2: Main properties of the C-MAPSS datasets .....	127
Table 6-3: Features of the C-MAPSS dataset.....	127
Table 6-4: C-MAPSS FD001 training hyperparameter search space and final optimisation values for implemented RUL prediction methods .....	131
Table 6-5: Prediction performance on C-MAPSS test datasets (RMSE, lower is better) .....	141
Table 6-6: Features of the FEMTO dataset .....	143
Table 6-7: FEMTO training hyperparameter search space and final optimisation values for LSTM .....	145
Table 6-8: Prediction performance on the FEMTO test dataset (RMSE, lower is better).....	146

---

Table B-1: Overview of pLSCF implementation variants in literature .....	183
Table D-1: Simulation parameters with corresponding dataset subfolder names and program code variables .....	188
Table D-2: Dataset folder and file structure .....	188
Table D-3: Execution steps for the conducted parametric simulations with Abaqus.....	191

# Nomenclature

## Operators

$\bullet^*$	Complex conjugate of a complex number or matrix entries
$\bullet^T$	Transpose of a matrix
$\bullet^H$	Hermitian (complex conjugate of the transpose) of a matrix
$\bullet^\dagger$	Moore-Penrose pseudo-inverse of a matrix
$\bar{\bullet}$	Average
$\text{Re}(\bullet)$	Real part of a complex number or matrix entries
$\text{Im}(\bullet)$	Imaginary part of a complex number or matrix entries
$ \bullet $	Absolute value, complex modulus, vector norm
$\angle \bullet$	Phase of a complex number
$\exp(\bullet) = e^\bullet$	Exponential function
$\ln(\bullet)$	Natural logarithm
$\delta(\bullet)$	Unit pulse function
$\tanh(\bullet)$	Hyperbolic tangent
$\text{adj}(\bullet)$	Adjugate matrix
$\det(\bullet)$	Matrix determinant
$\text{tr}(\bullet)$	Matrix trace
$\text{rank}(\bullet)$	Matrix rank
$\text{diag}(\bullet)$	Diagonal matrix with entries on the main diagonal
$\circ$	Elementwise (Hadamard) product
$\otimes$	Kronecker product
$\cap$	Intersection in set theory
$\setminus$	Relative complement in set theory

## Symbols

$j$	Imaginary unit, $j^2 = -1$
$t$	Time
$T$	Total duration
$d_{MD}$	Mahalanobis distance
$d_{l,m}$	Relative amplitude difference between order $l$ and $m$ in the AOBMA method
$h_{rat}$	Harmonic ratio
$\mathbb{C}$	Set of complex numbers
$\mathbb{R}$	Set of real numbers
$[I_N]$	Identity matrix of size $N \times N$

---

$[M]$	Mass matrix
$[C]$	Damping matrix
$[K]$	Stiffness matrix
$[H]$	Transfer function, frequency response function matrix
$[h]$	Impulse response function matrix
$[D]$	System matrix
$[K_{xx}]$	Covariance matrix
$R_{yy}$	Autocorrelation function
$w$	(Window) weighting function
$s$	Complex variable of the Laplace domain
$\{F\}$	Force vector
$\{u\}$	Displacement vector
$\{\dot{u}\}$	Velocity vector
$\{\ddot{u}\}$	Acceleration vector
$q$	Modal/generalised coordinate
$[S]$	Matrix of one-sided spectra
$[S^+]$	Matrix of half-spectra
$[K]$	Covariance matrix
$\{v\}$	Mode shape vector, eigenvector
$[V]$	Modal matrix
$\{g\}$	Operational reference vector
$[R]$	Residue matrix
$[LR]$	Lower residue matrix
$[UR]$	Upper residue matrix
$\lambda$	Eigenvalue/pole
$f$	Frequency
$f_\lambda$	Eigenfrequency
$f_{\lambda d}$	Damped eigenfrequency
$\omega$	Circular frequency
$\omega_\lambda$	Circular eigenfrequency
$\omega_{\lambda d}$	Damped circular eigenfrequency
$\sigma_\lambda$	Damping factor
$\xi_\lambda$	Damping ratio
$\eta_\lambda$	Hysteresis damping coefficient
$\theta$	Phase
$i_p$	Degree/order of a polynomial term
$i_o$	Output number

---

$i_r$	Reference number
$i_f$	Frequency number
$i_\lambda$	Pole/mode number
$N_p$	Highest degree/order of a polynomial
$N_o$	Total number of outputs
$N_r$	Total number of references
$N_f$	Total number of frequency lines
$N_\lambda$	Total number of poles/modes

## Abbreviations

AC	Alternating Current
AD	Angle Domain
AE	Autoencoder
AFPoly	Alias-Free Polyreference
AI	Artificial Intelligence
AOBMA	Averaged Order-Based Modal Analysis
BR	Balanced Realisation
CAE	Computer-Aided Engineering
CE	Cepstrum Editing
CFDD	Curve-fitting Frequency Domain Decomposition
C-MAPSS	Commercial Modular Aero-Propulsion System Simulation
CMSE	Cross-Modal Strain Energy
CNN	Convolutional Neural Network
COMAC	Coordinate Modal Assurance Criterion
CSD	Cross Spectral Density
DC	Direct Current
DCNN	Deep CNN
DFT	Discrete Fourier Transform
DI	Damage Index
DL	Deep Learning
DOF	Degree of Freedom
EFDD	Enhanced Frequency-Domain Decomposition
EMA	Experimental Modal Analysis
FDD	Frequency Domain Decomposition
FEM	Finite Element Method
FEMTO-ST	Franche-Comté Électronique Mécanique Thermique et Optique - Sciences et Technologies
FFT	Fast Fourier Transform

---

FRAC	Frequency Response Assurance Criterion
FRF	Frequency Response Function
FT	Fourier Transform
GA	Genetic Algorithm
GFD	Generalised Fractal Dimension
GPU	Graphics Processing Unit
GRU	Gated Recurrent Unit
GSM	Gapped Smoothing Method
HHT	Hilber-Hughes-Taylor
HI	Health Index
IATA	International Air Transport Association
IDFT	Inverse Discrete Fourier Transform
IFT	Inverse Fourier Transform
ITD	Ibrahim Time-Domain
IV	Instrumental Variable
LR	Lower Residual
LS	Least Squares
LSCE	Least Squares Complex Exponential
LSCF	Least Squares Complex Frequency Domain
LSFD	Least Squares Frequency Domain
LSTM	Long Short-Term Memory
LTI	Linear Time Invariant
MAC	Modal Assurance Criterion
MACX	Extended Modal Assurance Criterion
MACXP	Pole-Weighted Extended Modal Assurance Criterion
MD	Mahalanobis Distance
MDOF	Multiple Degree Of Freedom
MIMO	Multiple Input Multiple Output
ML	Machine Learning
MLP	Multi-Layer Perceptron
MPC	Modal Phase Collinearity
MSC	Mode Shape Curvature
MSDBI	Mode Shape Derivative-Based Damage Identification
MSED	Modal Strain Energy Decomposition
NL	Nonlinear
NN	Neural Network
OBMA	Order-Based Modal Analysis
ODS	Operational Deflection Shapes

---

OMA	Operational Modal Analysis
PDF	Probability Density Function
PHM	Prognostics and Health Monitoring
pLSCE	Polyreference Least-Squares Complex Exponential
pLSCF	Polyreference Least Squares Complex Frequency Domain
PSD	Power Spectral Density
RBF	Radial Basis Function
RFP	Rational Fraction Polynomial
RMFD	Right Matrix-Fraction Description
RMS	Root Mean Square
RMSE	Root Mean Square Error
RNN	Recurrent Neural Network
rpm	Rotations Per Minute
RUL	Remaining Useful Life
SDOF	Single Degree Of Freedom
SHM	Structural Health Monitoring
SIMO	Single Input Multiple Output
SISO	Single Input Single Output
SNR	Signal-to-Noise Ratio
SSI	Stochastic Subspace Identification
SSI-COV	Covariance-driven SSI
SSI-CVA	SSI Canonical Variate Analysis
SSI-DATA	Data-driven SSI
SSI-PC	SSI Principal Components
SSI-UPC	SSI Unweighted Principal Components
SVD	Singular Value Decomposition
SVM	Support Vector Machine
SVR	Support Vector Regression
TOMA	Transmissibility-based OMA
TP	Transient Phase
TSA	Time Synchronous Averaging
TVDFFT	Time Variant Discrete Fourier Transform
UR	Upper Residual
VK	Vold-Kalman
VSN	Virtual Sensor Network



# 1 Introduction

This chapter introduces the thesis by giving the background of its main research field as well as the associated relevance and motivation. Contributions and publications directly related to the thesis are also listed. Finally, an overview of the thesis is given in terms of chapter structure and content.

## 1.1 Wider scope and relevance of the research area

The wide availability and reliable operation of rotating machinery is crucial for many areas of our every-day lives. It spans industries, such as power generation; petrochemical production; manufacturing; road, air, and sea transportation; heat pump and air conditioning/refrigeration; aerospace; hard disk drives; textiles; and home appliances [1]. Throughout this chapter and subsequent chapters of this thesis, the focus is primarily on the aviation industry for the sake of specificity and conciseness, although the discussed topics and contributions remain generally applicable to a wider range of rotating machinery applications and industries.

The main domains of this thesis are subdivided into Operational Modal Analysis (OMA) and the prediction of Remaining Useful Life (RUL) of rotating machinery, which falls under the domain of predictive condition monitoring. Both fields deal with the evaluation of rotating machinery but have distinct relevant use cases. While OMA outputs modal parameters with primary use in the design and verification of rotating machinery, condition monitoring is concerned with providing information regarding the current or future machine condition, which is most relevant during the life cycle and towards the anticipated end-of-life or fault of the monitored machine.

### 1.1.1 Operational Modal Analysis (OMA)

The dynamic response of any mechanical structure is characterised by its modal parameters, like the mode shapes, damping ratios and eigenfrequencies (also known as natural frequencies or normal frequencies). Modal parameters play a major role during the design of mechanical components as well as system performance design, where the dynamic behaviour of multiple components must be considered at various operating conditions. Modal parameters, which are estimated from measurements of a physical structure, also serve to improve corresponding numerical models used in the development of new designs. This is achieved by model validation and model updating, where modal and material properties of the numerical model are compared and optimised to approach the characteristics of the reference physical structure. Otherwise, numerically estimated eigenfrequencies can often deviate at magnitudes around 30% from the physical structure due to difficulties to accurately model influencing factors such as the stiffness and mass distribution, boundary conditions, and non-structural components [2].

Modal parameters can change over the lifetime of a structure as they are influenced by the mechanical interaction of components, boundary conditions, temperature, and humidity [2]. Additionally, in case of systems with non-proportional damping or non-linear response, loading conditions representative of the final application scenario must be ensured for meaningful modal results [3]. Therefore, modal parameters derived during operating conditions of the tested structure are especially valuable. Operational Modal Analysis (OMA) must be employed to determine modal parameters of operating systems, since the excitation forces are unknown. This excitation is caused by the machine operation itself and in case of rotating machinery in particular, it can be caused by unbalance, rolling bearing elements, meshing gears, combustion and aerodynamic perturbations. This is the main difference to Experimental Modal Analysis (EMA), where the input excitation is known as in the case of shaker or hammer impact testing.

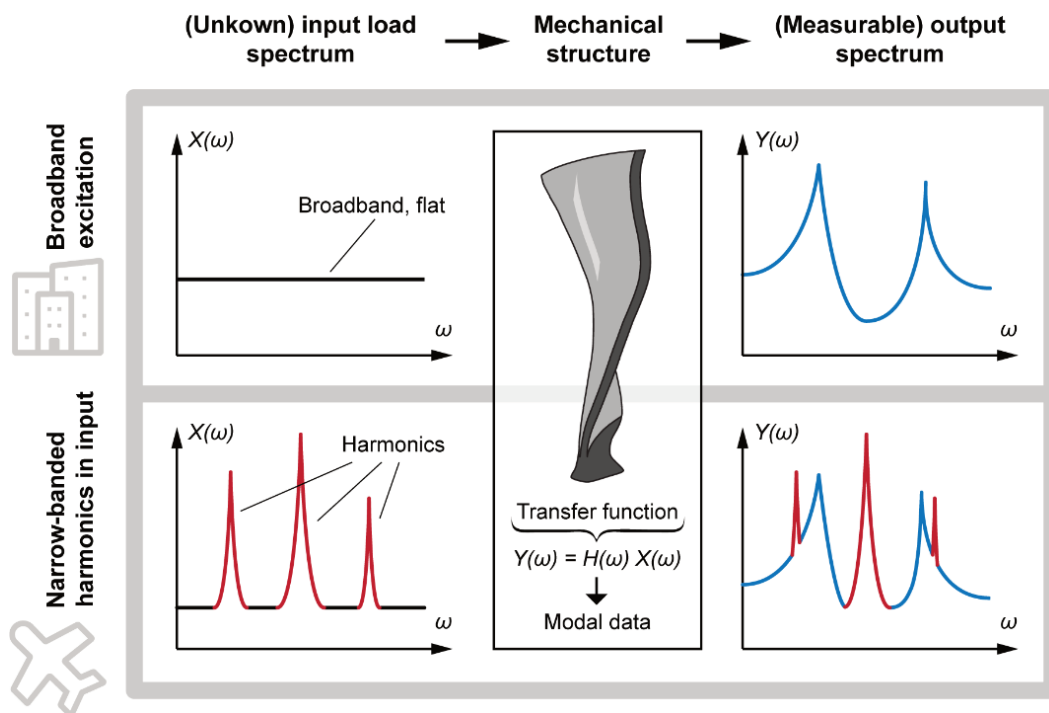


**Figure 1-1: Relationship between input  $X$  and output  $Y$  as a function of frequency  $\omega$  - broadband excitation with flat spectrum (top), excitation with input harmonics (bottom)**

In order to compensate this absent information, classic OMA methods presume the excitation force to have a flat broadband and zero mean frequency spectrum, i.e. the characteristics of white noise [4]–[6]. This is illustrated in the top portion of Figure 1-1 and is typically an appropriate approximation for civil engineering applications, where wind and traffic excitations suffice such conditions. In contrast to that, rotating systems generate predominantly harmonic, narrow-banded perturbations (bottom left of Figure 1-1), which violate this assumption and can therefore result in errors. For example, harmonic peaks can be falsely interpreted as structural modes and distort or mask estimated parameters of actual

structural modes [7]. These issues become more dominant the closer a harmonic and structural mode are located to each other [8], [9].

The issue of high harmonic amplitudes in the input force spectrum becomes more relevant in the context of transportation electrification. This is because additional sources for non-periodic excitation, e.g., due to friction or combustion, cease to exist with the reduction of components in electric engines compared to conventional combustion systems. This is even more severe in mechanical spinning tests, where components are tested in laboratory environment without contributions from other engine subsystems or wind, which would increase the level of random excitation. At the same time, spinning tests provide great potential for the acquisition of relevant modal parameters because of the tests' close representation of the rotating components in their final operating condition as opposed to measurements performed on stationary parts.

### 1.1.2 Condition monitoring

Increasingly strict requirements for fuel efficiency, environmental impact, and noise reduction motivate the development of new engine technology. In the domain of the civil aircraft industry, this has led to a trend of increasing turbofan diameters with high bypass ratios, the use of advanced materials and material treatment methods, more complex fan blade geometry, and geared multi-shaft engine configurations. Among others, these technologies are employed in the UltraFan engine, which is currently under developed by Rolls-Royce and expected to power future aircraft in the 2030s [10]. In spite of an increasing complexity of designs and tight operating margins [11], engine life cycle costs and safety remain top industry priorities.

Both related factors, cost and safety, are the main motivation for the development and utilisation of condition monitoring of turbofan engines [12]. Staying in the theme of civil aviation, it is shown that the aircraft engine is the primary and still increasing driver of maintenance cost in relation to total airline maintenance expenses, amounting alone to 41% in 2014 with an increase to 47% in 2018 [13].

Condition monitoring can be subdivided into diagnostics and prognostics tasks, with the latter being especially promising for anticipated benefits. As such, condition monitoring is expected to reduce cost by optimisation of planned maintenance through tailored logistics, inventory of spare parts, scale of repair work, and scheduling capacities based on evidenced need [12]. The fact that approximately 70% [14] of planned maintenance activities aimed at fault identification resulted in no findings emphasises the potential of condition-based maintenance. At the same time, approximately 20% to 35% [14] of aircraft unavailability during maintenance was due to unplanned maintenance. This is an overproportionally large amount in relation to the smaller share of aircraft affected by unplanned maintenance, which

makes an unplanned maintenance case much more costly than a planned maintenance case on average. Therefore, condition monitoring also provokes a wide interest from aircraft operators to reduce unplanned maintenance [14]. The prospect is to employ condition monitoring based on acquired operational aircraft data to identify previously unpredictable faults, allowing to plan and resolve these faults in time. Implications for cost and safety (including risks to human life) are enormous with the potential to prevent events such as unscheduled engine removals; component faults with secondary damage to subsystems; decreased efficiency due to faults such as engine bleed leaks, faulty active clearance, or variable geometry actuators [12].

The domain of data science in combination with automation and ML-based algorithms are seen by the research field as well as the aviation industry as foundational technologies to address the stated challenges [12], [14].

## 1.2 Original contributions of this work

The contributions of this thesis can be summarised into the following points, which cover the evaluation of state of the art in Chapter 2 and the main contributions from Chapter 4, Chapter 5, and Chapter 6.

- The initial contribution of this thesis is an **evaluation of the state of the art in existing literature from the perspective of OMA and RUL prediction for rotating machinery**. This covers a review of the broad range of methods for OMA and auxiliary signal processing of rotating machinery in Subchapter 2.1, followed by Subchapter 2.2 with a more specific evaluation of OBMA under various tests and comparison cases. The review work of Subchapter 2.1 [15] and Subchapter 2.2 [16] was published as separate dedicated peer-reviewed conference papers. Next, Subchapter 2.3 evaluates the landscape of existing open vibration datasets from rotating machinery and gauges their applicability in the fields of OMA and (predictive) condition monitoring. Finally, Subchapter 2.4 investigates the potential of modal parameter-based condition monitoring and evaluates the state of the art in RUL prediction by ML methods.
- The first **open simulation dataset for vibration signal processing and OMA of rotating machinery during acceleration** is introduced. The developed dataset contributes to more reproducible research and facilitates comparability between independent studies by providing a benchmark problem. Three varied operational parameters are included in the dataset to provide a foundation for parametric studies of future and existing methods. In addition to the time-series acceleration response of the simulated structure, the simulation source code is made publicly available with the intention to enable extensibility and adaptation of the dataset for future research. The

dataset is an extension of the simulation setup first introduced by the thesis author in a peer-reviewed journal publication [17] and is covered by a separate paper submitted on 06/08/2022 for peer-reviewed journal publication [18] along with the proposed open-source dataset [19].

- The novel method **Averaged Order-Based Modal Analysis (AOBMA)** is introduced and evaluated along with **Order-Based Modal Analysis (OBMA)** and a general **OMA** method during transient order excitation in a parametric comparison study. Compared to the existing OBMA method, the introduced AOBMA method provides a unified set of results with a higher consistency of accurate results. The accompanying parametric comparison study validates the AOBMA method. Furthermore, the impact of the excitation conditions in terms of harmonic order and random excitation amplitudes on the compared methods is evaluated. This gives new insight for the interpretation of results and selection between the compared methods depending on present excitation conditions. The novel AOBMA method and parametric comparison study underwent a peer review process and resulted in a journal publication [17] by the thesis author.
- A novel methodology for **data-efficient Remaining Useful Life (RUL) prediction from a limited number of run-to-failure training sequences** is introduced. The presented approach allows to improve model generalisation, leading to higher prediction accuracy when the number of training sequences is significantly reduced. Several implementations of the proposed methodology are evaluated and compared in terms of prediction performance and training duration depending on relative training data reduction. This work is based on a Neural Network (NN) architecture and the Mahalanobis Distance (MD) metric, which were introduced and demonstrated in a previous peer-reviewed journal publication [20] of the thesis author. The gained results from the RUL prediction study aid an informed selection between the compared methods depending on the availability of training data and computational resources, which can be related to requirements for energy consumption and the permissible environmental footprint. The novel methodology for RUL prediction and findings from the associated comparison study resulted in a peer-reviewed journal publication [21].

## 1.3 List of publications

### 1.3.1 Published

1. G. Sternharz and T. Kalganova, "Current Methods for Operational Modal Analysis of Rotating Machinery and Prospects of Machine Learning," in Proceedings of the 38th IMAC: Rotating Machinery, Optical Methods & Scanning LDV Methods, vol. 6, 2020, pp. 155–163. [15]
2. G. Sternharz, C. Mares, and T. Kalganova, "Performance of order-based modal analysis for operational rotating hardware considering excitations composed of various harmonic and random amplitudes," in Proceedings of ISMA 2020 - International Conference on Noise and Vibration Engineering, 2020, pp. 1465–1479. [16]
3. G. Sternharz, T. Kalganova, C. Mares, and M. Meyeringh, "Comparative performance assessment of methods for operational modal analysis during transient order excitation," Mechanical Systems and Signal Processing, vol. 169, pp. 108719 (1–29), 2022. [17]
4. G. Sternharz, J. Skackauskas, A. Elhalwagy, A. J. Grichnik, T. Kalganova, and M. N. Huda, "Self-Protected Virtual Sensor Network for Microcontroller Fault Detection," Sensors, vol. 22, no. 2, pp. 454 (1–27), 2022. [20]
5. G. Sternharz, A. Elhalwagy, and T. Kalganova, "Data-Efficient Estimation of Remaining Useful Life for Machinery with a Limited Number of Run-to-Failure Training Sequences," IEEE Access, vol. 10, pp. 129443–129464, 2022. [21]

### 1.3.2 Submitted for publication

6. G. Sternharz, T. Kalganova, and C. Mares, "Simulation Dataset for Signal Processing and Operational Modal Analysis of Rotating Machinery Vibration During Acceleration," Computing in Science & Engineering, pp. 1–10, 2022. [18] – Currently under review, submitted on 06/08/2022.
7. G. Sternharz, "Simulation Dataset for Signal Processing and Operational Modal Analysis of Rotating Machinery Vibration During Acceleration," Mendeley Data, 2022. [Online]. Available: <https://data.mendeley.com/datasets/8z2db4rswr/draft?a=9056040e-ab32-47bb-b1bc-9e331ec042be>. [19] – Currently under review with [18], submitted on 06/08/2022.

## 1.4 Structure and outline of the thesis

This subchapter gives an overview of the thesis structure and outlines the main content of each chapter. A schematic illustration of the thesis structure is given in Figure 1-2.

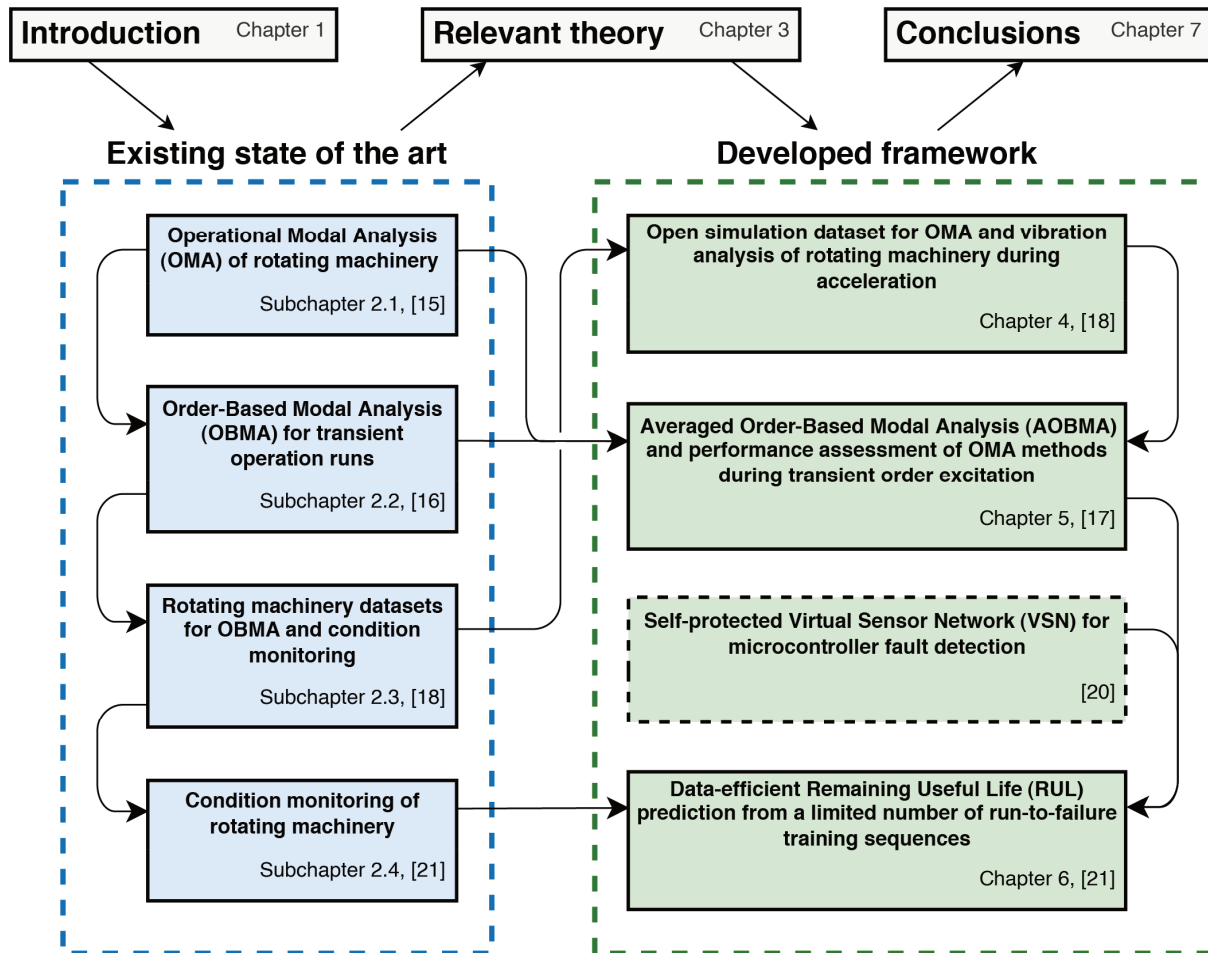


**Figure 1-2: Graphical structure and flow of the thesis**

Following this chapter, the existing state of the art is evaluated in Chapter 2. Existing methods to facilitate OMA despite disturbing harmonics from rotating machinery are evaluated in Subchapter 2.1. For cases in which the excitation is dominated by harmonic forces and in which random force contributions are insufficient to excite structural response, a transient acceleration or deceleration run is required to distribute the excitation force and achieve structural response over a broad range of measured frequencies. The OMA method titled Order-Based Modal Analysis (OBMA) is an existing method, which was developed for this purpose and proved in various case studies detailed in Subchapter 2.2.

However, certain limitations and unknowns are still linked to OBMA as identified by Subchapter 2.2. This includes the requirement of OBMA to analyse tracked orders individually, which produces fractured sets of results with added ambiguity and higher variance of modal parameter estimations. Furthermore, the existing body of research shows a lack of direct performance comparisons between OMA methods in general, including

OBMA in particular. At the same time, there is no systematic study analysing the performance of OBMA across a range of varied excitation conditions. A reason for this circumstance lies in the lack of suitable open datasets, as discussed in Subchapter 2.3.

The first part of Subchapter 2.4 evaluates the domain of condition monitoring in terms of existing methods based on modal parameters. However, besides the mentioned use cases of modal parameters, modal parameter-based condition monitoring methods have not been successfully demonstrated for predictive condition monitoring and are currently not suitable for most practical applications due to the required testing conditions. In contrast to that, ML-based predictive condition monitoring methods are proved in various applications of operational rotating machinery and are shown to achieve state-of-the-art performance as shown in the second part of Subchapter 2.4. However, the required amount of run-to-failure training sequences is a limiting factor for these methods since these data are time and cost-intensive to obtain, which is also supported by the overview of available datasets in Subchapter 2.3.

Chapter 3 provides the relevant terminology and acts as a reference of theoretical introductions to methods utilised in subsequent chapters of the thesis.

Chapter 4 develops an open-source simulation dataset of a structure excited by a rotating force at a simulated machine acceleration. The time-response in the dataset is provided at varying parameters, such as measurement noise, levels of harmonic and random input amplitudes as well as machine acceleration rate. This also addresses the gaps highlighted in Subchapter 2.1, Subchapter 2.2, and Subchapter 2.3, such as the lack of OMA comparison studies. The proposed dataset facilitates reproducibility and comparability of work both in this thesis and future research in this area.

In Chapter 5, this dataset is utilised for a comparative study on OBMA and on the impact of various operating conditions in terms of harmonic and random excitation amplitudes on estimation results. The findings of this study aid result interpretation and provide guidance for the application of OMA and OBMA at transient acceleration runs. Furthermore, several limitations of OBMA identified in Subchapter 2.2 are solved by the proposed AOBMA method, which results in higher accuracy of estimations compared to OBMA. Aiding clarity, AOBMA results are also comprised of a single set of results in contrast to the fractured result sets of OBMA.

Chapter 6 introduces a novel methodology for RUL prediction of rotating machinery, which is a significant task in predictive condition monitoring. The proposed methodology addresses the issue of the required training data amount demonstrated in Subchapter 2.4 by utilising data of entirely healthy and faulty condition data and employing data fusion of individual dataset features. The impact of this contribution is an increase in prediction accuracy when a



fraction of the original training sequences is available, which was demonstrated using an open dataset of simulated turbofan engine degradation. The chapter also analyses the associated reduction of training time and thus computational resources, which is a further benefit with implications for energy consumption and environmental sustainability.

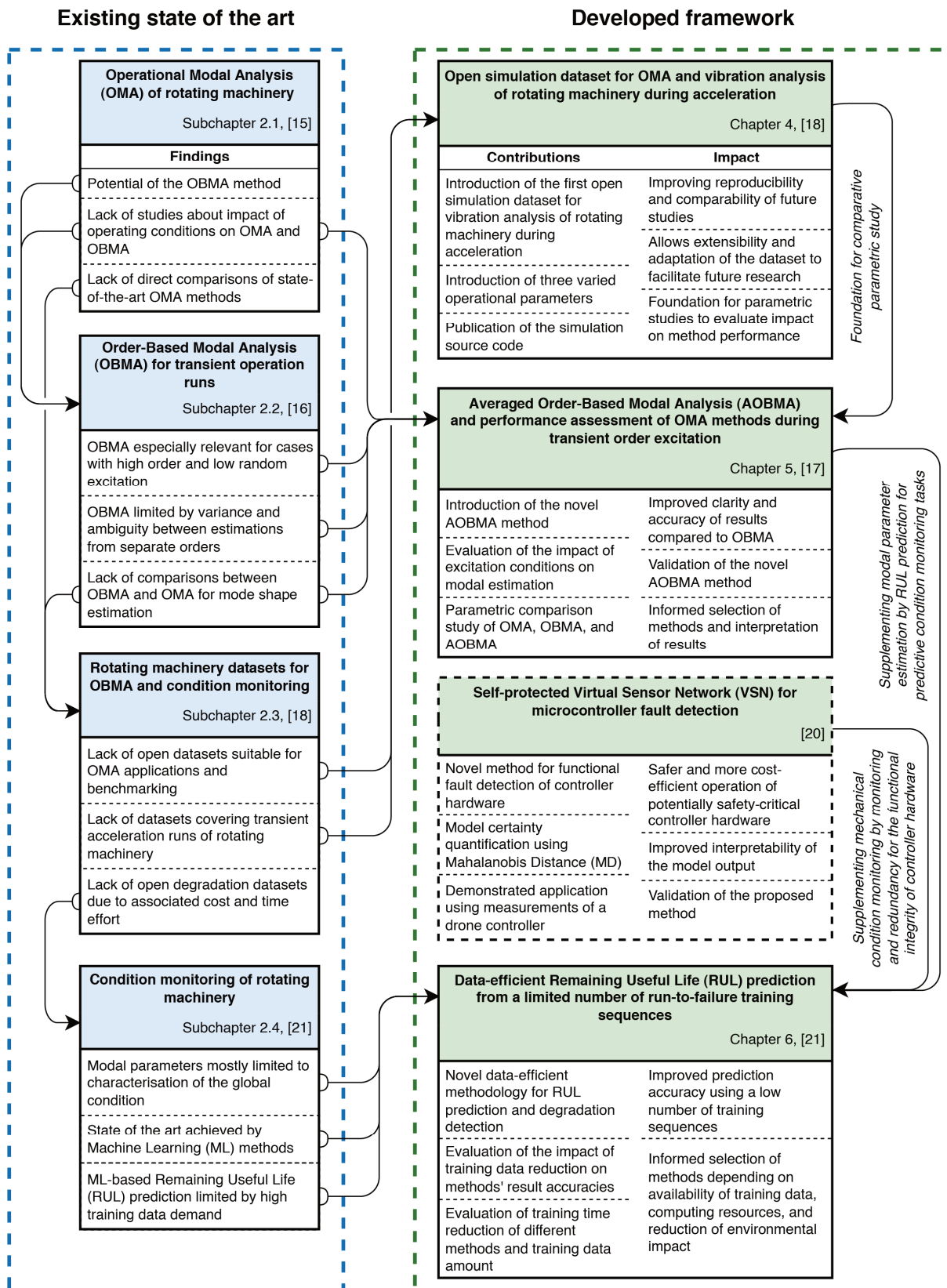
Finally, Chapter 7 draws overall conclusions from the research work presented in this thesis and gives recommendations for future research directions.

It should be noted that an additional novel method was published by the thesis author and is marked by a dashed border in the bottom right of Figure 1-2. It is based on the Virtual Sensor Network (VSN) technology and allows to identify the functional integrity of machine controller hardware [20]. While this thesis does not focus on this additional method, it is considered complementary to the proposed RUL prediction from Chapter 6. While the RUL prediction quantifies and predicts the degrading machine condition, the VSN-based method evaluates the functional integrity of the machine controller and can provide redundant controller outputs in case of detected malfunctioning due to hardware defects, software bugs, or malicious acts like sabotage/hacking. In addition, the VSN-based method provided supporting proof of methods later employed in the RUL prediction contained in this thesis, including the MD, Long Short-Term Memory (LSTM) NN, and Autoencoder (AE) NN.

Figure 1-3 provides a more detailed graphical summary of the discussed contributions and core chapters of the thesis.

The present chapter introduced the research field of this thesis and presented the outline of the thesis' structure and conducted work. The motivation for the research area was introduced based on the relevance of the evaluation of rotating machinery at different stages of the machine life cycle (incl. the design, test, and in-service phases) for a more reliable, efficient, and safe machine operation.

The next chapter is dedicated to an exploration of the current state of the art in the introduced domains to identify research gaps and thereby to provide a foundation and further motivation for the research work presented in course of this thesis.



## 2 State of the art in existing research

After the previous introductory chapter gave the background, overarching motivation, and outline of this thesis, the present chapter provides a critical review of the current state of the art in existing literature. The following subchapters are concerned with distinct aspects regarding the physical evaluation of rotating machinery.

Subchapter 2.1 covers a wide range of methods for OMA and auxiliary signal processing methods with applications for rotating machinery. This subchapter resulted in a peer-reviewed conference publication [15]. Based on the identification of the most relevant methods and their limitations in Subchapter 2.1, the next Subchapter 2.2 focuses on the OBMA method for analysis of transient acceleration or deceleration machine runs. This subchapter gave rise to a further peer-reviewed conference publication [16]. Subchapter 2.3 then investigates the existing landscape of publicly available vibration datasets of rotating machinery since suitable data is a foundational pillar for the development and verification of methods, including OBMA and condition monitoring methods. Subsequently, Subchapter 2.4 covers existing research in the field of condition monitoring by modal parameter-based methods, followed by the current state of the art in predictive condition monitoring methods, which are mostly ML-based. The final Subchapter 2.5 is used to summarise the main findings and conclusions of Chapter 2 to set out the path for the remaining chapters of the thesis.

### 2.1 Operational Modal Analysis (OMA) in the presence of harmonic excitation from rotating machinery

This subchapter covers OMA methods, which consider or have been tested in conditions containing harmonics in the input excitation, since this is a main characteristic of rotating machinery vibration. The following subchapters classify the methods based on the approach of how harmonics are considered within the respective methods. This subchapter resulted in a peer-reviewed conference publication [15] by the thesis author.

The objective of this subchapter is to provide a review of current methods that can be used for OMA of rotating machinery. The methods' strengths and limitations are highlighted to assist an informed decision between methods to be applied and to outline areas for further research.

#### 2.1.1 Methods not specifically adapted for input harmonics

There is a variety of OMA methods, which do not specifically account for harmonics originating from the input load. Nevertheless, several of these methods were tested in case studies dedicated to the methods' application in such conditions and show considerable performance in certain use cases.

### *Stochastic Subspace Identification (SSI) Methods*

Stochastic Subspace Identification (SSI) algorithms form a family of time-domain OMA methods and benefit from a large application experience in research and industry.

In 2015, Yang et al. [22] performed a comparison of three parametric time-domain OMA methods in the presence of harmonics using a simulated system with 5 degrees of freedom (DOF). The authors note that system responses, which can be attributed to harmonics in the excitation can be considered as non-structural modes with a theoretical damping value of zero. However, the following limitation should be noted with regards to simulation data instead of signals from actual operating machinery: It is observed that measurements of real systems result in damping ratios of harmonic peaks that are greater than zero and can reach values which inhibit a distinction between real structural modes and virtual harmonic modes [23], [24].

The covariance-driven Stochastic Subspace Identification (SSI-COV) showed the lowest performance as it detected the least amount of actual modes and produced spurious double poles instead of a single pole at frequencies with strong resonance response in the output. At the same time, the projection-based, i.e., data-driven Stochastic Subspace Identification (SSI-DATA) provided the best results with relatively clean stabilisation diagrams, most accurate detection of harmonics in terms of frequency and damping values close to zero. SSI-DATA was the only of the compared methods to correctly determine both the structural (34.5 Hz) and harmonic (34.6 Hz) mode at close proximity. This capability of the SSI-DATA method was also reported by Jacobsen in 2006 [7]. From the same signals, the Instrumental Variable (IV) method determined solely the harmonic as a stable pole, while the SSI-COV method failed to establish a stable pole throughout multiple model orders at either of the two peaks. The IV method showed less clean stabilisation diagrams compared to SSI-DATA. Although it detected less spurious numerical modes compared to SSI-DATA, it also showed less actual modes as stable poles [22].

The results are largely supported by a previous comparison study from 2001 [5], where the same OMA methods have been compared at the presence of pure white noise without harmonics in the excitation input. Even though the study found no observable differences between the performance of SSI-DATA and SSI-COV in the conducted simulation, the authors note that the SSI-DATA algorithm is numerically superior. However, the downside of higher computational cost, required by SSI-DATA, is reported as well [5], [25]. Similar to results of the previously discussed study, the IV method showed worse results in the estimated mode shapes and required a higher model order for mode identification.

Unfortunately, the introduced publication only provides a tabular/numerical comparison of falsely estimated modes due to harmonics while the comparison of estimated values for the

actual structural modes is limited to the resulting stability-diagrams [22]. The applicability to real operating structures with harmonics has yet to be investigated, since the provided comparison results are based on a simulated point-mass system. A potential downside of SSI methods is the relation between the modal frequencies of interest and required measurement time, which demands longer measurements for estimation of low frequency modes [7], [26]. Moreover, it has been found that SSI is susceptible to severely underquantified data, which is reported to occur during rocket launcher flight measurements [27].

#### *Poly-reference Least Squares Complex Frequency Domain (pLSCF) Method*

The poly-reference Least Squares Complex Frequency Domain (pLSCF) estimation has shown respectable results in a study of a real wind turbine at a constant rotating speed in operational conditions [23]. It provided approximately equal results compared to the modified Least Squares Complex Exponential (modified LSCE) time domain method, depending on the accuracy of assumed harmonic frequencies. The modified LSCE method requires harmonic frequencies to be provided before the algorithm is applied. Thus, it falls under the category of methods with explicit consideration of harmonics, presented in the upcoming Subchapter 2.1.4.

In an analysis of simulation data by the pLSCF method, it was shown that a harmonic frequency coinciding with a modal frequency led to spurious stable poles around this frequency [28]. The authors also performed real operational analyses: Data from a large diesel engine produced such strong harmonic peaks, that the algorithm falsely identified them as the sole modes of the structure. However, application on in-flight vibration measurements of a helicopter showed that the pLSCF method was able to detect modes despite harmonic disturbances. The authors propose Time Synchronous Averaging (TSA) for the reduction of harmonic disturbances from the time signal to enhance the subsequent modal estimation by the pLSCF or any other OMA method. Therefore, TSA will be presented in Subchapter 2.1.3.

Although different studies report successful utilisation of the SSI [22], [29] and pLSCF [8], [23], [28] methods for modal estimation of rotating machinery under operating conditions, it is believed that no direct performance comparison of these methods has been performed yet.

#### *Other modal estimation methods*

Compared to SSI-DATA methods, the methods Frequency Domain Decomposition (FDD) and Enhanced Frequency Domain Decomposition (EFDD) are less reliable in cases with close harmonic and structural modes, potentially producing biased estimations and wrong identification [7].

The In-Operational Modal Appropriation (INOPMA) method [30] and the Transient Phase (TP) method [31] both identify system resonances and harmonics using phase information. While the former achieves this through numerical appropriation with discrete sine signals, TP requires parameters, which are extracted by curve fitting of processed measurements. To this date, the application of TP has been demonstrated on simulated Single Degree Of Freedom (SDOF) systems only. Utilisation for real systems with Multiple Degree Of Freedom (MDOF) is not yet possible [31]. Moreover, the performance evaluation with harmonic disturbances only considered cases with harmonic amplitudes of up to 50% of the original system response. However, harmonics of rotating machinery can reach far higher amplitudes than the structural response [28], [32]. In a comparison to the Balanced Realisation (BR) method, which belongs to the SSI-COV category mentioned earlier, INOPMA showed lower variance and relative error in the estimated damping and eigenfrequency values [30], [33]. The drawback of INOPMA is that it relies on the slope of the phase difference curve in the frequency domain to distinguish between harmonics and structural modes. However, the slope depends on the damping of the identified resonance and therefore the limiting assumption of low harmonic damping ratios applies here as well. In summary, both methods have considerable drawbacks at the current stage in relation to the intended research application. Moreover, the performance of INOPMA and TP at close proximity of harmonic excitation frequencies and eigenfrequencies has yet to be analysed.

### 2.1.2 Methods for identification of harmonics

The group of methods presented in this subchapter provides means to identify measured signal components, which are caused by a harmonic excitation in the input spectrum. Since these methods do not output estimated modal parameters, they are not considered as OMA methods. However, these methods are useful in cases without sufficient knowledge of the excitation regarding potential harmonics. This could be the case for gear mesh frequencies if the gear configuration is unknown or for unexpected sources of harmonic excitation, like the electric current frequency [34][35].

Estimated modal data can be acquired with traditional OMA methods, which do not consider harmonic disturbances. By doing so, it is likely that harmonics are falsely detected as modes. However, they can be omitted by the analyst, provided that the harmonic frequencies are known or have been previously identified. Another scenario is to incorporate these methods as a pre-processing step in further data algorithms. This especially applies to methods presented in the next two subchapters, namely those, in which harmonics are reduced from the measurements or explicitly considered in the modal estimation.

In the context of rotating machinery and spinning tests, however, the current number of rotations per minute (rpm) is often known and recorded during operation. Thus, the fundamental frequency and higher harmonics can be easily derived without additional

analysis. Therefore, this subchapter is limited to a broad overview of existing literature in this area.

Several methods utilise the statistical properties of the measured signal to distinguish excitation harmonics from actual structural modes. The Probability Density Function (PDF), the derived Entropy index as well as the Kurtosis value fall into this category [7], [36]. The PDF can be also utilised to identify spurious mathematical modes, which can originate from the mode estimation procedure. However, both the PDF and Kurtosis are limited to cases with constant harmonic frequencies with low damping as shown in an experiment with an operating wind turbine [23].

Further research was conducted regarding the Kurtosis to increase processing speed by reducing the number of channels and frequency bands considered in the analysis [37] and to increase the certainty of the estimation by optimisation of the sample count, band filtering, etc. with the Optimised Spectral Kurtosis [35].

Other methods used to assist in identification of harmonics are the Short Time Fourier Transform and Singular Value Decomposition (SVD). Methods based on the results of OMA are the Visual Mode Shape Comparison, Modal Assurance Criterion (MAC) and Stabilization Diagram. An overview of these methods is provided in [7].

### 2.1.3 Methods for reduction of harmonics from the signal

The following methods aim to reduce disturbing harmonics, which do not originate from a structure response, from the measurement. While this procedure does not provide modal parameters by itself, it can facilitate the estimation of modal properties with a subsequently applied OMA method.

#### *Time Synchronous Averaging (TSA)*

The TSA method performs resampling of the original time signal to the order domain, transforming data samples per time interval to data samples per rotation angle. This requires that a known stationary speed must be present, or an accurate speed profile of the monitored machine must be known. The TSA signal isolates signal components, which are synchronous to the reference rotation (including its integer multiples, i.e. harmonics) as the remaining signal contributions are averaged out. By a subtraction of the TSA signal from the original signal (in the angle domain), signal components originating from harmonic excitation can be eliminated. Finally, the filtered signal is resampled back to the time domain, so it can be processed further by any OMA method. A limiting factor of this method is the processing time due to the involved double resampling. However, there is an equivalent formulation of the TSA, which applies the Fourier Transform (FT) to time-domain sections of individual rotation cycles and averages them in the frequency domain [38]. Since this approach does not require resampling and can be implemented with the Fast Fourier Transform (FFT)

instead, it can offer an advantage in processing time. A review comparing TSA algorithms using the order domain and frequency domain in further detail can be found in [39].

The TSA method was applied in a 6 DOF simulation [28] and despite a harmonic coinciding with a structural mode, the method was able to remove its disturbing influence on the subsequent modal estimation with the pLSCF method. Results of the same publication from a real operational in-flight helicopter and a running diesel engine showed that TSA led to much cleaner stabilisation diagrams and thus facilitated the estimation of structural modes. Unfortunately, the report lacks quantitative comparisons between simulated modal parameters and the estimated parameters obtained using the proposed method.

However, other OMA case studies showed mixed results [23], [40], [41] and indicate that the method's harmonic removal is hampered at the presence of variability in the operational speed profile. The reason for a reduced performance of TSA is not the speed variability itself but rather the accompanying variation in harmonic signal amplitudes. In such cases, the TSA will adapt an average amplitude of the synchronous signal components, which will not match the instantaneous (variable) harmonic amplitudes of the original signal. In this case, the subtraction of the TSA signal can result in an insufficient reduction of harmonics or even lead to the introduction of harmonic disturbances in signal sections, where the TSA amplitude is an overestimation of the instantaneous target values.

Some extensions of the TSA method exist, which address this limitation by modelling and introducing amplitude modulation to the modified TSA signal [42], [43]. While existing publications of these extended TSA algorithms seem to be limited to the fault analysis domain, they appear to have potential for OMA with signals suffering from harmonic contaminations with varying amplitudes.

### *Cepstrum editing*

Cepstrum Editing (CE) separates harmonic signals from the actual structural response by filtering, which is called "liftering" in the cepstrum domain. The cepstrum is usually computed from the original time-signal by first determining its FFT spectrum, which is subsequently log-scaled. Finally, the inverse FFT is applied to obtain the cepstrum.

In an application of CE, a notch "lifter" and exponential short-pass "lifter" (the equivalents of a frequency-domain notch and low-pass filter, respectively) were applied to the cepstrum from a wind turbine operating at constant speed. This procedure noticeably reduced harmonic peaks from the signal in the frequency domain and lead to a higher number of identified structural modes. TSA was not able to remove harmonics in this case, as stated above, presumably due to a wider spread of harmonic peaks of the wind turbine [40]. A similar result comparing CE and TSA is reported on a gearbox casing, which is excited by order harmonics with time-varying frequencies [41]. Similar observations were made when comparing CE to



Kurtosis and the Probability Density Function methods discussed in the previous Subchapter 2.1.2. Data from a wind turbine with an increased spread of harmonic peaks (interpreted as higher damping) showed that the Kurtosis method performed inconsistently, determining approximately half of the present harmonics. CE, on the other hand, was able to eliminate 4 out of 5 false modes due to harmonics [23].

Another operational dataset with constant harmonic components was measured from helicopter fuselage at steady flight. In this experiment, TSA removed one harmonic more than the CE procedure. However, the achieved reduction of harmonics was otherwise similar and the presented CE approach required less processing resources, since no resampling is needed in contrast to TSA [44].

However, it should be noted, that CE can introduce spurious numerical modes and additional damping [41]. In theory, the magnitude of this added damping can be determined and subtracted from the final results, however, a residual excess in damping values can still remain in some cases [40], [41].

#### *Other methods*

A method based on the Vold-Kalman filter [45] was originally developed for order-tracking. With some modifications of the original method, it was shown to remove harmonics from measurements of a wind turbine gearbox without distorting the phase information [34]. Unfortunately, the authors provide only a qualitative result of the filtering method, based on amplitude and phase graphs of the processed and unprocessed signal in the frequency domain. In these graphs, the method does not seem to completely remove every harmonic peak. In addition, the harmonic and structural mode frequencies appear to be well separated in this experiment although the specific frequency distance is not specified either. A deeper evaluation of the Vold-Kalman filter for harmonic reduction could be achieved with a comparison of OMA results based on the original and filtered signal including cases of close proximity between a harmonic peak and structural mode.

Methods presented by Jacobsen et al. [37], [46], [47] utilise Kurtosis, introduced in the previous Subchapter 2.1.2, to identify potential frequencies with harmonic excitation. Afterwards, a Singular Value Decomposition (SVD) plot of the measurements is calculated and the harmonics are reduced from the plot by linear interpolation. The modified SVD functions are then used in the Enhanced Frequency Domain Decomposition (EFDD) OMA method. In a later work [37], the authors incorporated the Curve-fitting Frequency Domain Decomposition (CFDD) as an alternative OMA method, since it is less sensitive to bias in the estimation due to the interpolation. As a result, an improved estimation of structural modes in close proximity or exact coincidence with a harmonic peak was achieved. However, at this point, it remains unclear how this updated and combined method of harmonic reduction and

modal estimation with CFDD compares to more established methods like pLSCF or SSI, discussed in Subchapter 2.1.1.

A further study [48] focuses on harmonics with both amplitude and frequency varying over time. The study compares two methods to filter time-varying harmonics from the response spectra in the frequency domain (based on angular domain and on short-time Fourier Transform) and two approaches in the time domain based on the complex demodulation method. The results indicate that the proposed harmonic removal filter based on complex demodulation leads to the lowest errors for the damping ratio estimated by subsequent OMA.

#### 2.1.4 OMA methods with explicit consideration of harmonics

OMA methods of this category require harmonic frequencies to be provided explicitly as input parameters and consider them in the modal analysis. The required frequencies can be acquired from the results of a harmonic identification method like those presented in Subchapter 2.1.2 or from knowledge of the excitation characteristics, e.g., based on engine order frequencies, derived from the rotation speed.

Methods proposed by Mohanty and Rixen [9], [49], [50] extend several existing OMA algorithms to explicitly take known harmonics into account for a more truthful system identification. In shaker experiments of the authors, the modified LSCE method showed noticeable improvement compared to the polyreference LSCE (pLSCE) method in terms of identification of closely spaced structural modes and harmonics [9]. Based on simulation data, Motte et al. [23] showed that the modified LSCE mostly provides more consistent results and a slightly more accurate estimation of the eigenfrequency and damping ratio compared to pLSCF. However, at close frequencies of a harmonic and structural mode, similar or slightly better estimation performance was observed in favour of pLSCF. It was also shown that exact knowledge of the harmonic frequency is essential for the modified LSCE method. In an experiment with an operational wind turbine, the method did not eliminate all harmonic peaks, which is explained by the imprecision of the wind turbine rpm measurements, which are required to calculate harmonic frequencies. It is also noted that the modified LSCE produces more spurious mathematical modes compared to pLSCF [23].

#### 2.1.5 OMA methods with implicit consideration of harmonics

The methods presented below are inherently not negatively affected by the presence of harmonics in the excitation spectrum. Despite this promising outlook, these methods have other limitations, which are also highlighted below.

##### *Transmissibility-based OMA (TOMA)*

Transmissibility-based OMA (TOMA) is capable of handling excitation forces that are heavily influenced by harmonic inputs or coloration of input noise [51]. This is due to the capability of

the method to determine modal system parameters directly, independently from the input spectrum. However, multiple transmissibility functions are required for this process, which requires their determination at different loading conditions. In context of mechanical spinning tests, this would result in a delay depending on the occurrence of different loading states within a test cycle, impeding real time analysis. Moreover, it is questionable if a change of operating conditions can provide a change in the loading conditions that is sufficient for the method. In addition, the method requires the number of uncorrelated input loads to be estimated. These factors inhibit an application in real operating scenarios, since these values are unknown. The performance of TOMA in real operational environment has not been demonstrated yet. Current experiments are limited to simulations [52] and laboratory set-ups [51] with a known number of spatially clearly separated and independently acting input loads. Although TOMA bears high potential for cases with severe deviations from the assumption of a white noise input spectrum, it can be concluded that this method is in an early stage of development. Therefore, it is currently not suitable for the intended use with rotating machinery.

#### *Order-Based Modal Analysis (OBMA)*

Order-Based Modal Analysis (OBMA) [53] is a method that follows a different approach compared to the previously presented OMA methods, i.e., OBMA utilizes harmonic input loads, originating from rotation orders of the running components.

However, at stationary operation, each of the harmonics in the input signal only covers a narrow frequency range, inhibiting the desired excitation of structural modes. Therefore, OBMA requires the vibration measurements to be performed during an acceleration or deceleration run of the evaluated machinery. Order tracking is performed to identify the amplitude and phase of individual orders as a function of rpm. Hence, the rotating speed, i.e., tacho signal is required. Afterwards, a tracked order function is provided as input for OMA. This method has been compared to OMA with pLSCF in operational experiments with wind turbine gearboxes [53] as well as acoustic and vibrational measurements from a 4-cylinder car [54], [55]. These studies showed that the processing of run-up conditions by OMA can lead to falsely identified modes, called end-of-order modes, which occur at the final frequencies of the present machine orders. OBMA bypasses this issue since it only considers a single order per analysis.

With the absence of sufficient random excitation in combination with an acceleration or deceleration run, it is expected that this method can outperform the previously introduced OMA methods. This is supported by a more recent study of a planetary gearbox [56], which was tested by hammer impact EMA, OMA with pLSCF and OBMA. It was found that the pLSCF method at stationary operating conditions only identified 8 out of 13 modes, which were captured by EMA and OBMA.

### 2.1.6 Summary

Findings from the presented review of existing OMA methods are discussed below. Afterwards, potential research areas for future work are highlighted.

There is a variety of methods, which have been used at the presence of harmonic signals in the excitation load as illustrated in the presented review. A qualitative comparison of the methods, which were shown to be especially promising for rotating machinery applications, is summarised in Table 2-1.

**Table 2-1: Qualitative comparison of OMA and preprocessing methods at different operating conditions; - ... - - - : limited to no applicability; + ... + + + : suitable to preferred applicability**

Method	Rotating machinery testing conditions	
	Stationary (constant speed)	Transient acceleration/deceleration
Order Based Modal Analysis (OBMA) [53] <sup>a</sup>	- - -	+ + +
Stochastic Subspace Identification (SSI) [22] <sup>a</sup>	+ + + *	+
Poly-reference Least Squares Complex Frequency Domain (pLSCF) [23] <sup>a</sup>	+ + + *	+
Time Synchronous Averaging (TSA) [39] <sup>b</sup>	+ + +	- -
Cepstrum Editing (CE) [40] <sup>b</sup>	+ +	+ +

a. Method for Operational Modal Analysis; b. Auxiliary signal preprocessing method; \*: Assuming moderate harmonic amplitudes

It should be noted that a clear comparison of the presented methods is often challenging. Therefore, in many cases there seem to be no concrete guidelines on criteria for selection of a specific method over the other due to a lack of quantitative comparisons. The methods' relative performances at different operating conditions, levels of measurement noise, sampling frequencies, different harmonic input amplitudes, proximity of response peaks, and rotating speed variability are mostly unknown. The same is true for computation durations required by individual methods. Numerical comparisons and sensitivity studies in future research can address this gap.

The SSI method family and pLSCF method have been identified as industry leading due to their performance and experience with these methods from tests in a wide range of applications. In addition, preprocessing techniques, like those from Subchapter 2.1.3 can successfully complement these methods. Despite this, no study was found, which would directly compare these OMA methods to investigate their strengths and weaknesses at specific testing conditions.

Individual OMA methods have specific strengths and weaknesses as outlined by Table 2-1. This observation is also supported by a controlled experimental case study of a metal plate under random and harmonic excitation. The response data was analysed by the thesis

author with several OMA methods, which is reported in Appendix A. Despite the well-spaced modes and negligible measurement noise of the experimental setup, different OMA methods provide different estimations of modal parameters. Hence, for future work, a two-step approach is suggested, which would estimate the current operating condition and utilize the most suitable OMA method. In addition, it should be considered to combine the output of multiple OMA methods into a single dataset of higher quality using data fusion.

Most of the presented studies, while considering harmonic inputs, only cover cases where the harmonic amplitude does not exceed the actual structural response. However, harmonics of rotating machinery can reach far higher amplitudes [28], [32], impeding modal estimation. In cases with high amplitudes of harmonic orders and low random excitation, OBMA poses a promising approach since it utilizes the harmonics, which are otherwise often detrimental. However, although the OBMA method requires harmonic order excitation, there is no existing study considering the level of order amplitudes required for the method, or which impact different amplitude levels have on its output. Therefore, the OBMA method is reviewed in further detail under consideration of the present excitation conditions in the following Subchapter 2.2.

## 2.2 Order-Based Modal Analysis (OBMA) for transient operation runs

As demonstrated by the previous Subchapter 2.1, current literature contains a variety of OMA and other signal processing methods, which have been tested and, in some cases, specifically adapted or developed with harmonic excitations due to rotating machinery in mind. The subchapter gave an overview of these OMA methods and a qualitative review of their performance in applications with harmonic input loads. A main conclusion was that OBMA is beneficial in the mentioned challenging cases where low random excitation amplitudes prevent modal estimation at stationary operating conditions.

Building on the previous Subchapter 2.1, the work forming the foundation for the present Subchapter 2.2 was published by the thesis author as a peer-reviewed conference paper [16]. It focuses on OBMA while considering the composition of the excitation in the reviewed case studies in terms of qualitative random and harmonic contributions. The understanding thereof is important since modal identification fundamentally depends on the present excitation forces, and since the presence of excitation orders is a requirement of OBMA. The aim is thereby to identify a relationship between the type of excitation and the performance of OBMA.

For this purpose, existing comparison case studies involving OBMA are grouped into three categories, represented by the rows of Table 2-2. The second column of Table 2-2 lays out

the structure inherited by the following subchapters, each of which focuses on an individual category of OBMA studies.

**Table 2-2: Categories of OBMA case studies in existing literature**

Category #	Subchapter	Research focus of the reviewed studies		Reference case used by the reviewed studies for comparison and validation	
		Method	Test conditions	Method	Test conditions
1	2.2.1	OBMA	Operational run-up	OMA	Operational run-up
2	2.2.2	OBMA	Operational run-up	OMA	Operational stationary
3	2.2.3	OBMA	Operational run-up	Simulation/ EMA/ OMA	Respective optimal conditions, such as hammer impact (EMA) or white noise shaker input (OMA)

### 2.2.1 Comparisons of solely operational run-up conditions

The previously mentioned OBMA studies (Subchapter 2.1.5) of a tested wind turbine gearbox [53] as well as acoustic [54] and vibrational measurements from a 4-cylinder car [55] fall under the first category depicted by Table 2-2. In these studies, linear operational run-ups (i.e. with a constant acceleration) were performed while the structural response as well as the tacho signal were recorded. Based on this data, OBMA was compared to a general OMA method, represented by operational pLSCF in its commercial PolyMax implementation.

In the observed frequency ranges, between 2 to 5 end-of-order modes were falsely identified when the general OMA method was applied to the tested wind turbine gearbox [53], car interior acoustics [54] and vibrational car measurements [55].

The case studies were conducted in a laboratory environment, namely on a car roller bench [55] or using a gearbox test rig [53]. Thus, environmental excitation forces are minimised, and the excitation source is primarily the operating machine itself, which increases the expected amplitude of harmonic input forces in relation to random input forces. While the car test cases involved a conventional combustion engine, the test rig for the wind turbine gearbox is operated by an electric motor, which can lead to a further reduction of random input due to its reduced number of mechanically interacting components.

In the wind turbine gearbox test [53], only the number and approximate frequency of modes identified by OBMA and OMA are compared to highlight the successful elimination of end-of-order modes by OBMA. However, neither differences nor absolute values of the estimated common modes' modal parameters are provided in this study. A comparison of the estimated modal parameters is also heavily limited in the studies involving a car structure: While the study with acoustic microphone measurements of a car interior [54] reports the OBMA

identification results for eigenfrequencies and damping ratios, it does not provide these values for the OMA identification. The case study of a large vibration measurement campaign of a car [55] with 144 measurement channels also does not provide values of the modal parameters estimated by OBMA and OMA. The comparison is limited to a MAC matrix between operational deflection shapes (ODS) and OMA mode shapes on one hand and between ODS and OBMA mode shapes on the other hand, without a direct comparison between OMA and OBMA mode shapes [55]. In fact, the other two mentioned case studies [53], [54] also do not consider the comparison of mode shapes, although in case of the acoustic measurement [54] this is due to the use of a single microphone.

In conclusion, the reviewed studies, which compare OMA and OBMA during operational run-up test conditions lack a comparison of the values or differences for the estimated modal parameters (i.e., eigenfrequencies, damping ratios and mode shapes). However, all three case studies show that OBMA avoids the issue of falsely identified end-of-order modes in contrast to the compared OMA method. The discussed lack of substantial random input forces might have reinforced the presence of end-of-order modes in the presented cases.

### 2.2.2 Comparisons of operational run-up and operational stationary conditions

A planetary gearbox [56] was evaluated by hammer impact EMA testing, a simulation model, OMA with the operational pLSCF (PolyMax) method at stationary operation and OBMA at an acceleration run of the driving motor. Since, as additional baselines, this case study includes EMA and numerical results, it could also be assigned to the third category in Table 2-2, i.e., to the following Subchapter 2.2.3. However, it was assigned to the present subchapter since it is the only identified study where the test is performed at stationary operating conditions for OMA and an acceleration run for OBMA.

The OMA method (at stationary operating conditions) only identified 8 out of 13 modes, that were captured by EMA and OBMA. OBMA determined partly much greater damping values with errors ranging between 5% and 316% relative to the EMA damping results. There is less relative error in eigenfrequencies at a maximum deviation of 8%. A comparison between estimated values from OMA and OBMA shows a much closer agreement: OBMA parameters deviate up to 4% and 49% in relation to OMA results for eigenfrequencies and damping ratios, respectively. This indicates that the observed differences in comparison to EMA are also due to the operation of the structure and not exclusively due to estimation errors introduced by OBMA specifically. Underlying changes of modal parameters at operating conditions can be caused by an increasing gearbox temperature, varying boundary conditions and gear mesh stiffness, as noted by the authors [56].

However, the relationship between the analysed orders and the presented modal results is not clear from the paper. Two dominant orders of the system are introduced and it is stated that both orders have been processed by OBMA using the operational pLSCF (PolyMax) method [56]. However, only a single set of modes estimated by OBMA is presented and it is not clear from which of the two orders the presented results originate.

The analysed test case leads to assume a low amount of random input in relation to harmonic excitation amplitudes, since it features an added rotational mass and consists of few components (two identical planetary gears in back-to-back configuration) driven by an electric motor. Therefore, the study confirms that a run of sweeping orders can be favourable for modal estimation if the alternative stationary operating condition does not provide enough input force to excite modes in the frequency range of interest. However, this observation rather concerns the operational conditions of the specific test structure and not the utilised OMA method. Depending on how pronounced the end-of-order effect would have been in this test case, regular OMA could have also provided usable results when applied to the run-up measurements. Finally, the study validates OBMA by demonstrating matching modes from EMA, OMA, and a simulated system. However, this excludes mode shapes or MAC values from OBMA and OMA, as they have not been reported in the study.

### 2.2.3 Comparisons of operational run-up and experimental/numerical response

Simulation case studies of OBMA include an 8 DOF model with a simulated rotating mass [57] and a plate structure with two force input locations producing crossing orders [58]. In both cases, the modal estimation results by OBMA correspond mostly well with the numerical reference solutions.

Two additional studies conducted physical experiments using controlled excitation setups for the baseline response. In the test of a locomotive frame/cabin assembly [55], hammer impact EMA provided reference results while a different test utilised white noise excitation by a shaker to acquire baseline OMA results of car mock-up [59]. In the latter case study, the operational run-up condition was emulated by the same shaker, resembling a harmonic multi-sweep input of 34 orders, which were subsequently processed by OBMA.

In the case of the 8 DOF model [57], OBMA in combination with Time Variant Discrete Fourier Transform (TVDFFT) order tracking resulted in maximum deviations of 3% and 106% for eigenfrequencies and damping ratios, respectively. The high relative error of the damping estimation is encountered in the first two modes, which are lightly damped. Excluding the first two modes, the maximum damping error is significantly lower at 1.8%. A similar effect can be observed from the locomotive experiment [55], where the damping ratio of a lightly damped mode was estimated by OBMA approximately 3 times higher compared to EMA. The plate



simulation study [58] draws a slightly different picture, since its lightly damped modes did not give rise to noticeably high estimation errors. Table 2-3 shows results from the case study of the car mock-up [59] for the first 9 modes but reports them differently to the original study. Instead of absolute values, Table 2-3 provides the minimum and maximum differences relative to the reference analysis for a clearer quantitative comparison. The eigenfrequencies show consistent results with a maximum error of 2.6%. The damping ratio and mode shapes (quantified by MAC values), however, have a high variance depending on the specific order used in the OBMA method, as highlighted by bold text within Table 2-3. For example, the relative error in the damping estimate of the third mode ranges from 2.4% to 85.4% depending on the chosen order. Unfortunately, from the four presented case studies of this Subchapter 2.2.3, mode shapes or MAC values have been only considered in the car mock-up study [59].

**Table 2-3: Estimation errors of different OBMA orders from a car mock-up study [59] (modified from original representation to show minimum/maximum relative errors)**

Error (deviation across analysed orders $l$ ) of eigenfrequency $f$ and damping ratio $\xi$ estimates relative to reference values (subscript "ref")						
Mode	Eigenfrequency $\left  \frac{f_l}{f_{ref}} - 1 \right  \cdot 100$		Damping ratio $\left  \frac{\xi_l}{\xi_{ref}} - 1 \right  \cdot 100$		MAC	
	Min. (%)	Max. (%)	Min. (%)	Max. (%)	Min.	Max.
1	1.3	1.7	0.0	7.1	0.50	0.70
2	0.9	1.3	<b>0.0</b>	<b>66.7</b>	0.79	0.82
3	0.0	2.6	<b>2.4</b>	<b>85.4</b>	<b>0.52</b>	<b>0.87</b>
4	0.2	2.6	<b>20.8</b>	<b>62.3</b>	0.69	0.82
5	0.5	1.4	<b>12.0</b>	<b>40.0</b>	0.94	0.96
6	1.2	2.0	0.0	13.3	<b>0.64</b>	<b>0.89</b>
7	0.5	1.3	17.6	29.4	0.76	0.91
8	0.0	0.3	80.0	106.7	<b>0.30</b>	<b>0.91</b>
9	0.2	0.5	13.3	33.3	<b>0.47</b>	<b>0.89</b>

It can be concluded from several studies [55], [57], that the damping ratios of lightly damped modes can be strongly overestimated, which should be considered when analysing lightly damped structures with OBMA. A plate simulation study [58] demonstrated that VK order tracking can be successfully applied to separate crossing orders and use them for modal identification with OBMA.

For more challenging estimation conditions and generalised findings, the plate simulation also included superposed measurement noise and two close structural modes. At the same time, however, it should be kept in mind that both simulations [57], [58] represent idealised and reduced models, which facilitates modal identification. For example, a purely harmonic

order input force (without noise contributions) was used in the simulations and the plate response was simulated by modal superposition of a reduced modal subspace with 6 modes. Similarly, the physical car-mock up experiment [59] was performed under idealised conditions with a controlled shaker excitation producing purely harmonic input forces. Depending on the specific application scenario, lower estimation performance can be expected if the test conditions are less predictable.

This assumption is supported by the locomotive case study, which contained run-up excitation by an operating diesel engine [55] and suffered of unmatched modes as well as higher baseline errors compared to other studies discussed in this subchapter. More specifically, the OBMA estimation results in the locomotive study identified 11 modes while EMA suggests that only 5 modes are present in the observed frequency range. However, it is not clear if this discrepancy is due to the specific characteristics of the locomotive's operational excitation or OBMA itself since no estimation results from other OMA methods are provided. The authors mention that the Frequency Response Function (FRF) curves acquired from EMA were noisy [55], which could also contribute to the observed discrepancy.

#### 2.2.4 Discussion

Different comparison types of OBMA as defined by Table 2-2 serve important but different purposes, which must be kept in mind when drawing conclusions from case studies reviewed in the previous subchapters.

The first category allows to directly compare the outputs of OBMA and OMA, since both methods are compared at the same operational run-up condition (including the excitation forces). However, due to incomplete or missing reports of estimated modal parameters, the reviewed papers do not achieve a quantitative comparison in terms of absolute or relative values between the methods. Nevertheless, the studies demonstrate that regular OMA methods can suffer from end-of-order modes and that OBMA successfully eliminates this issue [53]–[55]. All reviewed case studies show factors that typically reduce random excitation in comparison to harmonic input, which could contribute to the presence of end-of-order modes in these cases.

The study of the second category presents a case where OBMA estimations from a run-up are compared to OMA results from stationary operating conditions [56]. A limitation of this study is that it compares different types of excitation/operating conditions and different modal estimation methods (OBMA and a general OMA method) at the same time. Therefore, the methods are compared at two substantially different operating conditions, so the conclusions drawn from observed differences in estimated modes cannot be directly attributed to the respective modal estimation method. A main observation of the study is that OMA was not able to identify several modes, which have been detected by OBMA and confirmed by EMA.

This primarily shows that sweeping orders from an operational acceleration or deceleration run can be more suitable for modal estimation compared to a stationary operation. Due to the mentioned limitation, however, this general conclusion is not necessarily specific to OBMA.

Studies of the third category [55], [57]–[59] provide a general validation of OBMA but do not evaluate the modal estimation performance in comparison to other established OMA methods.

### 2.2.5 Summary

The previous subchapters of Subchapter 2.2 provided a critical review of current literature focusing on modal identification from operating rotating machinery with OBMA and general OMA under consideration of the excitation conditions. The present subchapter summarises the main findings while highlighting identified gaps in the research literature to promote further development of OBMA and OMA of rotating machinery.

The practical differences between OBMA and general OMA methods are summarised in Table 2-4, which lists the main benefits and limitations of these methods using a qualitative classification into four main types of operating conditions. The comparison illustrates that stationary operating conditions in combination with mainly harmonic (and low random) excitation are especially challenging for modal parameter estimation [28], [60], [56]. It can be therefore concluded, that in this case an acceleration or deceleration run should be preferred if the operation allows to generate sweeping orders covering the frequency range of interest.

A clear contribution of OBMA is the solution to the end-of-order issue [53]–[55]. Since potential end-of-order frequencies can be calculated from the tacho signal in advance, an alternative solution might be to reduce the resulting spurious spectral peaks from the vibration measurements by data processing (as discussed in Subchapter 2.1.3) or to reject end-of-order modes after modal estimation. However, these approaches might be limited in cases, where end-of-order modes mask or overlap with real structural modes. Furthermore, the known harmonic peak reduction methods from Subchapter 2.1.3 focus on stationary operating conditions or conditions with limited speed variability instead of full transient runs, so further research and development of these methods is required. The utilisation of OBMA, on the other hand, is limited by the requirement of an acceleration or deceleration run of the rotating component and the presence of a known speed profile. Therefore, to achieve optimal modal estimation throughout different operating conditions of a structure, a combination of OBMA with one or multiple OMA methods might be desirable and should be considered for future work.

**Table 2-4: Qualitative comparison of OBMA and general OMA at different operating conditions**

		Operating condition			
		Stationary		Sweeping orders	
Ratio of harmonic and random excitation		OMA	OBMA	OMA	OBMA
		Mainly harmonic	[28] (2007), [60] (2018), [56] (2018) - Modes not excited - Modes masked by harmonics + Harmonics can be partially reduced	× N/A	[54] (2006), [53] (2014) + Modes excited - Analysis band limited to sweep range - False end-of-order modes
Mainly random	[46] (2006), [47] (2007), [37] (2008), [44] (2012), [59] (2009) + Modes excited + Harmonics can be rejected/reduced	× N/A	- Not limited by sweep range* - (Weak) false end-of-order modes**	- Extraction band limited to sweep range - Weak order response amplitudes** - Extra analysis steps (order tracking, alternative results from different orders)	

N/A: Not applicable; \* Hypothesis (to be evaluated); \*\* Hypothesis is addressed by Chapter 5 [17] (2022)

It has been demonstrated that the choice of a tracked order can have a large influence on OBMA estimation results, leading to ambiguous results depending on the chosen orders [59]. Existing literature suggests a method for an automated determination/selection of most significant orders (based on local amplitude maxima in the mean order domain spectrum) [54]. However, the described variance of the results indicates that OBMA could be further improved by an additional estimation of the most suitable order per mode, or a combination of data acquired from multiple tracked orders by data fusion. This finding gave rise to the development of a novel method based on OBMA, presented later in Chapter 5.

Only one study [59] was identified, which directly compares the mode shapes of OBMA and general OMA. Therefore, it is worth to further evaluate the performance of OBMA with respect to mode shape estimation. This is also addressed by a comparison study in the upcoming Chapter 5.

Several studies show that the damping ratio of lightly damped modes can be severely overestimated by OBMA [55]–[57], [59]. Since this is likely a result of transient excitation, it can be assumed that a lower ramp-up speed as well as a greater excitation by random input compared to periodic input should alleviate this effect. However, from existing literature is not clear yet, which factors (such as the relative amount of periodic and random excitation or ramp-up rate) are relevant for this issue and to what degree. A deeper understanding would help for the planning of operational tests and the interpretation of test-results from

acceleration/deceleration runs. This is especially relevant since, as demonstrated before, such transient test conditions can lead to a more complete modal estimation [56].

No studies have been found, where OMA or OBMA are evaluated at mainly random excitation with a low periodic input of sweeping orders, which is reflected in Table 2-4. Thus, the specified characteristics of OMA and OBMA in this case is mostly based on assumptions. However, depending on the tested structure, such operating conditions can be encountered, so more research in this area is encouraged. This is also addressed in Chapter 5 by performing a quantitative comparison study, which utilises an independent variable governed by the relative amount of harmonic order excitation amplitudes and random excitation amplitudes.

All the reviewed studies focus on proprietary test cases. The lack of open benchmark data in the domain of vibration analysis applied to rotating machinery hampers comparisons across research groups in this field. A future open benchmark dataset could therefore promote further, more efficient development of OMA methods for rotating machinery. Therefore, a detailed survey of the existing open dataset landscape is conducted in the following Subchapter 2.3 and followed up by the introduction of an open simulation dataset of rotating machinery during acceleration in Chapter 4.

## 2.3 Rotating machinery datasets for OBMA and condition monitoring

The previous Subchapter 2.1 and Subchapter 2.2 found that the reviewed studies of OMA and OBMA for rotating machinery use proprietary vibration datasets, which hampers replicability of published research and obstructs performance comparisons of methods across different publications. The present Subchapter 2.3 reviews the current landscape of open vibration datasets and concludes that a contributing reason for the stated issues is a lack of suitable open datasets.

In addition, the survey of OBMA methods in the previous Subchapter 2.2 aimed to evaluate the impact of the excitation condition on OBMA and OMA performance. However, conclusions thereof were limited as previous studies do not consider nor quantify the potential impact of excitation conditions. The present subchapter evaluates existing datasets on this aspect since a suitable dataset with varying and quantified excitation conditions could be used address the stated gap of reproducibility and comparability for further research of OBMA. In addition, this subchapter also serves as an overview of open vibration datasets suitable for research in condition monitoring of rotating machinery. This subchapter forms part of a work, which is currently under peer review for journal publication [18].

### 2.3.1 Existing open datasets from rotating machinery vibration

The development, validation, and assessment of methods for vibration signal processing for rotating machinery requires access to suitable data. Existing open datasets suitable for OMA are mostly limited to civil engineering applications with vibration measurements from bridges [61]–[65], buildings [66]–[68], and other stationary structures [68]–[75]. Table 2-5 gives an overview of open vibration datasets originating from rotating machinery in chronological order of publication.

**Table 2-5: Summary of open datasets with vibration data of rotating machinery**

Dataset name, reference, year	Operating conditions	Data channels	Max. consecutive signal duration per run	Vibration sampling frequency
Case Western Reserve Seeded Bearing Fault Test Data [76] (2004)	<ul style="list-style-type: none"> <li>- 25 combinations of bearing fault locations/types/severities (incl. healthy baseline)</li> <li>- 4 constant speed/load combinations (1730-1797 rpm, 0-3 horsepower)</li> </ul>	- 3x vibration (acceleration)	10s	12kHz, partially 42kHz
Milling Data Set [77] (2007)	<ul style="list-style-type: none"> <li>- Degradation leading to flank wear</li> <li>- 6 constant operating conditions (variations of cut depths, materials, feeds)</li> </ul>	<ul style="list-style-type: none"> <li>- 2x RMS vibration (acceleration)</li> <li>- 2x RMS acoustic</li> <li>- 2x spindle motor current (DC and AC)</li> </ul>	36s	250Hz
IMS Bearing Degradation Data [78] (2007)	<ul style="list-style-type: none"> <li>- Degradation leading to 3 combinations of bearing fault locations/types</li> <li>- 1 operating condition (2000 rpm, 6000 lbs bearing load)</li> </ul>	- 4-8x vibration (acceleration)	1s	20kHz
Gearbox Fault Dataset – 2009 PHM Challenge [79]	<ul style="list-style-type: none"> <li>- 14 combinations of gear types/gear/bearing/shaft faults/fault locations (incl. healthy baseline)</li> <li>- 5 constant speed/load combinations (1800-3000 rpm, “high/low” load)</li> </ul>	<ul style="list-style-type: none"> <li>- 2x vibration (acceleration)</li> <li>- 1x rpm</li> </ul>	4s	66.6kHz
FEMTO-ST Bearing Degradation Data - 2012 PHM IEEE Challenge [80]	<ul style="list-style-type: none"> <li>- Natural degradation, leading to unclassified bearing faults</li> <li>- 3 constant speed/bearing load combinations (1500-1800 rpm, 4-5 kN)</li> </ul>	<ul style="list-style-type: none"> <li>- 2x vibration (acceleration)</li> <li>- 1x temperature</li> </ul>	0.1s	25.6kHz
Condition Based Maintenance Fault Database for Testing of Diagnostic and Prognostics Algorithms (MFPT) [81] (2013)	<ul style="list-style-type: none"> <li>- 6 bearing fault types (incl. healthy baseline)</li> <li>- 7 constant load conditions (0-300 lbs) at 1500 rpm (partially)</li> </ul>	- 1x vibration (acceleration)	6s	48.8kHz, partially 97.7kHz

Dataset name, reference, year	Operating conditions	Data channels	Max. consecutive signal duration per run	Vibration sampling frequency
Bearing Vibration Data under Time-varying Rotational Speed Conditions [82] (2018)	- 5 bearing fault types (incl. healthy baseline) - 4 operational conditions with different time-varying rotational speed progressions (e.g., 846-1740 rpm)	- 1x vibration (acceleration) - 1x rpm	10s	200kHz
The motor fault diagnosis experiment dataset [83], [84] (2019)	- 8 combinations of fault types/severities (short circuit, air gap, rotor bar, bearing, healthy baseline) - 1 operating condition (1497rpm, no load)	- 1x vibration (acceleration)	10s	10kHz
Experimental database for detecting and diagnosing rotor broken bar in a three-phase induction motor [85], [86] (2020)	- 5 broken rotor bar fault conditions (incl. healthy baseline) - 8 motor loading torques (0.5-4Nm) at 1715 rpm	- 5x vibration (velocity) - 6x electrical power (three-phase current and voltage)	18s	7.6kHz
Vibration Analysis on Rotating Shaft - Unbalance Detection of a Rotating Shaft Using Vibration Data [87] (2020)	- 5 unbalance severities (incl. healthy baseline) - 2 combinations of acceleration durations and increasing rotational speed (e.g. 630-2330 rpm)	- 3x vibration (acceleration) - 1x rpm - 1x motor input voltage	3220s	4.1kHz
Rotor & bearing vibration dataset [88] (2020)	- 5147 combinations of constant rotational speed values (240-1080rpm) and foundation stiffnesses (2.04-18.32MN/m)	- 2x vibration (displacement) - 6x bearing force	2.5s	2kHz
MAFAULDA Machinery Fault Database [89] (2021)	- 42 combinations of bearing fault locations/types and misalignment/unbalance severities (incl. healthy baseline) - 49 constant speed conditions (737-3686 rpm)	- 6x vibration (acceleration) - 1x rpm - 1x acoustic	5s	51.2kHz
<b>Proposed in Chapter 4: Open simulation dataset for OMA and vibration analysis of rotating machinery during acceleration [19] (2022)</b>	- 18 operating conditions (varying degrees of harmonic ratios, acceleration durations, measurement noise) during increasing rotational speed (300-1800rpm*)	- 18x vibration (acceleration) - 1x rpm	320s*	714.3 Hz*

\*Response data with arbitrary values are user-generatable by the provided source code

In the domain of rotating machinery, the available vibration datasets primarily focus on condition monitoring applications. With one exception [87], short durations (18s and less) of raw consecutive vibration recordings are used by the cited datasets, which limits the applicability of OMA depending on the present damping ratios and eigenfrequencies of interest [90], [91]. In addition, the estimation of mode shapes is hindered as most of the datasets provide only up to 3 acceleration channels with three datasets [78], [85], [89]

offering 5 to 8 accelerometer channels, respectively. Four datasets [79], [82], [87], [89] provide tachometer speed readings, which are required for common signal processing methods such as Time Synchronous Averaging (TSA) and order tracking. Finally, only two of the datasets [82], [87] cover acceleration or deceleration runs despite the potential of these transient operating conditions to provide the required excitation for OMA as identified in Subchapter 2.1 and further discussed in Subchapter 2.2.

### 2.3.2 Summary

The survey demonstrated a lack of open vibration datasets from rotating machinery during acceleration. It is therefore common for research publications in this field to define individual simulation data [56], [58] or to utilise proprietary operational data [34], [56], [92]. While the simulation setups described in existing publications can be reproduceable, the process of reproduction means additional effort and represents a potential error source in the reproduced model and parameter definition as well as the simulation thereof. The reviews in Subchapter 2.1 and Subchapter 2.2 also concluded that existing publications often lack direct performance evaluation of competing methods. Therefore, the sensitivities, i.e., the application-dependent strengths and weaknesses, of individual methods remain unclear.

A common benchmark dataset would enable quantitative evaluations of methods and comparisons between publications. While real measurements are important for the validation of signal processing methods, simulations are especially suited for comparative benchmarks due to the adjustability and knowledge of ground truth values, such as operating conditions and structural modal parameters.

This lack of an open vibration dataset is addressed in Chapter 4, which introduces an open parametric simulation dataset [19]. It is included in the last row of Table 2-5. As a simulation dataset, it provides numerical modal parameters and quantified excitation parameters, making it especially suitable for benchmark comparisons. Additional flexibility is provided by the publication of the simulation source code, ensuring replicability and extensibility of the dataset for future research.

Regarding condition monitoring, Table 2-5 shows that there is a much smaller number of open run-to-failure vibration datasets [77], [78], [80] compared to the number of open vibration datasets covering various faults and healthy baseline conditions without intermediate life cycle data [76], [79], [81]–[83], [85], [87]–[89]. A probable reason for that is that discrete condition data (i.e., distinct healthy or faulty data) are much more readily available and producible. Fault condition measurements can be acquired, for example, from diagnostic field data recorded after occurrence and detection of a fault. Alternatively, faults can be intentionally induced into machinery components for experimental acquisition of fault conditions without the need for potentially resource-intensive run-to-failure measurements.



This observation motivated the development of a novel method for RUL prediction of rotating machinery. This method, which is presented in Chapter 6, utilises discrete condition data and a reduced number of run-to-failure training sequences.

Building on the overview of open datasets suitable for condition monitoring, the following Subchapter 2.4 gives a literature review of methods for (predictive) condition monitoring of rotating machinery in existing literature.

## 2.4 Condition monitoring of rotating machinery

The previous Subchapter 2.3 explored the landscape of open vibration datasets from rotating machinery. The suitability of the existing datasets for OBMA and condition monitoring was discussed. It was found that most of the existing datasets focus on condition monitoring applications but are limited to classification tasks with a much lower number of degradation datasets, which are usually required for predictive condition monitoring tasks.

The present subchapter is introduced by an overview of the condition monitoring domain, presenting different categories of corresponding methods. In Subchapter 2.4.1, the current research and role of modal parameters from OMA and EMA in condition monitoring is reviewed. It is revealed that modal parameter-based condition monitoring is generally not yet practicable at this stage, especially for applications with rotating machinery and predictive condition monitoring in operational settings. As a result, the subsequent Subchapter 2.4.2 reviews current literature on methods specifically aimed at Remaining Useful Life (RUL) prediction of rotating machinery to identify strengths and limitations of the current state of the art, which is dominated by ML-based methods.

Condition monitoring aims to provide additional insight on the condition of a monitored machine or structure to increase safety, facilitate efficient operation, and optimise maintenance procedures. Relating to machinery with rotating components this domain is usually referred to as machine condition monitoring or machine health monitoring, while the term structural health monitoring is more common in reference to application in civil engineering. The field of condition monitoring can be subdivided into the areas of diagnostics (i.e., posterior event analysis) on one hand and prognostics (i.e., prior event analysis) on the other hand [93]. Diagnostics deals with aspects regarding the identification of a potential fault and the description of fault states. In contrast to that, prognostics aims to provide information for fault prevention focusing on characterisation of a fault likelihood or the expected duration until fault occurrence. This explains the relevance of predictive condition monitoring, as it has a greater prospect of preventing downtime compared to descriptive methods [93], [94]. A common form of predictive condition monitoring is RUL prediction.

Algorithms for condition monitoring can be further categorised based on the level of output information they provide (e.g., detection, localisation, and/or assessment of faults) [95].

Another common categorisation is based on the model foundation [96], which is either physics-based, data-driven, or a hybrid combining aspects of both approaches. However, further subcategories and differences in terminology can be encountered in literature, a detailed survey of which is given in [97]. Physics-based methods have the potential to operate on conditions previously never encountered during monitoring. However, physics-based approaches are often limited by their inflexibility to updating with on-line data and become impracticable for high degrees of system complexity and environment noise [96], [98], [99]. On the other hand, data-driven methods, which often utilise Artificial Intelligence (AI), typically achieve better statistical performance, are real-time capable and alleviate the need for manual feature engineering by algorithmic optimisation and transformations of the input space towards the prediction task [100]–[103]. Data-based prognostics methods largely benefitted from and developed alongside the advancements in Machine Learning (ML), computing power, and large-scale sensor data. A major limitation of these methods, however, is typically the large amount of required training data, which can be unfeasible to obtain due to time and cost restrictions. For RUL prediction tasks, the foundation of such training data is typically a multitude of machine units, which provide measurements across their full life cycles until failure.

#### 2.4.1 Modal parameter-based condition monitoring

As outlined previously in Chapter 1, modal parameters estimated during operation are important to design mechanical components and operating regimes, reducing noise, material stress, and potential premature failure; and to validate structural design and corresponding numerical models or optimise them using FEM model updating. In addition, modal analysis also finds use in condition monitoring. The underlying reasoning is that a degrading structural condition or fault is manifested by a change of structural properties, such as boundary conditions or stiffness, which in turn are reflected by a change of modal parameters of the structure. For this purpose, modal parameters are estimated and compared over time either in an experimental environment with controlled excitation forces (using EMA) or in operating conditions (using OMA).

Along with estimated eigenfrequencies and damping ratios, especially mode shapes are often included for modal parameter-based condition monitoring due to their potential to localise damage. Several indicators were developed to serve as damage-sensitive features. In a study of the numerical and experimental vibration response of a beam under several fault conditions [104], a direct performance comparison of the most common damage indicators is conducted.

A rather promising indicator is the Mode Shape Curvature (MSC), which is defined as the difference between the second derivatives of two compared mode shape vectors. Several methods are based on this metric and are related to the modal strain energy, such as the

Damage Index (DI); the Mode Shape Derivative-Based Damage Identification (MSDBI); and the Modal Strain Energy Decomposition (MSED). This family of methods showed the best performance in several comparison studies [94], [104]. Two studies [105], [106] on bridge field data were conducted using DI. As limiting factors, it should be noted that in the first study [105], damage was induced artificially by cutting into a bridge girder, following numerical modelling and field measurements of the affected girder before and after the induced damage conditions. The second study [106] evaluated naturally occurring crack damage of a bridge but also required a FEM model for baseline data and a specially designed impact hammer for the excitation of the physical structure. However, more recently published successful applications of these methods are limited to plate or beam-like structures [104], [107], [108] under controlled experimental conditions or numerical simulations.

Respectable performance is also reported for Wavelet transform of mode shapes [104]. However, certain factors impede its practical application, namely the requirement of high signal accuracy with low noise; knowledge of the tested structure for the interpretation of results; and the analysis of individual modes, each requiring separate analysis parameters [109].

Other common indicators used for mode shape-based damage detection and localisation include the Coordinate Modal Assurance Criterion (COMAC) [110]–[112]; the Modified Laplacian operator (MLO), also referred to as Gapped Smoothing Method (GSM); the Generalised Fractal Dimension (GFD); and the Cross-Modal Strain Energy (CMSE). However, these methods showed inferior performance in comparison to the previously listed alternatives and share the limitation of being predominantly applied to idealised structures and measurement setups [94], [104].

Addressing this issue, an evaluation of generalisability is found in a comparative study [94] of modal strain-energy-based methods, which identified DI and MSED as the most versatile and clear damage indicators. For this purpose, suboptimal numerical and experimental response data of a beam and a truss structure were used. For example, numerically determined mode shapes were contaminated with 2% noise. However, this can still be considered a limited disturbance considering that real measurements propagate errors due to the measurement equipment, signal processing, and curve fitting alone. In addition, a reduced number of measurement locations (6 instead of originally 20) of a beam was analysed to successfully identify the damage location with DI. However, the induced damage consisted of a minimum 25% cut depth of the beam, i.e., a significant structural disruption, contributing to a clearer damage indication.

A more practice-oriented study [113] in the domain of machine condition monitoring focused on damage detection of a ball screw in the feed system of an operating machine tool. A

single three-axial accelerometer was positioned at the support of the ball screw to facilitate measurements of its emitted vibration. Over the lifespan of the ball screw, acceleration measurements were processed by OMA. It was found that a damage condition led to an increased standard deviation of the estimated eigenfrequencies and damping ratios of the first and third modes. This result can be explained by a growing uncertainty in the modal estimation, likely due to disturbing superposed fault components in the response signal. Therefore, despite the successful indication of a fault condition, the identified modal parameters played an indirect role in this case. This supports the image that OMA-based condition monitoring is better suited for evaluation of fundamental structural change, be it due to environmental, operational, or significant damage conditions of the monitored structure [91], [94], [114].

To conclude, the validation of the discussed methods is currently often limited to plate or beam-like structures under experimental conditions or from numerical simulations, mostly in the context of civil engineering applications with few exceptions. This suggests that practical applications on complex structures, at operational conditions with higher levels of noise, a limited number of measurement locations, and a lack of numerical models, might be not feasible in many cases. This is supported by reported requirements of accurate measurements with high spatial resolution and low noise [104], [109], [115]. Hence, a lack of fault-sensitivity of current in-field modal parameter-based condition monitoring is observed [116]. This explains the observation that published verified applications mostly focus on structures with significant structural alterations. Consequentially, ML-based anomaly detection is suggested as an alternative or complementary approach to determine early-stage damage conditions [94], [117]. Although existing studies of modal-parameter based condition monitoring mostly focus on localisation and severity quantification of damage, the a priori detection of a fault state itself is often not considered and further predictive analysis, i.e., RUL prediction, is not addressed despite its relevance [94].

#### 2.4.2 Machine learning-based Remaining Useful Life (RUL) prediction

RUL prediction belongs to the domain of predictive condition monitoring and aims to quantify the time or number of cycles until the monitored machinery or component reaches a predefined degraded state, such as complete failure or a safety-critical condition. As such, RUL estimation can form a major part of a predictive maintenance approach with the potential to benefit economical and safety considerations. Costly machine failure and downtime can be reduced, and maintenance programmes optimised through prognostics-based planning. Otherwise potentially undetected faults or degradation conditions can be spotted, which is especially relevant for safety-critical applications.

This subchapter gives an overview of existing studies dealing with the issues of RUL prediction and training data reduction in this domain. Strengths and limitations of the

reviewed publications are outlined to identify potential research directions. This subchapter forms a part of a paper, which was published by the thesis author as a peer-reviewed journal article [21].

#### *NN-based RUL prediction*

Deep Learning (DL) based approaches for RUL prediction have grown in popularity in recent years due to a vast increase in available computational power allowing for a higher research output, as well as the possibility of more complex NN models. A variety of RUL application domains have utilised DL approaches [118]–[120]. For instance, one study [119] proposes an LSTM NN combined with attention mechanism and Particle Swarm Optimisation (PSO) for lithium battery RUL prediction. Another study [118] investigates wind turbine gearbox RUL prediction using ML and concludes that NN based methods provide the best accuracy out of the compared methods. The authors had access to a large volume of wind turbine Supervisory Control And Data Acquisition (SCADA) data as well as vibration data and found that fusing the two types of data as opposed to using just SCADA data can extend the prediction period from a month to up to 6 months, which empirically demonstrates the value of using a variety of data sources as opposed to just large quantities. Multi-feature fusion is utilised in this paper to take advantage of these benefits found in literature.

Recurrent Neural Network (RNN) models are highly popular for time-series inference tasks due to their long-term dependency handling ability. For instance, Guo et al [121] proposed an RNN Health Indicator, which utilises a novel feature selection process based on correlation and monotonicity. This work further proves the benefit of multivariate data for data-driven models as well as the effectiveness of RNN models for time-series modelling. However, due to the vanishing gradient problem commonly observed when training RNNs [122], [123], LSTM [124] and Gated Recurrent Unit (GRU) NNs [125] are preferred to traditional RNN architectures. These RNN variants subsequently perform better in the RUL problem that this work covers, and hence, LSTM is also used as a foundation in the present study. For instance, Zhang [126] proposes a 2-layer LSTM NN which takes advantage of attention mechanism to prioritise relevant feature learning and thereby improve the model efficiency, with a 1-dimensional Convolutional Neural Network (CNN) for feature extraction preceding it and a Multi-Layer Perceptron (MLP) which outputs the RUL value following it. Various studies make use of CNN [127], [128], which are primarily used in visual recognition tasks [129] but have also shown promise with time-series problems [130]. One such study [127] proposes a Deep CNN (DCNN) for the prediction of RUL. The proposed model is a multi-layered CNN which does not take advantage of pooling, as the authors noted its unsuitability for time series-based tasks due to their low dimensionality. The authors input data from various sensors into the model with a sliding window and output a single RUL regression value. The model was empirically validated on the C-MAPSS degradation dataset from

NASA, where the authors set a maximum constant of 125 for the RUL value across all motors. However, this means that the proposed model cannot predict further than 125 cycles from failure, which can be required in some practical cases.

### *HI-based RUL prediction*

The calculation of an HI as a means of feature dimensionality reduction was utilised before in previous studies [120], [121], [131], [132]. A study by Yang et al. [133] compared directly modelling the RUL and using the HI as an intermediate variable to estimate the RUL, and found that the proposed method, which utilises the latter is able to consistently outperform the former. The authors further noted that in practice, RUL can fluctuate based on changes in operating condition and measurement noise. The authors employ various methods of smoothing the HI degradation curve to account for these issues. Another method proposed by Wei et al. [134] uses a dynamic conditional variational autoencoder to construct the HI of multi-sensor systems. The authors also provide further evidence that HI-based RUL approaches are more effective than direct RUL modelling. However, whilst the method makes use of operating condition information which, as Wei et al. noted, may not be available for all systems, the authors prove the effectiveness of their approach regardless of the availability of this data.

However, in contrast to the present study, the aforementioned studies utilise complete datasets and do not investigate the prediction performance under limited data availability. Furthermore, the proposed approach for HI calculation is based on the MD and AE LSTM NN (depending on the implementation) and can take advantage of more feasibly obtainable discrete healthy/faulty condition data, if available, in addition to run-to-failure sequences.

### *RUL prediction from limited training data*

RUL prediction typically requires extensive data, covering a large amount of run-to-failure life cycle sequences, which has an adverse environmental footprint and may require substantial time and financial investments. This applies both for the acquisition of the data itself as well as the subsequent data processing and model generation.

Several research papers recognised this issue. Certain methods in the field of transfer learning focus on domain adaptation and operate on incomplete RUL labels [102], [135]–[137]. In these cases, model training is performed using labelled samples at certain machine conditions (in the source domain) in combination with unlabelled samples of other machine conditions (in the target domain). While these methods operate on fractionally labelled information, they still require complete sequences of input features, limiting the data reduction capability of these methods. The same limitation applies to the method presented in [138], which investigates gradual reduction of labelled training data. However, the full set

of training data is used throughout in a semi-supervised approach utilising Restricted Boltzmann Machine (RBM) and LSTM.

In the domain of RUL prediction of cutting tools, a study [139] utilises incomplete data covering the first part of the life cycle sequence and cutting it short before the life cycle end is reached. While sensor data is used for the training of a NN, the method is based on classic analytical models for tool wear, like those introduced by Takeyama, Murata [140] and Usui [141]. Therefore, this approach can be classified as a hybrid method and is limited in its application to cutting tools. Another paper [142] investigates the crack growth of steel plates and bearing degradation to estimate the RUL using sparse and fragmented data samples. However, the missing samples (either individually or in fragments) are randomly selected from the full life-cycle sequence, approximating the distribution of the original data range. Another study [143] constructs a prediction model by fitting a Bernstein distribution to the lifetime numbers and using its parameters to define an assumed degradation function. A large reduction in data-usage is achieved, however the drawback of this approach is that the initially assumed degradation function may not be representative of the actual degradation trend. Moreover, the method operates on a single degradation feature and this feature reaches a constant end value for every run-to-failure sequence, limiting the method's potential for more complex cases with signals, which are either multivariate or have varying value ranges per run-to-failure sequence. Two papers deal with the RUL prediction of wind turbine bearings [144], [145] from an incomplete life cycle sequence. The former study [144] uses a state-space model constructed from an empirical equation for bearing wear based on the spalling area propagation. Online degradation data is then used to update the state and predict the RUL with a particle filter. As another hybrid approach, it is limited in its application to rolling element bearings. In the latter study [145], an Elman NN is used to obtain a data-driven condition model instead. However, the main limitation of both studies is that just a single run-to-failure sequence is used for demonstration and validation, such that the methods' generalisation ability remains questionable.

A study [146] implemented a method based on Support Vector Machine (SVM), where a reduced training set was provided. Specifically, between 33% to 36% of bearing run-to-failure training sequences were shortened, while the remaining majority of training sequences remained complete. A limitation of this study is that the method outputs survival probability values instead of RUL values. Moreover, the prediction is limited to 9 discrete values, which is detrimental for an accurate prediction of the monitored machine condition. A similar SVM-based approach is followed in [147]. The potential of SVM-based RUL prediction, particularly at limited availability of training data, is also pointed out in a review study [97]. This is based on the high training data demand typically imposed by common NN-based methods in contrast to SVM and SVR, which motivates the use of SVR in the present study.

Whilst the topic of RUL is widely covered in literature, only a small proportion of these papers aims to address the topic of run-to-failure sequence availability. However, in a real-world environment, it is not always assured that full run-to-failure sequences will be available, which means that any approach which aims to have practical feasibility must account for a lack of data. To the best of the authors' knowledge, no currently existing methods for RUL prediction from limited data use open datasets, limiting reproducibility and comparability of existing publications. To address this issue, this paper utilises two open degradation datasets commonly used to validate RUL approaches, thus allowing for future studies to compare any new approaches to the present work and encourage research into more efficient RUL approaches that focus on data reduction techniques. The intention is to thereby increase the feasibility of practical application, where available training sequences might be limited, with an added environmental benefit of reduced power consumption of algorithms.

### 2.4.3 Summary

This subchapter reviewed methods for condition monitoring of rotating machinery. Evaluation of modal parameter-based condition monitoring showed that a variety of methods have been developed for this purpose. However, the target applications mostly concern civil engineering structures and are limited by idealised models, fault states, and measurement procedures, which limits practical applicability of these methods and requires further research.

Emphasis was then put on methods for prediction of RUL due to the relevance of this task in industry applications. While modal parameters are sensitive to changes of the global structural condition, the reviewed body of research shows that current data-based methods utilising AI algorithms show more proven case studies with practical applications in the domain of in-field condition monitoring and RUL prediction for rotating machinery. It was found that current state-of-the-art methods for RUL prediction are based on ML but are often limited by the requirement of vast lifecycle training data, which is usually both costly and time-intensive to obtain. This issue is addressed later in Chapter 6, which presents a data-efficient methodology for RUL prediction and compares its performance based on several of implementations with different AI-based methods.

The next Subchapter 2.5 summarises the main findings of Chapter 2, which reviewed the state of the art of research in the field of rotating machinery analysis from the perspective of OMA and condition monitoring. At the same time, conclusions are derived for further research work, which is addressed in course of this thesis.

## 2.5 Conclusions

Chapter 2 explored the current state of the art in relation to OMA and condition monitoring of rotating machinery. The main findings from its individual subchapters are summarised below and related to each other.



Subchapter 2.1 evaluated literature from the broad field of OMA methods and auxiliary signal processing methods for rotating machinery. Based on the relevance of the excitation from acceleration/deceleration runs for structures with low amplitudes of random excitation, the potential of the OBMA method was identified, as it is not affected by end-of-order modes in contrast to other common OMA methods [53]–[55]. Considering that the excitation force can vary substantially between applications and is generally unknown in OMA, it was concluded that there is a lack of systematic evaluations of the potential impact of excitation conditions on the performance of OMA methods. In a similar scope, a lack of direct performance comparisons between state-of-the-art methods was found. Such comparisons can contribute to more informed decisions across different OMA methods and applications as well as the interpretation of the methods' results.

Both the identified potential of OBMA and the lack of studies focusing on the potential impact of excitation conditions motivated the subsequent Subchapter 2.2. The subchapter identified the limitations of OBMA, including that each tracked machine order is processed individually, leading to ambiguous sets of estimated modal parameters covering partially overlapping frequency ranges. It was found that modal parameters processed in this manner have a high variance across the used machine orders [59]. The qualitative evaluation of excitation conditions in Subchapter 2.2 confirmed the assumption that in cases lacking random excitation, an acceleration/deceleration run can be required to achieve an excitation of the structure for subsequent modal estimation [28], [60], [56]. The subchapter also found indications that OBMA benefits from higher order excitation amplitudes. However, detailed findings were not possible due to a lack of existing quantitative studies, which consider the impact of different excitation conditions. An additional gap was identified in the lack of comparative studies involving OBMA, especially regarding the mode shapes estimations.

Suitable data is a foundation for the development, verification, and (comparative) evaluation of algorithms. As such, suitable data is required to address several of the research gaps stated above. For this reason, Subchapter 2.3 reviewed the current landscape of open vibration datasets of rotating machinery and evaluated their potential for applications in OMA and OBMA in particular. It was found that the existing datasets are mostly unsuitable for this purpose due to low durations of time-response signals [76], [78], [80], [81], [89], stationary operating speeds [79], [85], [88], low number of measurement locations [82], [83], [87], and the lack of accurate speed profiles, i.e., tachometer readings [77], [85], [88]. Instead, most of the existing datasets focus on applications for condition monitoring. In this regard, the subchapter found that most datasets provide distinct condition data (i.e., data from healthy machine condition on one hand and potentially several fault states on the other hand) [76], [79], [81]–[83], [85], [87]–[89]. At the same time, a much smaller number of datasets provides degradation data, which spans conditions of a progressively degrading machine condition

[77], [78], [80]. This observation is explained by a higher time and cost effort in the generation of degradation data compared to distinct condition data.

Subchapter 2.4 dealt with condition monitoring of rotating machinery, first evaluating of the state of the art in modal parameter-based condition monitoring methods, i.e., methods, which can operate on the output of methods covered by Subchapter 2.1 and Subchapter 2.2. The main finding was that, while there is potential in this approach, current methods are limited by controlled testing conditions with high requirements to data accuracy and spatial resolution [104], [109], [115]. In addition, current methods mostly focus on applications in civil engineering and have not been demonstrated for predictive condition monitoring tasks [94]. The presumed reason for this observation is that modal parameters provide a global characterisation of structural dynamics, while damage (especially at early stages) affects localised areas or components of the monitored structure. This explains that modal parameter-based condition monitoring often lacks sensitivity and is better suited for global characterisation of the structural condition [116]. Subsequently, the second part of Subchapter 2.4 focused on the state of the art in predictive maintenance, highlighting the strengths and weaknesses of different methods for RUL prediction. It was found that ML-based methods dominate the state of the art in this domain and show numerous successful case studies demonstrating their potential in applications for rotating machinery [118]–[120]. However, a common limitation of these methods is the requirement for training data, consisting of a large number of measured degradation runs, i.e., run-to-failure sequences. While certain studies recognised this issue, the existing methods are still limited, e.g., by using less labelled samples while still requiring otherwise complete training data [102], [135]–[137], by reducing sequence samples uniformly across sequences while still keeping all sequences [142], or by a lack of generalisability, where just a single run-to-failure sequence is used for the demonstration and verification of the method [144], [145].

The research gaps summarised in this chapter motivate the work presented in the following Chapter 4, Chapter 5, and Chapter 6 of this thesis. Prior to that, the next Chapter 3 gives the theoretical background for subsequent chapters by outlining relevant concepts and utilised methods.

### 3 Theoretical background and terminology

The previous Chapter 2 identified the advances and limitations of existing methods from current literature focusing on OMA and RUL prediction for rotating machinery. Based on these findings, this Chapter 3 introduces theory and methods, which are relevant to the contributions of the subsequent chapters.

First, relevant theory excerpts from the structural dynamics domain are given in Subchapter 3.1, which is based on previous work in frame of the author's Master thesis [148]. Main concepts of modal identification by OMA are introduced in Subchapter 3.2, allowing to estimate modal parameters from structural response measurements. This is followed up in Subchapter 3.3 by the introduction of other advanced methods for data modelling, which are aimed at general applications and are suitable components, for example, for data-based RUL prediction.

#### 3.1 Fundamental dynamic system equation

The fundamental dynamic system equation (also called equation of motion) is given in Equation (3.1). It can be derived from the force balance (second law of Newton) on a spring-mass-damper system [149]. The dynamic system is described by  $[M]$ ,  $[C]$ ,  $[K]$ , which are the mass, damping, and stiffness matrix, respectively. The linear second-order differential equation expresses the relation between the system's response in terms of displacement  $\{u\}$ , velocity  $\{\dot{u}\}$ , and acceleration  $\{\ddot{u}\}$  due to the acting force vector  $\{F\}$ .

$$[M]\{\ddot{u}(t)\} + [C]\{\dot{u}(t)\} + [K]\{u(t)\} = \{F(t)\} \quad (3.1)$$

This describes a dynamic MDOF system in time-domain under the following assumptions [149]:

- Masses are modelled as lumped point-masses.
- Spring stiffness force is assumed as linearly proportional to displacement.
- Viscous damping force is assumed as linearly proportional to velocity.
- The system is Linear Time Invariant (LTI).

Equation (3.1) also represents the relationship of dynamic problems in FEM, which is commonly used in industry due to its ability to model complex static and dynamic simulation setups. In FEM, a continuous displacement field is discretised into finite elements, which have discrete nodal displacements. Resulting equations are derived from the principle of virtual work (a type of variational principles), while accounting for the inertial force to satisfy the dynamic problem [150].

### 3.1.1 Eigenvalue problem

This subchapter describes the eigenvalue problem, which yields eigenfrequencies and corresponding mode shapes of the dynamic system.

First, the free undamped case is considered here. Hence, the damping matrix  $[C]$  is ignored. To gather the free structural response, a solution to the homogeneous (i.e., without applied loading  $\{F\}$ ) dynamic system equation in Equation (3.2) is pursued.

$$[M]\{\ddot{u}(t)\} + [K]\{u(t)\} = \{0\} \quad (3.2)$$

The system response  $\{u\}$  can be expressed in exponential form [151]:

$$\{u(t)\} = \{v\}e^{\lambda t} \quad (3.3)$$

The eigenvector  $\{v\}$  is composed of  $N$  DOFs and represents the mode shape. In contrast to  $\{u\}$ ,  $\{v\}$  is time-independent, and the time  $t$  is now included in the exponential function in Equation (3.3).

Deflections  $\{u\}$  are differentiated twice to provide accelerations  $\{\ddot{u}\}$ . Expressions for  $\{u\}$  and  $\{\ddot{u}\}$  are then substituted in the dynamic system from Equation (3.2), which results in a general eigenvalue problem given by Equation (3.4). In practice, it is typically solved by iterative numerical methods, such as the Lanczos algorithm [152] or QR algorithm [153].

$$(\lambda^2[M] + [K])\{v\} = \{0\} \quad (3.4)$$

This generalised eigenvalue problem is valid for a damping matrix  $[C]$ , which is a zero-matrix or a linear combination of  $[K]$  and  $[M]$  (i.e., assuming proportional damping). For the sake of completeness, it is noteworthy that the general eigenvalue problem in Equation (3.4) reduces to a standard eigenvalue problem of the matrix  $[K]$ , for the special case that  $[M]$  is the identity matrix, i.e.  $[M] = [I]$ .

A nontrivial solution requires  $\{x\} \neq \{0\}$ . Such solution is found by setting the determinant of the coefficient matrix to zero, which leads to the characteristic equation:

$$\det(\lambda^2[M] + [K]) = 0 \quad (3.5)$$

Expansion of the determinant results in a polynomial of  $N$ -th order. The roots of this polynomial can be solved and represent eigenvalues  $\lambda_n$  of the system, which occur in  $N$  complex conjugate pairs. Without the presence of damping, the resulting eigenvalues, as defined in Equation (3.8), only contain the imaginary component.

The calculated eigenvalues  $\lambda_n$  are then individually substituted in Equation (3.4). A single component of the eigenvector has to be set to an arbitrary value, e.g., 1. Afterwards, the equation system can be solved to acquire the remaining components of the eigenvector  $\{v\}$ , which corresponds to the substituted eigenvalue. As a result, the obtained eigenvectors are

normed to a single nodal DOF and express the relative deflection of the corresponding mode shape [150].

For the general case including a damping matrix, the same procedure detailed in this subchapter yields the polynomial eigenvalue problem in place of Equation (3.4):

$$(\lambda^2[M] + \lambda[C] + [K])\{v\} = \{0\} \quad (3.6)$$

It is addressed in an analogous way by solving the roots of the corresponding determinant:

$$\det(\lambda^2[M] + \lambda[C] + [K]) = 0 \quad (3.7)$$

Eigenvalues and eigenvectors are then determined in the same fashion as mentioned before. An important difference to the standard and generalised eigenvalue problems is that (with non-proportional damping), the eigenvectors cannot be used to uncouple the dynamic system of equations. However, an uncoupling can be achieved by a state space transformation, where the  $N$ -dimensional second-order differential equation of motion is transformed into a  $2N$ -dimensional first-order equation of motion.

An eigenvalue  $\lambda$  (also known as pole) is defined in terms of a (damped) circular eigenfrequency  $\omega_{\lambda d}$  and damping factor  $\sigma_\lambda$  of the system, as shown in Equation (3.8) [149].

$$\lambda, \lambda^* = -\sigma_\lambda \pm j\omega_{\lambda d} \quad (3.8)$$

It can be also defined by its circular eigenfrequency  $\omega_\lambda$ , and damping ratio  $\xi_\lambda$ :

$$\lambda, \lambda^* = -\xi_\lambda \omega_\lambda \pm j\sqrt{1 - \xi_\lambda^2} \omega_\lambda \quad (3.9)$$

Consequently, the eigenfrequency  $f_\lambda$ , damped eigenfrequency  $f_{\lambda d}$ , and damping ratio  $\xi_\lambda$  are derived from a pole  $\lambda$  as shown by Equations (3.10), (3.11), and (3.12), respectively [91].

$$f_\lambda = \frac{|\lambda|}{2\pi} \quad (3.10)$$

$$f_{\lambda d} = \frac{\text{Im}(\lambda)}{2\pi} \quad (3.11)$$

$$\xi_\lambda = -\frac{\text{Re}(\lambda)}{|\lambda|} \quad (3.12)$$

### 3.1.2 Newmark- $\beta$ method for implicit time integration

To calculate the time response of the dynamic system, the system equation can be integrated over time, which is the focus of this subchapter.

The Newmark- $\beta$  method is often incorporated to solve the dynamic differential equation and is presented in more detail below. It is an implicit solution scheme. Therefore, it determines

output values specifically at  $t+\Delta t$  unlike explicit approaches, which provide an extrapolated solution at  $t+\Delta t$  based on values at the current time  $t$  only.

Implicit methods are computationally more demanding because of the coupled equation system, which has to be solved in every time step. In contrast to that, explicit time step calculation can be performed with less effort per time step. However, explicit methods require smaller time steps while implicit methods provide higher accuracy and allow unconditional stability [154].

The Newmark- $\beta$  method is based on the assumption that the acceleration  $\{\ddot{u}\}$  varies linearly in every time step. The slope of the assumed linear acceleration function is configurable through Newmark integration parameters  $\gamma$  and  $\beta$ . These parameters have essential influence on characteristics of the numerical solution regarding stability, accuracy and numerical dissipation or damping, which is discussed further in Subchapter 4.4.

First, a time discretisation with a (fixed or variable) time step  $\Delta t$  is introduced and the system Equation (3.1) is modified into a stepwise (per iteration  $i$ ) linearized form. The time value is stated here in the subscript of time-dependent equation components, i.e.,  $\{u_{t+\Delta t}\} = \{u(t = t + \Delta t)\}$ . Delta values represent time step deviations of the corresponding output value, i.e.,  $\{\Delta u\} = \{u_{t+\Delta t}\} - \{u_t\}$ .

Integration of the estimated acceleration  $\{\ddot{u}_{t+\Delta t}\}$  leads to approximations for velocities  $\{\dot{u}_{t+\Delta t}\}$  and displacements  $\{u_{t+\Delta t}\}$ . The following equations can be formed to express these velocities  $\{\dot{u}_{t+\Delta t}\}$  and accelerations  $\{\ddot{u}_{t+\Delta t}\}$  as functions of  $\{u_{t+\Delta t}\}$  [155]:

$$\{\dot{u}_{t+\Delta t}\} = \frac{\gamma}{\beta\Delta t} (\{u_{t+\Delta t}\} - \{u_t\}) - \frac{\gamma - \beta}{\beta} \{\dot{u}_t\} - \frac{\gamma - 2\beta}{2\beta} \Delta t \{\ddot{u}_t\} \quad (3.13)$$

$$\{\ddot{u}_{t+\Delta t}\} = \frac{1}{\beta\Delta t^2} (\{u_{t+\Delta t}\} - \{u_t\}) - \frac{1}{\beta\Delta t} \{\dot{u}_t\} - \frac{1 - 2\beta}{2\beta} \{\ddot{u}_t\} \quad (3.14)$$

These equations are then substituted in Equation (3.1), so the dynamic equation can be formed into:

$$[K^*]\{u_{t+\Delta t}\} = \{F_{t+\Delta t}^*\} \quad (3.15)$$

It contains the effective stiffness matrix  $[K^*]$  and effective force vector  $\{F^*\}$ , which are defined as follows [156]:

$$[K^*] = [K] + \frac{\gamma}{\beta\Delta t} [C] + \frac{1}{\beta\Delta t^2} [M] \quad (3.16)$$

$$\begin{aligned} \{F_{t+\Delta t}^*\} = \{F_{t+\Delta t}\} + [C] & \left( \frac{1}{\beta\Delta t} \{u_t\} + \left(\frac{\gamma}{\beta} - 1\right) \{\dot{u}_t\} + \frac{\Delta t}{2} \left(\frac{\gamma}{\beta} - 2\right) \{\ddot{u}_t\} \right) \\ & + [M] \left( \frac{1}{\beta\Delta t^2} \{u_t\} + \frac{1}{\beta\Delta t} \{\dot{u}_t\} + \left(\frac{1}{2\beta} - 1\right) \{\ddot{u}_t\} \right) \end{aligned} \quad (3.17)$$

Therefore, the only unknown value in Equation (3.15) is  $\{u_{t+\Delta t}\}$ , which is determined and used to calculate the remaining response quantities using Equation (3.13) and Equation (3.14) before resuming to the subsequent time step iteration.

### 3.2 Modal identification (EMA and OMA)

The common general framework of modal identification is to use measurements describing the input-output relationship (in case of EMA) or output-only data (in case of OMA) to construct an analytical model of the target structure by the identification of suitable model parameters. Modal parameters are then finally extracted from the model. Although modal estimation can be also performed from nonparametric descriptions directly, nonparametric methods, such as the peak picking method, generally have lower accuracy and are more prone to error compared to parametric methods [91], [149]. Therefore, Figure 3-1 visualises a common framework for modal identification using parametric models. This framework is further discussed below.

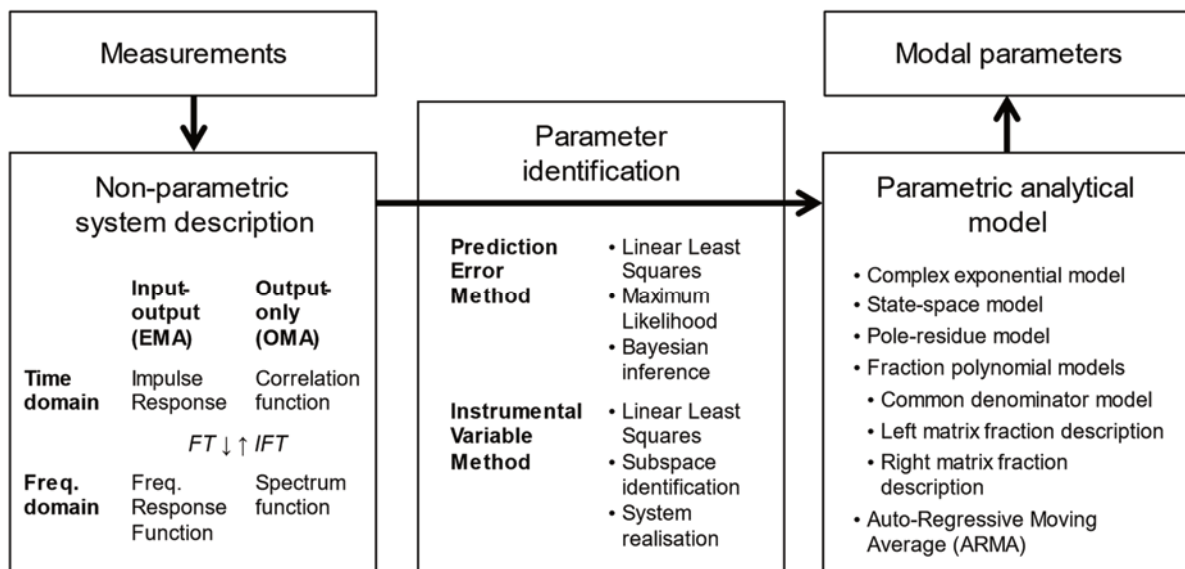


**Figure 3-1: Main components of EMA and OMA methods and their different variants**

Typically, the structural response is first represented by a nonparametric system description calculated from the measurements. As shown in the left block in Figure 3-1, these are typically estimations of transfer functions, frequency response functions, or impulse response functions for EMA. For OMA, the output-only counterparts are spectra, or correlation functions. Hence, the adaptation of EMA methods is often straight-forward, providing corresponding OMA methods [90].

Different mathematical models have been developed to represent the measured structure, with a list of common approaches given in the rightmost block in Figure 3-1. The model parameters are adjusted by parameter identification methods, aiming at a close representation of the underlying measurements. These methods can be associated with one of two categories according to [157], as highlighted in the middle block in Figure 3-1. The approaches following the prediction error method utilise numerical optimisation to minimise the difference between the modelled and measured output quantities while the class of instrumental variable methods are often based on correlations [157]. The linear LS method occurs under both categories, since it can be formulated as a special case under either framework.

Modal identification (EMA and OMA) is most commonly classified based on the method formulation into either time or frequency domain methods [91], [157]. However, implementations of a single approach can be often found with either formulation, as equivalent equations are often derived by a Fourier Transform (FT) or Inverse Fourier Transform (IFT), respectively [157]. Single-Degree Of Freedom (SDOF) methods are able to estimate a single mode only while Multiple-Degree Of Freedom (MDOF) consider multiple modes in a single analysis, making MDOF methods especially favourable in case of close or coincident modes [91]. Another distinction is made between local, global, and polyreference methods [149]. These terms are related to classifications as Single Input Single Output (SISO), Single Input Multiple Output (SIMO) and Multiple Input Multiple Output (MIMO), respectively, which are more common in the general system identification field (not exclusively for modal identification) [157]. This order describes a rising complexity and generality of modal identification methods. Local methods determine global modal parameters (i.e., eigenfrequencies and damping ratios) from a single measurement location (i.e., a single entry of the spectrum matrix for example) individually. Global methods derive estimations from measurements of several signal channels simultaneously (i.e., a single row or column of the spectrum matrix for example). Finally, polyreference methods consider the dynamic response both at several output channels as well as reference channels (in case of OMA), i.e., several columns and rows of the spectrum matrix simultaneously.

Different mathematical features and combinations of techniques (including those listed in Figure 3-1) constitute the existence of a variety of different OMA methods. Extensive overviews and relations between these approaches are found for example in [91], [157].

### 3.2.1 Relation between the transfer function and modal parameters

This subchapter demonstrates the relation between non-parametric system descriptions such as spectrum functions to the target modal parameters extracted from a model representation of the measured system.



For this purpose, it is practical to employ the equivalent Laplace-domain representation of the dynamic system in time-domain from Equation (3.1). After applying the Laplace transform and assuming initial conditions (velocities, displacements) as zero, Equation (3.18) is obtained [149], where  $s \in \mathbb{C}$  is the complex variable in the Laplace domain. The term  $[D(s)]$  highlighted in Equation (3.18) is referred to as the system matrix [149] or dynamic stiffness matrix [91]. It is worth pointing out, that corresponding derivations are also possible in the frequency domain by the Fourier transform [91]. They are readily obtained from the following equations in the Laplace domain by restricting  $s$  to the imaginary axis, i.e., by substituting  $s=j\omega$ .

$$\frac{([M]s^2 + [C]s + [K]) \{u(s)\}}{[D(s)]} = \{F(s)\} \quad (3.18)$$

Next, Equation (3.18) is rearranged into a ratio of the system response  $\{u\}$  to the input force  $\{F\}$ . The result is the inverse of the system matrix, which is known as the transfer function matrix  $[H(s)]$  shown in Equation (3.19).

$$[H(s)] = [D(s)]^{-1} = ([M]s^2 + [C]s + [K])^{-1} \quad (3.19)$$

The matrix can be also written in terms of its adjugate (also called the adjoint) and determinant [158], as shown in Equation (3.20), which allows several important insights.

$$[H(s)] = [D(s)]^{-1} = \frac{\text{adj}([D(s)])}{\det([D(s)])} = \frac{[R(s)]}{\det([D(s)])} \quad (3.20)$$

The adjugate of the system matrix in the numerator is known as the residue matrix  $[R(s)]$  and contains information on the mode shapes. At the same time, the determinant in the denominator of  $[H(s)]$  gives the characteristic system equation, which corresponds to the previously shown Equation (3.7) imposing the poles (i.e., eigenfrequencies and damping ratios) of the system. Since the determinant is a scalar value and a common denominator to the matrix elements of  $[R(s)]$ , its poles are considered global system parameters, while the mode shapes are local parameters, which depend on the measurement location (i.e., specific matrix element of  $[R(s)]$ ) [149].

Employing the partial fraction expansion to the transfer function gives the partial fraction form for  $N_\lambda$  modes, as shown in Equation (3.21) [91], [149].

$$[H(s)] = \sum_{i_\lambda=1}^{N_\lambda} \left( \frac{[R_{i_\lambda}]}{s - \lambda_{i_\lambda}} + \frac{[R_{i_\lambda}^*]}{s - \lambda_{i_\lambda}^*} \right) \quad (3.21)$$

The frequency-domain FRF shown in Equation (3.22) can be defined from Equation (3.21) by limiting the s-plane to the imaginary axis with  $s=j\omega$ , as mentioned before.

$$[H(\omega)] = \sum_{i_\lambda=1}^{N_\lambda} \left( \frac{[R_{i_\lambda}]}{j\omega - \lambda_{i_\lambda}} + \frac{[R_{i_\lambda}^*]}{j\omega - \lambda_{i_\lambda}^*} \right) \quad (3.22)$$

An alternative representation in the time domain is obtained by applying the inverse Laplace to the transfer function or the inverse Fourier transform to the FRF, which gives a model of the impulse response function  $[h(t)]$  in Equation (3.23) [91], [149].

$$[h(t)] = \sum_{i_\lambda=1}^{N_\lambda} \left( [R_{i_\lambda}]e^{\lambda_{i_\lambda}t} + [R_{i_\lambda}^*]e^{\lambda_{i_\lambda}^*t} \right) \quad (3.23)$$

In OMA, modal parameters are determined from output-only descriptions, i.e., from a spectrum matrix or correlation function matrix instead of FRF or impulse response function matrices, respectively. This is attributed to the relation between the FRF and spectrum matrix in Equation (3.24) [28], where  $[S_{xx}(\omega)]$  and  $[S_{yy}(\omega)]$  are the input and output spectrum matrix, respectively. Since only the output spectrum is known, white-noise is typically assumed as the input, making the input spectrum matrix constant and thus frequency-independent [90], [91].

$$[S_{yy}(\omega)] = [H(\omega)]^* [S_{xx}(\omega)] [H(\omega)]^T, \quad (3.24)$$

A detailed presentation of a full-featured OMA method is given in Appendix B. This includes the introduction to estimation of spectra and their modal decomposition for OMA. Appendix B then describes the pLSCF method, which is a MDOF polyreference method, based on the Right Matrix Fraction Description (RMFD) model with a linear LS parameter identification. Further details on the estimation of residues and mode shapes are provided in Appendix C with the LSF method, which is often used in combination with pLSCF.

### 3.2.2 Assumptions and limitations of OMA

This subchapter introduces common assumptions and limitations of OMA methods in relation to rotating machinery. Approaches to loosen the restrictions resulting from these assumptions are also highlighted in the following. This subchapter also serves as the basis for part of a peer-reviewed conference publication [16] by the author of this thesis.

#### *Unknown input loads*

Due to the lack of information on the input loading in operating conditions, a general downside of OMA is that the modal masses are not directly determined from the analysis procedure and therefore no mass-normalised mode shapes are obtained. However, a complete modal system identification requires modal masses to construct FRFs, which are often also required for further tasks like SHM [90]. The Mass Change Method and Mass-Stiffness Change Method are able to derive modal masses purely from OMA, but each require two measurement sets with a changed system mass or stiffness, respectively [159].

Since this is not feasible in many cases, another approach is to incorporate a mass matrix of the measured system from a corresponding FEM model, used to scale the mode shapes from OMA [160].

A further, general limitation is that there is no control of the loading distribution and direction of operational or environmental excitation, so that proper excitation of modes can be hindered. Since there is also no influence on the number of independent loads, in addition, especially the determination of closely spaced modes can be obstructed as well [90]. This aspect is discussed separately in relation to rotating machinery in the last section of this Subchapter 3.2.2.

#### *Linear Time-Invariant (LTI) system*

The estimation of modal parameters by modal analysis is in general based on the assumption that the tested system is Linear Time-Invariant (LTI) [90], [91]. This assumes that the dynamic behaviour of the structure does not change over time and that there is a linear input-output relationship.

However, this idealised assumption is not always sufficiently met. In rotating machinery, the operating condition can influence dynamic system parameters. Different rotating speeds introduce corresponding centrifugal forces. These loads can also affect boundary conditions of individual parts, e.g., originating from changes in the slot interfaces between discs and blades of turbomachinery. Changing environmental conditions, like temperature, can also noticeably influence the dynamic characteristics of a measured structure. For example, in gas turbines, high temperatures occur due to processes like combustion, compression and friction. In addition to the direct influence on material properties, like stiffness and damping, thermal expansion can cause geometric misalignments, and added clearances. Similarly, the viscosity of lubricating oil fluid depends on the temperature and therefore is subject to change with possible impact on the operation and modal properties of the operating machine.

To minimise potential errors from a violation of the LTI assumption, it is possible to account for these variabilities by analysing separate measurements, which are acquired at distinct operating and environmental conditions, individually [90], [91].

Moreover, the mathematical description of a dynamic system in a rotating frame introduces time-dependent components in the equations of motion, making the system time-variant [161]. These considerations are relevant when rotating parts are modelled or measured in their local coordinate system, i.e., rotating relative to the fixed frame of the system. In these cases, it is therefore reasonable to transform the degrees of freedom into a common coordinate system with an LTI description of the system. Different methods, like the Multi-Blade Coordinate (MBC) transformation or the Harmonic Power Spectrum (HPS) method are

used for this purpose [34], [115]. However, when rotating components are not evaluated directly, but rather affected non-rotating structures or components of rotating machinery are measured and analysed, these considerations are not relevant. This is also the case for the present thesis.

### *Flat broadband input spectrum*

While it is commonly assumed in OMA that input loading has properties of white noise, this is often violated as the spectrum of the input load is not flat. Instead, coloured noise is a more general description for input loads. However, as long as the excitation spectrum is broad enough to provide the excitation of modes to be estimated, the impact of an input with coloured noise is manageable. Typically the coloured noise is assumed to be the result of a loading filter, with an underlying load that follows the white noise assumption [90]. When applying such a filter to neutralise coloured noise input or to calibrate the sensor response, it is important to apply it consistently to all measured channels in order to avoid introducing mode shape estimation errors [90].

Rotating machinery is a special case, which violates the white noise input assumption. In addition to broadband excitation, high excitation amplitudes at discrete harmonic frequencies occur due to the periodic nature of rotating components. The frequency of a periodic excitation that corresponds to the rotating speed of an observed shaft is known as the fundamental frequency. In addition to this frequency, integer multiples of the fundamental frequency, known as harmonics, are commonly observed in the measured frequency spectrum as well.

Such multiples of the rotation frequency are more generally referred to as (engine or rotation) orders, which are not limited to integer values. Based on the measured rotational frequency in rotations per minute (rpm), in rotations per second (Hz) specified by  $f_1$  or in radians per second specified by  $\omega_1$  (known as the circular frequency or angular velocity), the frequency  $f_l$  of the  $l$ -th order is calculated as shown in Equation (3.25).

$$f_l(t) = l f_1(t) = l \frac{rpm(t)}{60} = l \frac{\omega_1(t)}{2\pi} \quad (3.25)$$

The described relations can be visualised with a Campbell diagram. The Campbell diagram in Figure 3-2 shows an exemplary assessment of the modal response of a fan blade in an operational environment [162]. The horizontal axis shows increasing engine rpm and the vertical axis provides the frequency range. The rising lines originating from the diagram root are the relevant order lines – in this example, the 12th engine order and its higher harmonics. Eigenfrequencies of the analysed fan blade are shown as approximately horizontal lines with a slightly positive slope. The circled areas of intersection represent the resonant states of the component at the corresponding engine speed.

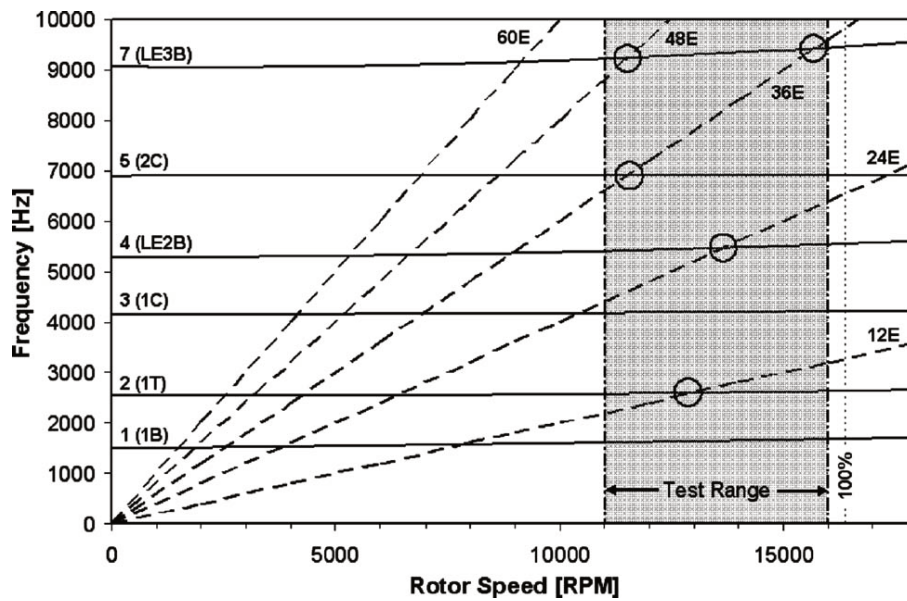


**Figure 3-2: Exemplary Campbell diagram, illustrating harmonic fan blade excitation due to rotation orders [162]**

The associated challenges for OMA, and the existing approaches to address these challenges, were presented in Subchapter 2.1, mostly for stationary operating conditions with  $f_1 \approx \text{const}$ . Subchapter 2.2 focused on the OBMA method for the analysis of transient acceleration and deceleration conditions. Further theory of OBMA and the transient excitation of rotating machinery is given in Subchapter 3.2.5.

#### *Distribution and correlation of input loads*

Depending on the specific configuration of the tested rotating machinery, the number of spatially separated and independent loads can vary. For example, it can be assumed that an in-flight operating aircraft engine is subjected to a larger number of independent loads compared to a rotating component on a spinning test rig, which is operated by an electric motor [90]. In contrast to the in-flight engine, the spinning test rig example features a much lower number of parts and subsystems, which can transmit and introduce independent loads to the structure. This loading condition is spatially limited by the bearing locations, where the vibration forces are transferred to the tested structure. Centrifugal unbalance forces are limited to the plane perpendicular to the rotating shaft, so modes of interest with main deflections in the shaft direction might remain unidentified due to a lack of excitation. In addition, the periodic loads in both axes of the plane are correlated, with a  $90^\circ$  phase difference [59]. Hence, the number of independent loads in the described example is close to one, making the identification of close modes more challenging [90]. Close modes often occur in structures with geometrical symmetry, torsional unbalances or light attachment parts, which have localised modes with frequencies similar to other modes of the structure [163]. At the same time, rotation symmetric geometries are common in rotating machinery. Examples for such components in aircraft engines include the inlet, casing, and exhaust nozzle.

In controlled vibration testing of large structures such as aircraft, where sine sweep excitation is induced at multiple input locations, the issue of correlated inputs is also encountered [164]. For example, a configuration of two shakers attached symmetrically to the aircraft wings, can be used to excite symmetrical modes by running both sweep inputs in sync, while asymmetrical modes are excited by performing a sweep excitation with 180° phase difference between one input and the other. However, the inputs at each test run are still correlated, which contradicts the requirement of uncorrelated forces for the conventional estimation of FRFs from multi-input test configurations [164].

For this case, several methods exist to construct FRFs for subsequent modal analysis and a classical approach is to calculate a common MIMO FRF matrix  $[H]$  from both the symmetric (subscript  $S$ ) and antisymmetric (subscript  $A$ ) runs using the relation in Equation (3.26) [164].  $\{\ddot{u}(\omega)\}$  is the acceleration vector and  $\{F(\omega)\}$  is the input force vector at frequency  $\omega$ .

$$[\{\ddot{u}(\omega)\}_S \{\ddot{u}(\omega)\}_A] = [H(\omega)] [\{F(\omega)\}_S \{F(\omega)\}_A] \quad (3.26)$$

However, since the symmetric and antisymmetric response sets have resonances at similar frequencies, the combined FRF will show closely spaced modes, which makes their accurate identification more challenging.

Therefore, an alternative is to construct an individual SIMO FRF matrix for the symmetric and antisymmetric test runs, which can be afterwards processed separately for modal identification. This procedure results in higher accuracy of the estimations compared to the modal identification from a combined FRF [164], [165]. However, this approach is only applicable in EMA, as there is no control over the input load in OMA and a combined response to different (correlated) loads is acquired.

### 3.2.3 Modal Assurance Criterion (MAC) and extended pole-weighted variants (MACX, MACXP)

The Modal Assurance Criterion (MAC) as well as extended and pole-weighted variants (MACX and MACXP), including their benefits and applications, are presented here. This subchapter was published in a peer-reviewed journal paper [17] by the author of this thesis.

The MAC [166] is a common metric to quantify the consistency between two mode shape vectors  $\{v_1\}$  and  $\{v_2\}$ . The MAC can be calculated by Equation (3.27), where  $\bullet^H$  denotes a complex conjugate transpose (i.e., Hermitian).

$$\text{MAC}(\{v_1\}, \{v_2\}) = \frac{|\langle v_1^H \{v_2\} \rangle|^2}{\langle v_1^H \{v_1\} \rangle \langle v_2^H \{v_2\} \rangle} \quad (3.27)$$

The MAC is well suited for modes shapes, where the individual mode shape vector components form a straight line in the complex plane [167]. Such mode shapes are called

monophase or are said to have a low degree of complexity or a high Modal Phase Collinearity (MPC) close to 1. However, for the general case of non-proportional damping in combination with close or repeated modes, this condition is not satisfied [161]. In such cases, the MAC value is not conclusive. The Extended Modal Assurance Criterion (MACX) [167] is a generalisation of the MAC and addresses its potential issues when applied to complex mode shapes. The MACX is defined by Equation (3.28), where  $\bullet^T$  is the transpose operation.

$$\text{MACX}(\{v_1\}, \{v_2\}) = \frac{(|\langle v_1^H \{v_2\} \rangle| + |\langle v_1^T \{v_2\} \rangle|)^2}{(\langle v_1^H \{v_1\} \rangle + |\langle v_1^T \{v_1\} \rangle|)(\langle v_2^H \{v_2\} \rangle + |\langle v_2^T \{v_2\} \rangle|)} \quad (3.28)$$

A further extension of MACX is the Pole-weighted MACX (MACXP). It can be considered as the application of the MACX to vectors  $\{V_1\}$  and  $\{V_2\}$ , which contain the free decay time series of individual DOFs with the eigenfrequency and damping ratio corresponding to the pole  $\lambda_1$  and  $\lambda_2$ , respectively. By evaluating the limits of the time interval  $\Delta t$  and number of time samples  $n_r$  in the free decays, the following equation can be constructed for MACXP [167], where  $\bullet^*$  is the complex conjugate:

$$\begin{aligned} \text{MACXP}(\{v_1\}, \{v_2\}) &= \lim_{\substack{\Delta t \rightarrow 0 \\ n_r \rightarrow \infty}} \text{MACX}(\{V_1\}, \{V_2\}) \\ &= \frac{\left( \frac{|\langle v_1^H \{v_2\} \rangle|}{|\lambda_1^* + \lambda_2|} + \frac{|\langle v_1^T \{v_2\} \rangle|}{|\lambda_1 + \lambda_2|} \right)^2}{\left( \frac{\langle v_1^H \{v_1\} \rangle}{2|\text{Re}(\lambda_1)|} + \frac{|\langle v_1^T \{v_1\} \rangle|}{2|\lambda_1|} \right) \left( \frac{\langle v_2^H \{v_2\} \rangle}{2|\text{Re}(\lambda_2)|} + \frac{|\langle v_2^T \{v_2\} \rangle|}{2|\lambda_1|} \right)} \end{aligned} \quad (3.29)$$

The MACX provides a consistent comparison of mode shape vectors with any type of complexity. The MACXP considers eigenfrequencies and damping ratios in addition to the mode shapes during the comparison of two modes. It can be therefore used to match modes from different estimations, which is utilised in later Chapter 5. Furthermore, MACXP is significantly less sensitive to a low spatial resolution compared to MAC or MACX, allowing to distinguish modes with a lower number of measurement locations [167].

### 3.2.4 Order tracking with the Time Variant Discrete Fourier Transform (TVDFFT)

The performance of several order tracking methods specifically for the use with OBMA have been evaluated in prior studies by Di Lorenzo et al. The authors report that the Angle Domain (AD) resampling-based order tracking [34], [55] along with the Vold-Kalman (VK) order tracking and the Time Variant Discrete Fourier Transform (TVDFFT) order tracking [57] provide the best results in terms of clean extracted order functions as well as the subsequent modal estimation results by OBMA. However, it is also noted, that the choice of a suitable order tracking method depends on the specific test conditions and requirements. For example, the VK and TVDFFT order tracking surpass the AD order tracking in cases with

close or crossing orders that need to be separated. Furthermore, the TVDFT method is computationally less demanding compared to VK and AD and thus advantageous in time-critical test conditions [55], [115].

In the following paragraphs, the TVDFT order tracking method is introduced by a comparison to the regular DFT and the main data processing steps involved. This subchapter forms a part of a peer-reviewed conference publication [16] by the author of this thesis.

The Fourier Transform (FT) can be seen as a cross-correlation between an analysed time signal  $x(t)$  and an analysing function. This becomes apparent when comparing the equations of the Fourier transform and the cross-correlation. In case of the FT, the analysing function (also called the basis function or kernel) is a complex sinusoid that, in correspondence with Euler's formula, can be equivalently expressed in exponential or sine-cosine form. These observations also apply to the Discrete Fourier Transform (DFT) in Equation (3.30) [168].

$$\begin{aligned} X_k &= \frac{1}{N} \sum_{n=0}^{N-1} \left( x_n \cdot \underbrace{e^{-j2\pi \frac{k}{N} n}}_{\text{analysing function}} \right) \\ &= \frac{1}{N} \sum_{n=0}^{N-1} \left( x_n \cdot \underbrace{\left( \cos\left(2\pi \frac{k}{N} n\right) - j \sin\left(2\pi \frac{k}{N} n\right) \right)}_{\text{analysing function}} \right), \end{aligned} \quad (3.30)$$

where

$X_k$	DFT for the $k$ -th frequency bin
$x_n = x(n \cdot \Delta t)$	Value of the $n$ -th signal sample
$N$	Total number of signal samples

The Inverse Discrete Fourier Transform (IDFT) transforms the frequency coefficients  $X_k$  back to the time samples  $x_n$  and, for the sake of completeness, is shown in Equation (3.31) [168].

$$x_n = \sum_{k=0}^{N-1} \left( X_k \cdot e^{j2\pi \frac{k}{N} n} \right) \quad (3.31)$$

It is worth noting that there are different common formulations and notations for the DFT in the literature depending on conventions and application areas. Differences can express themselves in the used scaling factor of the DFT and IDFT (e.g.,  $1/N$  in case of the DFT definition used in Equation (3.30) here) or the considered sampling interval (e.g.  $[0, N-1]$  used here). For example, the use of a centred interval like  $[-N/2, N/2]$  is more common in areas where spatially sampled data (e.g. image or surface data) is of interest, while an uncentred interval like  $[0, N-1]$  is often used in context of time sequences [169], [170].

Equation (3.30) is evaluated for individual integer values of  $k \in [0, N-1]$ . Hence, each of the resulting frequency bins  $X_k$  is obtained from the  $N$  signal samples  $x_n$  and a complex sinusoid



function with a constant frequency of  $k/N$  cycles per sample. Considering the sampling frequency  $f_s$  of the signal, the resulting frequency resolution of the DFT is calculated as  $\Delta f = f_s / N$  and the  $k$ -th frequency bin can be associated with the frequency  $f_k = k f_s / N = k \Delta f$  in Hertz ( $f_k$  cycles per second).

The TVDFT is formulated similar to the DFT as shown in Equation (3.32) below.

$$\begin{aligned} X_{o,l} &= \frac{1}{N} \sum_{n=0}^{N-1} (x_n \cdot e^{-j\varphi_{n,l}}) \\ &= \frac{1}{N} \sum_{n=0}^{N-1} \left( x_n \cdot \exp \left( -j l \Delta t \sum_{m=0}^{n-1} 2\pi f_{tacho}(m\Delta t) \right) \right), \end{aligned} \quad (3.32)$$

where

$X_{o,l} = X_l(o \cdot \Delta r)$  TVDFT for the  $l$ -th machine order and  $o$ -th signal block of  $\Delta r$  rotations

$f_{tacho}(m\Delta t)$   $m$ -th sample of the tacho signal in rotations per second (Hz)

The main difference of the TVDFT compared to the regular DFT lies in the analysing function, i.e. the complex sinusoid, marked in Equation (3.30). While the DFT uses a sinusoidal function with a constant frequency, the sinusoid of the TVDFT has a frequency that is time-dependent and corresponds to the instantaneous frequency of the analysed machine order  $l$ . Table 3-1 compares the equations for different formulations of the phase  $\varphi$  used in the complex analysing function  $e^{-j\varphi}$  of the DFT and TVDFT. The phase with a constant frequency (as is the case with DFT) is shown in Equations (3.34) and (3.35). Equations (3.36) and (3.37) describe a phase with a time-varying machine order frequency that is inferred from the tacho signal  $f_{tacho}$  (as used in TVDFT). The full derivation of the order phase  $\varphi_l$  from the tacho signal  $f_{tacho}$  is explained by Equation (3.33), which is based on the fact that the instantaneous phase  $\varphi$  corresponds to the integral of an instantaneous angular velocity  $\omega$ .

$$\varphi_l(t) = \int_0^t \omega_l(\tau) d\tau = \int_0^t 2\pi f_l(\tau) d\tau = l \int_0^t 2\pi f_{tacho}(\tau) d\tau \quad (3.33)$$

**Table 3-1: Different formulations of the instantaneous phase  $\varphi$  for the complex sinusoidal function  $e^{j\varphi}$**

	Continuous	Discrete
<b>Constant frequency</b>	$\varphi_f(t) = 2\pi \underbrace{f}_{=const.} t$ (3.34)	$\varphi_{n,k} = 2\pi \underbrace{\frac{k}{N}}_{=const.} n$ (3.35)
<b>Time-varying order frequency</b>	$\varphi_l(t) = l \int_0^t 2\pi \underbrace{f_{tacho}(\tau)}_{\neq const.} d\tau$ (3.36)	$\varphi_{n,l} = l \Delta t \sum_{m=0}^{n-1} 2\pi \underbrace{f_{tacho}(m\Delta t)}_{\neq const.}$ (3.37)

Equation (3.37) approximates the integral of the tacho signal  $f_{tacho}$  from Equation (3.36) as a summation of the rectangular areas spanned by its discrete samples and the sampling interval  $\Delta t$ . This method is known as the rectangle rule or the rectangle Riemann sum. Similarly, the trapezoidal rule or Simpson's method can be employed for the integral calculation.

In practice, order tracking with TVDFT can be implemented as the following procedure: First,  $N$  phase samples with the time-varying frequency of the target order  $l$  are calculated as defined in Equation (3.37). Subsequently, this sequence is used for the calculation of the complex sinusoidal function (i.e., the exponential function in Equation (3.32)), which has also  $N$  samples, like the analysed signal. In addition, the phase signal calculated from Equation (3.37) is used to determine at which sample indices a full rotation is completed by evaluating phase samples that cross an integer multiple of  $2\pi$ .

Based on these determined sample indices indicating a full rotation, the complex analysing function as well as the vibration time signal and tacho measurements are split into subsequent blocks of samples. Each block  $o$  then contains a constant integer number of machine revolutions  $\Delta r$  that can be set as a user parameter. This ensures a constant order bandwidth, which is beneficial for order tracking [171]. Finally, the TVDFT is applied to the vibration signal samples from each data block  $o$ , providing a TVDFT coefficient per data block. These coefficients can then be plotted over each data block's average of the analysed order frequency  $f_l$ , which is known from the tacho measurements as shown in Equation (3.25).

Like in regular DFT, the samples  $x_{o,n}$  from each processed data block  $o$  in Equation (3.32) can be also weighted by a window function to reduce leakage. In addition, the data blocks often do not cover an exact integer number of  $\Delta r$  due to the sampling discretisation, which also introduces leakage. Oversampling can be used to increase this precision and thus reduce leakage. Moreover, an Orthogonality Compensation Matrix (OCM) can be introduced to combat this effect and furthermore allow a more accurate order tracking of fast sweeping, closely spaced and crossing orders [171].

### 3.2.5 Order-Based Modal Analysis (OBMA)

The periodic input load  $F_l$  of an order  $l$  can be modelled as a rotating force (e.g. due to unbalance) and represented in a complex (2-dimensional) plane:

$$F_l(t) = A_l \exp(\pm j(l\omega_1 t + \theta_l)), \quad (3.38)$$

where  $\omega_1$  is the rotational speed,  $A_l$  and  $\theta_l$  are the amplitude and the phase of the excitation, respectively. The rotation can be counterclockwise or clockwise, represented by a negative

or positive exponent in Equation (3.38), respectively. An equivalent representation as a vector is given in Equation (3.39).

$$\begin{Bmatrix} F_{l,x}(t) \\ F_{l,y}(t) \end{Bmatrix} = \begin{Bmatrix} A_{l,x} \operatorname{Re}(\exp(j(l\omega_1 t + \theta_l))) \\ A_{l,y} \operatorname{Im}(\exp(j(\pm(l\omega_1 t + \theta_l)))) \end{Bmatrix} = \begin{Bmatrix} A_{l,x} \cos(l\omega_1 t + \theta_l) \\ A_{l,y} \sin(\pm(l\omega_1 t + \theta_l)) \end{Bmatrix} \quad (3.39)$$

Considering that the forces in X and Y direction are  $\pm 90^\circ$  out of phase and with the introduction of the Dirac delta function  $\delta(\bullet)$ , the input force can be also written in the frequency domain by Equation (3.40) [58]:

$$\begin{Bmatrix} F_{l,x}(\omega) \\ F_{l,y}(\omega) \end{Bmatrix} = \begin{Bmatrix} A_{l,x} \exp(j\theta_l) \delta(\omega - l\omega_1) \\ A_{l,y} (\pm j \exp(j\theta_l)) \delta(\omega - l\omega_1) \end{Bmatrix} \quad (3.40)$$

The system response vector  $\{X_l\}$  is derived from the two FRF matrix columns  $\{H_{(:,x)}\}$  and  $\{H_{(:,y)}\}$ , which are appended into a matrix, and multiplied by the vector of corresponding input components  $F_{l,x}$  and  $F_{l,y}$ , respectively:

$$\{X_l(\omega)\} = [\{H_{(:,x)}(\omega)\} \{H_{(:,y)}(\omega)\}] \begin{Bmatrix} F_{l,x}(\omega) \\ F_{l,y}(\omega) \end{Bmatrix} \quad (3.41)$$

From this point, equal amplitudes  $A_{l,x} = A_{l,y} = A_l$  in x and y direction are assumed. Thereafter, inserting the force from Equation (3.40) into Equation (3.41), multiplying and rearranging provides:

$$\{X_l(\omega)\} = A_l \exp(j\theta_l) \delta(\omega - l\omega_1) (\{H_{(:,x)}(\omega)\} \pm \{H_{(:,y)}(\omega)\}) \quad (3.42)$$

Assuming that the excitation amplitude  $A_l$  is proportional to the squared rotation speed  $\omega_1^2$ , like in the case of a centrifugal unbalance load, and considering that  $\omega_1 = \omega/l$ , the following proportionality is observed:

$$\{X_l(\omega)\} \propto \frac{\omega^2}{l^2} (\{H_{(:,x)}(\omega)\} \pm j\{H_{(:,y)}(\omega)\}) \quad (3.43)$$

A modal description (i.e. pole-residue model) of the FRF matrix can be used. If the FRF matrix columns are substituted with this form, the following relation is obtained [58], [59]:

$$\begin{aligned} \{X_l(\omega)\} \propto \frac{\omega^2}{l^2} & \left( [V](j\omega[I] - [A])^{-1} (\{L_x\} - j\{L_y\}) + \frac{1}{\omega^2} (\{LR_x\} - j\{LR_y\}) \right. \\ & \left. + (\{UR_x\} - j\{UR_y\}) \right), \end{aligned} \quad (3.44)$$

where  $[V]$  is the mode shape matrix,  $[A]$  is a diagonal matrix with the complex poles, and  $[L]$  is the modal participation matrix.  $[UR]$  and  $[LR]$  are the upper and lower residue matrix, respectively, to model the influence of out-of-band modes. For the sake of conciseness, a counterclockwise rotation is assumed in Equation (3.44).

From Equation (3.44), the impact of order excitation on the output spectrum with respect to the modal model can be concluded: The frequency-dependent input amplitude introduces a

frequency-dependent proportionality term in the output while the correlation leads to complex terms (specifically, the modal participation factors and upper and lower residuals) in the modal model.

The following considerations are possible under the assumption that the order input force is proportional to the rotational speed  $\omega_1^2$ , like the centrifugal (unbalance) force. This factor can be also described as the squared input frequency divided by the squared order number:  $\omega_1^2 = \omega^2/l^2$ . It follows that the displacement response due to order excitation is also proportional to  $\omega^2/l^2$ . The relation of acceleration FRFs, which are scaled by  $\omega^2$  in comparison to displacement FRFs, is also applicable to order responses. Therefore, accounting for the previous proportionality observations regarding the displacement response from an order, the acceleration order response is proportional to  $\omega^4/l^2$ .

In summary, employing OMA to analyse tracked machine orders has the following specifics compared to traditional modal analysis, which leads to the conclusion that OMA methods such as the operational pLSCF (see Appendix B) can be readily applied on tracked orders to perform OBMA [55], [59], [92].

- Displacement orders are proportional to  $\omega^2$ , and acceleration orders are proportional to  $\omega^4$ , while acceleration FRFs used in traditional modal analysis are proportional to  $\omega^2$ .
- The upper and lower residuals are complex, while they are real in traditional modal analysis.
- The participation factor is complex in both traditional modal analysis and OBMA.

### 3.3 Advanced data modelling for general applications

This subchapter introduces several methods for data modelling from a general application perspective, which is not bound by an underlying physical description such as the structural dynamics presented previously. This allows to model complex relationships based on the underlying data only and can thus be referred to as data learning [172].

#### 3.3.1 Linear Least Squares (LS) regression

LS is an approach used in regression analysis to determine an approximated solution for overdetermined systems. This is accomplished by minimising the total residual of the sum of squares of the variables observed. Depending on the problem, linear and non-linear LS can be used. Linear LS is often preferred due to simplicity and interpretability but can only be used when each coefficient is a constant or a product of a variable. Non-linear LS is more flexible with modelling capability but sacrifices the ease of interoperability that linear LS models offer. Below, the polynomial LS is presented, which is a subcategory of linear LS regression.

In polynomial LS, a function can be modelled by a polynomial in the form of Equation (3.45) with polynomial order  $N_p$  and coefficients  $a_{i_p}$ .

$$y = a_0 + a_1x + \dots + a_{i_p}x^{i_p} + \dots + a_{N_p}x^{N_p}, \quad (3.45)$$

which can also be represented by Equation (3.46) in matrix form for  $N$  samples of  $x$  and  $y$ .

$$\begin{aligned} \begin{pmatrix} y_1 \\ y_2 \\ \vdots \\ y_N \end{pmatrix} &= \begin{bmatrix} 1 & x_1 & \dots & x_1^{N_p} \\ 1 & x_2 & \dots & x_2^{N_p} \\ \vdots & \vdots & \ddots & \vdots \\ 1 & x_N & \dots & x_N^{N_p} \end{bmatrix} \begin{pmatrix} a_0 \\ a_1 \\ \vdots \\ a_{N_p} \end{pmatrix} \\ \{y\} &= [X] \{a\}. \end{aligned} \quad (3.46)$$

For overdetermined systems, i.e., where  $N_p < N - 1$ , an LS approximation of the polynomial coefficients can be obtained from

$$\{a\} = ([X^T][X])^{-1}[X^T]\{y\}. \quad (3.47)$$

### 3.3.2 Mahalanobis Distance (MD)

The MD [173] represents the deviation from a set  $[X]$  of multidimensional samples (i.e., the input space) to a sample  $\{x\}$  of the same dimensionality.

As such, the MD is a distance metric and not a modelling method itself. However, it can serve as a dimensionality reduction method and its output can supplement and, in some cases, substitute more general modelling approaches.

As a distance metric, the MD is always positive. In addition, the MD is a relative quantity in standard deviations, and therefore the application assumes a unimodal, standard underlying sample distribution. It also follows that the MD is scale-invariant towards its input samples, not requiring feature scaling.

The MD is calculated with Equation (3.48), which contains the inverse covariance matrix  $[K_{XX}^{-1}]$  of  $[X]$ , the vector of input feature means  $\{\mu\}$ , and the single multidimensional feature sample  $\{x\}$ .

$$d_{MD}(x) = \sqrt{(\{x\} - \{\mu\})^T [K_{XX}^{-1}] (\{x\} - \{\mu\})} \quad (3.48)$$

### 3.3.3 Support Vector Regression (SVR)

SVR [174] is a supervised machine learning algorithm used for regression analysis, where the goal is to predict a continuous target variable.

SVR is closely related to SVM [175], which is a classification algorithm. The main difference of SVM is that it attempts to find a hyperplane that maximises the margin between classes while minimising the misclassification error. SVR, on the other hand, attempts to find the best

possible hyperplane that fits the data by maximising the margin between the fit and the data points. This is done by mapping the training data into a higher-dimensional feature space using a kernel function. SVR uses a regularisation parameter  $p$  (or its inverse, the cost factor  $C$ ) to control the trade-off between maximising the margin and minimising the error on the training data, which is more generally known as the bias-variance trade-off.

### 3.3.4 Long Short-Term Memory (LSTM) Neural Network

The LSTM NN is a variant of the RNN architecture proposed by Hochreiter [124] to mitigate the vanishing gradient problem [122], [123]. The vanishing gradient commonly occurs when training a deep RNN using the backpropagation through time algorithm; when unrolling an RNN to update the weights, due to the depth of the network, the calculated derivatives are prone to exponentially “vanishing” or “exploding”. This is worsened by the shared weights of the RNN across time, which results in a higher likelihood of the vanishing or exploding gradient issue occurring in comparison to a standard feedforward network.

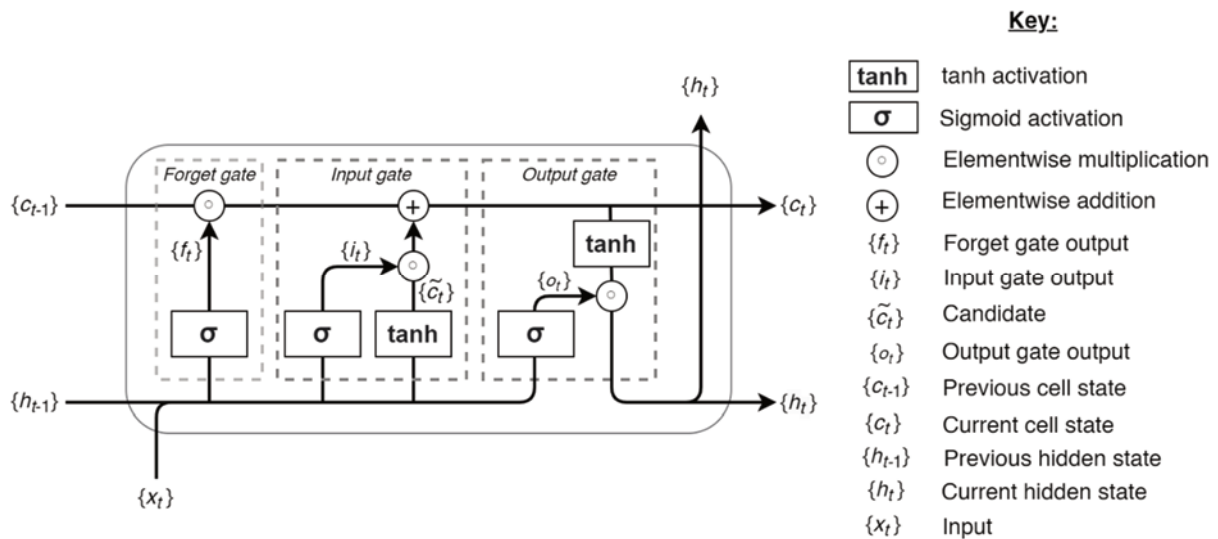


**Figure 3-3: Schematic architecture of an LSTM cell [21]**

The LSTM cell architecture, illustrated in Figure 3-3, addresses this issue using a specialised gate structure with three gates: forget gate, input gate and output gate. The forget gate, which outputs a vector  $\{f_t\}$ , determines which information is forgotten from the previous cell state based on the previous hidden cell state  $\{h_{t-1}\}$  and cell input  $\{x_t\}$  in the current cell state. This operation is mathematically represented in Equation (3.49). The input gate, which outputs a vector  $\{i_t\}$ , controls which information from the candidate vector  $\{\tilde{c}_t\}$  is stored in the cell state. The input gate is described in Equation (3.50), and the operation to determine the candidate values is described in Equation (3.51). The new cell state is determined by the elementwise product (also known as the Hadamard product and denoted by the operator  $\odot$ ) of the previous cell state with the forget gate output. This is followed by an elementwise addition with the Hadamard product of the input gate output and the candidate vector  $\{\tilde{c}_t\}$ .

This is mathematically described in Equation (3.52). The output gate output is determined using Equation (3.53), then used in the calculation for the new hidden state, described in Equation (3.54). Weight matrices and bias vectors are denoted by  $[W]$  and  $\{b\}$ , respectively. Subscripts  $f$ ,  $i$ , and  $o$  refer to the parameters of the forget, input, and output gate, respectively.

$$\{f_t\} = \sigma\left([W_f] \cdot \begin{Bmatrix} \{h_{t-1}\} \\ \{x_t\} \end{Bmatrix} + \{b_f\}\right) \quad (3.49)$$

$$\{i_t\} = \sigma\left([W_i] \cdot \begin{Bmatrix} \{h_{t-1}\} \\ \{x_t\} \end{Bmatrix} + \{b_i\}\right) \quad (3.50)$$

$$\{\tilde{c}_t\} = \tanh\left([W_c] \cdot \begin{Bmatrix} \{h_{t-1}\} \\ \{x_t\} \end{Bmatrix} + \{b_c\}\right) \quad (3.51)$$

$$\{c_t\} = \{f_t\} \circ \{c_{t-1}\} + \{i_t\} \circ \{\tilde{c}_t\} \quad (3.52)$$

$$\{o_t\} = \sigma\left([W_o] \cdot \begin{Bmatrix} \{h_{t-1}\} \\ \{x_t\} \end{Bmatrix} + \{b_o\}\right) \quad (3.53)$$

$$\{h_t\} = \{o_t\} \circ \tanh(\{c_t\}) \quad (3.54)$$

### Autoencoder (AE) Architecture

The AE architecture was introduced by Hinton [176] as a method of utilising unsupervised learning to model encodings of unlabelled data in latent space. The AE operates by encoding the input values using dimensionality reduction into latent space, then decoding the latent space representation to reconstruct the original input values. This operation is illustrated in Figure 3-4.

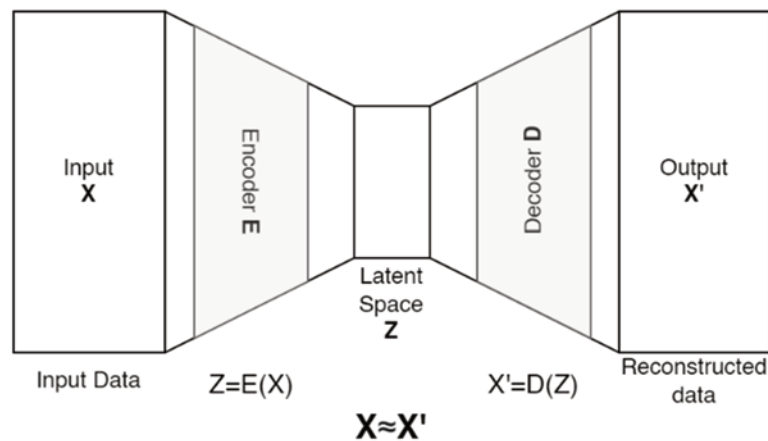
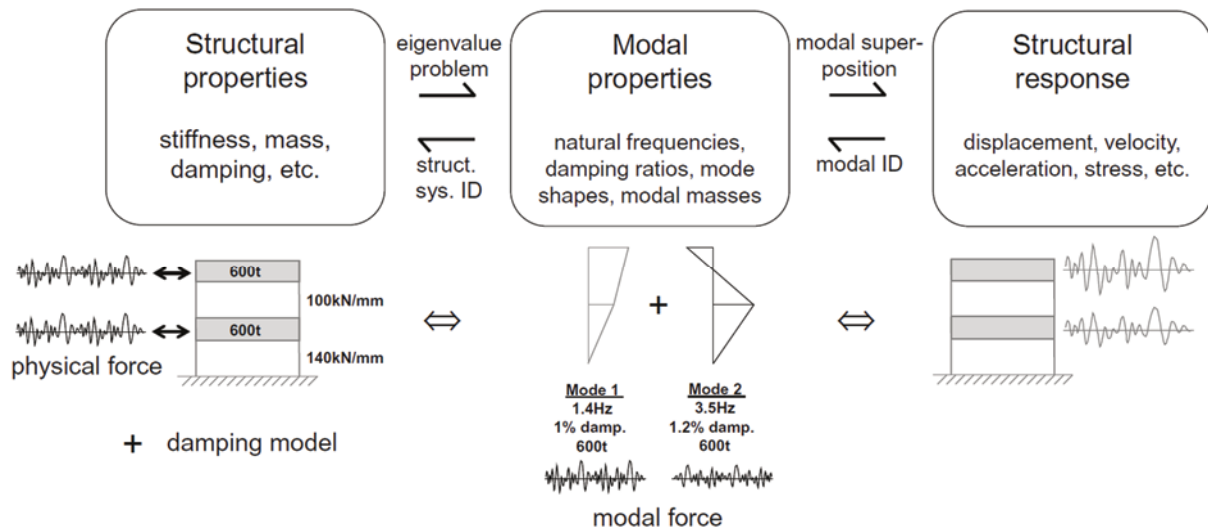


Figure 3-4: Schematic architecture of an AE model [21]

### 3.4 Conclusions

This chapter introduced the foundational theory and methods that are relevant to the contributions in the subsequent thesis chapters.



**Figure 3-5: Relation between structural quantities (blocks) through forward (right-pointing arrows) and inverse (left-pointing arrows) problems in structural dynamics [2]**

First, topics from the domain of structural dynamics were covered. Subchapter 3.1 focused on the fundamental dynamic equation and its solution by integration, yielding simulated structural responses. The eigenvalue problem was revisited, allowing to determine modal parameters from modelled system matrices. These tasks are classified as forward problems, while modal identification from measured or simulated structural response is considered a backward or inverse problem [2]. This relationship is illustrated in Figure 3-5. Subchapter 3.2 addressed the latter area with an introduction of common categories and the foundational theory of EMA and OMA for modal identification. Due to the relevance of order tracking in combination with the OBMA method for rotating machinery applications (identified from existing literature in Subchapter 2.1 and Subchapter 2.2), these methods were also introduced in Subchapter 3.2.

The subsequent Subchapter 3.3 presented methods of data modelling for general applications. This is especially relevant where the governing physical phenomena and constraints are unknown or infeasible to accurately describe a priori. The LS method was introduced, which is a common foundation for data modelling, including general regression tasks and modal identification discussed in Subchapter 3.2. More recent AI-based approaches for data modelling, including SVR and LSTM NN were presented as well, motivated by the findings from Subchapter 2.4 on the state of the art in the domain of condition monitoring and RUL prediction of rotating machinery.



---

A main contribution of this thesis is covered in the following Chapter 4, which introduces the first parametric open-source dataset of simulated rotating machinery vibration under acceleration conditions. Modal parameters and dynamic time-responses of this simulated structure are determined based on the theory provided in Subchapter 3.1.

## 4 Open simulation dataset for OMA and vibration analysis of rotating machinery during acceleration

The previous Chapter 3 introduced theory and methods, which are relevant in the further course of this thesis. The present chapter presents a major contribution of the thesis. It focuses on a novel simulation dataset, which is made publicly available [19] and proposed for application of OMA and other vibration-based signal processing methods for rotating machinery during acceleration. A part of this chapter, as noted separately in the corresponding subchapters, was published by the thesis author in a peer-reviewed journal paper [17]. The extended version, which is based on the current form of this chapter resulted in a submission of an additional journal paper [18], which is currently under peer review. The proposed open-source dataset was also submitted to an online repository [19]. Supplementary information on the dataset, such as the file structure and source code introduction, is also provided in Appendix D.

Supporting motivation of this work is provided by Subchapter 2.2, as it confirmed that acceleration/deceleration conditions can be required to achieve sufficient excitation of modes in cases with low ambient or operational random excitation. Subchapter 2.3 showed that current publicly available datasets suitable for OMA are typically limited to the civil engineering domain. At the same time, most existing vibration datasets from rotating machinery focus on condition monitoring applications, limiting their use for OMA. Consequently, current studies on OMA for rotating machinery use proprietary experimental or simulation data, which became clear from Subchapter 2.1 and Subchapter 2.2. The lack of a suitable open dataset contributes to further gaps identified in these subchapters, such as a limited comparability and the lack of studies evaluating the potential impact of excitation conditions on modal estimation results. Suitable open simulation data can also facilitate reproducibility of research and allow for systematic evaluations of the potential impact of various excitation conditions, as such parametrised datasets were found lacking in current literature in Subchapter 2.3. The overarching aim of the proposed dataset is to aid research and development of existing and future OMA and vibration signal processing algorithms conducted both by the author in course of this thesis and by fellow researchers in this field.

To address the stated issues related to a lack of suitable open data, a parametric simulation dataset is presented in this chapter and made publicly available. In summary, the contributions of this work are:

- Definition and publication of the first open dataset for vibration analysis of rotating machinery during acceleration.

- Providing suggested varied parameters with corresponding simulation data for parametric sensitivity studies.
- Providing source code and model definition files to aid further expansion and adaptation of the dataset for future research.

## 4.1 Model definition

A 2D structure was designed for the simulation dataset. This model was first introduced and published by the thesis author in a peer-reviewed journal paper [17] and is included in a separate journal paper submission [18], which is currently under peer review. The structure approximates a fan casing, which can be regarded as either installed on an operational aircraft or within a test rig for mechanical fan spinning tests. This structure consists of 9 nodes, which represent point masses and are connected with spring and dashpot elements with a total of 18 DOFs. The parameters of the structure's elements and its geometry are provided by Figure 4-1 and Table 4-1, respectively.

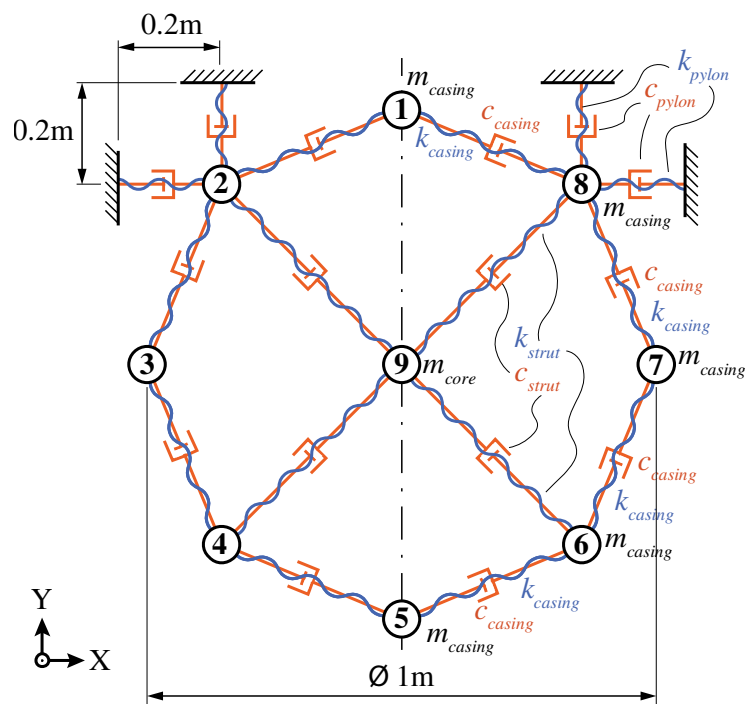


**Figure 4-1: Definition of the geometry and element types of the simulated dynamic structure**

**Table 4-1: Simulation parameters**

Mechanical properties
Masses: $m_{core} = 10\text{kg}$ , $m_{casing} = 1\text{kg}$
Stiffnesses: $k_{casing} = 500000\text{ N/m}$ , $k_{pylon} = 10^6\text{ N/m}$ , $k_{strut} = 500000\text{ N/m}$
Damping coefficients: $c_{casing} = 20\text{ Ns/m}$ , $c_{pylon} = 50\text{ Ns/m}$ , $c_{strut} = 30\text{ Ns/m}$
Time response simulation
Linear acceleration Newmark (implicit) time integration method
Simulation sampling frequency: $f_s = 5\text{ kHz}$

The reference modal parameters of the model are determined from a complex eigenvalue analysis of its system matrices using the “polyeig” function of MATLAB. The undamped eigenfrequencies and damping ratios are presented in Table 4-2. The corresponding complex mode shapes are given in Table 4-3 with real and imaginary values rounded to two decimal places. Each mode shape is normalised to the magnitude and phase of the largest mode shape component. Even though not immediately obvious from the geometry (Figure 4-1), the structure has two rigid body modes. These are listed as modes 1 and 2 with zero damping in Table 4-2.

The frequency spectra from the simulated model response at every DOF to random excitation are shown in Figure 4-2. For clearer interpretation, the spectra are arranged loosely corresponding to their respective DOF locations shown in Figure 4-1. Moreover, the eigenfrequencies are marked in the spectra by dashed vertical lines. The symmetric structure is reflected by the resulting response, showing equal spectrum progressions of, e.g., DOF 3X and DOF 7X shown in Figure 4-2.

The spectra are obtained using Welch's method from simulated responses with  $T=100s$  duration, which are split into 2.5s segments with 70% overlap and multiplied by the Hann window weighting function before spectrum averaging. This also applies to the subsequent spectra of this chapter unless stated otherwise. To aid conciseness, further plots of the system response in this chapter are limited to DOF 1X.

**Table 4-2: Reference values for eigenfrequencies and damping ratios of the simulated structure**

Mode	Eigenfrequency $f_{ref}$ (Hz)	Damping ratio $\xi_{ref}$	Mode	Eigenfrequency $f_{ref}$ (Hz)	Damping ratio $\xi_{ref}$
1	0.00	0.00%	10	120.56	1.75%
2	0.00	0.00%	11	138.70	2.24%
3	26.37	0.47%	12	160.25	2.28%
4	26.85	0.48%	13	177.05	2.30%
5	47.40	0.67%	14	198.82	2.60%
6	55.96	0.77%	15	207.42	3.35%
7	65.94	0.93%	16	212.39	3.28%
8	97.70	1.43%	17	229.57	3.18%
9	101.53	1.69%	18	239.84	3.27%

Table 4-3: Complex reference mode shapes of the simulated structure

DOF	Mode																	
	1	2	3	4	5	6	7	8	9	10	11	12	13	14	15	16	17	18
1X	0.00+0.00j	0.00+0.00j	0.00+0.00j	0.09+0.00j	0.00-0.00j	0.00+0.00j	0.42-0.00j	0.00+0.00j	0.97+0.01j	1.00+0.00j	0.00-0.00j	-0.47-0.00j	0.00-0.00j	0.04+0.01j	0.00+0.00j	0.46-0.02j	0.00+0.00j	-0.82+0.01j
1Y	0.00+0.00j	0.00+0.00j	-0.37-0.00j	0.00-0.00j	1.00+0.00j	1.00+0.00j	0.00-0.00j	-0.35+0.00j	0.00+0.00j	0.00-0.00j	-0.03+0.00j	0.00+0.00j	0.10+0.00j	0.00+0.00j	-0.17+0.00j	0.00+0.00j	-0.21+0.00j	0.00-0.00j
2X	0.00+0.00j	0.00+0.00j	-0.19-0.00j	0.16+0.00j	0.11-0.00j	0.10-0.00j	0.23-0.00j	0.11+0.00j	0.34+0.00j	0.32-0.00j	0.00-0.00j	-0.07+0.01j	-0.09-0.01j	0.13-0.02j	1.00+0.00j	-0.92+0.01j	0.72-0.01j	1.00+0.00j
2Y	0.00+0.00j	0.00+0.00j	0.15+0.00j	-0.18-0.00j	0.12-0.00j	-0.08-0.00j	0.27-0.00j	0.30-0.00j	0.40-0.00j	0.01-0.00j	0.12-0.00j	0.39-0.01j	-0.52+0.01j	-0.40+0.03j	-0.63+0.00j	1.00+0.00j	1.00-0.00j	0.86-0.00j
3X	1.00+0.00j	1.00+0.00j	-0.51-0.00j	-0.37-0.00j	0.35-0.00j	-0.93-0.00j	1.00+0.00j	0.33-0.00j	-0.12-0.00j	-0.18+0.00j	-0.05+0.00j	-0.22+0.00j	0.30-0.00j	0.13-0.00j	0.01+0.00j	-0.03-0.00j	-0.10+0.00j	-0.09+0.00j
3Y	-0.41+0.00j	-0.41+0.00j	0.25+0.00j	0.01-0.00j	0.12-0.00j	0.03-0.00j	0.54+0.00j	1.00+0.00j	0.86-0.00j	-0.22-0.01j	0.25-0.01j	1.00+0.00j	-0.80-0.00j	-0.23-0.01j	0.16-0.01j	-0.44+0.03j	-0.52+0.01j	-0.43+0.01j
4X	0.59+0.00j	0.59+0.00j	0.49-0.00j	0.67+0.00j	-0.03+0.00j	0.12-0.00j	-0.48+0.00j	-0.05-0.01j	0.81-0.01j	-0.16-0.00j	-1.00+0.00j	-0.59-0.01j	-0.68+0.01j	-0.64-0.00j	0.03-0.00j	-0.24+0.03j	-0.08+0.00j	-0.07+0.00j
4Y	-0.59+0.00j	-0.59+0.00j	0.62-0.00j	0.41-0.00j	0.04+0.00j	0.13-0.00j	0.31+0.00j	0.76-0.00j	0.70-0.01j	-0.36-0.00j	-0.48-0.00j	-0.98-0.01j	1.00+0.00j	0.45+0.00j	-0.09+0.01j	0.24-0.03j	0.16-0.00j	0.12-0.00j
5X	0.65+0.00j	0.65+0.00j	0.00-0.00j	0.52+0.00j	0.00-0.00j	0.00-0.00j	-0.76+0.00j	0.00+0.00j	1.00+0.00j	-0.05-0.01j	0.00-0.00j	0.99-0.00j	0.00+0.00j	1.00+0.00j	0.00+0.00j	0.31-0.05j	0.00+0.00j	0.08-0.00j
5Y	-0.44+0.00j	-0.44+0.00j	-0.69-0.00j	0.00-0.00j	0.26-0.00j	-0.95-0.00j	0.00+0.00j	-0.55-0.00j	0.00+0.00j	0.00-0.00j	-0.46+0.01j	0.00-0.00j	-0.35+0.00j	0.00-0.00j	0.01-0.00j	0.00+0.00j	-0.03+0.00j	0.00+0.00j
6X	0.33+0.00j	0.33+0.00j	-0.49+0.00j	0.67+0.00j	0.03-0.00j	-0.12+0.00j	-0.48+0.00j	0.05+0.01j	0.81-0.01j	-0.16-0.00j	1.00-0.00j	-0.59-0.01j	0.68-0.01j	-0.64-0.00j	-0.03+0.00j	-0.24+0.03j	0.08-0.00j	-0.07+0.00j
6Y	0.33+0.00j	0.33+0.00j	0.62-0.00j	-0.41+0.00j	0.04+0.00j	0.13-0.00j	-0.31-0.00j	0.76-0.00j	-0.70+0.01j	0.36+0.00j	-0.48-0.00j	0.98+0.01j	1.00-0.00j	-0.45-0.00j	-0.09+0.01j	-0.24+0.03j	0.16-0.00j	-0.12+0.00j
7X	0.56+0.00j	0.56+0.00j	0.51+0.00j	-0.37-0.00j	-0.35+0.00j	0.93+0.00j	1.00+0.00j	-0.33+0.00j	-0.12-0.00j	-0.18+0.00j	0.05-0.00j	-0.22+0.00j	-0.30+0.00j	0.13-0.00j	-0.01-0.00j	-0.03-0.00j	0.10-0.00j	-0.09+0.00j
7Y	0.23+0.00j	0.23+0.00j	0.25+0.00j	-0.01+0.00j	0.12-0.00j	0.03-0.00j	-0.54-0.00j	1.00+0.00j	-0.86+0.00j	0.22+0.01j	0.25-0.01j	-1.00+0.00j	-0.80-0.00j	0.23+0.01j	0.16-0.01j	0.44-0.03j	-0.52+0.01j	0.43-0.01j
8X	0.00+0.00j	0.00+0.00j	0.19+0.00j	0.16+0.00j	-0.11+0.00j	-0.10+0.00j	0.23-0.00j	-0.11-0.00j	0.34+0.00j	0.32-0.00j	0.00+0.00j	-0.07+0.01j	0.09+0.01j	0.13-0.02j	-1.00+0.00j	-0.92+0.01j	-0.72+0.01j	1.00+0.00j
8Y	0.00+0.00j	0.00+0.00j	0.15+0.00j	0.18+0.00j	0.12-0.00j	-0.08-0.00j	-0.27+0.00j	0.30-0.00j	-0.40+0.00j	-0.01+0.00j	0.12-0.00j	-0.39+0.01j	-0.52+0.01j	0.40-0.03j	-0.63+0.00j	-1.00-0.00j	1.00+0.00j	-0.86+0.00j
9X	0.00+0.00j	0.00+0.00j	0.00-0.00j	1.00+0.00j	0.00-0.00j	0.00-0.00j	0.15-0.00j	0.00-0.00j	-0.24+0.00j	0.02+0.00j	0.00+0.00j	0.11+0.00j	0.00-0.00j	-0.01+0.00j	0.00-0.00j	0.06+0.00j	0.00+0.00j	0.00-0.00j
9Y	0.00+0.00j	0.00+0.00j	1.00-0.00j	0.00+0.00j	0.08+0.00j	-0.15+0.00j	0.00-0.00j	-0.16+0.00j	0.00+0.00j	0.00-0.00j	0.10+0.00j	0.00+0.00j	0.00-0.00j	0.00+0.00j	0.05+0.00j	0.00+0.00j	-0.01-0.00j	0.00+0.00j

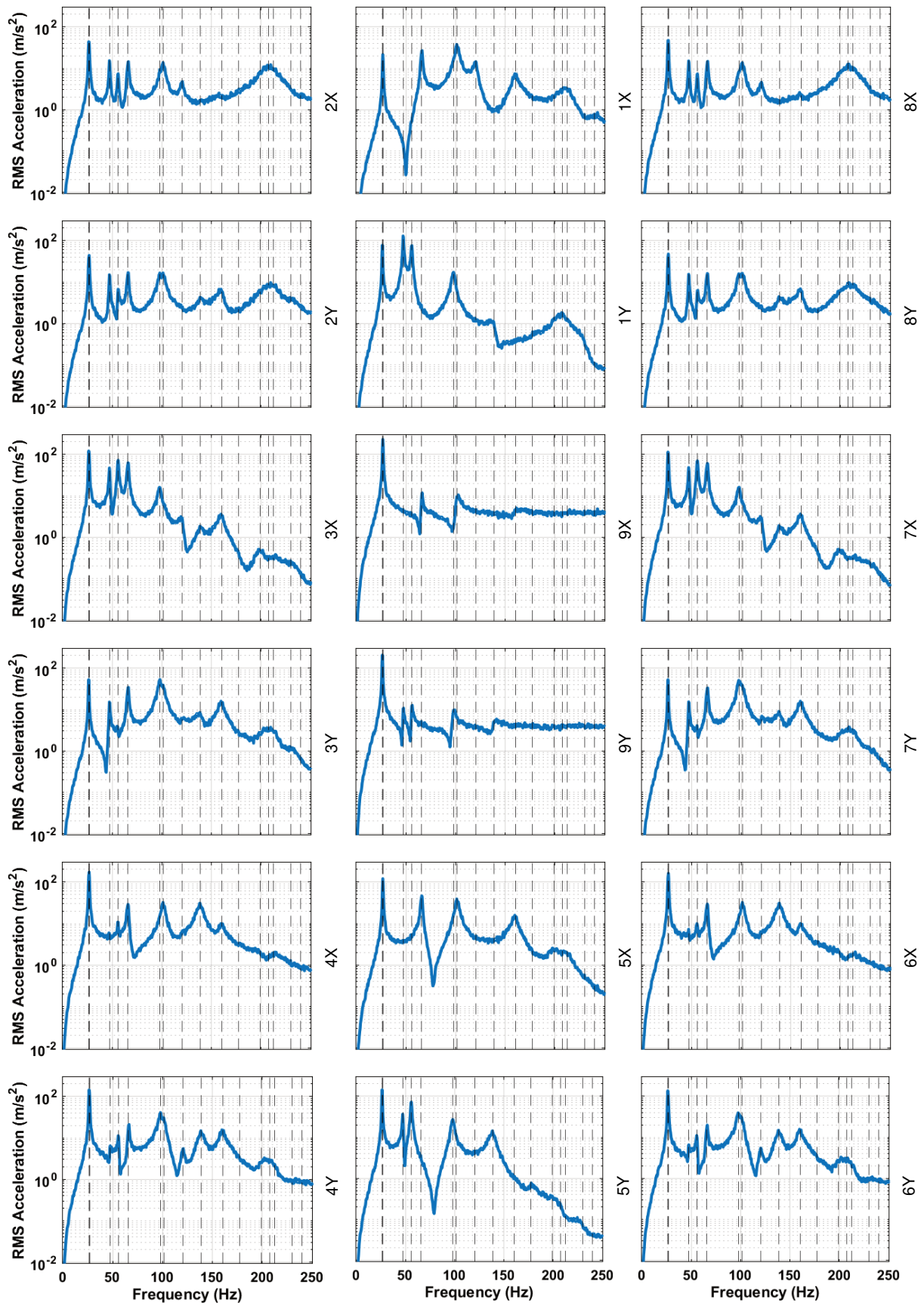


Figure 4-2: Linear auto spectra of the model response from all DOFs to random excitation

## 4.2 Varied parameters of the forced response

External forces in X and Y directions are simulated to act on the shaft, which is represented by the central node 9 in Figure 4-1. It is therefore assumed as the location, which transmits harmonic and random operational forces originating from a fan, compressor, driving turbine, or (electric) motor.

Three parameters are introduced as independent variables, which are described in more detail and formally defined in the following Subchapter 4.2.1 to Subchapter 4.2.3. Table 4-4 gives an overview of the parametric values initially provided in the dataset of simulated time responses. However, this dataset foundation can readily be extended using the provided definitions and source code, adding further values, parameter combinations, and new parameters as required by the specific study.

**Table 4-4: Simulated values and combinations of parameters initially provided in the extendable dataset**

Sub-dataset title	Harmonic ratio $h_{rat}$ (%)	Run-up duration $T$ (s)	Noise ratio $n_{rat}$ (%)
Varied harmonic ratio	0, 20, 40, 60, 80, 100	100	0.0
Varied run-up durations	80	10, 20, 40, 80, 160, 320	0.0
Varied noise ratios	60	100	0.0, 0.5, 1, 2, 4, 8, 16

### 4.2.1 Harmonic amplitude ratio

The simulated forces on node 9 are composed of varying amplitude proportions of random force and rotating force vectors (i.e., machine orders) in the XY-plane. This proportion is quantified by a harmonic ratio. The present subchapter introducing this parameter was published by the thesis author as a part of a peer-reviewed journal paper [17].

Equation (4.1) provides the definition of the harmonic ratio and its values simulated in the dataset. It describes the ratio of harmonic (i.e., order) RMS amplitude  $RMS(x_l(t))$  to the sum of harmonic and random RMS amplitudes  $RMS(x_l(t)) + RMS(x_r(t))$ . This was implemented using MATLAB, where the time-functions of the individual input orders (“chirp” function) and the random contribution (“randn” function) are generated with RMS values of each function according to Equation (4.1) and then superposed to a single excitation function.

$$h_{rat} = \frac{RMS(x_l(t))}{RMS(x_l(t)) + RMS(x_r(t))} \in \{0.0, 0.2, 0.4, 0.6, 0.8, 1.0\} \quad (4.1)$$

The sum  $RMS(x_l(t)) + RMS(x_r(t))$  increases linearly with increasing rpm over time  $t$  according to Equation (4.2), where  $\Sigma_{r1}=200N$  and  $\Sigma_{r2}=4000N$  are the RMS sums at the beginning and end of a simulation run, respectively. As shown in Table 4-4, the simulation

duration for varying harmonic ratios is chosen as  $T=100$ s. The simulated model response for increasing harmonic ratios is illustrated in Figure 4-3.

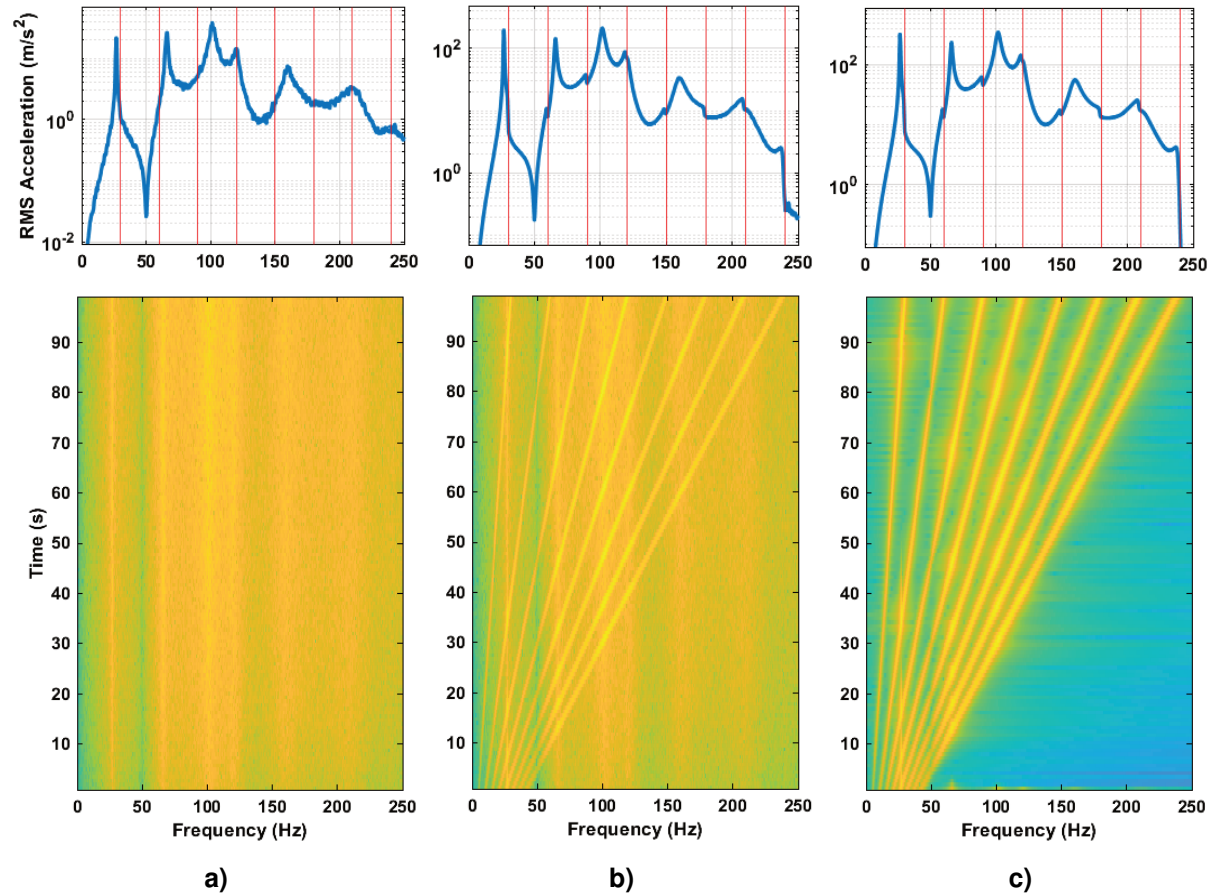


**Figure 4-3: Spectra and spectrograms of the model response at DOF 1X with harmonic ratios  $h_{rat}$  of a) 0.0; b) 0.6; c) 1.0**

$$\text{RMS}(x_l(t)) + \text{RMS}(x_r(t)) = \Sigma_{t1} + (\Sigma_{t2} - \Sigma_{t1}) \frac{t}{T} = 200N + 3800N \frac{t}{T} \quad (4.2)$$

The frequency  $f_1$  of the first order  $l = 1$  (i.e., the fundamental frequency) is increased linearly from  $f_{1,t1}=5$ Hz to  $f_{1,t2}=30$ Hz over time as specified by Equation (4.3). This equates to a run-up from 300rpm to 1800rpm.

$$f_1(t) = f_{1,t1} + (f_{1,t2} - f_{1,t1}) \frac{t}{T} = 5\text{Hz} + 25\text{Hz} \frac{t}{T} \quad (4.3)$$

The frequencies of the rotation forces (i.e., orders  $l$ ) are derived from the fundamental frequency (order  $l = 1$ ) as per Equation (4.4). That is, the first 8 orders are included in the simulation.

$$f_l(t) = l f_1(t), \quad l \in \{1, 2, 3, 4, 5, 6, 7, 8\} \quad (4.4)$$

#### 4.2.2 Duration and acceleration rate

In contrast to the variation of the harmonic ratio introduced in the previous subchapter, the sweep acceleration has been evaluated before in terms of its impact on resulting frequency spectra [177]–[179] and order tracking with subsequent modal estimation by OBMA [115],



[180]. An impact of these effects is also observed in the analysis of the presented dataset, which is performed and presented later in Subchapter 5.2.3 in frame of a comparative parametric study. Nevertheless, the inclusion of this parameter in the proposed dataset is of high relevance, as it facilitates research of future methods dealing with various sweep acceleration rates and to promote comparability between future and existing methods.

The acceleration rate can be expressed from Equation (3.25) as the order frequency's rate of change  $\dot{f}_l$  in Hz/s (or  $s^{-2}$ ). Assuming a linear increase of order frequencies, i.e., a constant frequency acceleration rate, as defined in Equation (4.3), the run-up duration  $T$  is related to the acceleration rate  $\dot{f}_l$  as:

$$\dot{f}_l(T) = \frac{(f_{l,t2} - f_{l,t1})}{T} \quad (4.5)$$

It is established that the errors of the eigenfrequency estimations are approximately proportional to the square root of the absolute sweep (or order) acceleration rate  $\sqrt{|\dot{f}_l|}$  [177]. Considering this nonlinear relationship, it is opted to use a logarithmic spacing between the parameter values for the simulated durations  $T$ , specified below.

$$T \in \{10s, 20s, 40s, 80s, 160s, 320s\} \quad (4.6)$$

This assigns a finer granularity to shorter durations, i.e. higher acceleration rates. Figure 4-4 plots the approximate proportionality factor of the eigenfrequency estimation bias [177] over values of  $T$  in logarithmic and linear spacing. The benefit of logarithmic spacing of  $T$  is visible as it provides a more even distribution of resulting proportionality values compared to linear spacing.

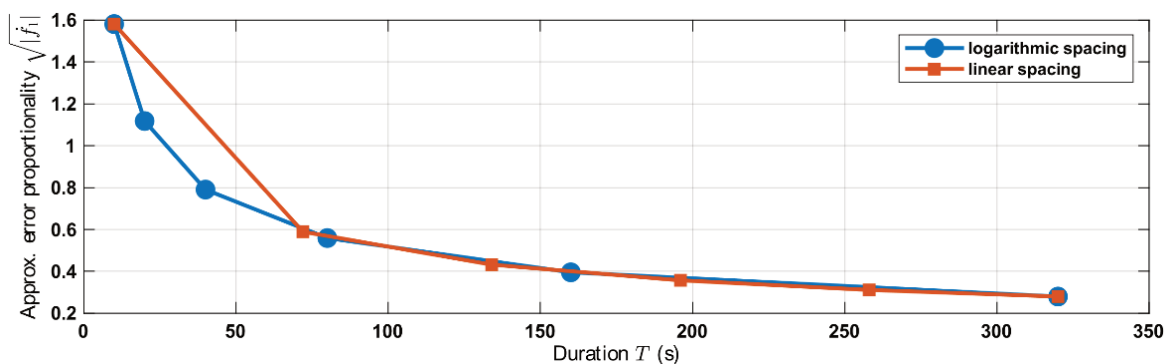


**Figure 4-4: Approximate proportionality factors for eigenfrequency estimation errors from spectra of order  $l=1$  over run-up durations  $T$ ; comparing the implemented logarithmic scaling of  $T$  to linear spacing**

### 4.2.3 Measurement noise

To gauge the sensitivity of vibration signal processing methods to measurement noise, the following levels of white gaussian noise are superposed to the simulated time response. The

noise levels are defined as the proportion between the power of the noise signal  $x_n(t)$  and the power of output signals  $x_s(t)$  averaged over all  $N_o$  output channels, i.e., model DOFs.

$$n_{rat} = \left( \frac{RMS(x_n(t))}{\frac{1}{N_o} \sum_{i_o}^{N_o} RMS(x_{s,i_o}(t))} \right)^2 \in \{0\%, 0.5\%, 1\%, 2\%, 4\%, 8\%, 16\%\} \quad (4.7)$$

The inverse of these values provides the equivalent values of the signal-to-noise-ratio (SNR), which is commonly represented on a logarithmic scale in decibels as per Equation (4.8).

$$SNR_{dB} = 10 \log_{10} \left( \frac{1}{n_{rat}} \right) \quad (4.8)$$

Figure 4-5 shows averaged spectra and spectrograms from a subset of simulated model responses in increasing order of noise ratios. The spectra illustrate that the noise floor is increasing with the noise ratio. At high noise ratios, the output noise floor almost entirely overcasts the system response to random excitation, as seen by the mostly missing vertical resonance lines in the spectrogram in Figure 4-5 c). In this case, the observable system response is primarily driven by the order excitation, which underlines the relevance of transient conditions for vibration analysis.

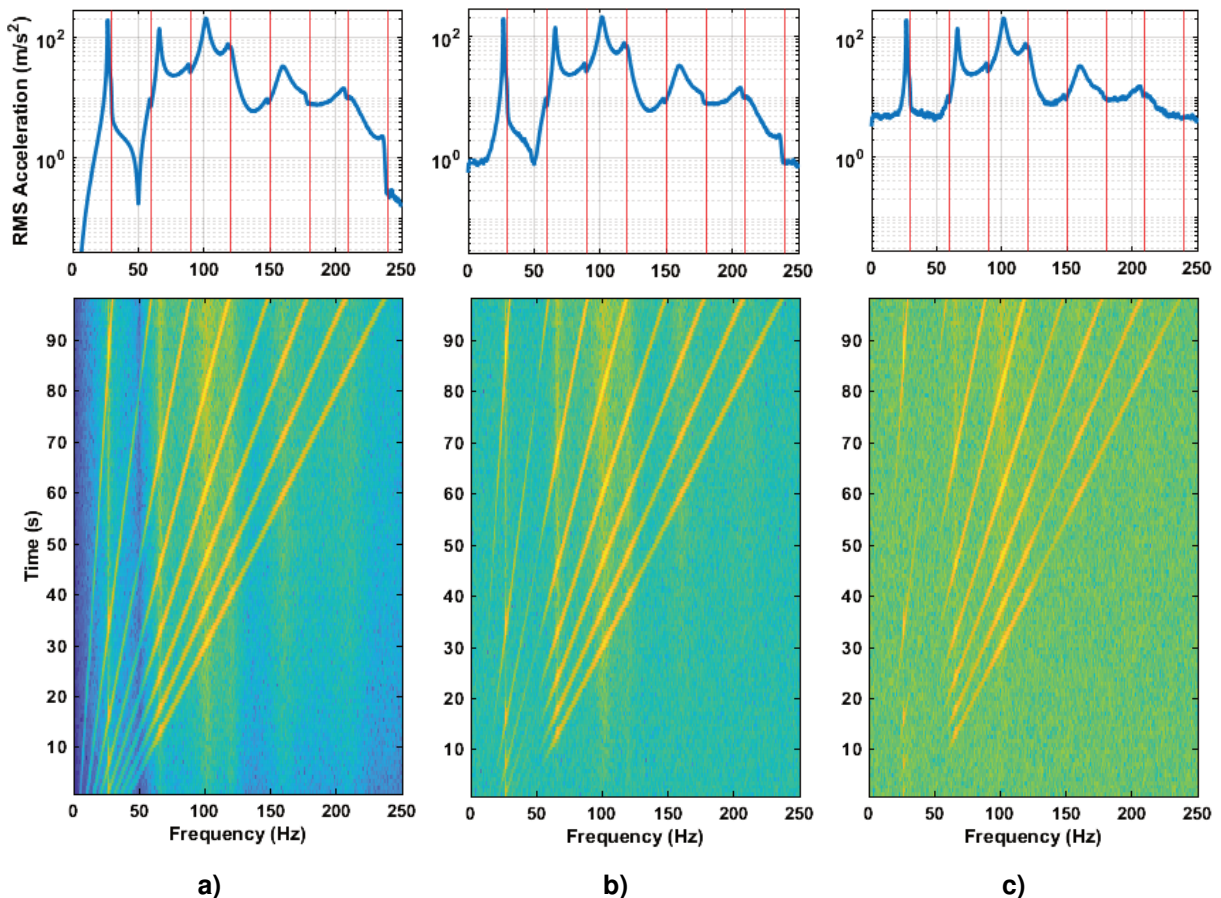


**Figure 4-5: Spectra and spectrograms of the model response at DOF 1X with harmonic ratios  $h_{rat}=0.6$  and noise ratios  $n_{rat}$  of a) 0.0%; b) 0.5%; c) 16%**

## 4.3 Characteristics of input and output spectra resulting from order excitation

This subchapter uses data from the simulation setup to illustrate the impact of harmonic order excitation on the response spectrum and to discuss the end-of-order effect. The presented results of this subchapter form a part of a peer-reviewed journal publication [17] of the author of this thesis.

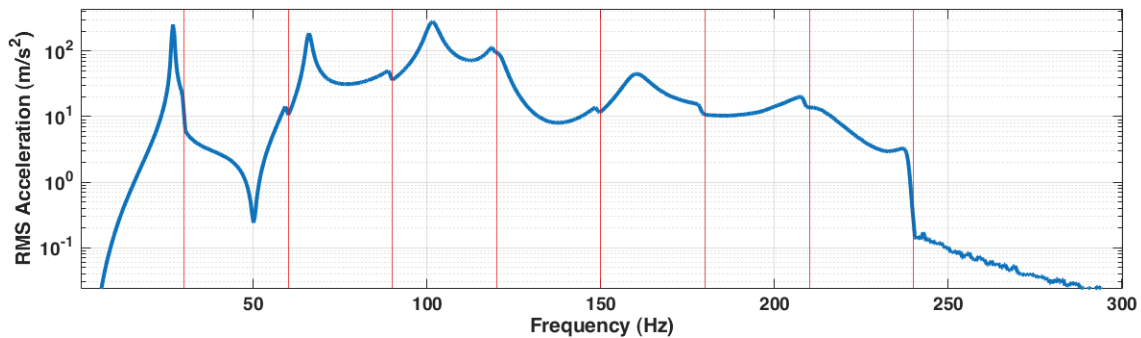


**Figure 4-6: Acceleration output spectrum of the simulated structure at node 1 (see Figure 4-1), X direction, harmonic ratio 0.8**

Figure 4-6 shows the linear auto-spectrum of the model's response calculated using Welch's method from the MATLAB toolbox ABRAVIBE [181]. The spectrum shows discontinuities at the frequencies, where individual orders end (marked with vertical red lines). They are due to the end-of-order effect but can be misinterpreted as the system response by common OMA methods and can thus lead to falsely identified modes [53]–[55]. The origin of this phenomenon becomes clear when visualising the spectrum and spectrogram of the input force in Figure 4-7.

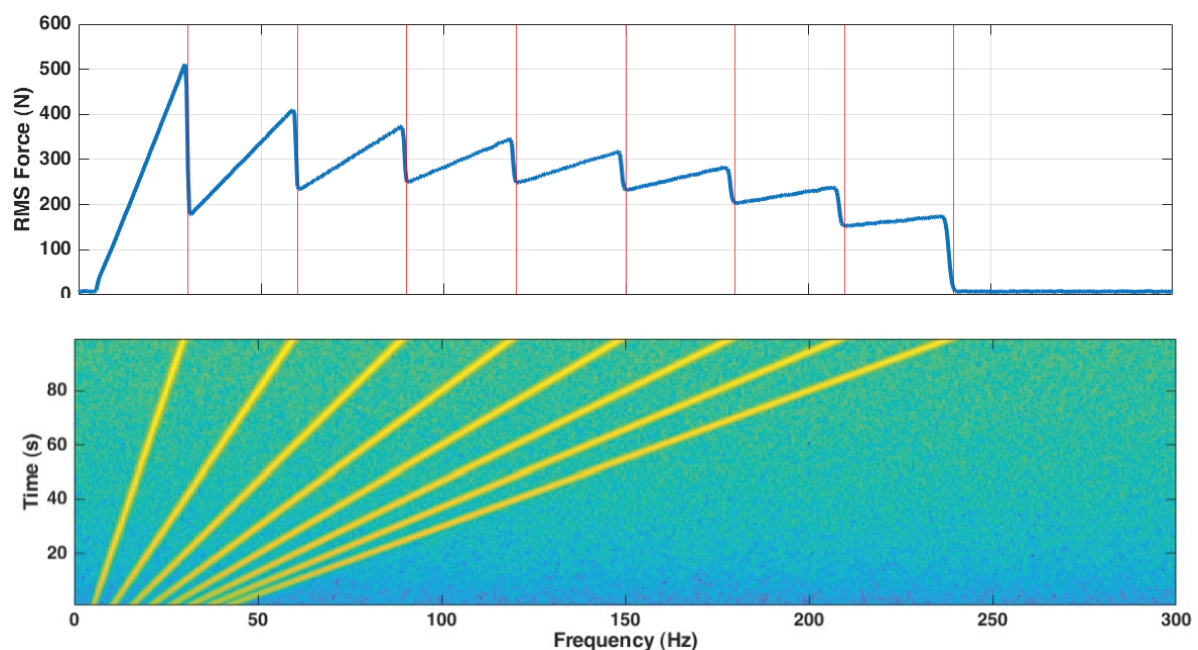


**Figure 4-7: Force input spectrum (top) and spectrogram (bottom) of the simulated structure**

The input orders can be regarded as an excitation by multiple simultaneous sweeps with different sweeping rates. The underlying individual orders with linearly increasing amplitudes (defined in Equation (4.2)) are visible in the input spectrum plot. A sawtooth pattern is formed due to the abrupt ending of the individual orders' contribution to the excitation. This strong deviation from a flat input spectrum is reflected in the output spectrum in Figure 4-6. The greatest distortion in Figure 4-7 (top) is visible at the frequency range of the first order, which shows the highest amplitude slope as well as the greatest abrupt decrease at its end. This trend decreases with higher orders.

This progression can be attributed to two factors:

1. Increasing frequency bandwidths (i.e., decreasing sweeping rates) of increasing orders result in lower spectral amplitudes. The reason is that the FT of a sweep is proportional to  $\sqrt{T/(2W)}$ , where  $T$  is the total sweep duration and  $W$  is the frequency bandwidth of the sweep. This has been shown for sweeps with a linear frequency function and constant amplitude [182].
2. The rows of the spectrogram in Figure 4-7 (bottom) can be considered as colour-coded spectra of (overlapping) time blocks of the original signal. The averaging of these individual spectra represents Welch's method, which estimates the overall spectrum shown in the top portion of Figure 4-7. When multiple orders cover a certain frequency range, they all contribute to the resulting average (i.e., the estimated spectrum amplitude) in this range. At rising frequencies, less and less orders are present in the excitation, leading to the smallest spectrogram amplitudes above 210 Hz, where solely the last order is contributing to the excitation.

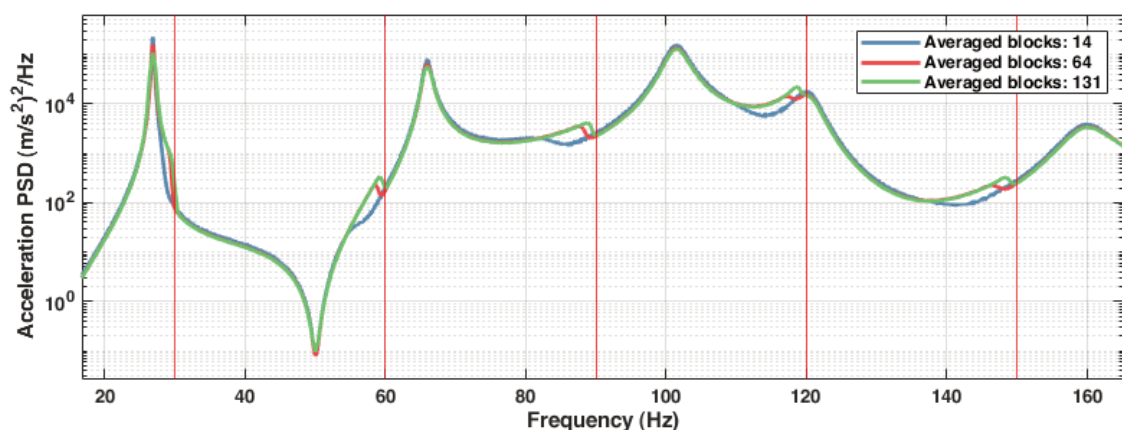


**Figure 4-8: PSD estimations for increasing number of averaged blocks with 70% overlap in Welch's method, red vertical lines mark the calculated end-of-order frequencies**

It was observed that higher harmonic ratios (i.e., greater order amplitudes with a steeper increase over rpm) produce stronger end-of-order distortions. In addition, a higher number of spectrum averages used in Welch's method leads to sharper end-of-order peaks as shown in

Figure 4-8. These distortions are still visible for lower numbers of averaged blocks but appear more smeared and shifted to lower frequencies compared to the calculated end-of-order frequencies marked with red vertical lines in Figure 4-8.

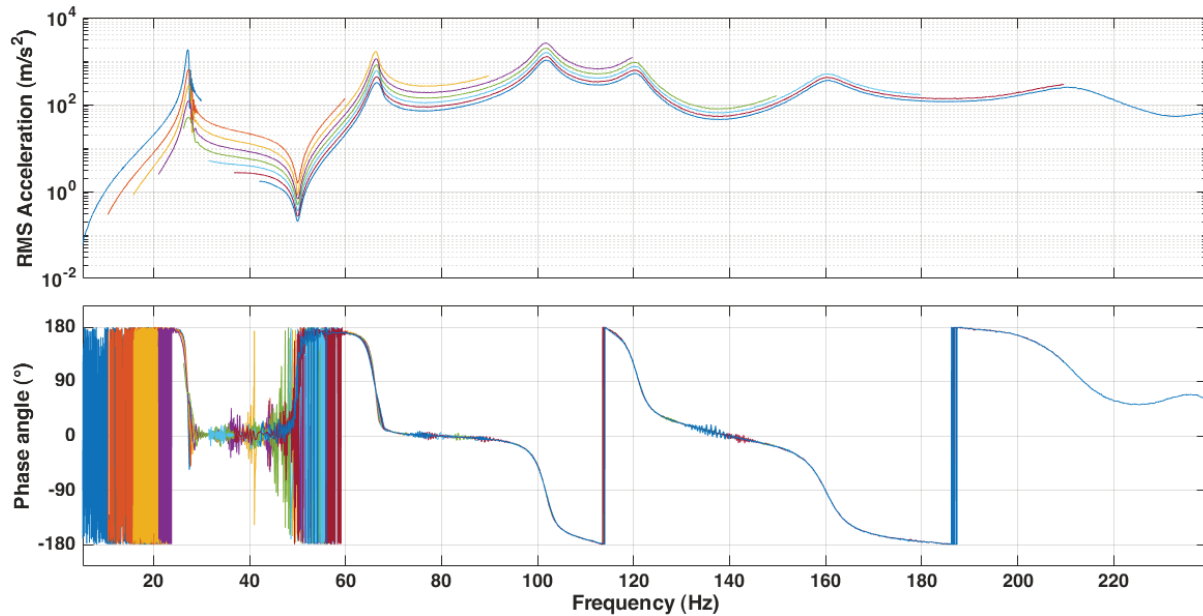


**Figure 4-9: Individual extracted response orders**

By applying order tracking to the output signal, individual response orders can be extracted, which are shown in Figure 4-9. It is visible, that the individual orders are free of discontinuities present in Figure 4-6. This fact is utilised by the OBMA method, which performs OMA based on individual orders. However, this leads to multiple sets of modal results with overlapping frequency ranges, which can aggravate the interpretation of the results.

A possible solution to this limitation as well as an approach to reduce uncorrelated noise in the tracked orders is to average the extracted orders into a combined signal, which is the foundation of the proposed AOBMA method introduced in Chapter 5.

## 4.4 Accuracy of the simulation response

This subchapter investigates the validity of the time responses obtained with the implicit Newmark- $\beta$  integration scheme and discusses easily overseen sources of simulation errors.

Integration methods for the time-domain solution of the dynamic equation of motion (Equation (3.1)) are categorised into implicit and explicit methods. Compared to explicit methods, implicit integration schemes are computationally more demanding per time step due to the required matrix decomposition to solve a coupled system of equations (Equation (3.15)) for the displacement at the next time step. However, implicit methods can be formulated for unconditional stability, which allows to run simulations with substantially larger (and thus fewer) time steps [183], [184]. In consequence, it is often more efficient to use

implicit time-integration for problems with larger timescales, while explicit solutions are advised for problems requiring small time intervals to resolve abrupt events and their nonlinearities [185]. Examples of typical applications for explicit time solvers include buckling, crash, and detonation setups.

The implicit time-integration Newmark- $\beta$  method was chosen as the foundation to simulate time responses for the presented dataset. It is characterised by high accuracy, user-adjustable dissipation properties and configuration capability for unconditional stability [186]. This explains the common use of the Newmark- $\beta$  method. For example, it is the default method for transient simulations in the commercial software packages ANSYS [187], Nastran [188], and Abaqus, which uses the Hilber-Hughes-Taylor (HHT) method (an extension of Newmark- $\beta$ ) by default [183]. Unconditional stability refers to the simulation time interval, which can be chosen arbitrarily large while still obtaining a mathematically stable solution. This is a desirable property of Newmark- $\beta$  allowing to minimise the number of time steps required for a simulation run, thus reducing computing time and resource demand [183]. Instead, the simulation case at hand dictates the required simulation time interval  $\Delta t = 1/f_{s,sim}$ , which must be chosen sufficiently small to resolve the forcing functions and the potentially nonlinear system response at the highest frequency of interest  $f_{max}$ .

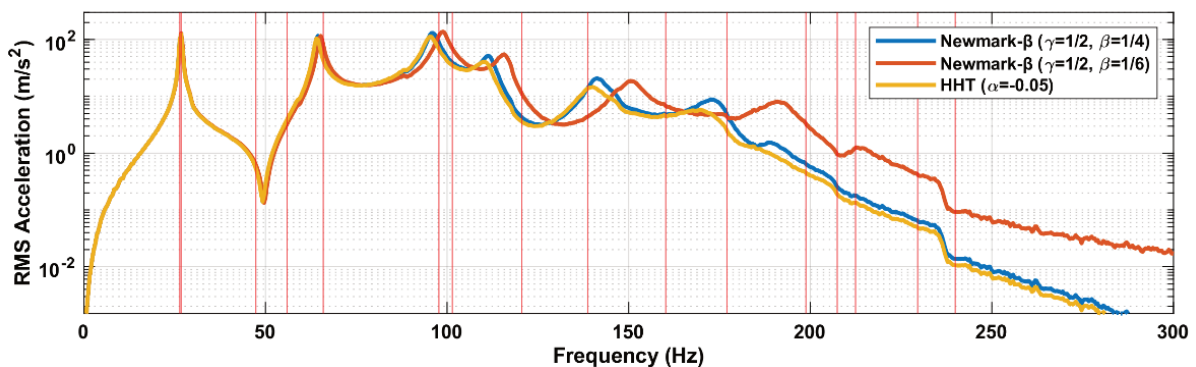


**Figure 4-10: Overlaid spectra of the response simulated with three different integration schemes at a simulation step frequency  $f_{s,sim}=752\text{Hz}$ , leading to numerical softening with resonances shifted to lower frequencies; red vertical lines indicate system eigenfrequencies from the eigensolution**

However, it is important to note, that basing the simulated time resolution on the Nyquist criterion (i.e.,  $1/\Delta t = f_{s,sim} \geq 2f_{max} = f_{Nyq}$ ) is insufficient for accurate simulation results. This is illustrated with Figure 4-10, which is based on simulations with the Newmark- $\beta$  method (implemented using MATLAB) and the HHT method (executed by Abaqus). The shown spectra are obtained from simulations with a simulation step frequency  $f_{s,sim}=752\text{Hz}$ , which provides a Nyquist frequency  $f_{Nyq}=376\text{Hz}$  covering the frequency range of interest. However, starting from around 100Hz, the resonance peaks of all graphs in Figure 4-10 are noticeably shifted to lower frequencies compared to the reference eigenfrequencies, which are illustrated with vertical red lines. The Newmark- $\beta$  method is used in two common

configurations, determined by the integration parameters of  $\gamma=1/2$ ,  $\beta=1/4$  (referred to as the constant acceleration method) and  $\gamma=1/2$ ,  $\beta=1/6$  (referred to as the linear acceleration method). As indicated by the names, the acceleration between simulated time steps is approximated to vary either linearly or have an average constant value.

The effect of shifted frequencies results in a simulated system response that suggests a reduced stiffness and can thus be referred to as numerical softening. This error source can be easily confused with softening effects of nonlinearity [189] and/or overseen, especially in case of nonlinear and large system simulations, which can inhibit finer time resolution due to the associated computational effort. Another contributing factor is that only one previous study [190] and few citing publications appear to point out numerical softening. In other work, this simulation error is referred to as period elongation [187] or periodicity error [184]  $\epsilon_{pe}$ . A simplified relationship (i.e. not considering the impact of damping) [184] between  $\epsilon_{pe}$  and the simulation step frequency factor  $\frac{f_{s, sim}}{f_{max}}(\epsilon_{pe})$  is given in Table 4-5 both for the constant acceleration and linear acceleration methods.

**Table 4-5: Integration parameters and characteristics of the Newmark- $\beta$  configurations as the constant acceleration method and linear acceleration method**

Newmark- $\beta$ scheme	Integration parameters	Approximate simulation step frequency factor $\frac{f_{s, sim}}{f_{max}}(\epsilon_{pe})$ [184]	Required simulation step frequency factor $\frac{f_{s, sim}}{f_{max}}$	
			For elongation error $\epsilon_{pe}=1\%$	For numerical stability, Eq. (4.9)
Constant acceleration method	$\gamma=1/2, \beta=1/4$	$\frac{2\pi}{\sqrt{12\epsilon_{pe}}}$	18.14	0 (unconditionally stable)
Linear acceleration method	$\gamma=1/2, \beta=1/6$	$\frac{2\pi}{\sqrt{24\epsilon_{pe}}}$	12.83	1.81

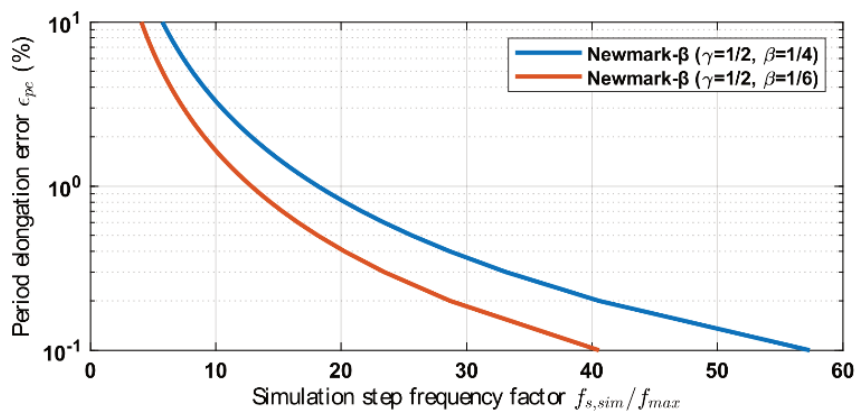


**Figure 4-11: Period elongation error (responsible for numerical softening) as a function of simulation step frequency  $f_{s, sim}$  relative to the response frequency  $f_{max}$**

The equations  $\frac{f_{s, sim}}{f_{max}}(\epsilon_{pe})$  are plotted for both configurations in Figure 4-11. For the constant acceleration method ( $\gamma=1/2$ ,  $\beta=1/4$ ), an error  $\epsilon_{pe} \leq 1\%$  is achieved with a simulation step frequency factor of  $\frac{f_{s, sim}}{f_{max}} \geq 18.14$ . This is in agreement with the ANSYS user's guide [187], which recommends 20 as the minimum value. The linear approximation follows the actual system response closer compared to the constant acceleration method, so a smaller amount of numerical softening is obtained from the linear acceleration method ( $\gamma=1/2$ ,  $\beta=1/6$ ), which is also observed in Figure 4-10. On the other hand, the linear acceleration method is conditionally stable as described by the stability criterion in Equation (4.9). However, since the stability criterion of the linear acceleration method is  $\frac{f_{s, sim}}{f_{max}}(\gamma = \frac{1}{2}, \beta = 1/6) \approx 1.81 < \frac{f_{s, sim}}{f_{max}}(\epsilon_{pe} = 1\%) \approx 12.83$ , the stability will be normally simultaneously assured if the elongation error  $\epsilon_{pe}$  is limited to 1%.

$$\frac{f_{s, sim}}{f_{max}}(\gamma, \beta) = \pi \sqrt{2\gamma - 4\beta} \quad (4.9)$$

Another factor to consider is potential numerical damping introduced by the time integration. Such dissipation is introduced by the Newmark- $\beta$  method for values  $\gamma > 1/2$ . Hence, the constant and linear acceleration method configurations are free of numerical damping.

The HHT method improves the numerical damping characteristics of the Newmark- $\beta$  method and introduces an additional parameter  $\alpha$ , which is used to vary the amount of induced numerical damping. In Abaqus, a value of  $\alpha = -0.05$  is used per default for transient dynamic simulations [183]. The impact of numerical damping of the HHT method with  $\alpha = -0.05$  is visible in Figure 4-10 at approximately 140Hz and 170Hz, where the resonance peaks appear flatter compared to those of the Newmark- $\beta$  method. The purpose is to improve the simulation accuracy at the presence of contact problems, which can introduce effects of non-physical negative damping [154], [183]. Since the present simulation study is free of contact definitions, these considerations are not applicable. Moreover, any numerical damping would distort the system response in relation to the originally defined physical system properties governed by the system matrices. Therefore, it would interfere with the intended use case of the simulation dataset to quantify the performance of OMA methods.

For validation, both the Newmark- $\beta$  implementation as well as the HHT method with a value of  $\alpha = 0$  are run at the simulation step frequency  $f_{s, sim} = 5\text{kHz}$  and plotted in Figure 4-12. In contrast to Figure 4-10, the spectra of both methods match in Figure 4-12 and the resonance peaks align with the eigenfrequencies marked with the red vertical lines. The simulation time resolution with  $f_{s, sim} = 5\text{kHz}$  is therefore also used as the foundation in the generated dataset. To reduce the generated data volume while preserving the information in the frequency



range of the model response, the time signals are low-pass filtered and downsampled to a sampling frequency of 714Hz.

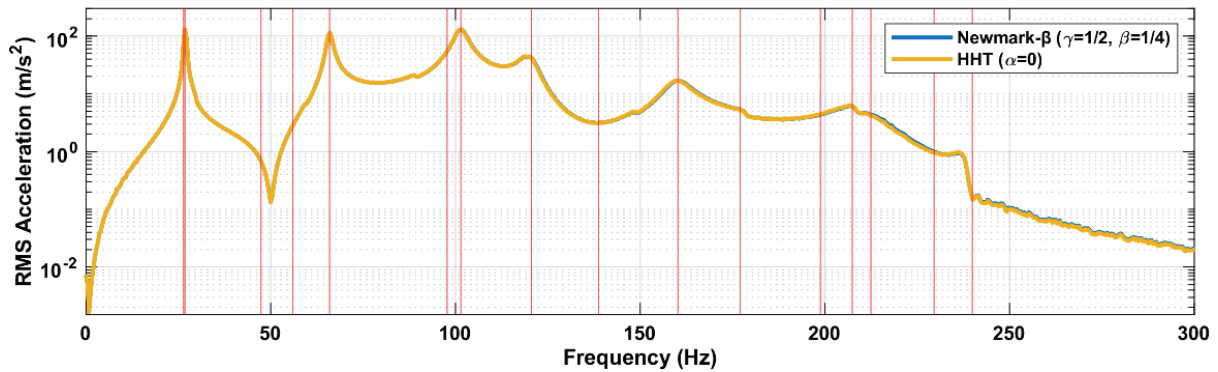


**Figure 4-12: Overlaid spectra of the response simulated with the Newmark- $\beta$  and HHT methods at a simulation step frequency of 5kHz; as desired, the resonance peaks match the red vertical lines, which indicate system eigenfrequencies from the eigensolution**

## 4.5 Conclusions

This work presented the first open simulation dataset focusing on rotating machinery vibration during transient acceleration conditions. Three parameters were defined as independent variables and included in the simulation data with varied values. The varied operating conditions covered by the dataset contribute to its applicability to a wide range of rotating machinery cases. Furthermore, the presented parameters make the dataset readily applicable for parametric studies, evaluating the impact of individual operating conditions on compared signal processing or OMA methods. Since there is currently a lack of such studies as concluded from Subchapter 2.1 and Subchapter 2.2, this dataset provides a foundation to address this gap.

Moreover, further extension of the dataset is facilitated by the provision of source code, which is provided with the core time response data. This facilitates the generation of additional simulation scenarios, which are suitable for future research questions of fellow researchers in this field.

The model setup with multiple excitation orders acting in combination with random input forces at a single location of the structure contradicts the ideal OMA assumption of distributed and uncorrelated random excitations. The presented dataset therefore represents more challenging analysis conditions. The dataset directly targets the lack of existing open datasets of rotating machinery under acceleration conditions, which was identified in Subchapter 2.3. It has therefore the potential to contribute to further improvements in the domain of OMA and vibration signal processing of rotating machinery. As a simulation dataset with known reference values of modal parameters, it is especially suitable to act as a benchmark problem.

Subchapter 4.3 investigated the impact of order excitation, which is characteristic for rotating machinery at acceleration runs, on the dynamic response of the structure. This excitation was visualised as the underlying cause for non-physical end-of-order modes, which are avoided with the help of OBMA. Sources of simulation errors in terms of numerical damping and numerical softening were investigated and their impact on the present dataset was illustrated in Subchapter 4.4. This assures sufficient accuracy of the proposed dataset and highlights potential sources for error to members of the research and engineering community, so these issues can be correctly interpreted and avoided.

The next Chapter 5 builds on the proposed dataset to develop the novel AOBMA method, which addresses several limitations of OBMA. The dataset is also used to perform a parametric comparative study involving AOBMA, OBMA, and a traditional OMA method using the harmonic ratio introduced in Subchapter 4.2.1.

---

## 5 Introduction of Averaged Order-Based Modal Analysis (AOBMA) and performance assessment of OMA methods during transient order excitation

As concluded by the survey in Subchapter 2.2, transient acceleration or deceleration runs represent a relevant test condition for structures, which experience a low amount of broadband random excitation during operation. In these cases, orders present themselves as a favourable source of excitation. However, this type of excitation can result in distortions of the response spectrum at the ending frequencies of individual orders. These end-of-order distortions can introduce spurious or biased modal estimations.

The literature review in Subchapter 2.1 identified Order-Based Modal Analysis (OBMA) as a promising OMA method, which was developed specifically for the transient test case and is not affected by end-of-order distortions. However, some downsides are associated with OBMA because it performs modal analysis for each relevant order individually. In addition to the associated analysis effort, this produces multiple sets of modal estimations with ambiguous results.

This chapter introduces an extension of OBMA to address these issues and was published as a peer-reviewed journal paper [17] by the thesis author. The proposed method, called Averaged Order-Based Modal Analysis (AOBMA), applies scaling and (weighted) averaging to extracted orders prior to the modal estimation step. A Monte-Carlo study based on the simulation data presented in the previous Chapter 4 is utilised to compare the modal estimation performance of traditional OMA, OBMA and AOBMA. Different ratios of harmonic and random excitation amplitudes are simulated to gauge the impact of the excitation's composition. In addition, all methods are also applied to operational measurements from a turbofan casing during run-up. The results indicate that AOBMA produces a higher accuracy in the estimated modal parameters compared to OBMA. Moreover, while OMA was more successful in the estimation of closely spaced modes, it was surpassed by AOBMA and OBMA regarding the accuracy of mode shape estimations.

### 5.1 Introduction and motivation

As discussed earlier in Subchapter 3.2.2, traditional OMA methods rely on the assumption of uncorrelated input forces with zero mean and a flat spectrum (i.e. the characteristics of white noise) [4]. Deviations from this assumption can lead to false or biased modal estimations [7]–[9], thus making results of OMA more challenging to interpret. This is not only true for rotating machinery at stationary operating conditions, where the input orders result in narrow-banded

peaks in the force spectrum but also for transient acceleration or deceleration runs, which produce so-called end-of-order distortions, as was shown in Subchapter 4.3.

Most methods and studies consider the case of (approximately) stationary operation, while the analysis of rotating machinery at transient acceleration or deceleration operating conditions is a less researched field. However, in test cases where broadband forces during operation are too low for sufficient excitation of modes, transient runs with order excitation can lead to a more complete modal estimation, which was discussed in Subchapter 2.2. OBMA is specifically developed for measurement data from transient runs and has the benefit that it is free of spurious end-of-order modes, which can be falsely identified by common OMA methods [53]–[55].

Subchapter 2.2 provides a detailed survey of existing case studies of OBMA and considers the amount of periodic and random excitation. However, it was also found, that the potential impact of the force composition was not explicitly considered by existing previous studies, which hinders conclusions on this question. The present chapter addresses this gap by systematically analysing the simulation setup introduced in the previous Chapter 4, which features varying ratios of harmonic and random excitation amplitudes. The potential impact of the excitation force composition is a relevant research question since it is test case specific and could determine suitable data processing or analysis methods. For example, a single turbofan component, which is driven by an electromagnetic motor in a laboratory spinning test will likely experience a greater order excitation and a lower degree of operational random forces compared to a turbofan engine under operational and environmental forces in flight.

It was also found in Subchapter 2.2, that there is limited literature, which quantifies the modal estimation performance of OBMA in comparison to alternative, traditional OMA methods. For example, just a single case study was found, which provided a comparison of mode shape estimations between OBMA and OMA using the Modal Assurance Criterion (MAC) [59]. Multiple studies observed OBMA partially resulting in high overestimation errors of damping ratios, especially in the case of lightly damped modes [55]–[57], [59]. Since OBMA processes tracked orders individually, each processed order of a dynamic structure provides a separate set of modal estimations. These sets of results can vary notably from one order to another [59], increasing the effort in analysis and result interpretation. This is likely linked to an increased amount of noise in individual order spectra compared to averaged spectrum estimations, which are obtained by the Welch's method for example. However, due to their transient nature, extracted order spectra cannot be averaged in the same fashion [48].

This chapter addresses the stated issues and provides the following contributions:

- The impact of the force composition (in terms of harmonic and random amplitudes) on modal estimation results is systematically analysed using a parametric Monte Carlo simulation study.
- The modal estimation accuracy of OBMA is evaluated in terms of deviations from simulation reference parameters as well as in comparison to a traditional OMA method using operational test measurements.
- A novel method and extension of OBMA, the Averaged Order-based Modal Analysis (AOBMA), is introduced, aiming to address the issue of separate result sets with partially great estimation error differences.
- For validation and performance assessment, AOBMA is applied alongside OBMA and a reference OMA method to response data from simulation data as well as operational data of a turbofan casing during acceleration.

Following this introduction, this chapter is structured as follows. Subchapter 5.2 gives an overview of the compared modal analysis methods, which is followed up by the theory and implementation details of the novel AOBMA method. Next, the test setups for the used simulation and operational data are presented along with the analysis methodology for validation and performance assessment of the compared modal estimation methods in Subchapter 5.3. Subchapter 5.4 covers the results from the parametric simulation study and the operational test measurements. Finally, conclusions and suggestions for future work are given in Subchapter 5.5.

## 5.2 Overview and development of relevant theory

In the first following subchapter, an overview and the relation of each of the compared OMA methods is given. Subsequently, the theory and implementation details of AOBMA are covered.

### 5.2.1 Overview of compared OMA methods

As the foundational OMA method, the Alias-Free Polyreference (AFPoly) method [191] is used in this study. This frequency-domain modal estimation method is implemented in the software MEscape. Both AFPoly and pLSCF [192] are based on the orthogonal Rational Fraction Polynomial (RFP) method [193]. In comparison to RFP, AFPoly introduces a generalized companion matrix, which resolves the issue of ill-conditioning of modal models with high polynomial orders. Since the method operates in the Laplace domain, it has the benefit that the impact (i.e., aliasing) of out-of-band modes is avoided, resulting in less computational modes and clearer stabilisation diagrams. This is in contrast to other common OMA methods, which operate in the discrete-time domain or z-domain, including the

(polyreference) Least Squares Complex Exponential (pLSCE) and Complex Frequency (pLSCF) methods [191], [194]. The flipside of this advantage is the potential limitation from numerical ill-conditioning at wide frequency ranges and model orders as discussed in Appendix B.3.1. The AFPoly method is used hereafter in three configurations:

1. Cross-spectra-based Operational Modal Analysis (OMA)
2. Order-Based Modal Analysis (OBMA)
3. Averaged Order-Based Modal Analysis (AOBMA)

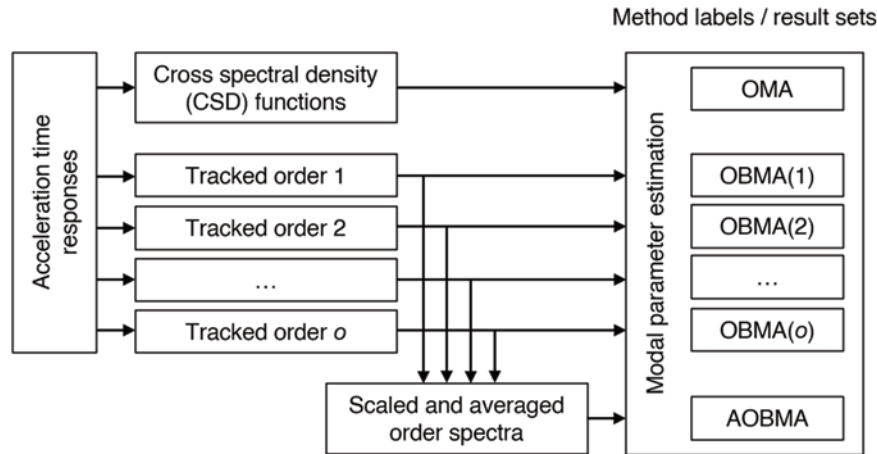


**Figure 5-1: Processing steps of the compared methods OMA, OBMA and AOBMA**

Each method is introduced further below and the relation between the methods is visualised in Figure 5-1.

In a classical OMA application, Cross Spectral Densities (CSD) are calculated from the DOFs' acceleration responses with Welch's method and are used as the inputs to the OMA method. As a common OMA procedure, this approach is simply denoted "OMA" in the following and acts as the reference method for this study.

For OBMA, individual order functions are extracted from the acceleration response at each DOF by order tracking. The requirements are that a tachometer signal is available to provide the rotations per minute (rpm) and that an acceleration or deceleration run of the operating machine is measured, where the extracted orders cover a desired frequency range for later analysis. For the present paper, order tracking is performed using resampling to the angle-domain (AD). This method was compared with other order tracking algorithms for the specific use with OBMA before and provided satisfying results [34], [115]. For more constrained test conditions, e.g., with the presence of crossing orders, alternative methods are available, including the Time Variant Discrete Fourier Transform (TVDFFT) and Vold-Kalman (VK) order tracking. In the AD method, angular resampling of the original time-domain data provides order-synchronous signals. Afterwards, the FT is applied to obtain order-domain spectra, which are assembled into an order-rpm spectrogram. In this spectrogram, each row represents an order as a function of rpm, so the orders of interests are easily extracted. A

frequency-domain response is estimated by converting the rpm axis values to the instantaneous frequencies of the  $l$ -th order using the relationship in Equation (3.25), which is repeated below for convenience. Finally, each of the extracted orders is processed by a modal estimation algorithm individually, resulting in a set of estimated modal parameters per order.

$$f_l = (l \text{ rpm})/60$$

AOBMA is based on the same steps as OBMA with the addition that the extracted orders are averaged into a single spectrum before applying modal estimation. To avoid discontinuities between orders without splitting the extracted orders to smaller sections (more on this in Subchapter 5.2.2), the averaged orders should have similar magnitudes across their combined frequency range. Since the order amplitudes generally are not similar, the orders are first scaled by calculating the relative amplitude differences between subsequent orders. These difference functions are then used to detrend individual orders to a common level before a (weighted) averaging of the orders is applied. AOBMA is explained in more detail in the following Subchapter 5.2.2.

### 5.2.2 Order scaling and averaging in the AOBMA method

This subchapter sets the theoretical foundation for the introduced AOBMA method. To supplement the theoretical descriptions, the subsequent Subchapter 5.2.3 illustrates and discusses the application steps of the proposed method in practice based on simulated run-up response data from Chapter 4.

Figure 5-2 gives an overview of the processing steps and illustrates the data flow of AOBMA with references to the corresponding equations, which are presented in the course of this subchapter.

Order averaging is not possible in a straightforward manner. Since the orders cover different frequency ranges and generally have different amplitudes, an average without further processing would suffer from similar discontinuities as the original output spectrum (see Figure 4-6). Previously, this issue has been addressed by subdividing the orders into frequency sections, where no contributing order begins or ends [54]. The downside of this approach is that either certain orders must be excluded from the averaging, or the resulting sections would become impracticably small for modal analysis. As an alternative, the present work introduces an order scaling step prior to averaging, as described below. This allows averaging of all selected orders over their combined frequency range.

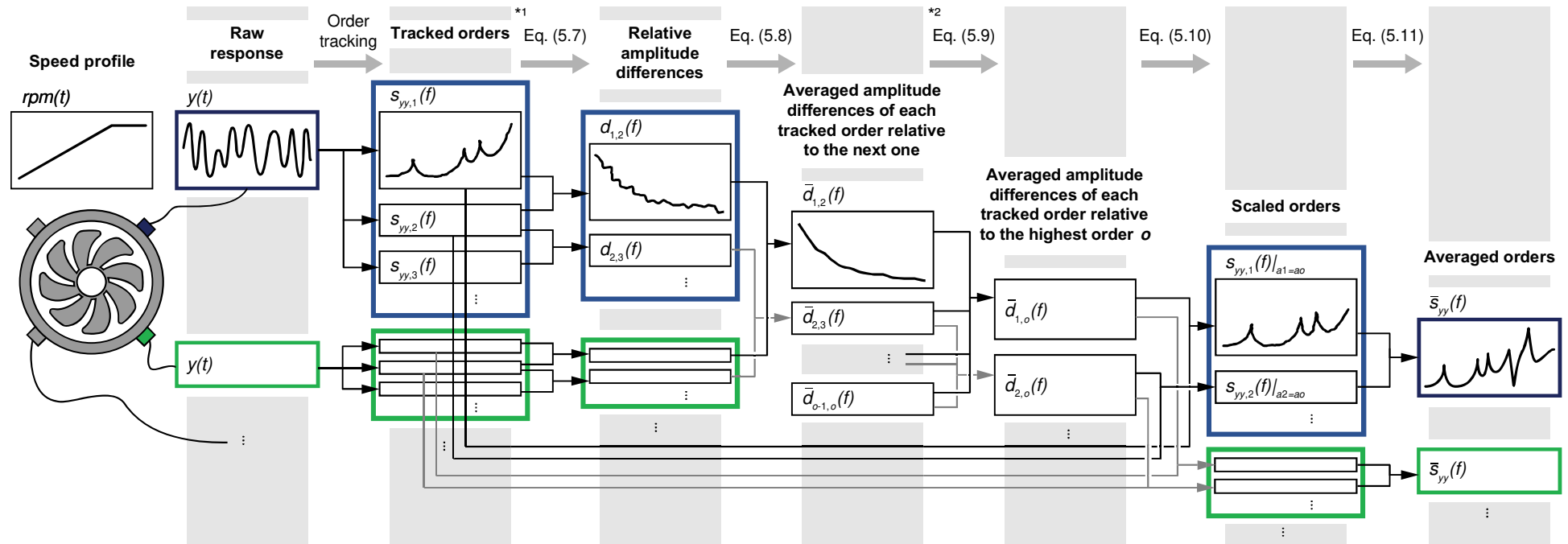


Figure 5-2: Procedural diagram of AOBMA; additional steps covered in Subchapter 5.2.3:  $*1$  prior to Eq. (5.7), interpolation of tracked orders to common frequency values;  $*2$  prior to Eq. (5.9), smoothing (e.g. moving average) due to order spectrum distortions



A tracked response order of a structure can be represented as a complex function of the excitation order frequency. This function is an estimate of the system response spectrum to an individual excitation order at a specific measurement location or DOF. For an order  $l$ , these response spectra can be constructed into an  $(N \times N)$  spectral matrix  $[S_{yy,l}]$ , where the diagonal entries represent the auto-spectra of individual DOFs and the off-diagonal entries are the cross-spectra between DOFs.

By considering the relation between the frequency-domain force input and response output of the structure, which is given by the FRF matrix  $[H]$ , the relation between input and output spectrum matrices is obtained as discussed in Subchapter 3.2 with Equation (3.24). This relation can be applied to order spectra, providing Equation (5.1).

$$[S_{yy,l}(f)] = [H(f)]^* [S_{xx,l}(f)] [H(f)]^T, \quad (5.1)$$

where  $[S_{yy,l}]$  is the spectral response matrix due to the excitation of a single order  $l$  described by the spectral input matrix  $[S_{xx,l}]$ .

The rotating input force of an order acts as a sinusoidal signal with a  $90^\circ$  (i.e.,  $\pi/2$ ) phase shift between the DOFs in X and Y directions. The Fourier transform of these order waveforms can be represented by complex functions (where  $j = \sqrt{-1}$  is the imaginary unit) in the frequency domain (with magnitude  $a_l(f)$  and phase  $\varphi_l(f)$  over frequency  $f$ ) as shown in Equation (5.2) and in Equation (5.3) for the X and Y direction, respectively.

$$s_{xx,l}^{(X)}(f) = a_l(f) e^{j(\varphi_l(f))} \quad (5.2)$$

$$s_{xx,l}^{(Y)}(f) = a_l(f) e^{j(\varphi_l(f) + \frac{\pi}{2})} \quad (5.3)$$

Auto and cross spectra are calculated as the Fourier transform of the auto and cross correlation functions or from the spectra of the analysed signals [195], [196]. Equation (5.4) shows the auto power spectra and Equation (5.5) shows the cross power spectra for the spectrum functions given in Equation (5.2) and Equation (5.3).

$$s_{xx,l}^{(X)} s_{xx,l}^{(X)*} = a_l e^{j\varphi_l} a_l e^{-j\varphi_l} = a_l^2; \quad s_{xx,l}^{(Y)} s_{xx,l}^{(Y)*} = a_l e^{j(\varphi_l + \frac{\pi}{2})} a_l e^{-j(\varphi_l + \frac{\pi}{2})} = a_l^2 \quad (5.4)$$

$$s_{xx,l}^{(Y)} s_{xx,l}^{(X)*} = a_l^2 e^{j(\varphi_l + \frac{\pi}{2} - \varphi_l)} = a_l^2 e^{j\frac{\pi}{2}}; \quad s_{xx,l}^{(X)} s_{xx,l}^{(Y)*} = a_l^2 e^{j(\varphi_l - \varphi_l - \frac{\pi}{2})} = a_l^2 e^{j(-\frac{\pi}{2})} \quad (5.5)$$

In case of the simulated model from Chapter 4, this force is applied to the central node 9, which represents the shaft location (Figure 4-1). Assuming that the order input DOFs occupy the first 2 diagonal entries of  $[S_{xx,l}]$ , it can thus be written as shown in Equation (5.6), where the remaining entries are zeros, since no input loads are applied to other DOFs.

$$[S_{xx,l}(f)] = a_l^2(f) \begin{bmatrix} 1 & e^{j\frac{\pi}{2}} & 0 & \dots \\ e^{j(-\frac{\pi}{2})} & 1 & 0 & \dots \\ 0 & 0 & 0 & \dots \\ \vdots & \vdots & \vdots & \ddots \end{bmatrix} = a_l^2(f)[S_{xx}(f)] \quad (5.6)$$

The function  $a_l^2(f)$  represents the power spectrum amplitude, which determines the frequency range covered by order  $l$  and the frequency-dependence, e.g., due to the linear amplitude increase like in the presented simulation.

Both the non-flat input spectrum and the correlated excitation in X and Y directions (manifested in the off-diagonal terms of  $[S_{xx,l}]$  in Equation (5.6)) oppose the assumption of uncorrelated white noise in common OMA theory. The impact of these characteristics of order excitation on the output spectrum with respect to the modal model has been derived in previous studies [53], [58], [59] and was covered in Subchapter 3.2.5. It is shown that a frequency-dependent proportionality term is introduced in the output and specific components of the modal model (namely the participation factors and upper and lower residuals) become complex. From that, it is concluded and demonstrated that modal identification methods, which estimate a common denominator (i.e. characteristic) polynomial (in contrast to partial fraction estimators), are suited for modal estimation from this type of output spectra [55], [92].

Under the assumption that subsequent excitation orders have a similar force distribution described by  $[S_{xx}]$ , the main difference between the orders lies in the power spectrum amplitudes  $a_l^2(f)$ . The description of  $[S_{xx,l}]$  in Equation (5.6) can be substituted into Equation (5.1). Considering the elements of matrix  $[S_{yy,l}]$ , it becomes clear that the ratio of output spectra between subsequent orders  $l$  is driven by the relative difference between the input force amplitudes  $a_l^2(f)$  of subsequent orders:

$$\frac{s_{yy,l}^{(n,m)}(f)}{s_{yy,l+1}^{(n,m)}(f)} = \frac{a_l^2(f)}{a_{l+1}^2(f)} = d_{l,l+1}(f) \quad (5.7)$$

Where  $s_{yy,l}^{(n,m)}$  denotes the element of the output spectrum matrix  $[S_{yy,l}]$  of order  $l$  at row  $n$  and column  $m$ . Thus, the relative amplitude difference  $d_{l,l+1}$  can be estimated from the response spectrum at any DOF, provided that the response is present in the measurement locations, i.e., is not affected by a modal node in the frequency of interest. As shown by Equation (5.7), the resulting ratio function  $d_{l,l+1}$  is theoretically independent from the specific DOF or the element  $(n, m)$  of the output spectrum matrix. However, in practice the result will be influenced by errors due to measurements at nodal positions, nonlinear responses, measurement or processing methods and the associated noise.

It is possible to reduce the uncorrelated errors and noise in  $d_{l,l+1}$  by calculating its values from different DOFs or elements  $(n,m)$  of the output spectrum matrix. Subsequent averaging of the individual estimates for  $d_{l,l+1}$  provides the averaged estimation  $\bar{d}_{l,l+1}$ :

$$\bar{d}_{l,l+1}(f) = \frac{1}{N} \sum_{n=1}^N \left( \frac{1}{N} \sum_{m=1}^N \frac{s_{yy,l}^{(n,m)}(f)}{s_{yy,l+1}^{(n,m)}(f)} \right) \quad (5.8)$$

The averaged difference function  $\bar{d}_{l,l+1}$  between subsequent orders can then be used to eliminate the magnitude differences, which are due to different input order amplitudes  $a_l$  between those orders. This aligns the magnitudes of the output orders to facilitate subsequent order averaging.

To apply the presented method beyond the common (i.e. intersecting) frequency range of all orders, the edge values of the difference functions  $\bar{d}_{l,l+1}$  in Equation (5.8) are extended to cover the full frequency range of order  $l$ . This ensures that the final averaged spectrum covers a frequency range, which is a union (and not just an intersection) of the individual orders' frequency ranges. This is a benefit of AOBMA compared to OBMA, where the spectral content is divided into several orders with different, partially overlapping frequency ranges.

A difference function can be computed between arbitrary orders  $l$  and  $o > l$  by multiplying the difference functions of intermediate orders:

$$\bar{d}_{l,o}(f) = \prod_{i=l}^{o-1} \bar{d}_{i,i+1}(f) \quad (5.9)$$

The highest order  $o$  is selected as the reference to calculate scaling factors for the remaining orders according to Equation (5.9). At every frequency value  $f$ , spectrum values of the order  $l$  are divided by the difference ratio values  $\bar{d}_{l,l+1}$  as per Equation (5.10). This results in spectra of order  $l$  with magnitudes scaled to the input order amplitude  $a_o$  of the reference order  $o$ .

$$\frac{1}{\bar{d}_{l,o}(f)} [S_{yy,l}(f)] = [S_{yy,l}(f)]_{a_l=a_o} \quad (5.10)$$

Finally, the scaled orders  $l \dots o$  are averaged over common frequencies  $f$ :

$$[\bar{S}_{yy}(f)] = \frac{1}{o-l+1} \sum_{i=l}^o [S_{yy,i}(f)]_{a_i=a_o} \quad (5.11)$$

For simplicity, Equation (5.11) shows an average of the orders with equal weighting. Alternatively, a weighted average can be applied to emphasize the influence of the most significant orders. In the present work, a frequency-dependent weighted averaging of orders based on the original (unscaled) order magnitudes was implemented to favour orders with

higher energy content at individual frequency values. This addresses the issue that the quality of results from OBMA depends noticeably on the chosen order as observed in [59]. The approach also extends a previous work [54], where significant orders were chosen for OBMA without further consideration of frequency-dependence. This is relevant in the sense that a certain order might be suitable for a certain frequency range, while modal identification in a different frequency area might benefit from a different order.

Because a higher frequency modulation rate increases distortions of obtained order spectra [25,26] (further discussed and illustrated in the following subchapter with Figure 5-6), it can be reasonable to assign a greater weight to lower orders. This can be done explicitly, e.g., by taking the inverse of the order number as the weighting factor for the corresponding order spectrum. However, the mentioned magnitude-weighting accomplishes that implicitly because order input forces typically increase as a function of rpm while the rate of frequency progression is order-dependent as shown in Equation (3.25). That is, lower orders have a higher rate of increasing magnitude over their order frequency compared to higher orders.

### 5.2.3 Implementation and application of AOBMA

While the last subchapter serves as a theoretical description, the paragraphs below focus on aspects of the practical implementation of AOBMA, such as the presence of discretely sampled data. This subchapter also illustrates the methods' application using the same simulated response data, which was presented earlier in Chapter 4.

Since orders are extracted as a function of rpm or time, the first step is to interpolate the orders to common frequency values. Let  $F_l$  be such set of discrete frequencies  $f_{l,i}$  with samples  $i$  of order  $l$  after the interpolation. The overlapping frequency range  $F_{l \cap l+1}$  of two subsequent output order functions,  $y_{l,i}$  and  $y_{l+1,i}$ , is determined as  $F_{l \cap l+1} = (F_l \cap F_{l+1})$ .

Next, relative difference functions  $d_{l,l+1}$  of the orders' magnitudes are calculated for all  $f_{l \cap l+1,i} = F_{l \cap l+1}$  according to Equation (5.7) for each channel individually. A noise reduction can be achieved by averaging the resulting difference functions for each subsequent order across all channels as per Equation (5.8).

If the lower order  $l$  covers frequencies outside the frequencies of the higher order  $l + 1$ , i.e., if  $F_l \setminus F_{l+1} \neq \emptyset$  (where  $\setminus$  denotes the relative complement in set theory), values at the edges of  $d_{l,l+1}$  are extended to cover the full frequency range  $F_l$  of order  $l$ .

Figure 5-3 shows the averaged difference functions  $\bar{d}_{l,l+1}$  between all subsequent orders of a simulation run (using harmonic ratio 0.8, Equation (4.1)). The left part of the illustration is based on orders extracted from the acceleration response of the structure. For validation, the right section provides scaling functions, which are determined from input force orders directly. Recall that the goal is to determine (and afterwards to reduce) the magnitude trend

difference between response orders due to different amplitudes of input orders. Order difference functions (Figure 5-3, left), which were determined from the tracked response orders follow the overall progression of the true difference functions (Figure 5-3, right) of the inputs. This underlines that these input force differences in fact can be estimated from the response signal.

However, noticeable deviations occur at resonant frequencies of the structure and are visible as spikes (Figure 5-3, left). These spikes are explained by distortions in the response order spectra at resonance peaks [177], [178], shown in Figure 5-6. They occur when relating the instantaneous sweeping excitation frequency to the response frequency and depend on the sweep rate of the excitation [179]. The averaging of order scaling functions across different channels does not alleviate these distortions as they are present across different channels. However, uncorrelated noise is reduced, which is visible in the output order difference functions (Figure 5-3, left), where averaging across all 18 channels is used. In contrast to that, the plots of the input order difference functions (Figure 5-3, right) are based on an average of just 2 signals (from order excitations in X and Y direction) and thus show greater noise.

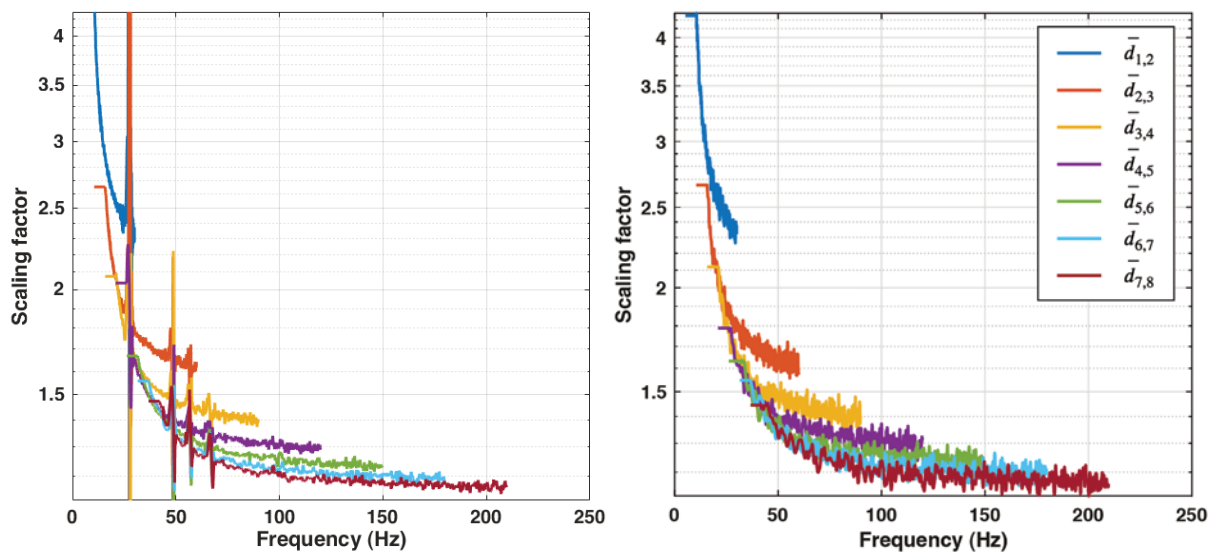


**Figure 5-3: Averaged difference functions of subsequent orders based on order output acceleration (left) and order input force (right)**

Afterwards, a moving average is applied to the scaling functions  $\bar{d}_{l,l+1}$ . This ensures that 1) the noise in the difference functions is further reduced while preserving the estimated difference trend and 2) the sharp peaks in Figure 5-3 (left) due to the mentioned resonance distortions are alleviated. Alternatively, a fitting function can be determined for  $\bar{d}_{l,l+1}$ , e.g., from polynomial fit by employing the LS method. The resulting estimated trend function is denoted  $\tilde{d}_{l,l+1}$ .

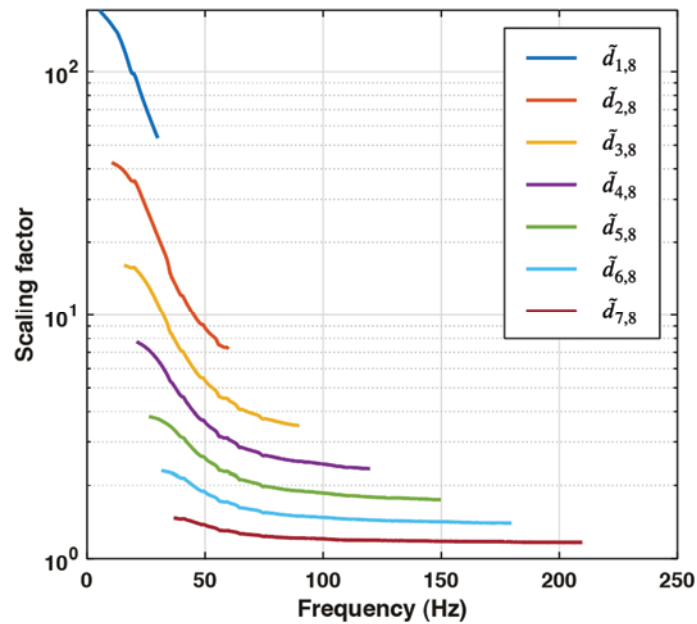


**Figure 5-4: Trend functions from each order  $l$  to the highest order  $o=8$**

To find the direct trend relation between each order to the highest present order, the subsequent order difference functions of higher orders are multiplied as explained by Equation (5.9). For example, the scaling of order  $l = 4$  to order  $o = 8$  is determined as  $\tilde{d}_{4,8} = \tilde{d}_{4,5}\tilde{d}_{5,6}\tilde{d}_{6,7}\tilde{d}_{7,8}$ . Figure 5-4 shows the resulting trend difference estimations from each order to the highest tracked order.

According to Equation (5.10), the estimated trend differences  $\tilde{d}_{l,o}$  are used to scale the magnitude of each order  $|y_l|$  to the common magnitude level of the highest order  $|y_o|$ . Figure 5-5 shows the individual orders in their original (unscaled) and resulting scaled form. It is visible that the magnitudes of the scaled orders (plotted as bold lines) align well to the highest order.

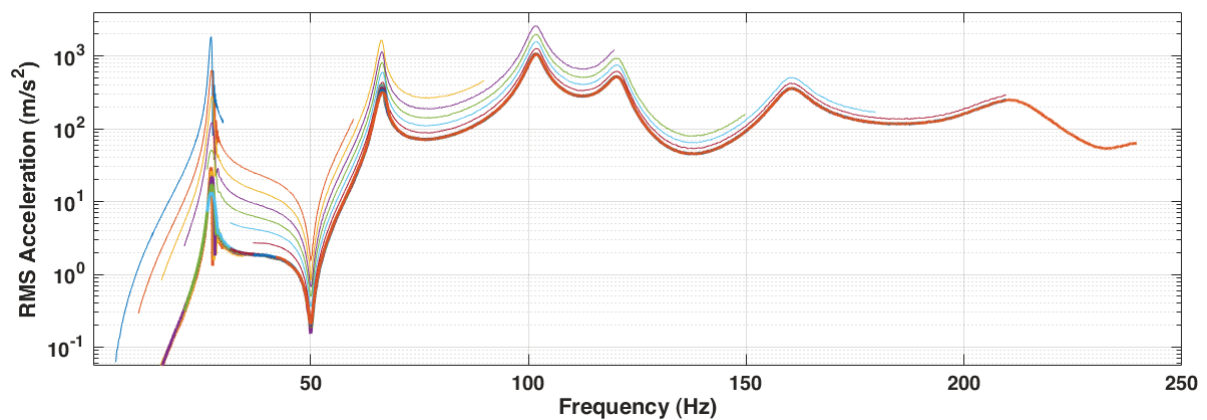


**Figure 5-5: Individual order magnitudes before scaling (light lines) and after scaling (bold lines)**

Zooming into the first resonance peak in Figure 5-6 shows that small-scale differences between orders are preserved while the magnitude level alignment is ensured along the whole frequency range.

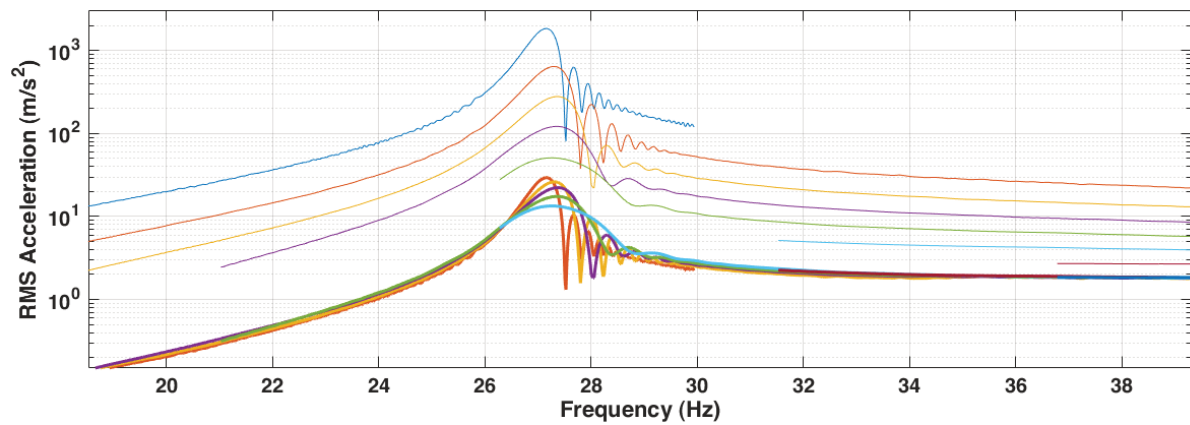


**Figure 5-6: Individual order magnitudes before scaling (light lines) and after scaling (bold lines) around the first resonance**

The distortion impact of higher orders on the resonance spectrum is visible in Figure 5-6. Detailed discussions on this phenomenon can be found in [177], [178]. The effect is especially pronounced on lightly damped modes, which is also the case here. With greater excitation sweep rates (i.e., higher orders), two effects are observed:

1. The resonance peak is shifted to the sweeping direction, which can lead to an overestimation of eigenfrequencies in case of a positive sweep rate as in the present simulation. Vice versa, a negative sweep rate (i.e., decreasing excitation frequency over time) would promote an underestimation of eigenfrequencies.
2. The resonance peak becomes flatter, which produces an overestimation of the modal damping.

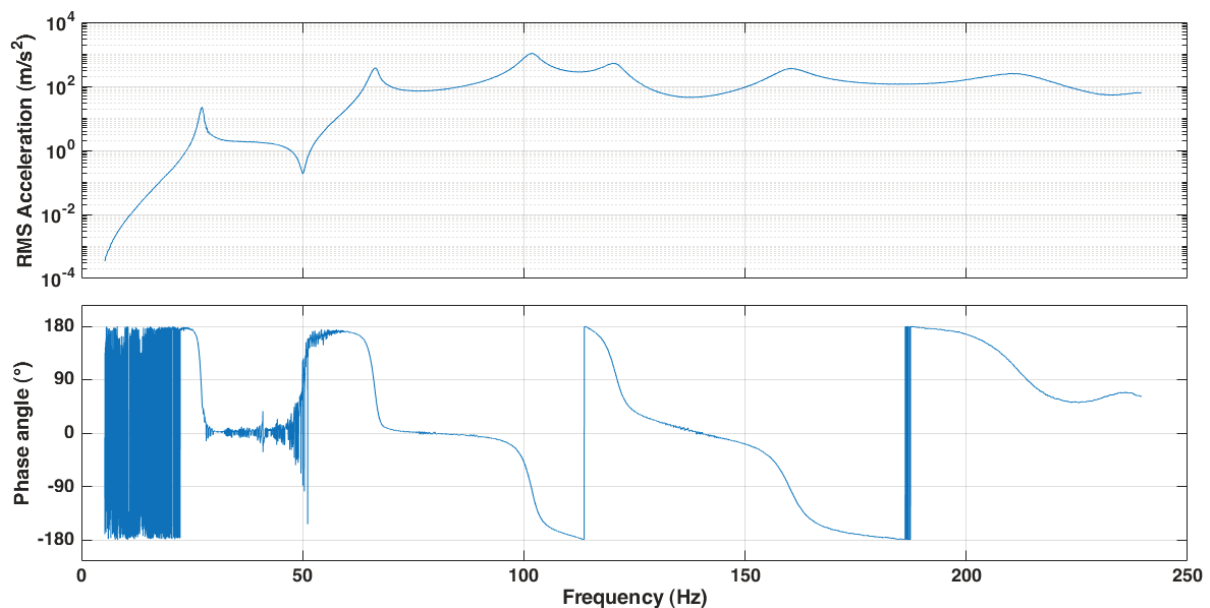


**Figure 5-7: Resulting response signal after order scaling and averaging with AOBMA**

Finally, the orders can be averaged into the result shown in Figure 5-7 using Equation (5.10). In contrast to the overall response spectrum in Figure 4-6, the resulting average does not show discontinuities at the ending frequencies of orders. In comparison to the individual orders in Figure 4-9, the averaged magnitude is aligned to a common level and the phase signal shows less noise. Furthermore, the partial frequency ranges of individual orders are combined into a single spectrum signal covering their full combined frequency range.

The present study focuses on the dynamic response of a stationary structure, which is subjected to periodic excitation by a contiguous rotating structure, like a fan or disc assembly. It should be noted that this rotating structure itself can exhibit rpm-dependent eigenfrequencies due to gyroscopic effects [197]. On the stationary structure, these resonances would thus emerge as an excitation with rpm-dependent amplitude and become part of the measured response of the combined system. The order spectra are associated with the individual order frequencies, which differ from the rpm by the factor  $l$  (see Equation (3.25)). This means that the measured response peak arising from an rpm-dependent eigenfrequency of the rotating structure would occur at different frequencies for different tracked orders. This has to be considered during the smoothing (e.g., by a suitable moving average window size), so that the sharp distortions shown in Figure 5-3 (left) are removed while amplitude changes due to rpm-dependent eigenfrequencies are preserved in the difference functions. Otherwise, there is a risk that a single rpm-dependent mode contributes to the averaged signal with multiple peaks at different frequencies. Besides that, when each order is scaled to the highest order in AOBMA (Equation (5.10)), the resulting averaged order spectrum will correspond to this highest reference order in terms of the rpm-dependent eigenfrequencies. While the present study does not further consider the influence of rpm-dependent eigenfrequencies, such conditions can be assessed further in the future with a dataset, which incorporates gyroscopic effects.

## 5.3 Methodology

Acceleration response data from the simulation model from Chapter 4 are used for a parametric comparison study in this work. In addition, operational measurements of a turbofan casing during acceleration are used. The purpose is to validate the novel AOBMA method and to compare the modal estimation performance of OMA, OBMA and AOBMA. Both datasets are introduced in the following subchapters together with the used analysis methodology.

### 5.3.1 Parametric simulation study

The simulation model and dataset developed in Chapter 4 is used as the foundation for the parametric study. The dataset is extended by repeated simulation runs with randomly sampled input force to perform a Monte Carlo analysis. For this purpose, each distinct



harmonic ratio  $h_{rat}<1$  (see Equation (4.1)) is simulated with 30 runs each to determine the means and confidence intervals of estimated modal parameters. The harmonic ratio  $h_{rat}=1$  is simulated by a single run due to the deterministic nature of the purely harmonic order excitation. Since the harmonic ratio of  $h_{rat}=0$  is free of orders, no order tracking and subsequent modal analysis by order-based methods (OBMA and AOBMA) is performed for this parameter value. Therefore, the resulting Monte Carlo parametric simulation study features a total of 121 simulation runs.

All compared modal estimation methods (OMA, OBMA and AOBMA) were first applied to a small subset of randomly selected simulation runs to determine a suitable range of common stabilisation criteria for modal identification. Within the determined range of stabilisation criteria, 4 different combinations of frequency and damping tolerances were then used in a batch analysis of all simulation runs to estimate the potential impact of the stabilisation criteria on the obtained results. The modal parameter results from the 3 estimation methods were then stored for a subsequent comparison with the reference results (i.e., eigenfrequencies, damping ratios and mode shapes) from the simulation. The main trends and observations remained consistent within the range of tested stabilisation criteria. A final representative set of stabilisation criteria is used for the presented results and is given in Table 5-1.

**Table 5-1: Stabilisation criteria for modal identification**

<b>Stabilisation criterion</b>	<b>Used value, (tested range)</b>
Frequency tolerance (Hz)	0.2 (0.2...0.3)
Damping ratio tolerance (%)	1.5 (0.5...2)
Maximum model order	25
Minimum number of stable poles within the frequency and damping tolerances	4

The MACX and MACXP are used in the comparative analysis of modal estimation results, since these metrics extend the MAC to applications with complex modes as explained in Subchapter 3.2.3. The MACXP is utilised to match estimated modes to reference modes. First, a matrix of MACXP values is constructed between the numerical reference modal parameters and the modal estimation set from a simulation run. This step is analogous to the construction of the more common MAC matrix. In contrast to the MAC value, however, the MACXP is less sensitive to mode shape complexity and also considers eigenfrequencies and damping ratios of the compared modes (see Subchapter 3.2.3). Higher values of the resulting MACXP matrix indicate matching modes, which are then compared further. Additionally, tolerances of the relative estimation errors are introduced as matching criteria. In the present case, the estimated eigenfrequency  $f_{est}$  (quantified by the relative error) and mode shape (quantified by the MACX) of the estimation must stay within the tolerances

specified by Table 5-2 to be considered a matched mode. These values were chosen to exclude outliers from the comparison and declutter the comparison plots. Estimations, that do not meet these tolerances are defined as unmatched modes and can occur due to noise, end-of-order modes, or numerical spurious modes.

**Table 5-2: Tolerance criteria for matched mode estimations**

Tolerance quantity	Lower bound (incl.)	Upper bound (incl.)
Relative eigenfrequency error $(f_{est} - f_{ref})/f_{ref}$	-1%	1%
MACX (Equation (3.28))	0.6	1

Estimation results from the individual methods, OBMA, AOBMA and OMA are compared in Subchapter 5.4.

### 5.3.2 Operational run-up of a turbofan casing

To validate the presented AOBMA method in a real-world test case, it is also applied to operational vibration data of a mechanical spinning test. The estimation results are then compared to outputs from OMA and OBMA.

The used mechanical test rig hosts a fan/casing assembly of a commercial turbofan engine. The measurements were conducted at the mechanical testing facilities of Rolls-Royce Deutschland Ltd., and the resulting dataset was kindly provided for the purpose of the presented analysis. The fan is driven directly by an electromagnetic motor. Due to the lack of combustion and environmental forces, an increased contribution of harmonic order input is expected in relation to random excitation amplitudes. The fan casing is instrumented with accelerometers at 12 positions illustrated in Figure 5-8. One triaxial accelerometer is used at position 4. The remaining positions host 11 uniaxial accelerometers oriented in the normal direction of the cylindrical surface area of the casing. Hence, a total of 14 accelerometer data channels is recorded. In addition, the rotation speed is acquired from a pulse signal reading. The measurement signals are sampled at a frequency of 65 kHz but low-pass filtered and downsampled to achieve a lower Nyquist frequency of interest. Such a high sampling frequency is used as standard practice in the test facility, which conducted the measurement campaign to provide leeway in the acquired bandwidth against potential contingencies during the test. The analysed measurement data covers a run-up of the fan with the lowest acceleration rate provided by the fan speed control unit, resulting in a measurement duration of 190s.

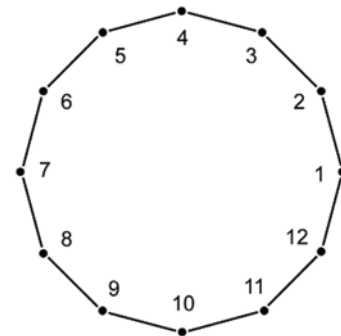


**Figure 5-8: Positions of accelerometers at the instrumented fan casing**

In contrast to the simulation-based analysis from the previous subchapter, true reference modal parameters of the real tested structure are unknown. Therefore, modal estimation results from traditional OMA are used as the baseline to compare and validate results from OBMA and AOBMA. The same procedure as described in the previous subchapter is used to find matching modes for the comparison of their estimated parameters by different methods.

## 5.4 Results and discussion

The first subchapter below uses data of the parametric simulation study (Subchapter 5.3.1) to compare the estimation accuracy of OMA, OBMA and AOBMA while considering the potential impact of the harmonic ratio. Afterwards, the three methods are applied to operational measurements of the test setup presented in Subchapter 5.3.2.

### 5.4.1 Comparative performance assessment of OMA, OBMA and AOBMA

In the following, OMA, OBMA and AOBMA are first applied to the maximum frequency range available to each method. Afterwards, the results of an additional approach based on averaging of OBMA results in post-processing are introduced and discussed. Finally, OBMA and AOBMA are applied to a common, narrowed analysis bandwidth (covering modes 3-4 only) to isolate the impact of the analysis band on the estimation performance.

Only orders  $l \in \{1,3,5,8\}$  of the simulation are used for the following OBMA results and the specific source order is specified in brackets as OBMA( $l$ ). This reduced set of orders is used to support conciseness of the following plots and discussions. The included orders are selected to be spread approximately equal across the range of all orders. All 8 excitation orders are simulated with the same amplitude function over rpm or time (Equation (4.2)), so there is no inherent preference of the picked orders of the subset and their individual differences are limited to the sweep rates and covered frequency ranges. The same reduced set of 4 orders is also processed within the presented AOBMA results below to ensure better comparability.

#### *Modal estimations over the maximum frequency range of each method*

In this section, the maximum frequency range of each method is used for modal analysis. For OMA, an analysis band from 0Hz to 270Hz is chosen to cover all eigenfrequencies (Table 4-2). The full frequency bands of individual orders, determined by Equations (4.3) and (4.4), are used for OBMA. Consequently, their combined frequency ranges provide the used analysis band of 5Hz to 240Hz for AOBMA.

Figure 5-9 shows for each mode (on the horizontal axis) the count of simulation runs (on the vertical axis), where this mode was matched according to the criteria from Table 5-2. Since there are 30 simulation runs per discrete harmonic ratio below 1.0, the maximum number of

matches per mode and harmonic ratio is 30. An exception is the purely harmonic (and thus deterministic) excitation with a harmonic ratio of 1.0, where only 1 simulation run was performed. Focusing on  $OBMA(l)$ , it is evident that the range of matched reference modes on the horizontal axis increases if a higher order  $l$  is used. This is simply due to the increasing frequency range, which is covered by higher orders.

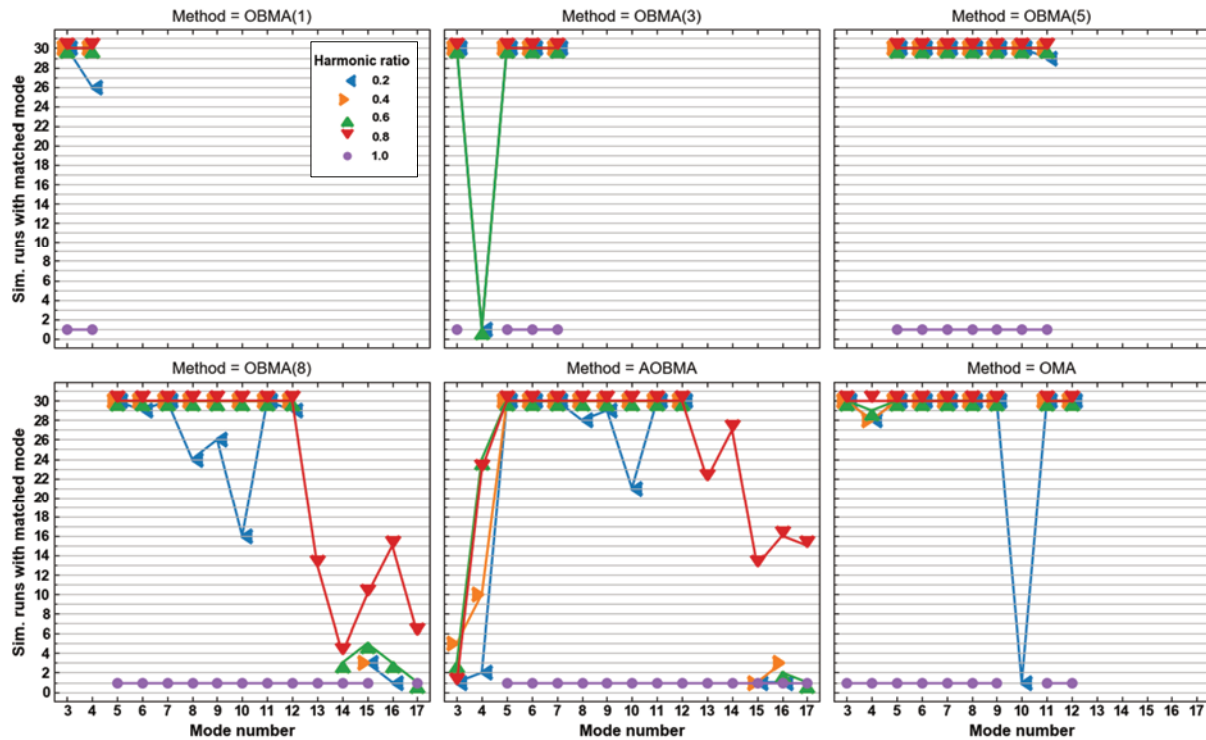


**Figure 5-9: Count of simulation runs with a matched estimation of the reference mode. For OBMA results, the individual source orders (1, 3, 5, 8) are specified in brackets.**

Within individual methods, the overlaid plots of harmonic ratios are mostly consistent, except for certain modes that are more challenging to identify. This is the case for reference modes number 3 and 4, which have close eigenfrequencies with a difference below 0.5Hz (Table 4-2).  $OBMA(1)$  and OMA achieve the highest number of matches for these modes. The difference between the results of  $OBMA(1)$  and  $OBMA(3)$  is likely due to the increased distortion of the spectrum of order 3 compared to order 1 (Figure 5-6).  $OBMA(1)$  results in a substantially higher number of matched estimations of mode 3 compared to AOBMA. Whether this is due to the smaller frequency range of  $OBMA(1)$  or a potential impact of order averaging by AOBMA will be evaluated in the last section of this Subchapter 5.4.1.

Another clear dip in the number of matches appears in  $OBMA(8)$  at mode number 10 and is also reflected in AOBMA. However, this dip is limited to a low harmonic ratio of 0.2. OMA identifies this mode only once in the 121 simulation runs. Between modes 5-12, the proposed AOBMA method is free of gaps in contrast to OMA and shows a less pronounced dip compared to OBMA, which can be attributed to a noise reduction by averaging of orders. Modes 13 and up are not identified by OMA either. A reason might be the increased damping

ratios of these modes in combination with the end-of-order effect, which produces small-scale distortions of the spectrum as shown in Figure 4-6. AOBMA and OBMA(8) are able to identify these higher modes, albeit with a trend that higher harmonic ratios lead to a greater number of matches.

None of the methods successfully matched mode 18. The reason is that the maximum frequency of the highest order 8 (240Hz) is very close to this mode's eigenfrequency (239.84Hz). This mode is therefore not sufficiently covered by the frequency range of OBMA(8) and AOBMA. While this restriction does not apply to OMA, it is not able to identify this mode either, likely due to the substantial end-of-order distortion of the spectrum at this frequency, which is visible in Figure 4-6.

The results can be summarised with Figure 5-10 (left), which shows how many different modes from a single simulation run have been matched on average. Each data point represents the mean value of 30 simulation runs (for harmonic ratios below 1.0). The vertical error bars extending from the data points visualise 95% confidence intervals around the mean.

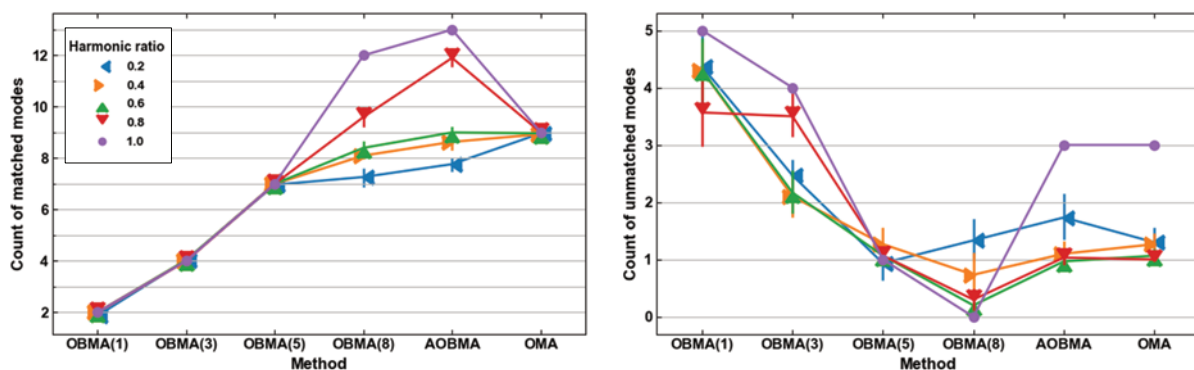


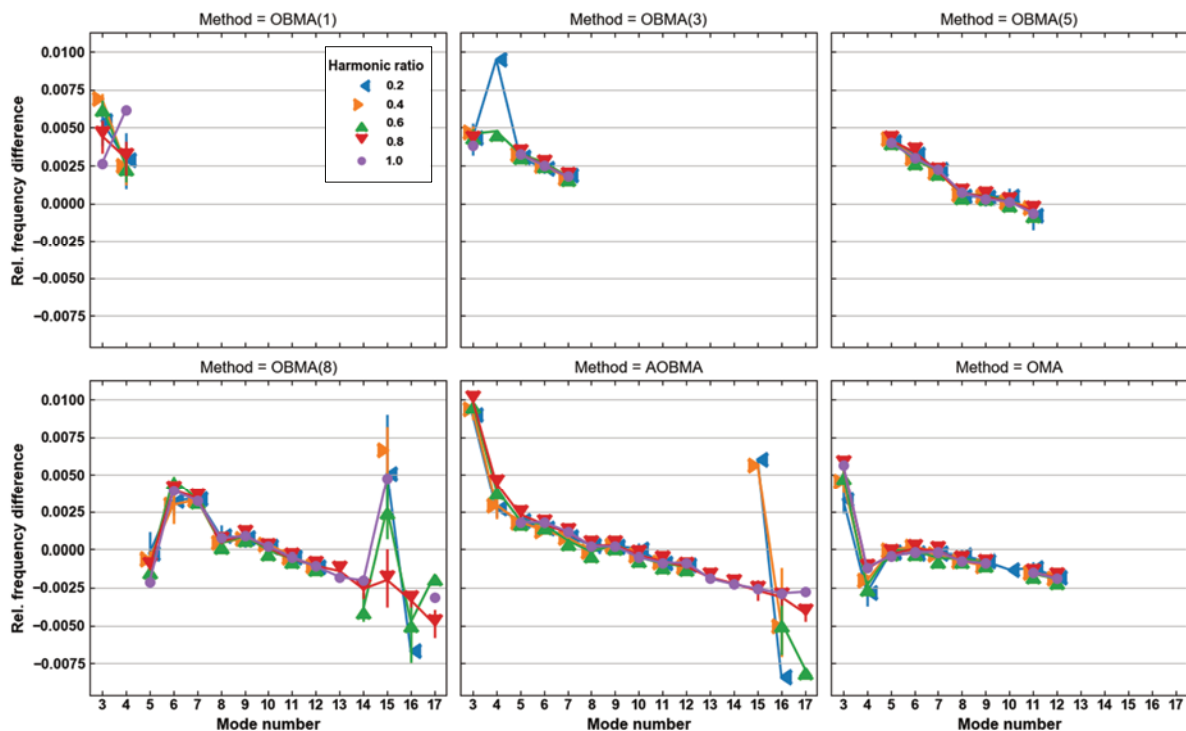
**Figure 5-10: Average count of matched (left) and unmatched (right) modes per single simulation run**

It is visible that OBMA(8) and AOBMA benefit from higher harmonic ratios while OMA is mostly unaffected. However, even at low harmonic ratios of 0.2 and 0.4, the number of modes matched with AOBMA approaches the number of modes matched with OMA. Overall, the proposed AOBMA method provides the greatest number of matched modes. That is, AOBMA correctly identified between 11.9 to 13 modes on average at high harmonic ratios of 0.8 and 1.0, while OBMA(8) detected averages between 9.5 to 12 of matched modes and OMA detected 9 modes at the same conditions.

For completeness, Figure 5-10 (right) also shows the count of unmatched modes, which exceed the tolerances from Table 5-2. Only a minor impact of the harmonic ratio is visible: the low harmonic ratio of 0.2 results in slightly elevated unmatched count values, especially in OBMA(8) and AOBMA. Unmatched count values of the harmonic ratio 1.0 follow the overall trend more coarsely because each plotted point is based on a single sample (i.e.,

simulation run). In contrast to that, data points of other harmonic ratios are based on 30 samples, resulting in more representative average values. OBMA(1) shows the highest amount of unmatched modes compared to OBMA results of higher orders because order 1 covers the smallest frequency range and the modal model is overfitting resulting in spurious mode estimations. The dip of the number of unmatched modes in OBMA(8) is also explained by the frequency range of order 8, which starts at 40Hz and thus omits the challenging modes 3-4, as seen in Figure 5-9. Finally, AOBMA and OMA show similar counts of unmatched modes in Figure 5-10 (right) despite more matched modes in favour of AOBMA in Figure 5-10 (left).

Next, the accuracy of the methods regarding individual estimated modal parameters of the matched modes is compared.



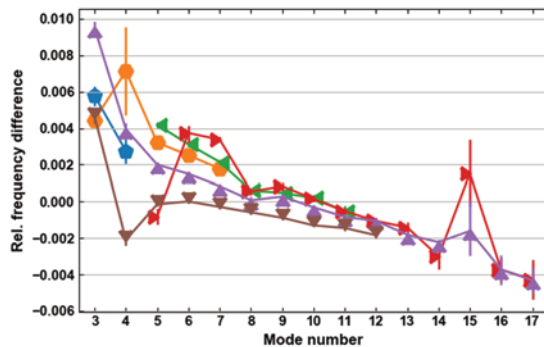
**Figure 5-11: Relative eigenfrequency errors  $(f_{est} - f_{ref})/f_{ref}$  of matched mode estimations by different methods for individual harmonic ratios, where  $f_{est}$  and  $f_{ref}$  are the estimated and reference eigenfrequencies, respectively**

Figure 5-11 shows the relative errors of estimated eigenfrequencies. Considering the error tolerance of  $\pm 1\%$  (Table 5-2) and the consistency of the results in Figure 5-11 (with limited outliers), the accuracy of estimated eigenfrequencies in this simulation study is high across all methods. An impact of the harmonic ratio is visible in the form of more accurate estimations with increasing harmonic ratios in order-based methods. For example, this is the case for the mode 4 of OBMA(3), modes 14-16 of OBMA(8) and AOBMA. A stronger impact of harmonic ratios was observed and discussed in the previous results of Figure 5-9 and Figure 5-10. In contrast to that, the overall impact on the estimation accuracy of modal

parameters is minor since the graphs of different harmonic ratios mostly overlap for all modal estimation methods.

Therefore, hereafter, results of individual harmonic ratios are averaged into single plots to increase conciseness and facilitate the comparison of the methods by overlaying their plots.

Figure 5-12 combines the eigenfrequency results from Figure 5-11 in such way.



**Figure 5-12: Relative eigenfrequency errors of matched mode estimations by different methods (for the legend refer to Figure 5-13)**

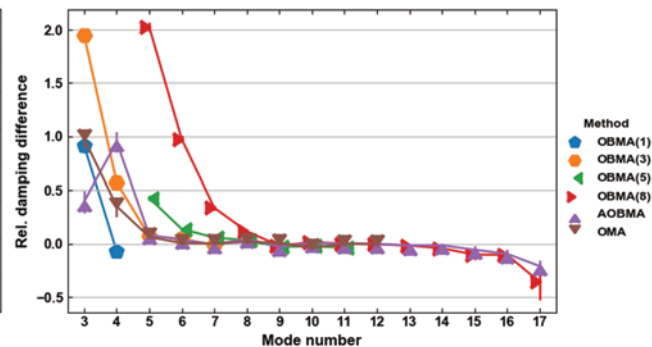


**Figure 5-13: Relative damping ratio errors ( $\xi_{est} - \xi_{ref}$ ) /  $\xi_{ref}$  of matched mode estimations by different methods, where  $\xi_{est}$  and  $\xi_{ref}$  are the estimated and reference damping ratios, respectively**

In Figure 5-12, the result of averaging with the proposed AOBMA method is visible. Aside from mode 3, which is also based on much fewer AOBMA estimation samples (Figure 5-9), AOBMA produces more consistent results compared to OBMA and mitigates increased error values of OBMA(8) at modes 6-7. Eigenfrequencies of lower, lightly damped modes are overestimated by the order-based methods OBMA and AOBMA due to the distortion effect described with Figure 5-6.

The same effect is also responsible for the large overestimation of damping ratios (with differences up to approximately 200%) by OBMA, which are shown in Figure 5-13. It is visible that higher orders produce greater overestimations compared to lower orders used within OBMA, which is in conjunction with earlier observations from Figure 5-6. AOBMA reduces these error deflections and delivers more consistent results compared to individual OBMA outputs because the negative impact of higher orders is mitigated by spectrum averaging with lower orders carrying less distortions. This is additionally reinforced by a weighted averaging in AOBMA, which implicitly favours the contribution of lower orders as noted in the ending paragraphs of Subchapter 5.2.2. As a result, the accuracy of eigenfrequency and damping ratio estimations by AOBMA approaches the results from OMA, which is not affected by the order spectrum distortion effect.

Comparing the mean absolute values of relative eigenfrequency errors (Figure 5-12) across modes, OMA has the lowest value of 0.0013 compared to AOBMA with 0.0016, which is similar to the value of 0.0017 provided by OBMA(8) in the common range of identified modes 5-12. The same comparison regarding damping ratios (Figure 5-13) across modes 5-12

gives lowest mean absolute relative errors of 0.02 in favour of OMA, closely followed by AOBMA with 0.03 and OBMA(8) with a notably higher value of 0.32.

**Table 5-3: Mode shape deflections from modes 3, 5, 7, 9, 11 – numerical reference and estimations by OMA and AOBMA at harmonic ratio 0.8**

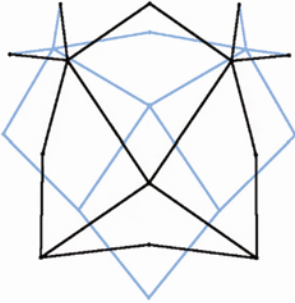
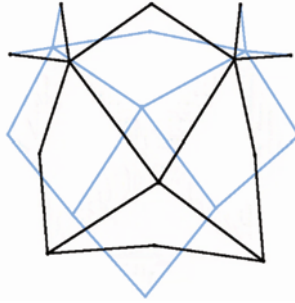
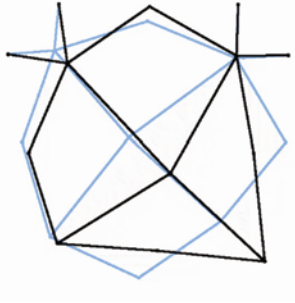
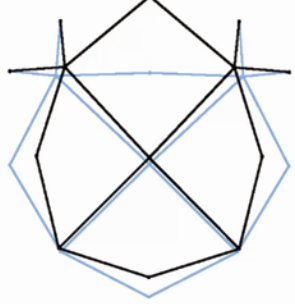
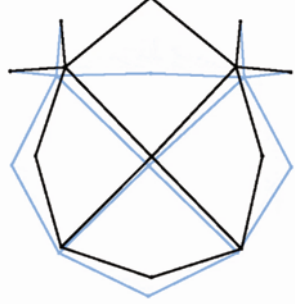
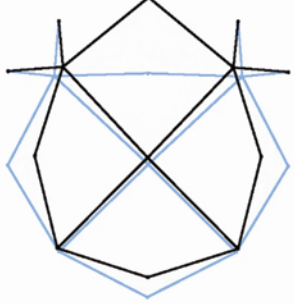
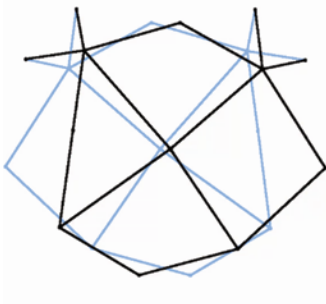
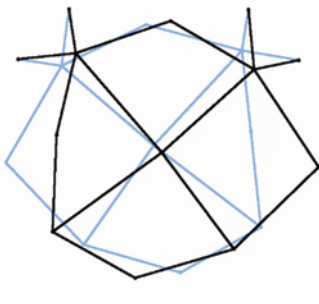
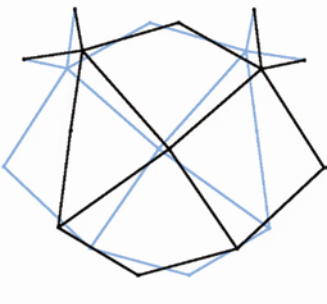
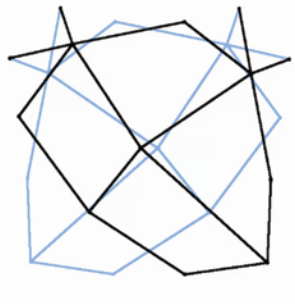
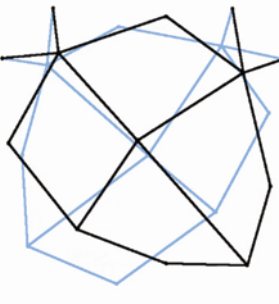
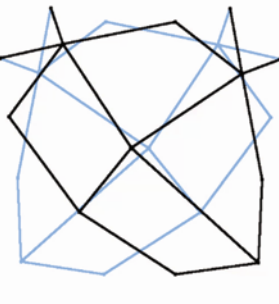
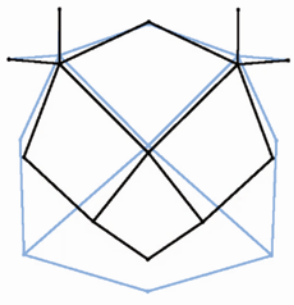
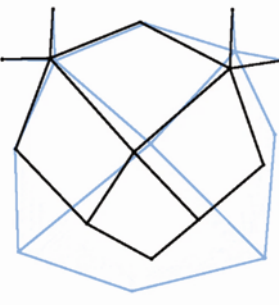
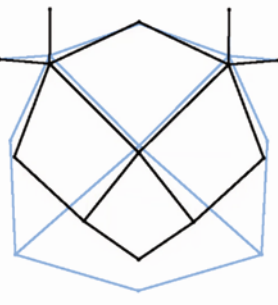
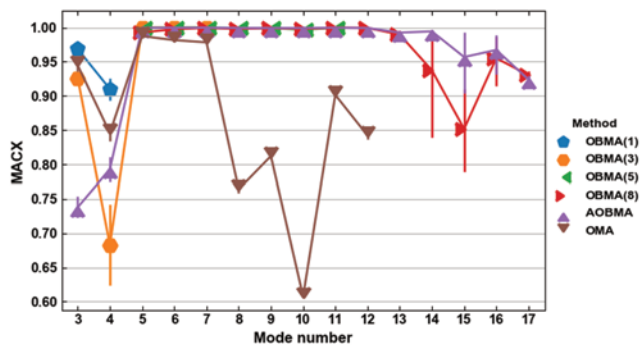
Mode	Reference	OMA	AOBMA
3			
5			
7			
9			
11			

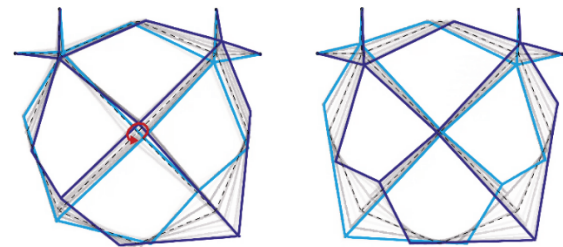


Table 5-3 shows the mode shape deflections of the structure, determined from the numerical reference calculation, and from the estimations by OMA and by AOBMA. To aid conciseness, every second estimated mode, which is determined by both methods, is included. For a condensed and quantified comparison of all estimated modes, the estimation performance of mode shapes is quantified by MACX values in Figure 5-14. The MACX values are calculated between the matched mode estimations and the true reference mode shapes of the simulated structure. In line with previous results, the close modes 3 and 4 are not reliably discriminated by the order-based methods. As a result, the AOBMA mode shape estimation (mode 3 in Table 5-3) appears as a distorted combination of the true reference mode shapes of modes 3 and 4.

Apart from this, Figure 5-14 shows that OBMA and AOBMA provide similar results and clearly surpass OMA in the estimation of mode shapes: while the difference is small in modes 5-7, greater differences are visible in modes 8-12, where OBMA and AOBMA still provide MACX values close to 1. The difference can be summarised by comparing averages across the common range of modes 5-12, where the mean MACX of AOBMA and OBMA(8) is above 0.99 while OMA results in a lower accuracy at an mean MACX of 0.86. A decreased mean and increased variance of MACX values from OBMA and AOBMA is visible at mode 14 and up. The discrepancy between the performance of OBMA/AOBMA and OMA is likely related to the present excitation condition (mixed random and correlated harmonic order excitation at a single location).



**Figure 5-14: MACX values of matched mode estimations by different methods**



**Figure 5-15: Overlaid deflections of mode 12 estimated at harmonic ratio 0.8 by OMA (left) and AOBMA (right), dashed lines show the undeflected state, red arrow follows the trace of the central node (left)**

For a closer analysis, Figure 5-16 is limited to modes 6-12 and shows the degree of mode shape complexity using the MPC value for individual levels of the harmonic ratio. In addition, 30 simulation runs with a harmonic ratio of 0.0 (i.e., purely random excitation) are included in the analysis by OMA. The mode shape estimation of OMA seems to be affected by the phase of the (sweeping) order input, resulting in increased complexity of the estimated mode shapes. OBMA and AOBMA, on the other hand, provide consistently low mode shape complexity (with MPC values close to 1) for harmonic ratios of 0.2 and up.

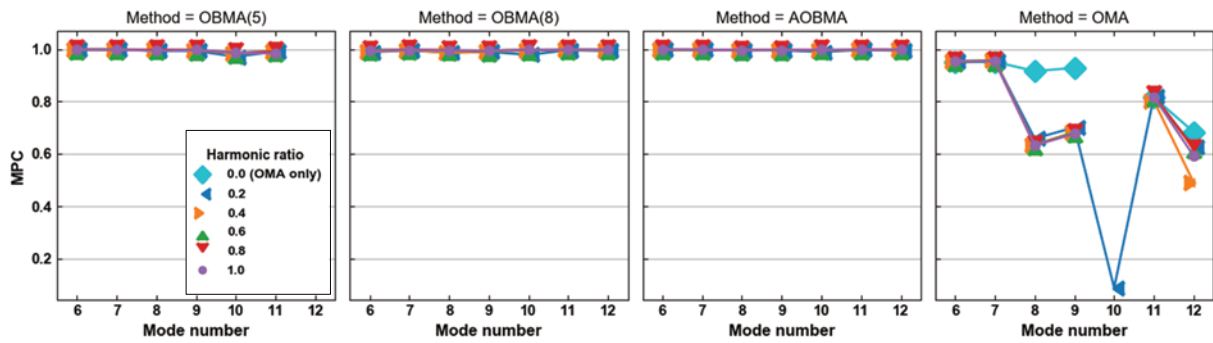


**Figure 5-16: MPC of mode shape estimations by different methods for individual harmonic ratios**

This is also supported by an observation of the estimated mode shapes on the structure. For example, Figure 5-15 shows the overlaid deflections of a vibration cycle for the mode shape estimation of mode 12 at harmonic ratio 0.8 by OMA (left) and AOBMA (right). At the illustrated scale, the AOBMA mode shape is indistinguishable from the reference mode shape and shows antisymmetric deflections. The OMA estimation (Figure 5-15, left), on the other hand, matches these reference deflections well on the right part of the structure (e.g., at node 6, Figure 4-1) but fails to do so at the nodes of the left half of the structure. In addition, the impact of the rotating excitation on the OMA estimation is visible, resulting in a circular motion of the central node illustrated by the ellipsoidal trace line in Figure 5-15 (left). This in turn explains a decreased MPC value of the OMA estimation (Figure 5-16). During order tracking, each tracked response order is phase-referenced with a sinusoidal reference signal of the input order, which is synthesised using the rpm signal and the corresponding order number [115], [171]. It appears that OBMA and AOBMA benefit from this phase-referencing of the output signal, leading to a more accurate mode shape estimation.

#### *Averaging of OBMA results in post-processing*

This section presents and discusses results obtained from an alternative averaging approach. Instead of averaging of order spectra in pre-processing as presented before, the modal estimations of each mode obtained from OBMA are averaged across different orders in post-processing. In the following, this method is denoted “Post-AOBMA” and averages the previously presented results of OBMA estimations from orders 1, 3, 5, 8. In analogy with the weighted averaging in AOBMA (Subchapter 5.2.2), a higher weighting of lower orders is also implemented in Post-AOBMA by using the inverse of the order number as the weighting factor for modal estimations from the corresponding orders. The following plots in Figure 5-17 to Figure 5-20 show the modal estimation performance of Post-AOBMA. For reference, the previously presented results of AOBMA and OBMA(8) are included as well.

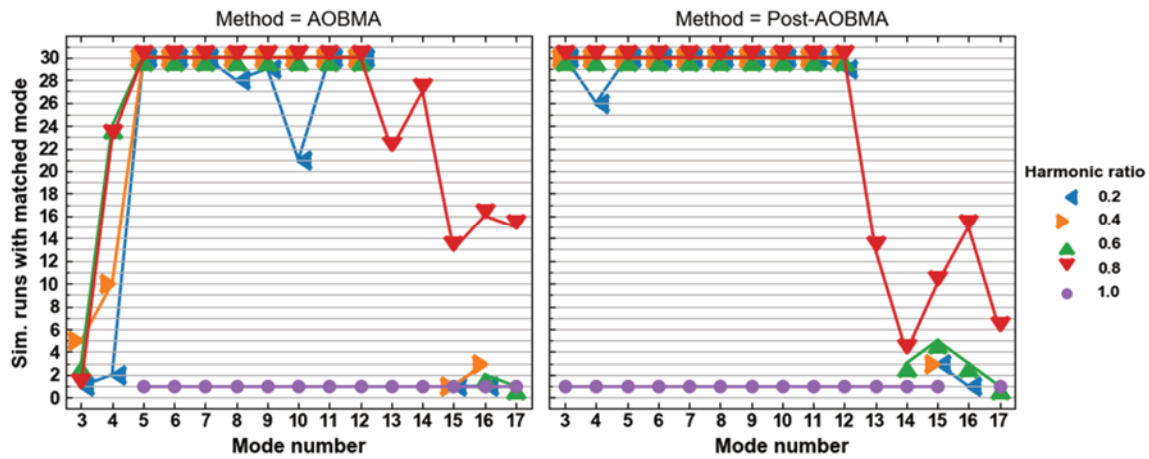


**Figure 5-17: Count of simulation runs with a matched mode estimation by AOBMA and Post-AOBMA**

In Figure 5-17, Post-AOBMA shows a higher number of simulation runs with matched modes compared to AOBMA results for modes 3-4 and for a harmonic ratio of 0.2 in the range of modes 8-10. The reason is that Post-AOBMA benefits from the fact that OBMA(1) and OBMA(3) more often identify modes 3-4 while OBMA(5) more often identifies modes 8-10 compared to AOBMA (Figure 5-9). However, this elevated performance of OBMA(1) and OBMA(3) is also due to their smaller frequency band and comes at the cost of increased spurious modes as discussed with Figure 5-10 (right). This question is further evaluated in the last section of this Subchapter 5.4.1. Moreover, in the presented setup, Post-AOBMA has the advantage that averaged OBMA results of individual orders are already matched to a set of true reference modal parameters. In a real-world application of Post-AOBMA (where true modal parameters are unknown) the mode matching should be performed between individual OBMA results themselves. While this can be implemented algorithmically (e.g., utilising the MACXP), it constitutes an error source for Post-AOBMA results, which is not considered here. In contrast to that, this requirement of mode matching between orders does not apply to AOBMA because it is based on pre-processing.

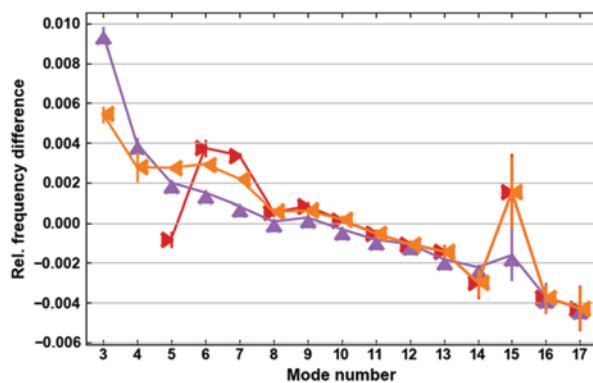


**Figure 5-18: Relative eigenfrequency errors of mode estimations by OBMA(8), AOBMA, Post-AOBMA (for the legend refer to Figure 5-20)**

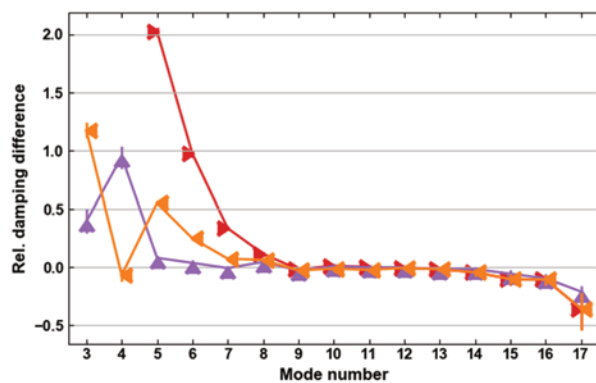


**Figure 5-19: Relative damping ratio errors of mode estimations by OBMA(8), AOBMA, Post-AOBMA (for the legend refer to Figure 5-20)**

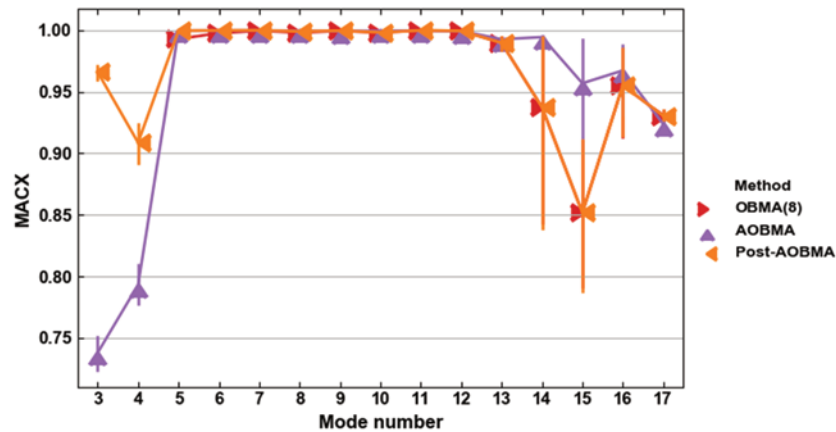


**Figure 5-20: MACX values of mode estimations by OBMA(8), AOBMA, Post-AOBMA**

From Figure 5-18 to Figure 5-20 it is visible that, in the upper frequency range, the results of Post-AOBMA are identical to those of OBMA(8), which is due to the lack of other orders' contributions in the frequency range of mode 12 and up (Figure 5-9). For the closely spaced modes 3-4, Post-AOBMA shows favourable performance in the estimation of modal parameters. However, this performance is likely elevated due to factors discussed in the previous paragraph. Leaving aside modes 3-4, AOBMA shows a greater mean estimation performance for all modal parameters compared to Post-AOBMA. This is also the case for mode numbers above 11, even though both AOBMA and Post-AOBMA are solely based on order 8 in this frequency range since order 5 ends at 150Hz. However, this can be related to a reduced number of modes identified in this frequency range (Figure 5-9), contributing to a higher uncertainty of the results indicated by larger vertical bars, especially visible in Figure 5-20. Besides that, averaging by AOBMA reduces the variance in the processed spectra, potentially leading to a reduced error bias during the modal estimation. It was shown that averaging of the frequency spectrum has an impact on modal estimation performance, albeit primarily on the variance of modal parameters estimated in (regular) OMA by the pLSCF method [198].

#### *Comparison of OBMA and AOBMA at a common, narrowed analysis bandwidth*

Due to different frequency ranges of individual orders (Equation (4.4)), the previously presented results are obtained not only by different estimation methods but also utilise different analysis bandwidths. Great estimation differences of modes 3-4 between OBMA(1), OBMA(3) (and consequently Post-AOBMA) on one hand and AOBMA on the other hand were observed in the previous sections of this Subchapter 5.4.1.

Therefore, this section compares the estimation performance of these methods using the common analysis bandwidth of 25Hz covering modes 3-4. More precisely, the analysis band of AOBMA is reduced to match the frequency range of OBMA(1), i.e., 5Hz-30Hz. The analysis band of OBMA(3) is shortened to cover the same bandwidth of 25Hz, resulting in a range of 15Hz-40Hz. This alleviates the advantage of Post-OBMA noted in the previous

section for a clearer comparison and allows to gauge a potential impact of order averaging on the estimation of closely spaced modes. The same stabilisation criteria are used for the following results as before (Table 5-1), except for the required minimum number of stable poles, which is increased to 10 to avoid overfitting with identifications of spurious modes.

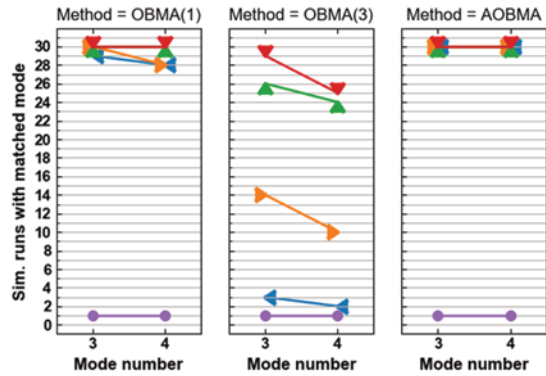


Figure 5-21: Count of simulation runs with a matched mode, 25 Hz analysis bandwidth (for the legend refer to Figure 5-22)

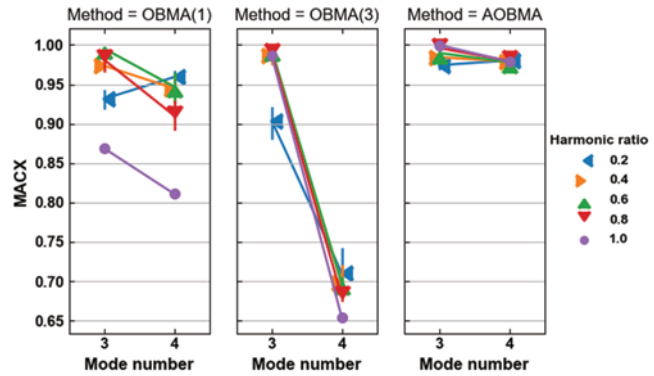


Figure 5-22: MACX values of matched mode estimations, 25 Hz analysis bandwidth

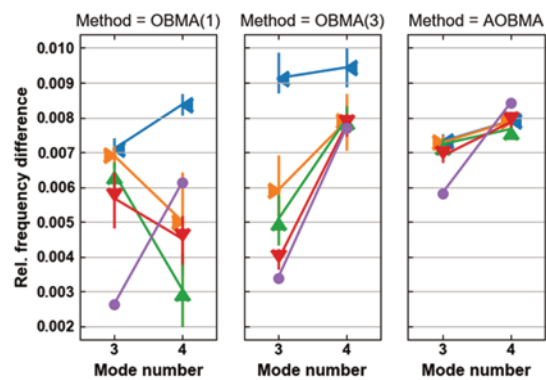


Figure 5-23: Relative eigenfrequency errors of matched mode estimations, 25 Hz analysis bandwidth (for the legend refer to Figure 5-22)

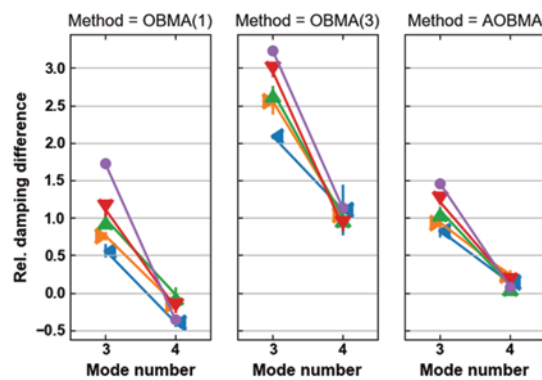


Figure 5-24: Relative damping ratio errors of matched mode estimations, 25 Hz analysis bandwidth (for the legend refer to Figure 5-22)

As expected from previous discussions (Figure 5-6), OBMA(3) mostly shows a decreased performance compared to OBMA(1) in Figure 5-21 to Figure 5-24 because of the increased spectrum distortion at higher frequency modulation rates of higher orders. In AOBMA, the spread of modal parameter estimations between different harmonic ratios (Figure 5-21 to Figure 5-24) appears smaller compared to OBMA(1) and OBMA(3). This indicates a positive effect of AOBMA at low harmonic ratios, which show a decreased performance in OBMA(1) and OBMA(3), especially at the eigenfrequency (Figure 5-23) and damping ratio (Figure 5-24) estimations. Overall, AOBMA does not show worse results compared to OBMA(3) and partially surpasses the performance of OBMA(1). Based on this, it can be concluded that the estimation of the closely spaced modes 3-4 is not negatively affected by order averaging in AOBMA compared to OBMA. Instead, the estimation performance benefits from a narrow analysis band in this range.

### 5.4.2 Operational run-up of a turbofan casing

In this subchapter, first, spectra from the unprocessed time response are compared to the response spectrum estimate from the proposed AOBMA method. Afterwards, differences in modal parameter estimations between OBMA and AOBMA in relation to OMA are presented and discussed.

In the following, rpm, frequency ( $f_{norm}$ ), and amplitude values are provided in normalised units, which are scaled in relation to their respective maximum values in the analysed measurement.

Figure 5-25 shows a spectrum from the response in radial direction at position 4 (Figure 5-8). Ending frequencies of orders 1, 2, 3 are highlighted in the graph with red vertical lines. On closer inspection, discontinuities are observed at some of these frequencies. These discontinuities can be attributed to the end-of-order effect. The distortion is especially pronounced at the ending frequency of order 1 ( $f_{norm} = 0.25$ ) and potentially order 2 ( $f_{norm} = 0.5$ ). This stronger impact of the end-of-order effect on frequencies of low orders is in agreement with the observations and explanations from the simulated structure (Figure 4-7) in Subchapter 4.3.

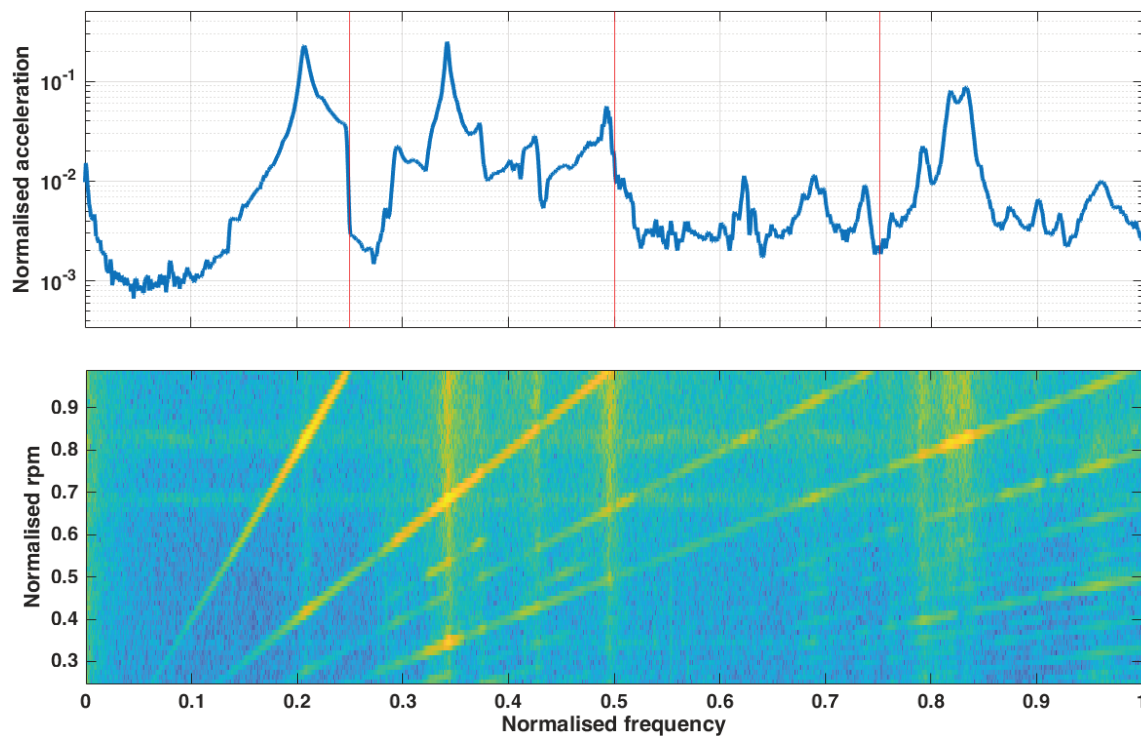


**Figure 5-25: Acceleration spectrum (top) and spectrogram (bottom) from operational run-up data**

The orders 1, 2, 3 and 4 were tracked from the response data and, according to the presented AOBMA method, scaled and averaged, resulting in the spectrum of the same channel shown in Figure 5-26. A clear difference in both spectra is visible in the frequency range of the first order. Its impact on the spectrum amplitude is reduced and the discontinuity

at its ending frequency ( $f_{norm} = 0.25$ ) is eliminated in Figure 5-26. The impact of the second order's ending frequency at  $f_{norm} = 0.5$  is difficult to judge from Figure 5-25 alone, because it appears to coincide with a resonance. However, the peak at this frequency is reduced in the order-based spectrum in Figure 5-26, indicating that an impact of the end-of-order effect on this area is indeed present in Figure 5-25.

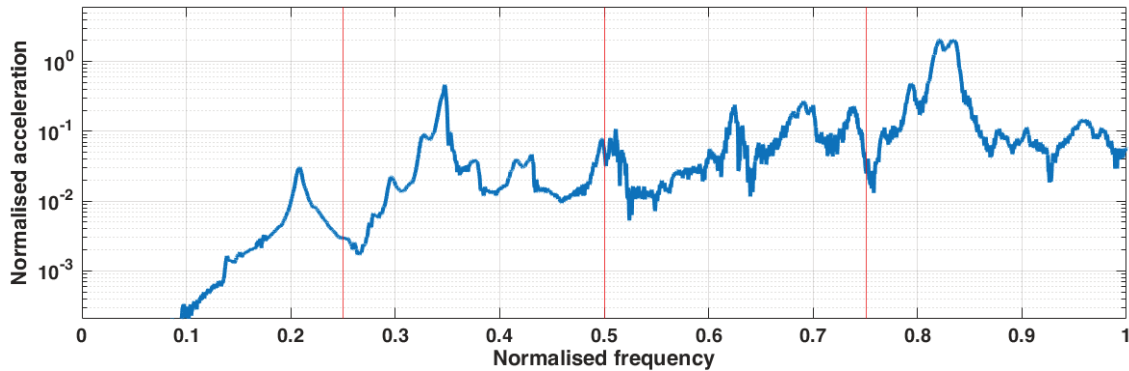


**Figure 5-26: Acceleration magnitude spectrum from scaled and averaged orders (AOBMA)**

OMA estimated the most modes with a count of 21, followed by AOBMA with 18 modes. In OBMA, the orders 4, 3, 2 and 1 determined 16, 15, 7 and 2 modes, respectively. In contrast to the simulation data, no tolerance criteria for mode matching are used here, so all modes estimated by OBMA and AOBMA are matched and are included in the following graphs. Another difference to the simulation study is that OMA estimation results are used as reference values since the true modal parameters of the structure are unknown.

Figure 5-27 to Figure 5-29 show all relative difference values of estimated modal parameters in relation to OMA results for individual modes. The results of individual modes are summarised in Figure 5-30 to Figure 5-32 into error plots with mean values and confidence intervals of the estimation differences over all modes combined.

Figure 5-29 shows that the estimated mode shape of mode 1 has a much greater correlation between OMA and OBMA(1) compared to AOBMA. These mode shape estimations are plotted in Figure 5-34 and clear differences between the estimation methods are visible although they all indicate an overall ellipsoidal deflection, typical for the first circumferential mode of a cylindrical structure. The OBMA(1) mode shape shows symmetry about the horizontal axis but a lack thereof about the vertical axis, while the OMA mode shape seems to be superposed with rigid body motion with clear displacement components along the horizontal axis. In contrast to that, the MACX value indicates consistent results for the mode shape of mode 15 between OMA, OBMA(4) and AOBMA in Figure 5-29, which is also confirmed by the mode shapes in Figure 5-35.

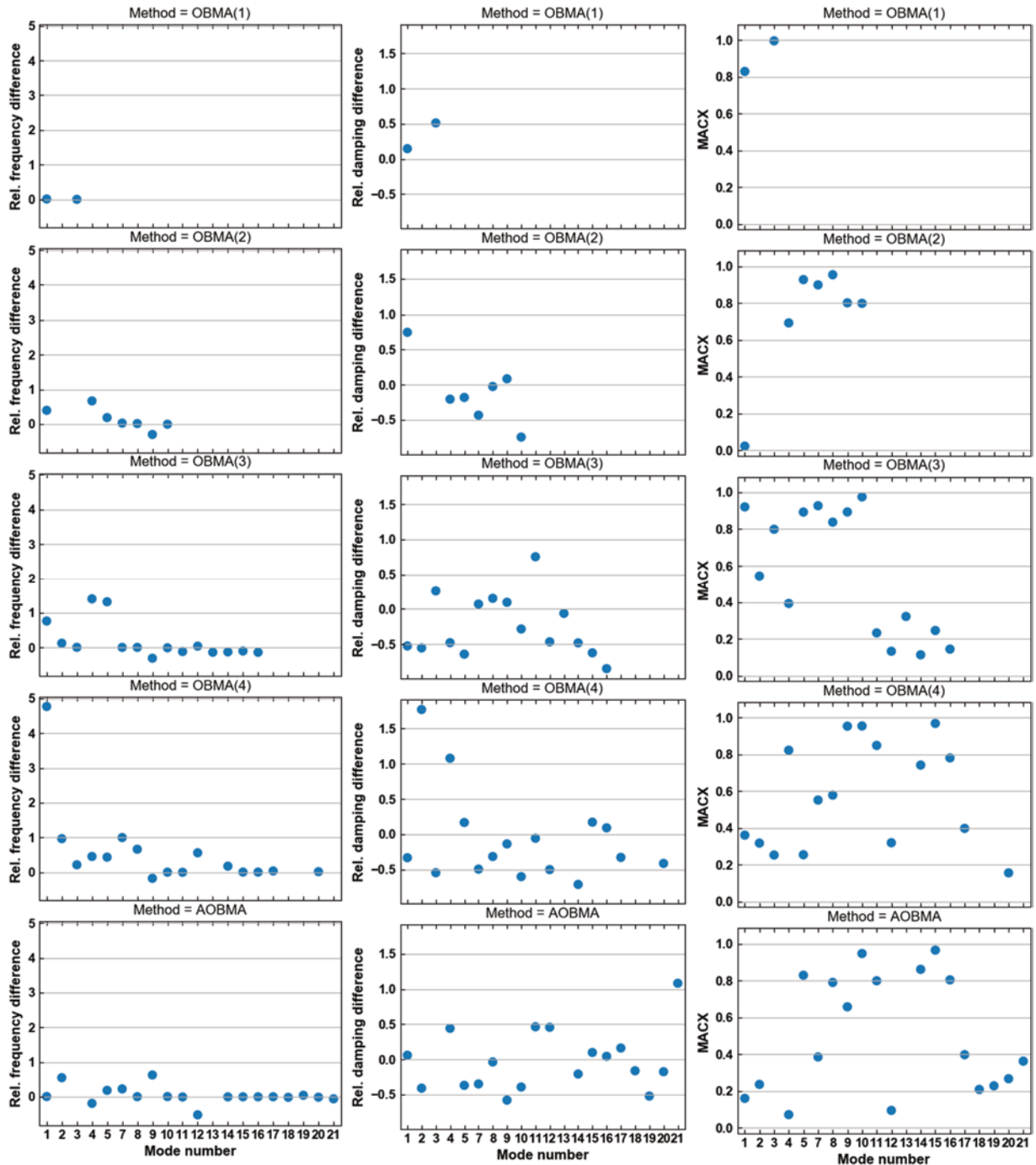


**Figure 5-27: Eigenfrequency differences  $(f_{est} - f_{OMA})/f_{OMA}$  relative to OMA results**

**Figure 5-28: Damping ratio differences  $(\xi_{est} - \xi_{OMA})/\xi_{OMA}$  relative to OMA results**

**Figure 5-29: MACX values between mode shape results from OMA and the specified methods**

In Figure 5-30, OBMA(1) shows the smallest mean difference and confidence interval in relative eigenfrequency differences compared to OMA. However, this is also promoted by the small frequency range of order 1, resulting in only two estimated modes as shown in Figure 5-27. Apart from that, AOBMA delivers estimated eigenfrequencies and damping ratios, which show smaller variance and mean difference compared to OBMA as seen in Figure 5-30 and Figure 5-31, respectively.



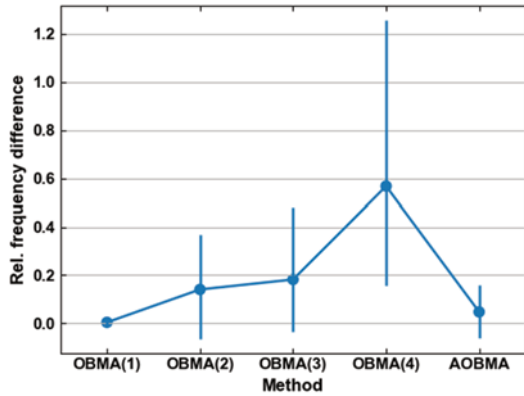


Figure 5-30: Mean eigenfrequency differences relative to OMA results

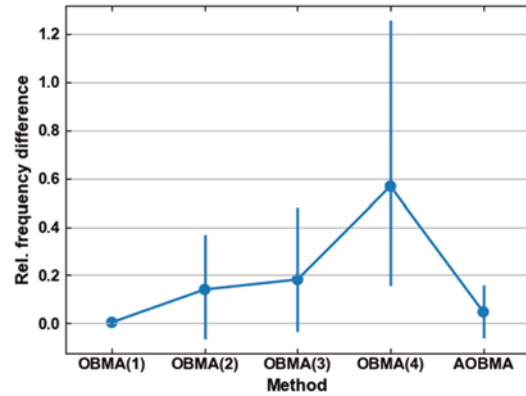


Figure 5-31: Mean damping ratio differences relative to OMA results

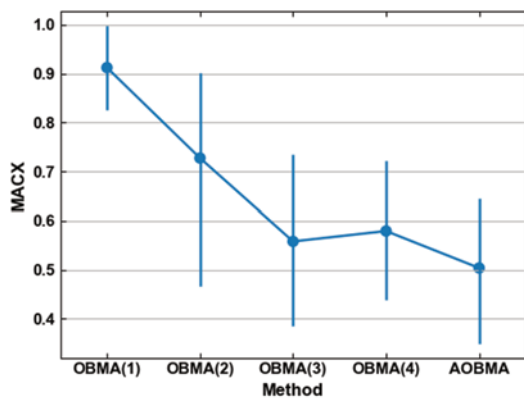


Figure 5-32: Mean MACX values between mode shape results from OMA and the specified methods

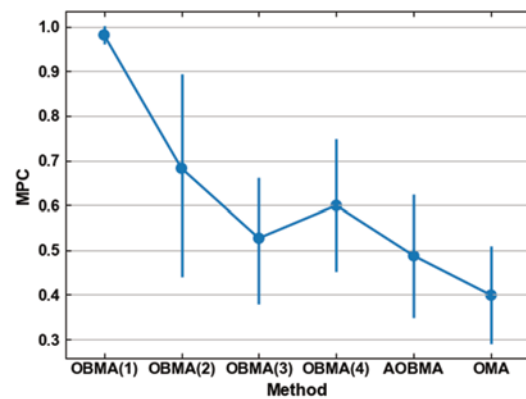


Figure 5-33: Mean MPC values of mode shape results from all methods

In Figure 5-32, the lowest average MACX value is obtained from AOBMA. On first sight, this contradicts the observations from the simulation study in Figure 5-14, where MACX values from AOBMA are among the highest. However, here the reference mode shapes originate from (imperfect) OMA estimations while the simulation study uses numerical reference parameters from the eigensolution.

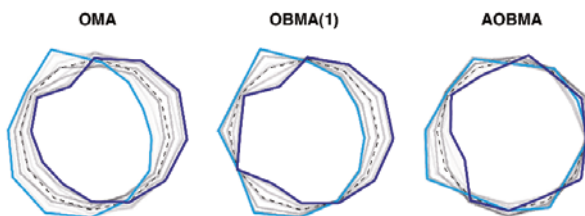


Figure 5-34: Overlaid deflections of mode 1 estimated by OMA, OBMA(1), AOBMA

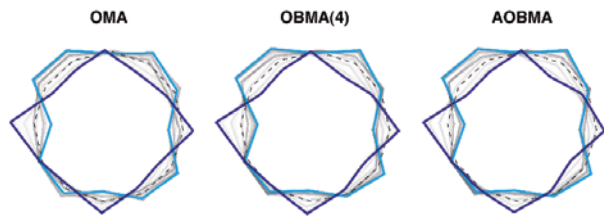


Figure 5-35: Overlaid deflections of mode 15 estimated by OMA, OBMA(4), AOBMA

As observed in the simulation study, mode shape estimations by OMA were less accurate compared to OBMA and AOBMA. Therefore, low MACX values between OBMA/AOBMA and

OMA may indicate less accurate estimations by OMA and not the other way around. This assumption is also supported by the comparison of the mode shape complexity in Figure 5-33, where OMA shows mode shape estimations with higher complexity (i.e., lower MPC values) compared to OBMA and AOBMA, which is in conjunction with observations from the simulation study.

## 5.5 Conclusions

This work introduced the AOBMA method, which extends OBMA by including intermediate steps of scaling and (weighted) averaging of tracked orders. To validate the proposed method, AOBMA was applied to simulation and real operational data along with OBMA and traditional OMA. Based on this, a comparative study of the three methods was performed to assess their modal estimation performance. In the simulation study, the harmonic ratio was used as an independent variable to estimate the impact of harmonic and random contributions in the excitation. The results showed that, with harmonic ratios of 0.6 and up, AOBMA identified a similar or higher number of modes in the specified error range (Figure 5-10). For example, at a harmonic ratio of 0.8, AOBMA correctly identified the greatest number of 11.9 modes on average, while OBMA determined an average of 9.5 modes at most (from order 8) and OMA determined 9 modes. However, OMA surpassed the order-based methods in the identification of two very closely spaced modes.

End-of-order distortions are present but relatively limited in the presented simulation, even at high harmonic ratios, as shown in Figure 4-6. This likely explains why no clear impact of these distortions and of different harmonic ratios on OMA was observed (Figure 5-10, left). However, the spectrum from operational measurements in this paper (Figure 5-25, top) as well as previous studies [53]–[55] illustrate that stronger end-of-order distortions are common. Since order-based methods are not affected by these distortions, OBMA and AOBMA benefit in such cases, even though it was not observed in the simulation study of this chapter.

A benefit of the proposed AOBMA method is the reduction of analysis effort in comparison to OBMA, since estimates from individual orders with fractional, partially overlapping frequency ranges are combined into a single data source in AOBMA. Hence, AOBMA solves OBMA's limitation of ambiguous results depending on the chosen order as highlighted in Subchapter 2.2. The issue of high variance of OBMA results depending on the used order is addressed by AOBMA, as it achieves a noise reduction through averaging of orders and is able to emphasise most significant orders by the application of weighted averaging. As a result, AOBMA provided more consistently low error values of eigenfrequencies and damping ratios compared to individual OBMA results and approached the performance of OMA. This was most visible for the damping ratio estimation performance (Figure 5-13). When averaged

across 9 common modes, absolute relative errors from AOBMA estimations were substantially lower at 0.03 compared to 0.32 of OBMA(8). This trend was observed in the analysis results of simulation (Figure 5-12, Figure 5-13) as well as real operational data (Figure 5-30, Figure 5-31). The alternative Post-AOBMA method (i.e. averaging of OBMA estimations in post-processing) was examined but does not outperform AOBMA in this study assuming that similar frequency analysis bandwidths are used (see Subchapter 5.4.1). Post-AOBMA requires the additional step of mode matching across different orders but is free of the required order scaling and averaging steps of AOBMA. Nevertheless, as Post-AOBMA showed an improvement over OBMA results, further research on this method, including algorithmic mode-matching and additional case studies, is encouraged.

The presented conclusions are possible due to the performed comparative simulation study, which is based on the dataset presented in Chapter 4. This work is the first to systematically evaluate the impact of excitation conditions on OBMA and OMA performance. It thus addresses the lack of such studies stated in Subchapter 2.2. The results showed that OBMA and AOBMA were still applicable in the presented case at conditions with low relative harmonic excitation of 0.2 and 0.4. Furthermore, it was observed, that the main impact of the harmonic excitation ratio affected less the accuracy of OBMA and AOBMA estimations but rather the number of overall identified modes (Figure 5-10).

Addressing another gap identified in Subchapter 2.2, this study also focused on quantification and comparison of the mode shape estimation performance. In this regard, OBMA and AOBMA surpassed OMA in the simulation study (Figure 5-14). I.e., across 8 identified modes in the same frequency range, AOBMA and OBMA estimated modes at a high accuracy with MACX above 0.99 whereas OMA provided a lower average MACX of 0.86. This observation was also supported by the analysis of real measurements (Figure 5-33), even though they lead to a less conclusive assessment due to a lack of true reference mode shapes from the real structure. Order excitation was identified as the likely origin for degraded mode shape estimations in OMA (Figure 5-16). In contrast to that, order tracking in OBMA and AOBMA seems to prevent a negative impact of the excitation orders by phase-referencing. To the best of the authors' knowledge, this work is the first to make this finding, thereby extending the existing use cases for OBMA and AOBMA.

While AOBMA reduces the variance of individual OBMA results, the specific orders used in AOBMA still have a major impact on the achieved results, since the orders form the data foundation of the method. In future work, additional metrics (apart from relative order amplitudes) for the selection of relevant orders and weighting factors for weighted averaging in AOBMA should be evaluated. A correlation-based tool such as the Frequency Response Assurance Criterion (FRAC) could serve to identify and group orders with similar spectra or to create weighting factors depending on the spectrum similarity. This approach can be also

useful to determine orders, which meet the assumption of similar force distributions (see Subchapter 5.2.2) and are thus especially suitable for averaging. Moreover, a modal model, which incorporates the distorted shape of resonances in order spectra (Figure 5-6) could further enhance the performance of OBMA and AOBMA, especially in the estimation of closely spaced and weakly damped modes. As explained in the ending paragraph of Subchapter 5.2.3, the research on AOBMA can be developed by evaluating the impact of gyroscopic effects in more detail based on corresponding data. Finally, additional independent variables, such as measurement noise or machine acceleration rate from the dataset in presented in Chapter 4, can be included in future studies to estimate their impact on the compared methods in the future.

This chapter proposed the new AOBMA method and presented a comparative simulation study, providing contributions in the domain of modal analysis of rotating machinery. By comparison, the next Chapter 6 focuses on evaluation of rotating machinery measurements from the perspective of predictive condition monitoring. The aim is to address the limitation of current methods for RUL prediction, which require large amounts of run-to-failure sequences as training data.

## 6 Data-efficient estimation of Remaining Useful Life (RUL) for machinery with a limited number of run-to-failure training sequences

The previous chapter introduced a novel method for OMA of rotating machinery during operation at transient acceleration or deceleration conditions. It addresses limitations of previous OMA methods discussed in Subchapter 2.1 and Subchapter 2.2, contributing to a more comprehensive and accurate estimation of modal parameters of structures under excitation from rotating components during acceleration. As highlighted in Chapter 1, modal parameters crucial for reducing noise emissions and the risk of premature damage due to dynamic stress. Furthermore, modal parameters are used to aid design iterations of mechanical components and to optimise numerical models by FEM model updating. With regard to condition monitoring, Subchapter 2.4 revealed that modal parameters are mostly suitable for the evaluation of the structural condition at a global scale but lack sensitivity for operational applications and require further research, especially in the field of predictive condition monitoring.

This is a research area with great relevance to industrial applications as it can serve as a foundation for safer, more cost-efficient operation and maintenance. RUL prediction plays an important part in this field and has seen significant advances from the introduction of ML methods. However, as identified from existing literature in Subchapter 2.4, these methods typically require model training with a large number of run-to-failure sequences, which are often not feasible to obtain due to the required time and cost investments. Compared to the acquisition of these run-to-failure sequences, samples of solely healthy or faulty machinery data (hereafter also referred to as binary condition data), are much more readily available and producible. This observation is based on Subchapter 2.3, which identified a much smaller number of open run-to-failure vibration datasets [77], [78], [80] compared to the number of open vibration datasets covering various faults and healthy baseline conditions without intermediate life cycle data [76], [79], [81]–[83], [85], [87]–[89].

In addition to the labour, hardware and energy cost associated with comprehensive run-to-failure tests, the environmental impact should be considered. Adverse effects of energy consumption, such as greenhouse gas emissions represent an increasing reason for concern across industries, including the domains of AI and ML [199]–[201]. At the same time, only a minority of current publications in the AI space appear to address the training efficiency of the proposed methods [199], [201].

These considerations provide the reasoning for the methodology proposed in this chapter. Binary (i.e., healthy and faulty) condition data is used to form models, which quantify the

current machine deviation from the healthy and faulty state. As this data is easier to obtain compared to full run-to-failure sequences, these models can take advantage from such additional binary training cases, if available. Alternatively, the healthy and faulty conditions are extracted from the start and end section of available run-to-failure training sequences. This condition deviation data is then used to calculate a Health Index (HI) value, which in turn is processed to detect the occurrence of initial degradation. The available (limited) number of run-to-failure training sequences is then processed to generate corresponding HI training functions, which are then used to train a RUL prediction model.

The resulting contributions of the present work are summarised below.

- A novel methodology for RUL prediction and degradation detection from a limited number of run-to-failure training sequences is introduced. It is the first approach taking advantage of distinct (healthy and faulty) condition data for training, in addition to (limited) run-to-failure training sequences.
- A novel HI calculation method is proposed, implemented using MD and AE, to model the current deviation from the healthy and faulty machine state, followed by the HI calculation from the ratio of these modelled condition deviations. In a broader sense, this represents a novel feature reduction and data fusion approach for machine condition data.
- Several variants of the proposed methodology (based on MD, AE, LS, LSTM, and SVR) are implemented and compared in terms of prediction accuracy, variance, and training time requirements on a varied reduced number of training sequences.
- In contrast to previous publications dealing with RUL prediction from limited training data, the proposed methodology is applied to two public benchmark datasets (C-MAPSS and FEMTO), indicating its capability to improve model generalisation compared to baseline LSTM prediction and providing insights into reduction of training duration due to training data reduction.

The work of this chapter resulted in a journal publication [21] after a peer review process. In the following Subchapter 6.1, an overview of the proposed methodology is presented with subchapters devoted to details of its main processing steps. The next Subchapter 6.2 and Subchapter 6.3 cover two open datasets used for validation and comparison of the proposed methodology, including the presentation and discussion of obtained results. Finally, Subchapter 6.4 presents the main findings, giving conclusions, as well as current challenges and suggestions for future work in the domain of RUL prediction.

## 6.1 Proposed methodology for data-efficient RUL prediction

This subchapter presents the proposed methodology by first providing an initial outline, which is then followed up by subchapters covering details of the involved steps and methods.

The proposed methodology consists of three main steps, which are indicated in the overview graphic in Figure 6-1 with a reference to the corresponding subchapter. First (Subchapter 6.1.1), the health and the fault condition models are created from binary (i.e., healthy or faulty) condition data. A limited number of run-to-failure training sequences is then fed into the health and fault models, providing health and fault condition deviation sequences ( $d_h$  and  $d_f$ ), respectively. In the second step (Subchapter 6.1.2), both values are combined through the calculation of an HI value. The HI is then used in a degradation detection step, which provides an additional component of monitoring information and can be used to separate relevant degradation data from healthy condition data downstream. In the final step (Subchapter 6.1.3), the degradation data is processed by a prediction model, which outputs the final RUL prediction.

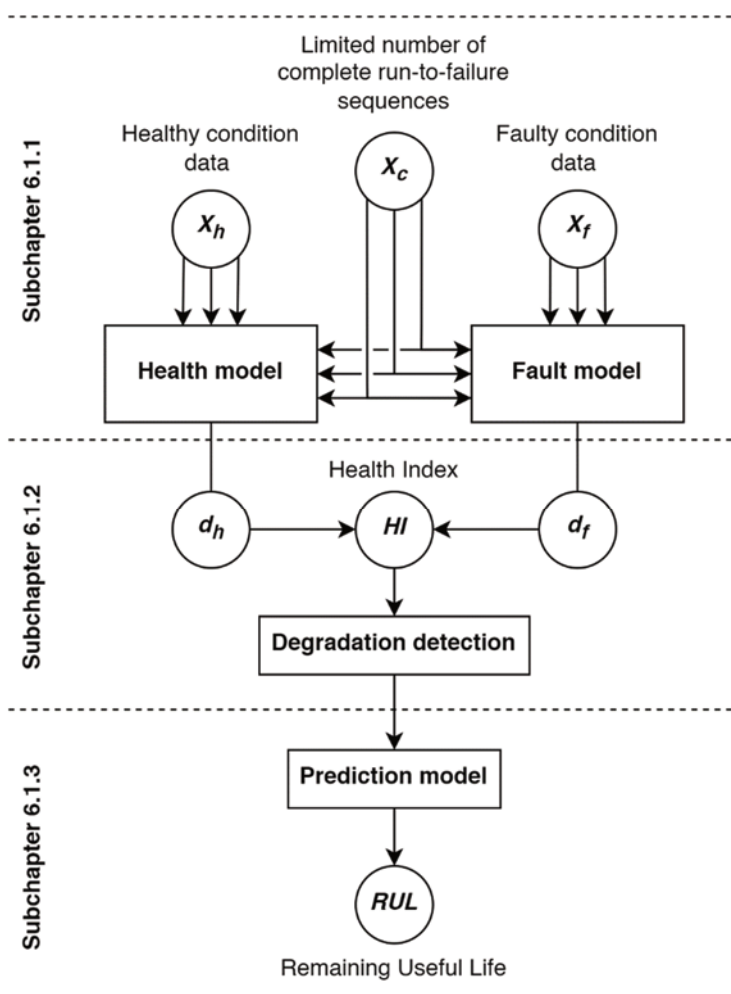


Figure 6-1: Overview graphic of the proposed RUL prediction method

The health and the fault model (and thus the HI) are created based on two approaches, i.e., MD [173] and LSTM AE NN [202]. For the RUL prediction model, three approaches are used, namely quadratic polynomial LS extrapolation (QPoly), SVR [174], and LSTM NN [124]. The proposed approaches are presented, and their results are compared in course of this study.

In addition, a direct RUL prediction based on the dataset features (i.e., without HI calculation) is performed as the baseline for the comparison to evaluate the impact of the introduced condition deviation and HI features.

Table 6-1 lists all combinations of methods, which are implemented, validated, and compared in this study. Since different variants of the proposed methodology are implemented based on different methods, the combined methods, forming the foundation for each approach, are given in Table 6-1 as well.

**Table 6-1: Implemented and compared RUL prediction methods**

Abbreviation	Method for health and fault models	+	Method for RUL prediction
LSTM (baseline)	N/A	+	LSTM Neural Network
MD-QPoly (proposed)	Mahalanobis Distance	+	Quadratic Polynomial Least Squares Regression
MD-SVR (proposed)	Mahalanobis Distance	+	Support Vector Regression
AE-SVR (proposed)	LSTM Autoencoder Neural Network	+	Support Vector Regression
MD-LSTM (proposed)	Mahalanobis Distance	+	LSTM Neural Network

### 6.1.1 Machine condition deviation

As the foundation for the HI calculation (addressed in Subchapter 6.1.2), the deviation  $d_h$  of the current machine condition sample  $x$  from the completely healthy condition data  $[X_h]$  on one hand and the deviation  $d_f$  from the completely degraded condition data  $[X_f]$  on the other hand shall be determined in an unsupervised manner. With data-efficiency in mind, data for both reference conditions are used for training, while full run-to-failure sequences are not required.

In the present study, two approaches are implemented and later compared for this task: LSTM AE NN, and MD. Both methods are utilised to construct two models each. The “health model” (providing the deviation  $d_h$ ) is constructed from  $[X_h]$  while the “fault model” is conditioned from  $[X_f]$  (providing the deviation  $d_f$ ).

Condition data  $[X_h]$  and  $[X_f]$  can be obtained from dedicated measurements or available run-to-failure sequences by assuming that the first and last  $n_{hf}$  samples represent the healthy and faulty condition, respectively. Then, a run-to-failure sequence  $[X]$  with  $N$  samples, can be subdivided into  $[X_h]$ ,  $[X_f]$ , and the intermediate degradation data  $[X_{itm}]$ , the latter of which



is not used by the health and fault models. This is described by Equation (6.1), where  $\langle x_i \rangle$  represents the  $i$ -th multivariate data sample of the sequence  $[X]$ .

$$[X] = \begin{bmatrix} [X_h] \\ [X_{itm}] \\ [X_f] \end{bmatrix} = \begin{bmatrix} \begin{bmatrix} \langle x_1 \rangle \\ \vdots \\ \langle x_{n_{hf}} \rangle \end{bmatrix} \\ \langle x_{n_{hf}+1} \rangle \\ \vdots \\ \langle x_{N-n_{hf}-1} \rangle \\ \begin{bmatrix} \langle x_{N-n_{hf}} \rangle \\ \vdots \\ \langle x_N \rangle \end{bmatrix} \end{bmatrix} \quad (6.1)$$

### *LSTM Autoencoder*

After training of the AE NN with binary condition data  $[X_h]$  or  $[X_f]$ , the desired deviation value  $d_h$  or  $d_f$  is obtained as the difference between the current condition sample  $x$  and its corresponding AE reconstruction as described by Equation (6.2).

$$\begin{aligned} d_h &= x - D_h(E_h(x)) \\ d_f &= x - D_f(E_f(x)) \end{aligned} \quad (6.2)$$

To use multiple features for the AE-based condition deviation models, the deviations of individual features are combined into a single function by normalisation and averaging. Progressions of a raw feature, its AE reconstruction and the reconstruction error are shown later in the results subchapter for both the healthy and the faulty condition deviation models in Figure 6-12 and Figure 6-13, respectively.

### *Mahalanobis Distance*

The MD-based health and fault models are created from Equation (3.48), where the health data  $[X_h]$  and fault data  $[X_f]$  are used to calculate the respective covariance matrix  $[K_{xx}]$  and mean feature vector  $\{\mu\}$  for the respective health or fault model. The output of Equation (3.48) then represents the health deviation  $d_h$  or fault deviation  $d_f$ , respectively.

### *Feature subset optimisation by the Genetic Algorithm (GA)*

In frame of the proposed method, the MD is utilised to quantify the deviation  $d$  of current machine condition to a reference (healthy or faulty) condition. For this purpose, it is desirable to maximise the MD between opposing (i.e., healthy and faulty) condition data  $[X_h]$  and  $[X_f]$ . This is achieved by the selection of a data feature subset  $S$ , which is optimised towards the maximum MD separation  $d_{sep}$  defined in Equation (6.3). The equation contains MD values  $d_h([X_h])$  between individual healthy samples  $\langle x_h \rangle$  and the healthy reference state  $[X_h]$ , as well as the opposing MD values  $d_f([X_h])$  between individual healthy samples  $\langle x_h \rangle$  and the faulty reference state data  $[X_f]$ . A Genetic Algorithm (GA) is implemented and employed in the present study for this optimisation task.

In generation 0, an initial population of feature subsets is randomly selected. On one hand, the average  $\bar{d}_h$  of MD values is calculated between the reference set  $[X_h]$  and each of its samples  $\langle x_h \rangle$ . On the other hand, the average  $\bar{d}_f$  of MD values is calculated between the reference set  $[X_f]$  and each of the opposing set's samples  $\langle x_h \rangle$ . The objective function of averaged MD separation  $\bar{d}_{sep}$  is represented by Equation (6.3), which is then maximised by the GA. In each generation, the objective function of each population member (i.e., feature subset candidate  $S$ ) is evaluated and the 5 highest ranking members are selected for crossover to breed a descendent population (i.e., the next generation), assigning or dismissing individual features based on the parents' properties. A 30% mutation rate (chance of random feature inclusion/reduction into  $S$ ) is introduced, and 5 randomly selected members are retained into the next generation to avoid convergence on a local optimum.

$$\max_S \bar{d}_{sep} = \bar{d}_h([X_h(S)]) - \bar{d}_f([X_h(S)]) \quad (6.3)$$

### 6.1.2 Health Index (HI) calculation

The HI aims to represent a measure of the relative health condition of the monitored machine, where a value of 1 typically indicates the condition of a new or unworn machine and a value of 0 indicates a condition of machine failure, a critical fault or a degraded condition requiring maintenance.

With data-efficiency in mind, the goal of the proposed HI generation is to generate HI values at any stage of the engine life cycle, utilising solely binary (i.e., healthy and faulty) conditions for the constructed model. As such, the proposed method for HI calculation is largely unsupervised.

The variance in condition signatures and degradation progressions of different monitored machines leads to varying ranges of the condition deviation output by the fault and health model. Despite that, a normalised HI within the interval  $[0, 1]$  is obtained by calculating a ratio involving the deviation outputs of the health model  $d_h$  and fault model  $d_f$  given in Equation (6.4). This approach was utilised previously in Subchapter 4 for the quantification of harmonic and random vibration contributions by the harmonic ratio (Equation (4.1)). To balance the contributions of both the fault and health model, min-max scaling is applied to the output of the health and fault model individually based on training data. It should be noted that full run-to-failure sequences are not required to determine the scaling parameters, as the minimum and maximum deviation output is obtained from available healthy and faulty condition data.

$$HI(\langle x \rangle) = \frac{d_f(\langle x \rangle)}{d_h(\langle x \rangle) + d_f(\langle x \rangle)} \quad (6.4)$$

The deviation functions  $d_f$  and  $d_h$  based on MD are shown later in the results subchapter in Figure 6-10 for an exemplary run-to-failure sequence from the C-MAPSS FD001 training dataset.

After application of Equation (6.4), the obtained HI is smoothed by a moving average. The range of the smoothed HI obtained from training data  $[X_h]$  and  $[X_f]$  is then used to calculate min-max scaling parameters for the HI. A HI resulting from the deviation sequences of Figure 6-10 is shown in Figure 6-11.

### *Degradation detection*

The determination of the HI can be considered as a feature reduction process to a single quantity. The occurrence of the degradation start is detected from the HI by assuming that a predefined number of initial HI samples of each sequence represents the healthy machine condition. A threshold is determined from 3 standard deviations of these initial healthy HI samples. Additionally, a tolerance of 5 samples exceeding this threshold is allowed to lower the sensitivity of the triggered degradation detection to outliers.

As seen from the sequence later in Figure 6-11, a typical progression of the HI has a consistently high value at the beginning of the run. This phase represents the healthy condition, as it does not indicate a decline of the machine health. Since a degradation trend has not yet developed, it is assumed that a machine-specific and meaningful RUL prediction cannot be obtained during this phase. A common approach to address this issue is to exclude all training samples or relabel those above a certain RUL value to a predefined constant value (in case of C-MAPSS, typically between 120 and 130) [127], [138], [203]–[206]. However, this approach neglects variability between individual machine units.

In contrast to that, the two-step procedure of unit-based degradation detection followed by RUL prediction provides several advantages. On one hand, earlier RUL prediction is possible, provided that the specific machine shows an earlier degradation trend. On the other hand, non-meaningful RUL predictions (on healthy condition data prior to a degradation trend) can be avoided or indicated as such to the monitoring operator.

### 6.1.3 Remaining Useful Life (RUL) prediction

The RUL prediction step is based on a model, which relates the determined reduced features (condition deviation and HI) to the actual RUL value. Three different methods for this task are presented in the following sections.

#### *Polynomial Least Squares Regression*

After the degradation point is detected (see Subchapter 6.1.2), thereafter following HI samples of each sequence are used to fit a polynomial function using LS. This avoids non-

meaningful predictions on healthy conditions prior to a degradation trend and simplifies the function shape, leading to a closer fit using lower polynomial orders.

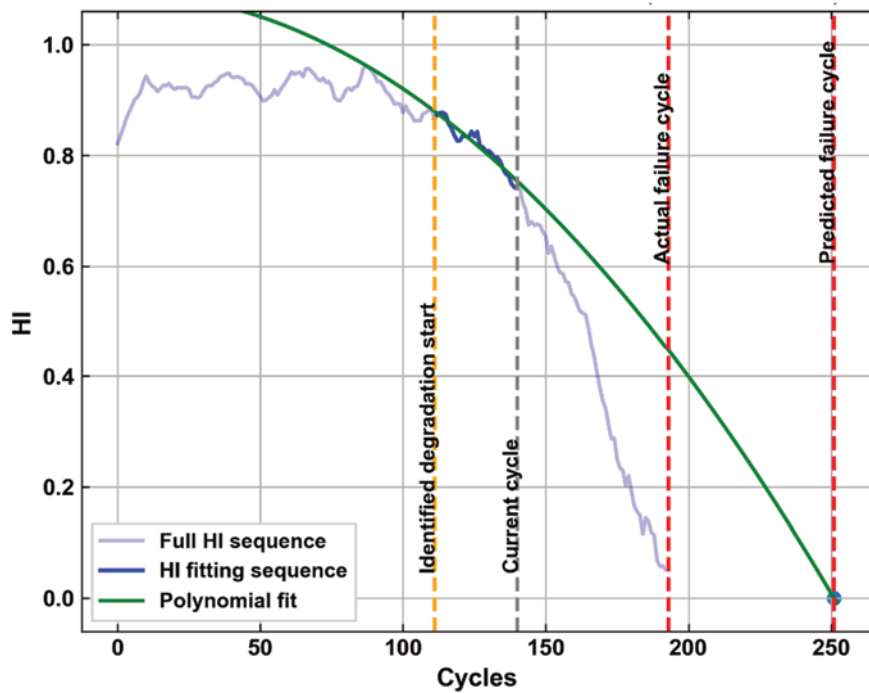


Figure 6-2. Quadratic polynomial fit for RUL prediction on an MD-based HI sequence calculated from a C-MAPSS FD001 training sequence at current cycle 140, leading to a predicted failure cycle overestimation by 58 cycles

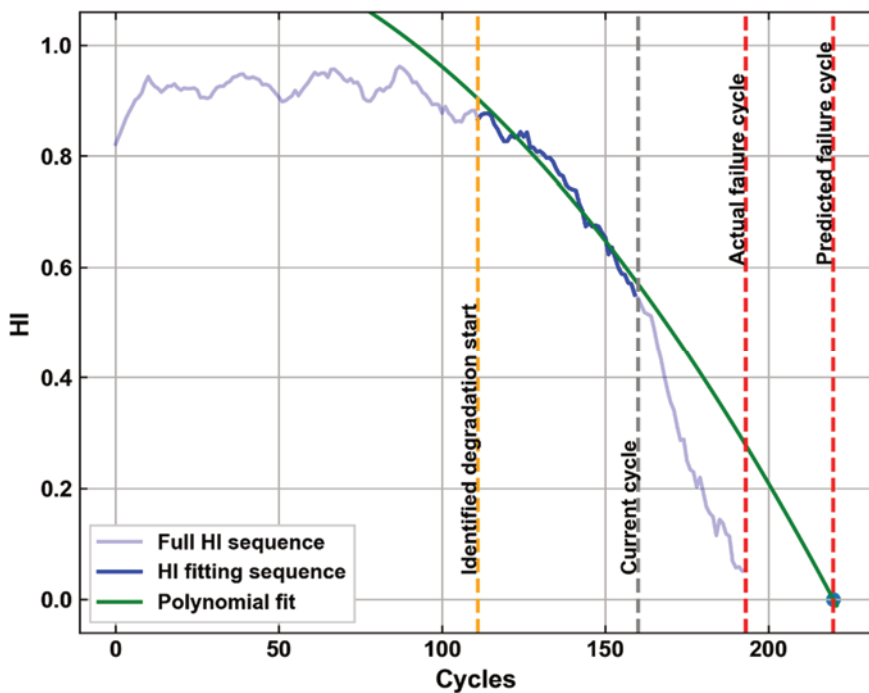


Figure 6-3. Quadratic polynomial fit for RUL prediction on an MD-based HI sequence calculated from a C-MAPSS FD001 training sequence at current cycle 160, reducing the predicted failure cycle overestimation to 27 cycles

A second order (i.e., quadratic) polynomial is fitted in this study. Figure 6-2 and Figure 6-3 show an exemplary full MD-based HI sequence (see Subchapter 6.1.2) at two different times, i.e., cycles, of prediction.

The polynomial is fitted to the data between the detected degradation start and the most recent HI observation at the current cycle  $t_c$ . Therefore, the current cycle has an impact on the resulting RUL prediction. Since more data becomes available in Figure 6-3 ( $t_c=160$ ) compared to Figure 6-2 ( $t_c=140$ ) for the polynomial fit during the progression through the operating cycles, a better fit is achieved in Figure 6-3, i.e., towards the end of the HI sequence, leading to a more accurate prediction.

The closest polynomial root at a future time value represents the predicted failure cycle  $t_{f,pred}$  of the corresponding machine. The predicted RUL is then calculated as  $RUL_{pred} = t_{f,pred} - t_c$ .

### *Support Vector Regression*

To consider time-dependency of the degradation in the SVR prediction, a lookback is introduced using an HI offset of -50 samples from the current sample as an additional input feature. Both the offset and current HI samples are fed into the SVR model to predict the RUL. As outlined in the theory Subchapter 3.3.3, the SVR produces a hyperplane, relating the input features to the predicted output RUL value. Data points from 5 run-to-failure training sequences from C-MAPSS FD001 are shown with the resulting 3D plane in Figure 6-4.

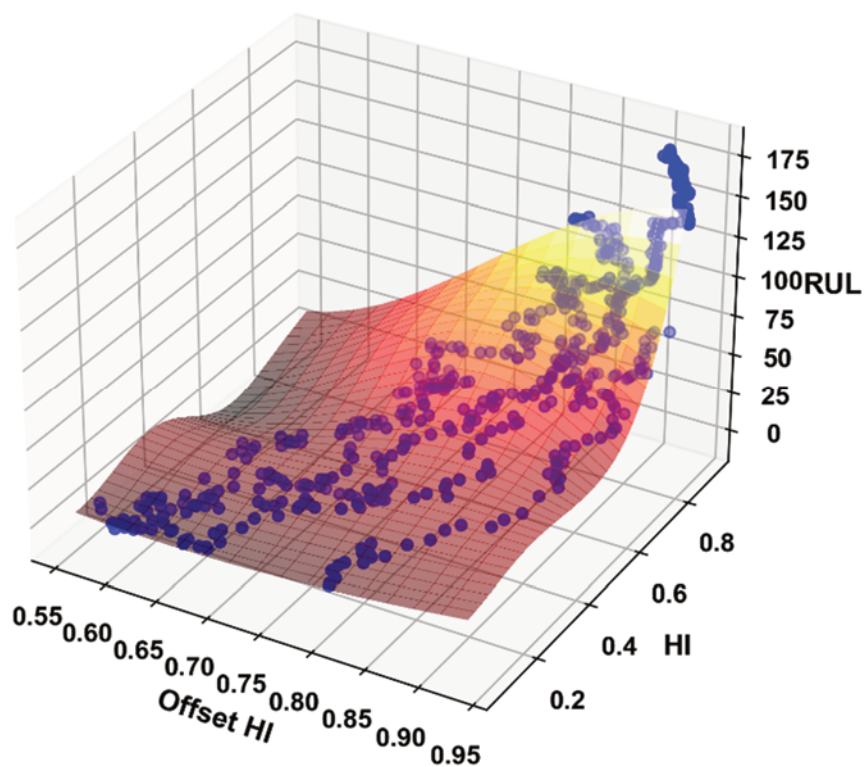


Figure 6-4. Data points of 5 complete C-MAPSS FD001 training sequences and resulting SVR plane for RUL prediction

The Radial Basis Function (RBF) is used as the SVR kernel and the regularisation parameter  $p$  and epsilon-tube parameter  $\epsilon$  are optimised as discussed later in Subchapter 6.2.1.

### *LSTM Neural Network*

An LSTM NN, as described in Subchapter 3.3.4, is a common choice for RUL prediction problems due to the LSTM's ability to incorporate time-dependency of input features into the mapping function to output the desired prediction variable. For the proposed method, three inputs are used: the condition deviations from the MD-based fault and health models (see Subchapter 6.1.1) with the resulting HI ratio (see Subchapter 6.1.2) are provided as inputs to the LSTM model for RUL prediction. The proposed method is referred to as MD-LSTM in the following.

For a baseline comparison with a more traditional approach, the raw original dataset features are used as inputs to the LSTM model, without condition deviation and HI functions. In accordance with the typical approach of existing literature [127], [138], [203]–[206], the effective prediction range is limited to a maximum RUL of 125 by relabelling earlier training data to this RUL value. For a direct comparison of the used input features' impact, this training approach is used for both the proposed MD-LSTM method and baseline LSTM method.

The feature matrix of each engine sequence is then subdivided into smaller rolling sequences of a chosen window length. These overlapping partial sequences serve as samples fed into the model. The used window length is optimised together with other model hyperparameters, incl. the number of hidden LSTM layers, as specified later in Subchapter 6.2.1. On each LSTM layer, a dropout rate of 0.2 is applied to combat overfitting.

In the following Subchapter 6.2 and Subchapter 6.3, two open datasets are presented and used to compare and validate the proposed RUL prediction method. Each dataset subchapter is structured into an introduction of the corresponding dataset, model training procedure for individual methods, and performance comparison of different methods as a function of the number of available run-to-failure training sequences.

## **6.2 Application to simulated turbofan engine degradation data**

An open dataset of turbofan engine degradation [207] was developed by NASA through simulation with the software tool C-MAPSS (Commercial Modular Aero-Propulsion System Simulation). As summarised by Table 6-2 the full dataset package consists of 4 datasets, which are referred to as FD001 - FD004 and differ by the number of operating conditions and failing engine components, i.e., fault conditions.

**Table 6-2: Main properties of the C-MAPSS datasets**

Dataset	Operating conditions	Fault conditions	Training sequences	Test sequences
FD001	1	1	100	100
FD002	6	1	260	259
FD003	1	2	100	100
FD004	6	2	249	248

Additionally, the datasets differ by the number of test sequences and the maximum available number of run-to-failure training sequences, each of which covers the life span of an aircraft engine starting from an unknown state of initial wear. The provided test sequences are cut short before the failure event at RUL values, which should be estimated by RUL prediction. Each dataset sample represents one flight-cycle and includes 26 multivariate features. As all training sequences reach  $RUL=0$ , the target RUL labels are calculated from the flight cycle vector  $t$  as  $RUL=abs(\max(t)-t)$  and subsequently added to the available set of features. All dataset features are listed in Table 6-3.

**Table 6-3: Features of the C-MAPSS dataset**

Feature ID	Description
0	Engine number
1	Time (cycles)
2	Operational setting 1
3	Operational setting 2
4	Operational setting 3
5	Sensor 1
6	Sensor 2
...	...
25	Sensor 21
26	RUL (target output variable)

A colour-coded correlation matrix of all features in C-MAPSS FD001 is shown in Figure 6-5. Some features consist of constant values without a meaningful representation of correlation values and are therefore omitted from Figure 6-5 as blank entries. Certain features show a clear positive or negative correlation with the target RUL variable (feature 26), which indicates their potential value in RUL prediction. However, the correlation matrix also shows that several features are highly correlated among each other, potentially providing redundant information.

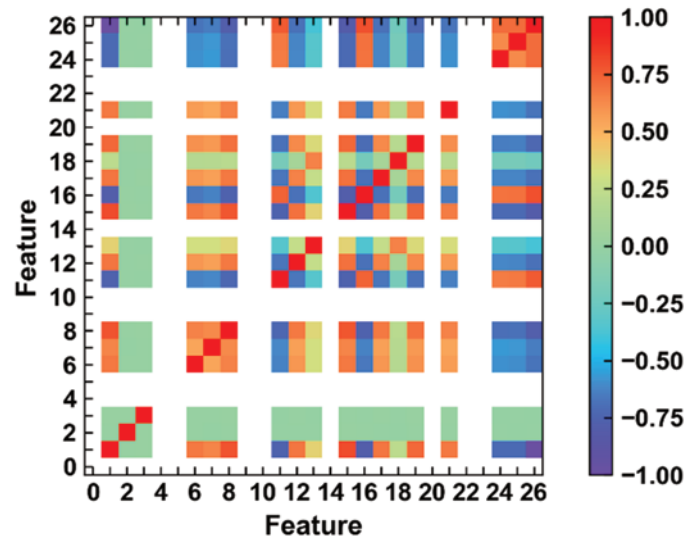


Figure 6-5: Correlation matrix of C-MAPSS FD001 training dataset features, constant features displayed in white

### 6.2.1 Model training

In case of the healthy and faulty condition deviation models (HI generation stage), the first and last  $n_m$  samples (representing health and fault condition data, respectively) are extracted from each sequence of the full training set and used for training. Prior to this, the following approach is used for datasets FD002 and FD004 to consider the impact of different operating conditions on degradation trend signatures: The samples of each training set are first subdivided into 6 subsets based on the 6 operating conditions (see Table 6-2). A separate condition deviation model is then calculated and used for each distinct operating condition.

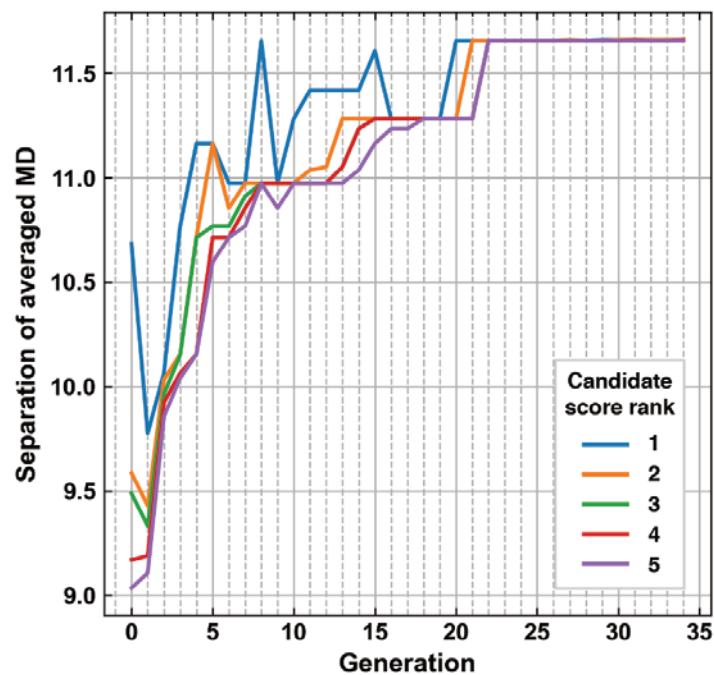
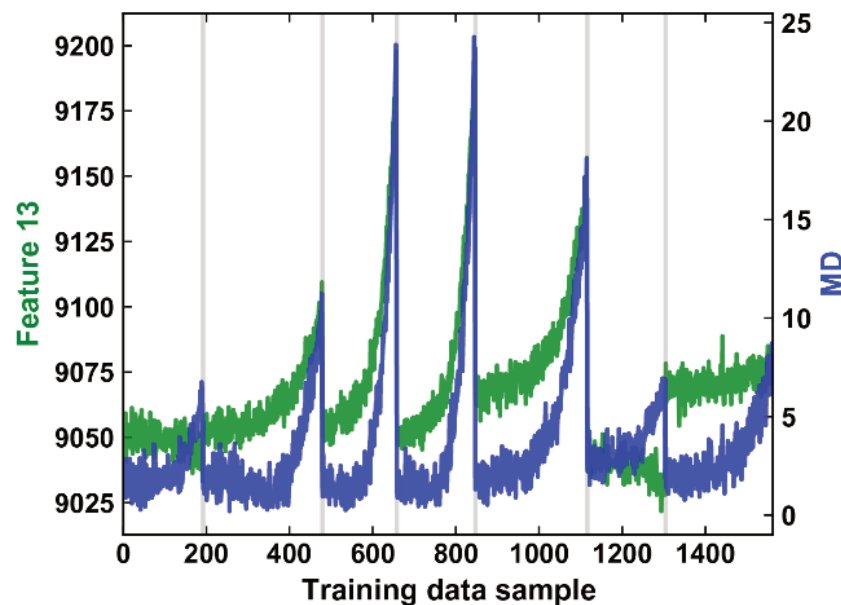


Figure 6-6: MD-based GA optimisation of 5 best scoring feature subset candidates per generation, C-MAPSS FD001 training data



According to the procedure outlined in Subchapter 6.1.1, a GA is executed on C-MAPSS FD001 for 100 generations. As seen in Figure 6-6, the GA converges to a maximum average MD separation after approximately 30 generations, providing a final list of highest scoring feature subsets. As a result of the optimisation, the features 13, 15, 19 of the C-MAPSS dataset are chosen in this study for MD calculation. While separate optimisations for the FD002 - FD004 datasets and for individual operating conditions could lead to further performance improvements, the stated MD input features identified from FD001 are used throughout all C-MAPSS dataset for consistency and were found to provide satisfactory results.

Figure 6-7 shows the MD applied to 7 exemplary run-to-failure training sequences. The merit of the MD becomes visible compared to one of the relevant raw input features: in the two rightmost sequences, the raw feature 13 does not show a clear degradation trend towards the respective failure cycle, whereas the MD of the multivariate input from features 13, 15, 19 shows a monotonic increase on average with a maximum MD at the lifecycle end.



**Figure 6-7: Progression of raw feature 13 and MD (combining features 13, 15, 19) for 7 complete C-MAPSS FD001 training sequences**

For the initial model training and search of optimised hyperparameters of the prediction model, a reduced set of  $N_{tr,red}=20$  (out of  $N_{tr}=100$ ) complete run-to-failure sequences is assumed to be available.

A randomised grid search of hyperparameters is performed by subdividing the training data of the  $N_{tr,red}=20$  complete sequences into 18 training sequences and 2 validation sequences for scoring of hyperparameter sets. Each evaluated set of hyperparameters is repeatedly trained and scored 10 times, whereafter the mean validation scores are used to determine the final hyperparameter values.

To reduce the dimensionality of the hyperparameter search space and computing time, a subset of hyperparameters is optimised for each of the implemented models (Table 6-1). That is, related hyperparameter optimisation results from a preceding method optimisation are retained for other methods. This is illustrated with Figure 6-8, where each method (represented by a block) lists its optimised hyperparameters. Arrows indicate which hyperparameter results are taken over from one optimisation to a different one. The specific search space per hyperparameter and final optimised values are given in Table 6-4. As the hyperparameters shown in the last column of Table 6-4 are used for the implemented models, these values simultaneously provide the definition of the used NN structures, which are also visualised in Figure 6-9.

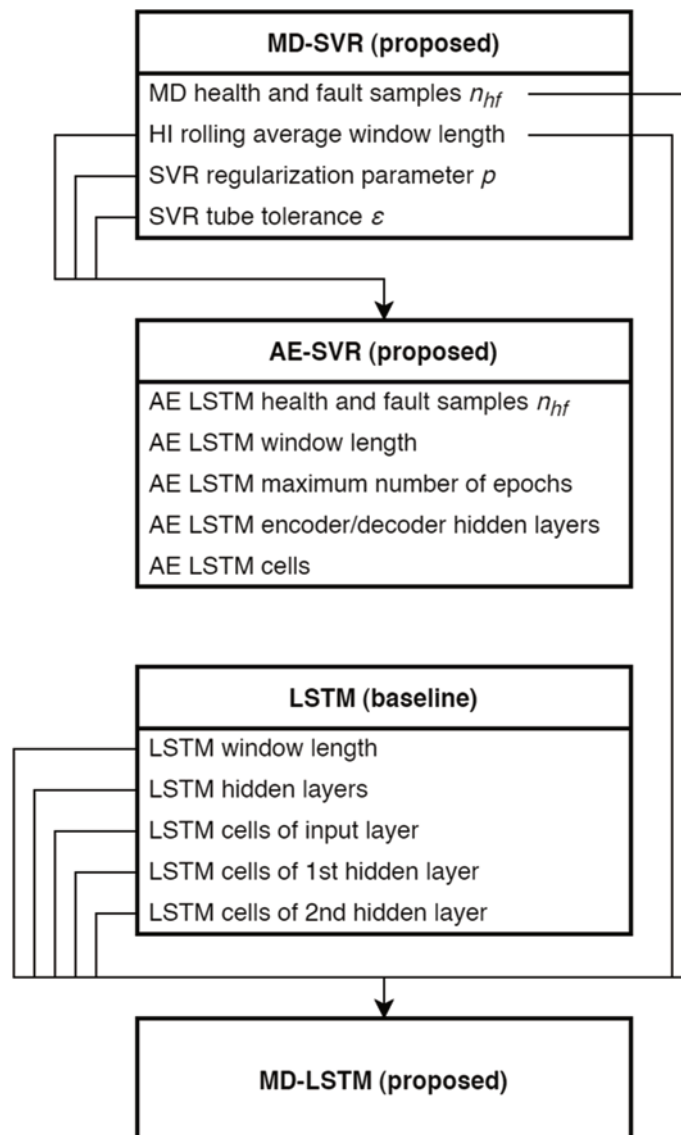


**Figure 6-8: Usage of optimised hyperparameters between implemented methods**

As shown in Figure 6-8, the proposed MD-LSTM method combines optimised parameters for HI-generation from MD-SVR and the LSTM hyperparameters optimised for the baseline LSTM method. By this approach, the direct impact of the proposed feature set reduction on

LSTM model performance with limited data can be observed. It should be noted that this procedure favours the baseline LSTM method, because a hyperparameter optimisation specifically for the proposed MD-LSTM method could further improve its performance. For the introduced HI-generation step (in methods MD-SVR, AE-SVR, MD-LSTM),  $n_{hf}$  first and last samples from each sequence of the full training set are extracted and used.

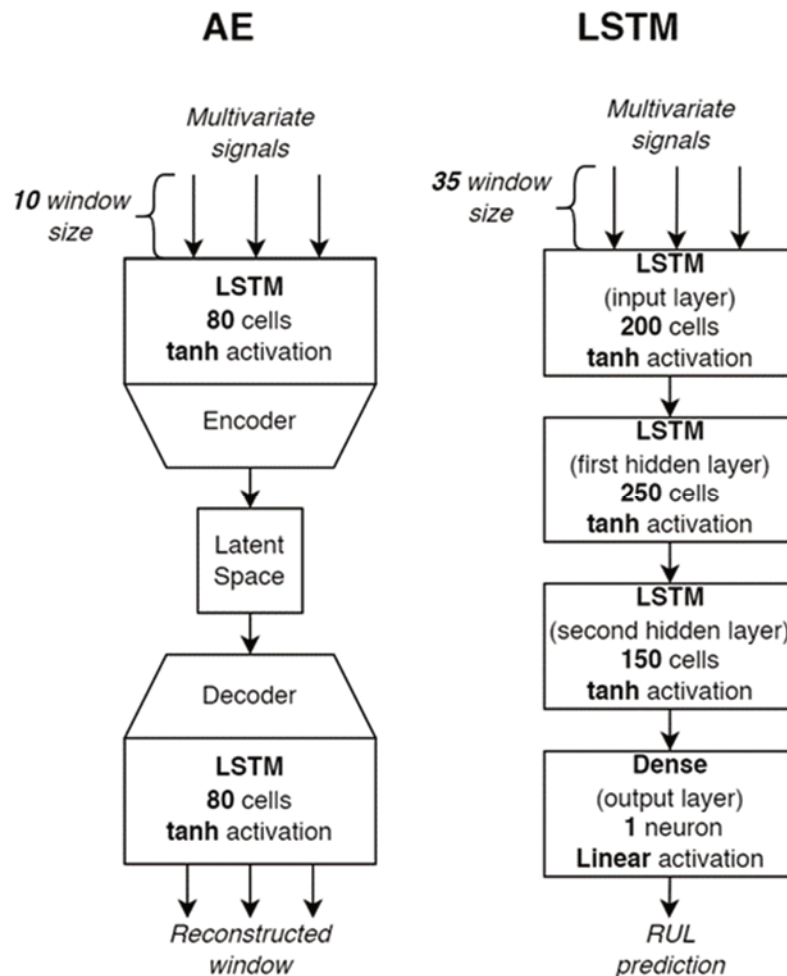


Figure 6-9: Used NN structures: AE condition deviation model (left); LSTM RUL prediction model (right)

Table 6-4: C-MAPSS FD001 training hyperparameter search space and final optimisation values for implemented RUL prediction methods

Parameter	Search space	Final (used) value
<b>MD-SVR (proposed)</b>		
MD health and fault samples $n_{hf}$	{5, 15, 25, 35, 45}	5
HI rolling average window length	{5, 10, 15, 20}	10
SVR regularization parameter $C$	{50, 150, 250, 350, 450, 550}	150
SVR tube tolerance $\epsilon$	{10, 30, 50, 70}	10

Parameter	Search space	Final (used) value
<b>AE-SVR (proposed)</b>		
AE LSTM health and fault samples $n_{hf}$	{25, 50, 75}	25
AE LSTM window length	{5, 10, 15, 20}	10
AE LSTM maximum number of epochs	{10, 110, 210, 310}	10
AE LSTM encoder/decoder hidden layers	{0, 1, 2}	0
AE LSTM cells	{5, 20, 35, 50, 65, 80, 95, 110}	80
<b>LSTM (baseline)</b>		
LSTM window length	{5, 20, 35, 50, 65}	35
LSTM hidden layers	{0, 1, 2, 3, 4}	2
LSTM cells of input layer	{50, 100, 150, 200, 250, 300}	200
LSTM cells of 1st hidden layer	{50, 100, 150, 200, 250, 300}	250
LSTM cells of 2nd hidden layer	{50, 100, 150, 200, 250, 300}	150

### 6.2.2 Health Index (HI) calculation

Corresponding to the procedure detailed in Subchapter 6.1.1, HI progressions are created by MD on one hand and by LSTM AE on the other hand. Results from both methods are presented and discussed below.

#### *Mahalanobis Distance-based HI*

Using Equation (3.48), MD-based models for healthy condition deviation  $d_h$  and faulty condition deviation  $d_f$  are conditioned. The output MD of both models for a complete run-to-failure validation sequence is plotted in Figure 6-10.

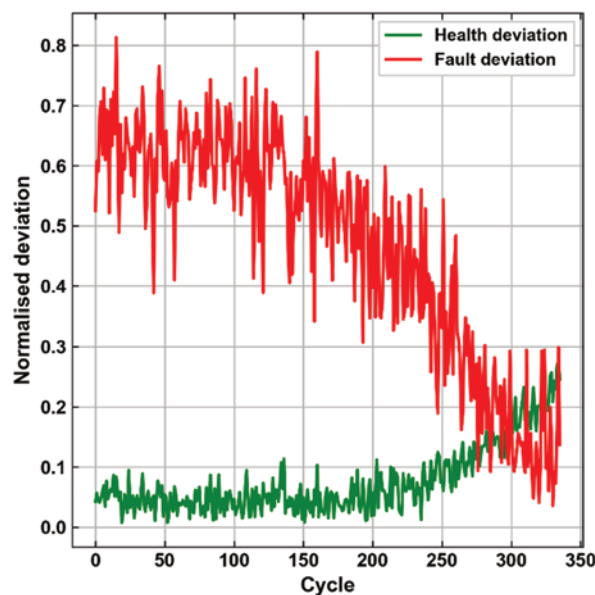


Figure 6-10: Overlaid MD-based health deviation  $d_h$  and fault deviation  $d_f$  for an exemplary run-to-failure sequence

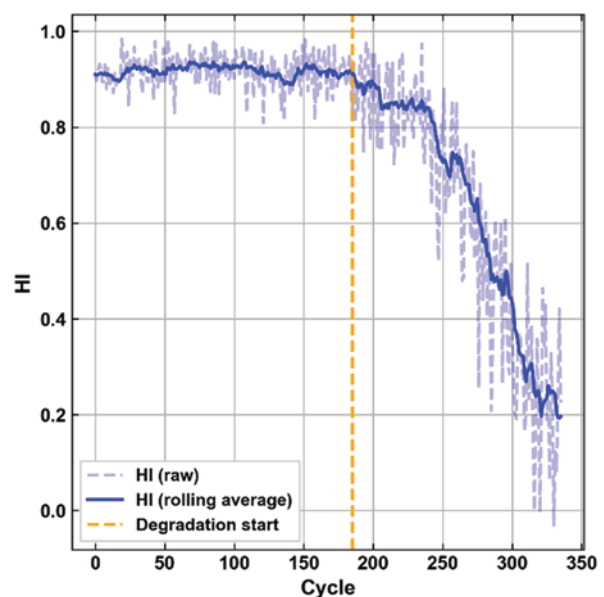
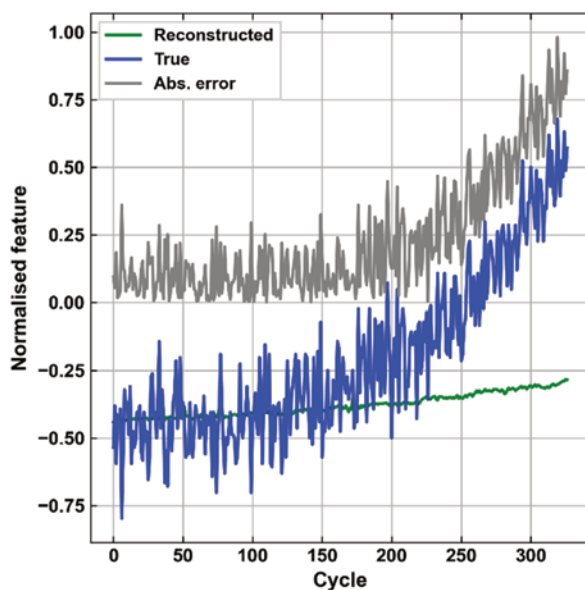


Figure 6-11: HI resulting from MD-based health and fault deviations in Figure 6-10 after scaling and rolling average

As per the procedure described in Subchapter 6.1.2, the HI shown in Figure 6-11 is determined from the condition deviation functions shown in Figure 6-10. In addition, the flight cycle with a starting degradation is determined according to Subchapter 6.1.2 and is also highlighted in Figure 6-11.

### *LSTM Autoencoder-based HI*

Outputs of the AE-based condition deviation fault and health models are shown in Figure 6-12 and Figure 6-13, respectively. In addition to early stopping on model convergence, the number of epochs is used as an optimised hyperparameter (as shown under AE-SVR in Table 6-4). It was observed that limiting the number of epochs aids in preventing the adaptation of the model to unseen data, as the purpose of the AE is to provide an accurate reconstruction of the reference (healthy or faulty) condition only. Both figures show that the AE reconstruction aligns closely to the reference state, while producing a higher reconstruction error at the opposing state. As a result, the reconstruction error increases towards the faulty condition in Figure 6-12 (health model) and decreases towards the faulty condition in Figure 6-13 (fault model), as desired.



**Figure 6-12: AE reconstruction for healthy condition data of feature 13**

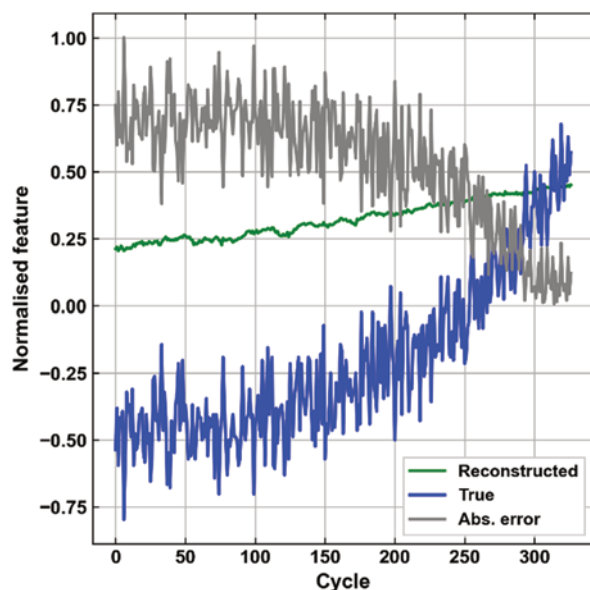


**Figure 6-13: AE reconstruction for faulty condition data of feature 13**

The resulting AE-based health and fault deviation functions are overlaid in Figure 6-14 and the corresponding HI is shown in Figure 6-15. Compared to the MD-based deviation and HI functions, the AE-based alternatives show a clearer distinction between the healthy and faulty conditions. This is visible in the clearer crossing of the AE-based condition deviation functions (comparing Figure 6-10 and Figure 6-14) and a lower AE-based HI value at the final degradation cycle (comparing Figure 6-11 and Figure 6-15). However, it is important to note that the AE-based method requires substantially more computing resources compared to the MD-based counterpart.

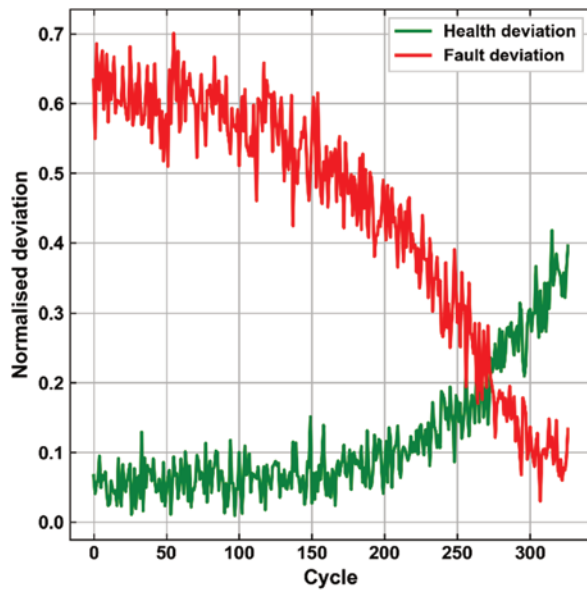


**Figure 6-14: Overlaid AE-based health deviation  $d_h$  and fault deviation  $d_f$  for an exemplary run-to-failure sequence**

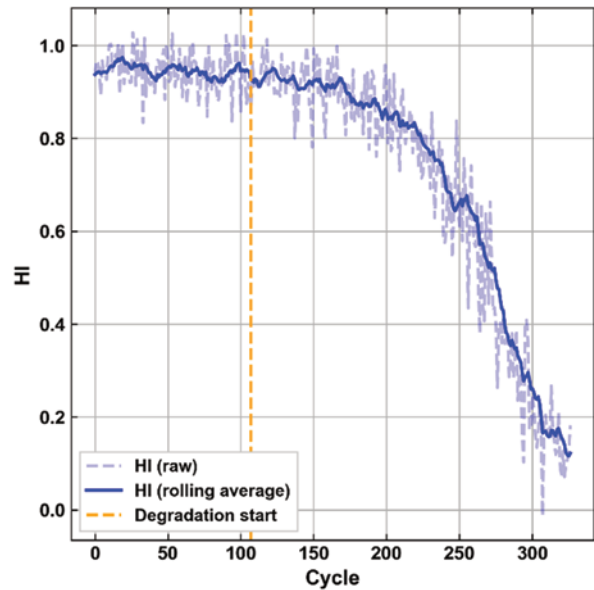


**Figure 6-15: HI resulting from AE-based health and fault deviations in Figure 6-14 after scaling and rolling average**

### 6.2.3 RUL prediction results

Based on condition deviations and HI presented in the previous section, RUL prediction is performed with various methods presented previously in Subchapter 6.1.3. The implemented method configurations are individually listed in Table 6-1.

It is reasonable to focus on the pairing of the SVR methods (MD-SVR and AE-SVR) for one comparison, and the LSTM-based prediction methods (baseline LSTM and proposed MD-LSTM) for another comparison. The reason for this is that both SVR methods only differ in the used HI-generation approach (either AE or MD-based) and therefore allow a direct comparison of those HI-generation methods regarding their impact on RUL prediction performance. On the other hand, the LSTM RUL prediction methods give insight into the difference of the proposed features (condition deviation and HI) in comparison to a direct prediction from raw dataset features. The LS prediction method (MD-QPoly) is treated separately, as it is the only presented method, which does not require any training sequences and is independent thereof.

Figure 6-16 and Figure 6-17 show RUL prediction results on 5 validation sequences from training with a reduced number of  $N_{tr,red}=20$  sequences, for MD-SVR and AE-SVR, respectively. The merits of degradation detection become apparent as it provides an additional binary assessment of each machine's condition and indicates whether a meaningful RUL prediction can be expected. The determined pre-degradation (healthy) machine condition is highlighted with green in both graphs. Except for the second engine sequence in Figure 6-16 and Figure 6-17, the AE-SVR shows a similar or earlier degradation

detection compared to MD-SVR. This indicates a clearer degradation trend in favour of the AE-based HI method, similar to the observations discussed in the previous section.

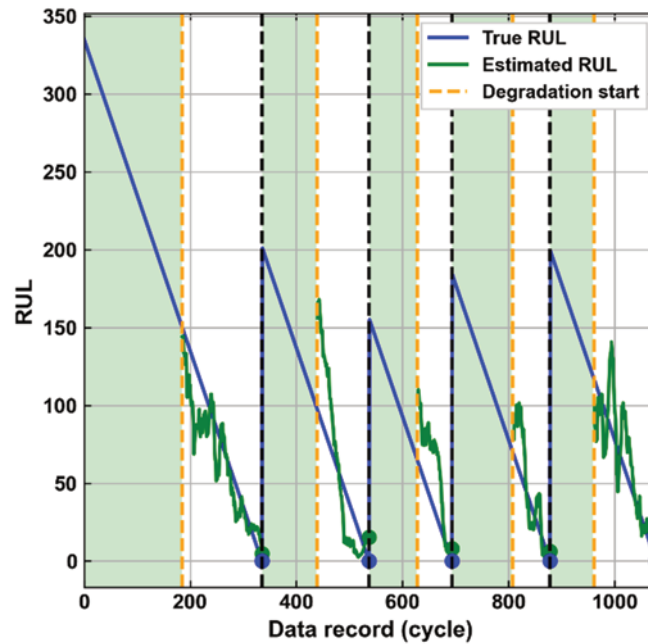


Figure 6-16: MD-SVR predictions of RUL based on 20 training sequences for 5 validation sequences (i.e., engines)

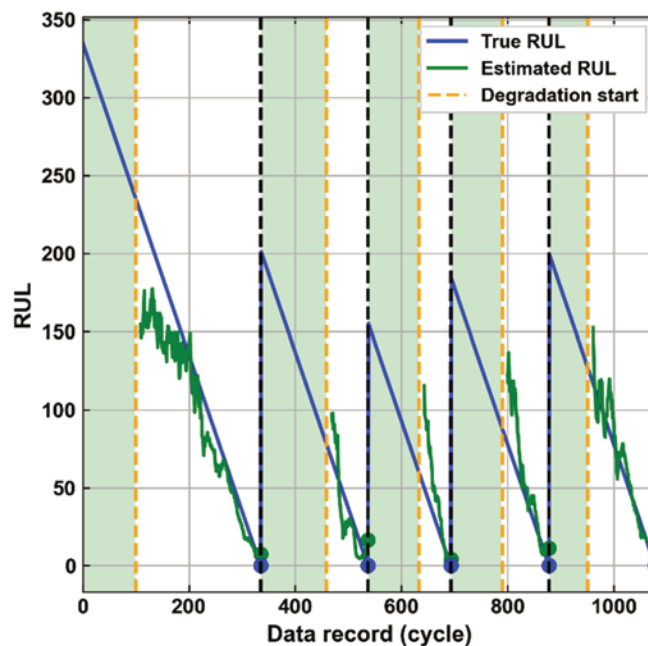


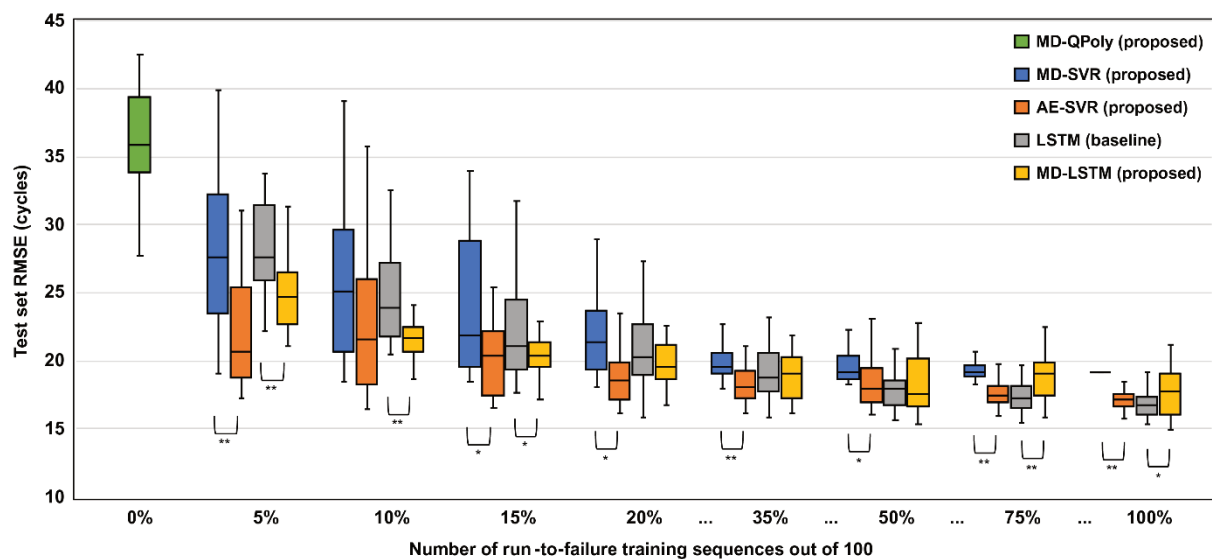
Figure 6-17: AE-SVR predictions of RUL based on 20 training sequences for 5 validation sequences (i.e., engines)

Figure 6-18 compares the RUL prediction performance on the C-MAPSS FD001 dataset for all methods listed in Table 6-1. To estimate the impact of a limited number of training sequences, comparisons are conducted for an increasing number of training sequences  $N_{tr,red}$  plotted on the horizontal axis of Figure 6-18 as a percentage of the full training set with  $N_{tr}=100$ . The root mean square error (RMSE) is calculated according to Equation (6.5)

between the predicted final RUL values  $RUL_{pred}$  and true final RUL values  $RUL_{true}$  of the test dataset with  $N_{te}=100$  sequences.

$$RMSE = \sqrt{\frac{\sum_{i=1}^{N_{te}} (RUL_{pred,i} - RUL_{true,i})^2}{N_{te}}} \quad (6.5)$$

For each box-and-whisker entry in Figure 6-18, the specified method (indicated by the legend) is trained 30 times with the specified number of training sequences (indicated by the horizontal axis) drawn randomly from the full set of  $N_{tr}=100$  training sequences. Each of the trained models is evaluated on the full set of  $N_{te}=100$  test sequences, providing one RMSE value. The repetition provides a more reliable performance assessment and leads to 30 RMSE test scores per test condition, which make up each individual entry in Figure 6-18. It should be also noted that increasing intervals of values on the horizontal axis are used, i.e., percentage point intervals of 5 between 0% - 20%; 15 between 20% - 50%; 25 between 50% - 100%. This is done for a more detailed comparison in the low data range, because the RMSE values shows a higher gradient in this range (left part of Figure 6-18) compared to results from high data usage (right part of Figure 6-18).



**Figure 6-18: Prediction performance on the C-MAPSS FD001 test dataset over 30 runs per each box and whisker (RMSE, lower is better) of MD-QPoly, MD-SVR, AE-SVR, LSTM, MD-LSTM (\* $p < 0.05$ , \*\* $p < 0.01$ )**

P-values between both SVR methods (AE-SVR, MD-SVR) and between both LSTM methods (LSTM, MD-LSTM) are indicated in Figure 6-18. Low p-values below 0.05 are obtained on most comparisons, suggesting statistical significance. However, several result distributions (e.g., MD-SVR, AE-SVR, LSTM at  $N_{tr,red}=15$  training sequences) are skewed, as can be seen by the unsymmetrical inter-quartile ranges and whiskers. As such, the underlying sample distributions deviate from the normal distribution and p-values should be interpreted with care in those cases.



The mostly observed positive skewness (with a long tail towards higher RMSE values) is likely related to the influence of a few irregular outlier sequences in the full training set (with  $N_{tr}=100$  sequences), which are randomly drawn into the reduced subset of training sequences (e.g., with  $N_{tr,red}=15$  sequences). Affected training runs result in a higher test RMSE. As the number of training sequences is increased (towards the right side of Figure 6-18), the proportion, and thus impact, of an individual outlier sequence is mitigated by remaining training sequences. Therefore, the resulting RMSE scores reach a rather symmetrical distribution starting from  $N_{tr,red}=35$  training sequences as shown by Figure 6-18.

A general trend in Figure 6-18 shows that the RUL prediction methods benefit from greater numbers of training sequences both in terms of increased average prediction accuracies as well as a reduced variance of the prediction results. This highlights the importance of the presented methodology, employing 30 repeated training/testing runs per experiment. This is especially relevant at training cases with reduced numbers of used training sequences, which is the focus of this paper. However, Figure 6-18 also shows that even at full (i.e., 100%) training set utilisation, there is still a significant prediction variance on the NN-based compared methods. At the same time, most existing publications using the C MAPSS dataset (e.g., [120], [203], [208]) report performance based on a single test evaluation only and thus do not account for the variance due to the stochastic nature of the presented NN-based methods. This omits relevant information on prediction consistency and likely leads to biased results since a best run might be reported, which is not representative of an average expected performance in real-world applications.

MD-QPoly is the only method that functions independently from training sequences and only requires fault and health condition data for conditioning of the MD-based fault and health models. This feature allows MD-QPoly to be utilised without any training data containing run-to-failure sequences but also leads to a wide dispersion of the RMSE range and highest overall RMSE values compared to other methods with available training sequences in Figure 6-18. This method can be further extended by expert knowledge or run-to-failure training data by employing the constrained LS method. For example, the range of estimated polynomial coefficients from run-to-failure training sequences can be stored to set coefficient boundaries for polynomial fits of HI sequences during the test or operational stage. The RUL is then predicted on unseen (i.e., test) data with the function constraints determined from training data.

At the cost of substantially higher computing demand, the previous observations in favour of AE-based HI are also reflected in the RUL prediction performance, as AE-SVR shows consistently lower overall RMSE values compared to MD-SVR in Figure 6-18. Nevertheless, MD-based condition and HI features used in the MD-LSTM method led to improved prediction performance of the proposed MD-LSTM method at limited numbers of training

sequences below 20% compared to the baseline LSTM approach. This demonstrates that the proposed method improves the generalisation ability of the LSTM-based prediction when a vastly limited number of training sequences is available. In addition, Figure 6-18 shows that the proposed MD-LSTM method also results in the lowest RMSE variance in the low range of training sequences among the compared methods.

At a larger training set above 75%, the LSTM model can take advantage of the higher complexity of raw features, outperforming MD-LSTM by a small margin and performing similar to AE-SVR. These results suggest that LSTM-based RUL prediction would likely further benefit from AE-based HI generation. Such a method (i.e., AE-LSTM) should be considered for future work, as it has the potential to further outperform both MD-LSTM and the baseline LSTM method across the full range of reduced training sequences.

Figure 6-19 shows the training durations for individual methods over increasing percentages of used training sequences on the horizontal axis. On the vertical axis, average durations (over 30 runs) are provided in percentages relative to the traditional approach, which is represented by the baseline LSTM method utilising the full training set with 100% of training sequences. Model training is performed on an AMD Ryzen Threadripper 3990X 64-core CPU with 256 GB RAM. NN-based methods (AE-SVR, LSTM, MD-LSTM) are trained on an NVIDIA RTX A6000 GPU with a batch size of 512 until model convergence (i.e., until no improvement in validation loss over the past 10 epochs is gained).

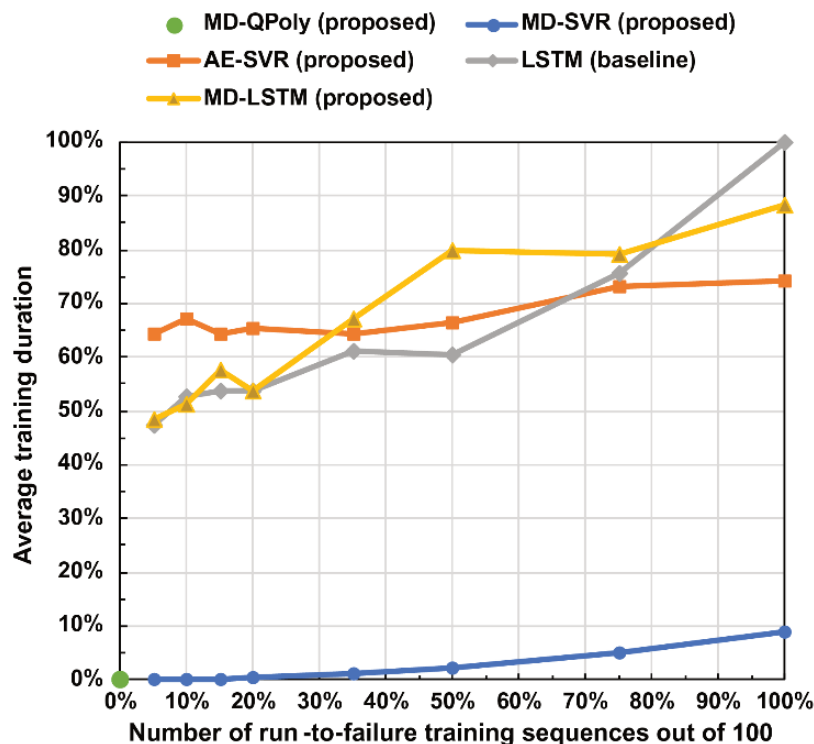
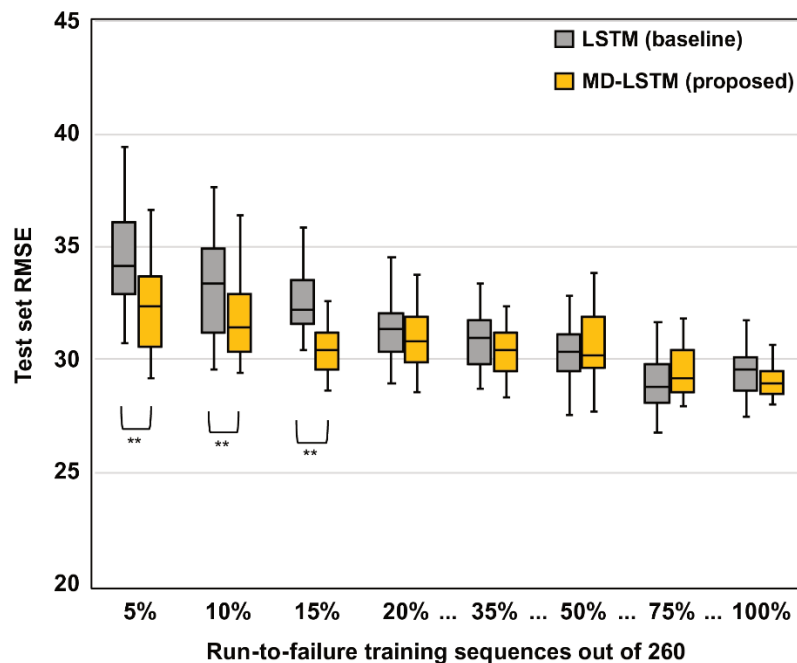


Figure 6-19: Average training durations over 30 runs per each data point of compared methods (C-MAPSS FD001), relative to LSTM (baseline) at full training set size of 100%

A reduction of the number of training sequences is shown to have a clear impact, reducing training durations across all methods. NN training accounts for the majority of the observed time requirements, while the conditioning of MD and SVR models are substantially less demanding. As such, MD-SVR provides a 91% training time reduction for the full training set at a 14% increase in average RUL RMSE compared to the LSTM baseline. Despite a reduced number of NN inputs in MD-LSTM compared to LSTM, both methods show a similar progression of training time. The AE-SVR duration curve has a lower slope compared to LSTM and MD-LSTM due to the different NN architecture inherent to the AE NN model.

Concluding from the comparison on the C-MAPSS FD001 dataset, the proposed MD-LSTM method can be considered as the overall most beneficial for RUL prediction with a limited number of training sequences as it provides the lowest overall RMSE scores (along with AE-SVR) and lowest RMSE variance in the presented case. At the same time, the training time demand of MD-LSTM represents a compromise between NN-free methods (MD-QPoly and MD-SVR) and the AE-SVR method.

Based on this result, the proposed MD-LSTM method is compared further on the datasets C-MAPSS FD002 – FD004 in Figure 6-20 – Figure 6-22. Supplementary to the box and whisker plots of the RUL prediction results, the average and standard deviation values of prediction RMSE from all C-MAPSS datasets FD001 – FD004 are summarised in numerical form in Table 6-5.



**Figure 6-20: Prediction performance on the C-MAPSS FD002 test dataset over 30 runs per each box and whisker (RMSE, lower is better) of LSTM and MD-LSTM (\*\*p<0.01)**

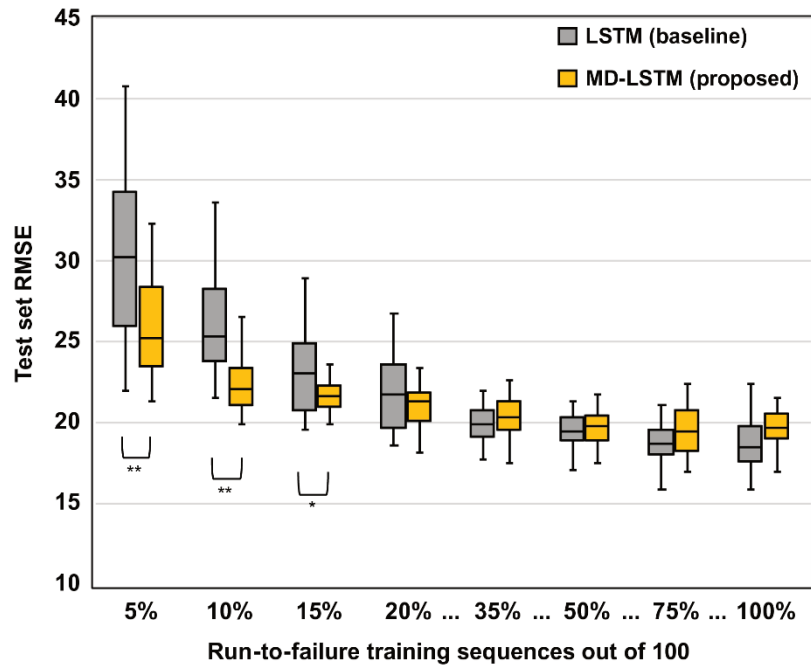


Figure 6-21: Prediction performance on the C-MAPSS FD003 test dataset over 30 runs per each box and whisker (RMSE, lower is better) of LSTM and MD-LSTM (\* $p < 0.05$ , \*\* $p < 0.01$ )

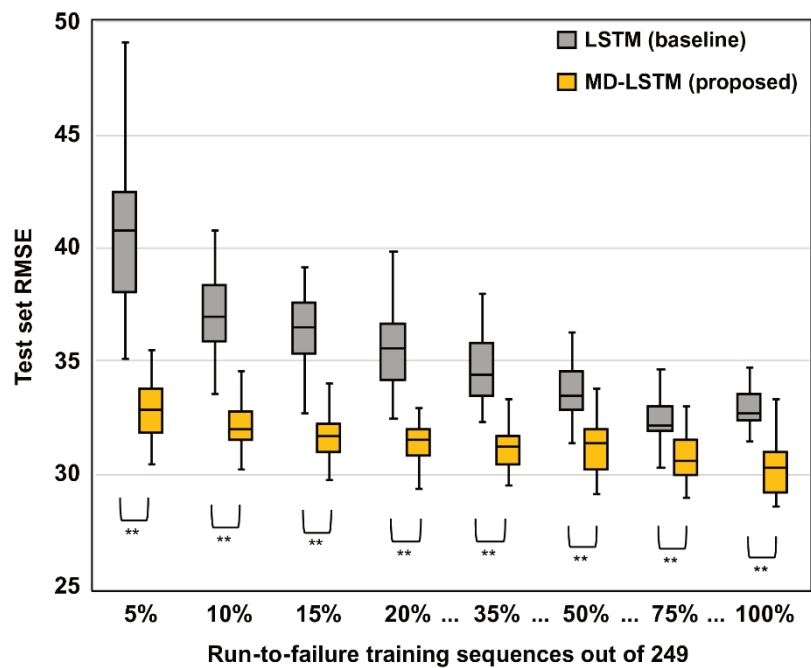


Figure 6-22: Prediction performance on the C-MAPSS FD004 test dataset over 30 runs per each box and whisker (RMSE, lower is better) of LSTM and MD-LSTM (\*\* $p < 0.01$ )

**Table 6-5: Prediction performance on C-MAPSS test datasets (RMSE, lower is better)**

Method	Relative number of run-to-failure training sequences																
	5%		10%		15%		20%		35%		50%		75%		100%		
	Avg.	Std.	Avg.	Std.	Avg.	Std.	Avg.	Std.	Avg.	Std.	Avg.	Std.	Avg.	Std.	Avg.	Std.	
<b>C-MAPSS FD001</b>																	
MD-QPoly (proposed)	36.1*	3.9*															
MD-SVR (proposed)	28.3	6.2	26.5	7.6	26.5	10.2	22.0	3.3	20.9	4.5	20.0	3.1	19.3	<b>0.6</b>	19.2	<b>&lt;0.1</b>	
AE-SVR (proposed)	<b>22.2</b>	4.3	23.8	7.5	22.2	7.2	<b>19.6</b>	4.8	<b>18.3</b>	<b>1.6</b>	18.5	1.9	17.7	1.3	17.2	0.6	
LSTM (baseline)	28.1	3.5	24.6	3.1	22.0	3.3	20.8	2.8	19.0	1.8	<b>17.8</b>	<b>1.3</b>	<b>17.4</b>	1.1	<b>16.8</b>	1.0	
MD-LSTM (proposed)	24.9	<b>2.7</b>	<b>21.7</b>	<b>2.1</b>	<b>20.5</b>	<b>1.7</b>	19.7	<b>1.5</b>	19.1	1.9	18.2	2.1	18.8	1.6	17.7	1.6	
<b>C-MAPSS FD002</b>																	
LSTM (baseline)	34.4	2.1	33.2	2.1	32.7	1.6	31.4	<b>1.3</b>	31.0	1.5	<b>30.3</b>	<b>1.3</b>	<b>29.1</b>	<b>1.3</b>	29.5	1.1	
MD-LSTM (proposed)	<b>32.2</b>	<b>1.9</b>	<b>31.8</b>	<b>1.9</b>	<b>30.6</b>	<b>1.4</b>	<b>30.9</b>	1.6	<b>30.4</b>	<b>1.2</b>	31.0	2.8	29.6	1.4	<b>29.2</b>	<b>1.0</b>	
<b>C-MAPSS FD003</b>																	
LSTM (baseline)	30.1	4.9	26.0	3.1	23.3	2.9	21.6	2.1	<b>19.9</b>	<b>1.1</b>	<b>19.5</b>	1.2	<b>18.7</b>	<b>1.2</b>	<b>18.6</b>	1.7	
MD-LSTM (proposed)	<b>25.7</b>	<b>2.9</b>	<b>22.7</b>	<b>2.3</b>	<b>21.8</b>	<b>1.2</b>	<b>21.2</b>	<b>1.6</b>	20.3	1.3	19.7	<b>1.1</b>	19.5	1.5	19.6	<b>1.2</b>	
<b>C-MAPSS FD004</b>																	
LSTM (baseline)	40.6	3.1	37.1	1.6	36.4	1.7	35.7	2.1	34.9	1.8	33.7	<b>1.3</b>	32.5	<b>0.9</b>	33.0	<b>1.1</b>	
MD-LSTM (proposed)	<b>32.8</b>	<b>1.3</b>	<b>32.1</b>	<b>1.2</b>	<b>31.7</b>	<b>0.9</b>	<b>31.5</b>	<b>1.2</b>	<b>31.2</b>	<b>0.9</b>	<b>31.5</b>	1.8	<b>30.8</b>	1.3	<b>30.3</b>	1.2	

Avg.: average; Std.: standard deviation; \*Results independent of the number of used training sequences

It is visible that the overall performance of both the baseline LSTM and the proposed MD-LSTM methods is decreased when applied to C MAPSS FD002 – FD004 (leading to higher RMSE values in Figure 6-20 – Figure 6-22) compared to the FD001 dataset (Figure 6-18). This is explained by a higher data complexity due to an increased number of operating and/or failure conditions in the FD002 – FD004 datasets as shown in Table 6-2. Hence, FD004 shows the highest absolute RMSE values both for the baseline and proposed RUL prediction methods in comparison to datasets FD001 – FD003 (see Table 6-5). At the same time, FD004 shows the clearest separation between the performance scores of the baseline LSTM and the proposed MD-LSTM methods in Figure 6-22.

As in previous cases, the greatest difference in favour of the proposed MD-LSTM method is visible at highly reduced numbers of available training sequences in Figure 6-22. This is also reflected by the values in Table 6-5, where MD-LSTM shows an average RMSE of 32.8 at a

training sequence reduction to 5%. This corresponds to a 19.2% prediction improvement in relation to the baseline LSTM method with an average RMSE of 40.6. Additionally, MD-LSTM outperforms the baseline LSTM method at the whole range of reduced FD004 training sequences, including the full training set, i.e., at 100% of used training sequences).

This indicates that the presented approach significantly reduces data complexity of the raw FD004 dataset features while preserving relevant degradation information, which is represented by the generated condition deviation and HI functions. It should be also noted, that, while the full FD004 training set (with  $N_{tr}=249$ ) is larger than e.g., FD001 (with  $N_{tr}=100$ ), it has the lowest ratio of training sequences to operating and fault conditions (i.e.,  $249/8 = 31.125$ ) among all C-MAPSS datasets. Hence, the baseline LSTM method would likely benefit from a greater number of FD004 training sequences beyond 100%. This is also supported by the rather linear trend of decreasing RMSE values displayed by LSTM (baseline) in Figure 6-22, which seems further away from reaching convergence at 100% compared to other datasets in Figure 6-18, Figure 6-20, and Figure 6-21. At the same time, the issue of great training data demand is alleviated by the proposed MD-LSTM method, providing improved generalisability, which explains the clear performance increase especially on FD004 (Figure 6-22) in favour of MD-LSTM.

### 6.3 Application to vibration data of bearing degradation

A bearing degradation dataset [80] was presented in frame of the IEEE PHM 2012 Data Challenge. The dataset was generated by the FEMTO-ST institute utilising a mechanical test rig "PROGNOSTIA". 3 load conditions were applied by the test rig, promoting an accelerated degradation of the test bearings. A total of 6 run-to-failure sequences are provided in the training set and 11 sequences in the test set. Degradation sequences of the test set are truncated to assess the RUL prediction performance of models based on the estimation error at the end of those sequences. The dataset contains accelerometer readings, with time series of acceleration measured in the vertical and horizontal axes of the test bearings. Additional temperature measurements are provided in the dataset as well, but only for 4 out of 6 training sequences and 7 out of 11 test sequences. For consistency, only the accelerometer channels are considered in this work. The accelerometer measurements are provided in segments of 1/10s duration, each obtained in intervals of 10s at a sampling frequency of 25.6kHz.

**Table 6-6: Features of the FEMTO dataset**

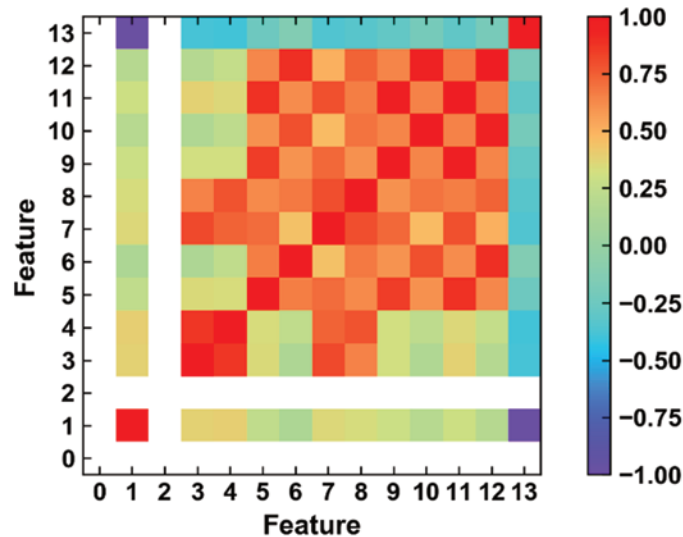
Feat. ID	Description	Equation
0	Run number	N/A
1	Time (minutes)	N/A
2	Operating condition number	N/A
3	RMS (H)	$\sqrt{\frac{1}{N} \sum_{i=1}^N x_i^2},$ <p>where <math>x</math> is the data sample and <math>N</math> is the number of samples in the processed window</p>
4	RMS (V)	
5	Kurtosis (H)	$\sqrt{\frac{\sum_{i=1}^N (x_i - \bar{x})^4}{(N-1)\sigma^4}},$ <p>where <math>\bar{x}</math> is the mean and <math>\sigma</math> is the standard deviation</p>
6	Kurtosis (V)	
7	Absolute maximum (H)	$\max( x )$
8	Absolute maximum (V)	
9	Crest factor (H)	$\frac{\max( x )}{\sqrt{\frac{1}{N} \sum_{i=1}^N x_i^2}}$
10	Crest factor (V)	
11	Impulse factor (H)	$\frac{\max( x )}{\frac{1}{N} \sum_{i=1}^N  x_i }$
12	Impulse factor (V)	
13	RUL (target output variable)	$ t - \max(t) ,$

where  $t$  is the time vector

N/A: Not applicable; H: Horizontal direction accelerometer; V: Vertical direction accelerometer

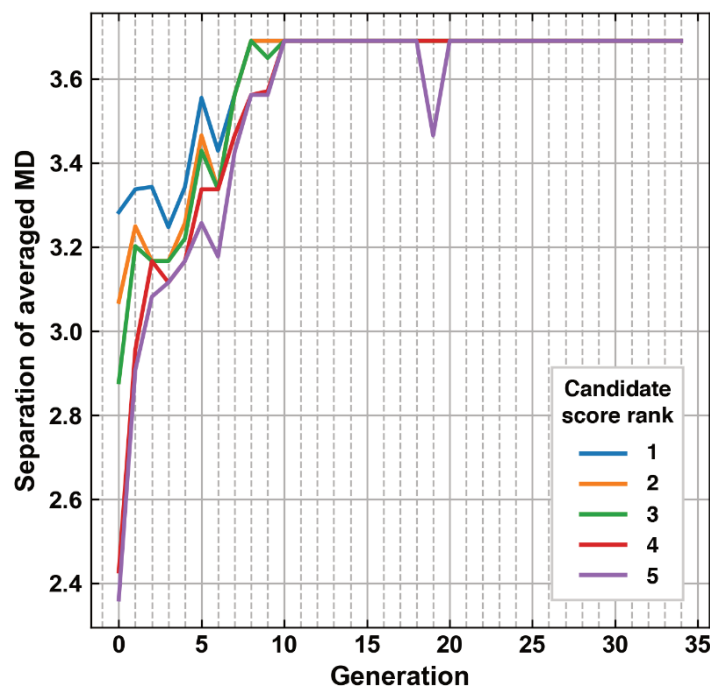
Statistical features, commonly used for vibration condition monitoring [209], are calculated from both acceleration signals and arranged into a feature matrix. One segment of continuous 1/10s signals is thereby processed to a single statistical value sample. The resulting feature set is described in Table 6-6 and serves as the foundation of the following experiments. The dataset contains run-to-failure sequences, each obtained at one of 3 operating conditions. The operating condition is denoted by a number 1 (4000 N, 1800 rpm), 2 (4200 N, 1650 rpm), or 3 (5000 N, 1500 rpm), which is included as feature 2 as shown in Table 6-6.

Figure 6-23 shows the correlation matrix of all features of the training set. Feature 2 (the condition number) shows a blank field, due to its constant value per run-to-failure sequence. Most features show a high positive correlation with each other. As expected, the RUL value (feature 13) is negatively correlated to the sequence time (feature 1).



**Figure 6-23: Correlation matrix of FEMTO training dataset features, constant features displayed in white**

Analogous to the procedure in the C-MAPSS dataset, features of the FEMTO dataset are processed by GA optimisation (see Subchapter 6.1.1) to determine a feature subset providing maximum MD separation. Convergence of the 5 best scoring subsets per generation is shown in Figure 6-24. The features 4, 7, 8, 9, 12 are determined by this procedure and chosen as inputs for the MD calculation.



**Figure 6-24: MD-based GA optimisation of 5 best scoring feature subset candidates per generation, FEMTO training data**

Figure 6-25 shows a plot of both the acceleration RMS in vertical direction (feature 4) and an overlay of the MD-based health condition deviation. The full training set of 6 run-to-failure sequences is covered by Figure 6-25. While the resemblance of feature 4 is visible in the MD, the MD shows a clearer slope between the start and end of each training sequence,



which is a desired outcome. Figure 6-25 also illustrates challenging characteristics of the dataset: The shown sequences have a wide range of inconsistent durations, feature values and noise levels.

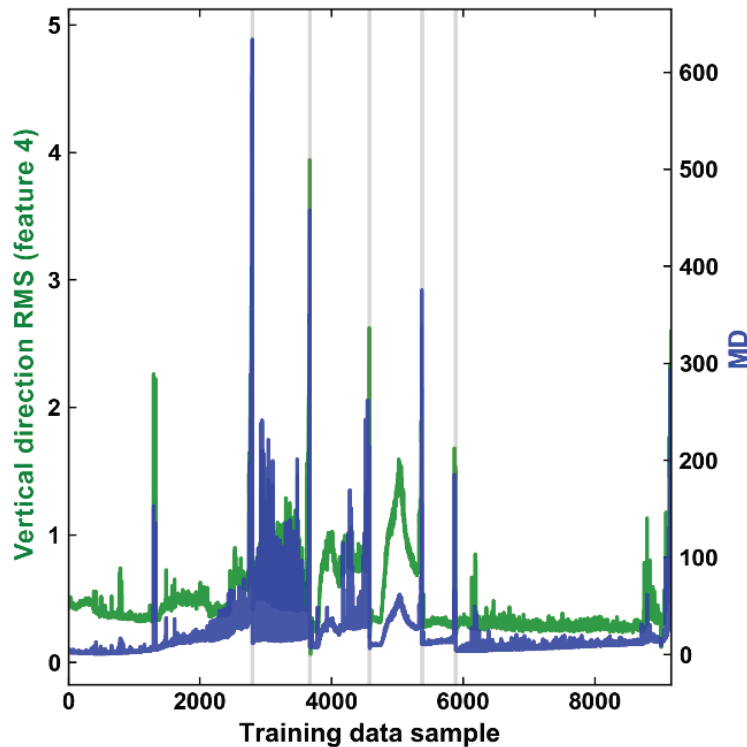


**Figure 6-25: Progression of raw feature 4 and MD (combining features 4, 7, 8, 9, 12) for 6 complete training sequences**

From the observations on the C-MAPSS results, it was found that the MD-LSTM method combines satisfying characteristics in terms of prediction variance, and prediction accuracy at reduced numbers of training sequences. The MD-LSTM method is therefore applied to the FEMTO dataset and compared to the baseline LSTM method in the following.

A similar procedure to the one in Subchapter 6.2 is used for the hyperparameter search. Table 6-7 shows the hyperparameter search space, which is optimised by a random grid search. A split of 4 training and 2 validation sequences is used for the hyperparameter optimisation. The final hyperparameter values are determined from the best validation score of the baseline LSTM method.

**Table 6-7: FEMTO training hyperparameter search space and final optimisation values for LSTM**

Parameter	Search space	Final value
LSTM window length	{5, 35, 65, 95, 125}	95
LSTM hidden layers	{0, 1, 2, 3, 4}	2
LSTM cells of input layer	{50, 100, 150, 200, 250, 300}	250
LSTM cells of 1st hidden layer	{50, 100, 150, 200, 250, 300}	200
LSTM cells of 2nd hidden layer	{50, 100, 150, 200, 250, 300}	250

Afterwards, the final model architecture is applied to both the baseline LSTM and the proposed MD-LSTM methods. Model training is performed on both methods with an increasing number of training sequences (between 1 and 6) and each time evaluated on the full test set with 30 repetitions per model training and evaluation run.

Similar to the C-MAPSS results (e.g., Figure 6-18), an overall trend of decreasing RUL prediction RMSE is visible over an increasing number of used training sequences in Figure 6-26. However, the differences between the compared the baseline LSTM and the proposed MD-LSTM methods are less clear here. The results show similar performance with a wider RUL dispersion of MD-LSTM up to 4 out of 6 (i.e., 66.7%) training sequences. At 6 (i.e., 100%) training sequences, however, MD-LSTM outperforms the baseline LSTM method as shown in Figure 6-26 and Table 6-8.

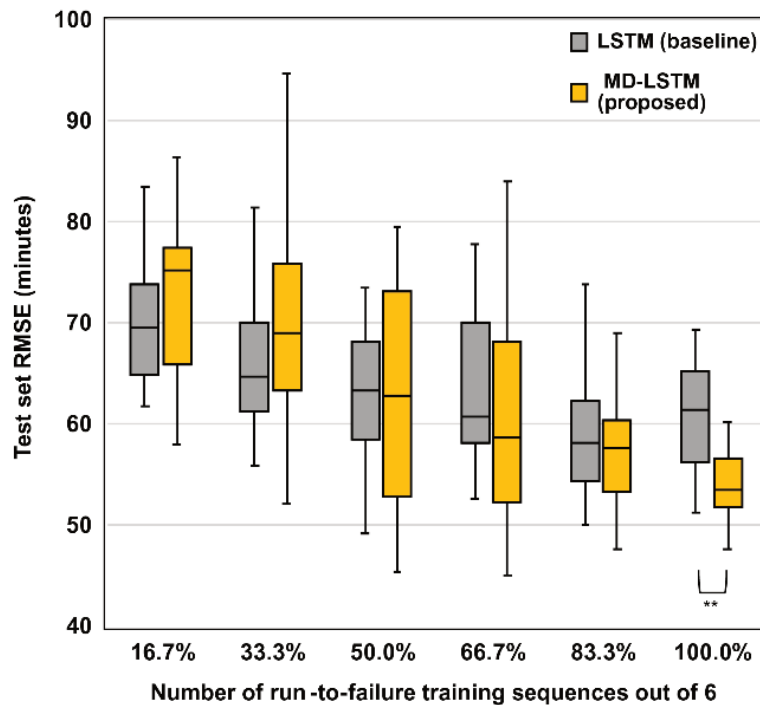


Figure 6-26: Prediction performance on the FEMTO test dataset over 30 runs per each box and whisker (RMSE, lower is better) of LSTM, MD-LSTM (\*\* $p < 0.01$ )

Table 6-8: Prediction performance on the FEMTO test dataset (RMSE, lower is better)

Method	Relative number of run-to-failure training sequences											
	16.7%		33.3%		50.0%		66.7%		83.3%		100.0%	
	Avg.	Std.	Avg.	Std.	Avg.	Std.	Avg.	Std.	Avg.	Std.	Avg.	Std.
LSTM (baseline)	70.4	5.9	66.1	6.6	63.2	7.6	63.7	7.0	58.7	5.5	60.5	5.2
MD-LSTM (proposed)	73.7	10.2	69.6	8.8	63.4	10.8	60.5	9.4	58.0	6.9	54.6	5.2

Avg.: average; Std.: standard deviation

Several factors likely contribute to a less conclusive method comparison by the FEMTO dataset compared to C-MAPSS. In comparison to the C-MAPSS dataset, a smaller range of possible training sequences (6 in contrast to 100) is available in the FEMTO dataset for the evaluation of an increasing training sequence count. The number of used features in the FEMTO dataset (Table 6-6) is smaller than the number of features in the C-MAPSS dataset (Table 6-3), so a greater ratio of feature reduction is achieved by HI generation on the C-MAPSS dataset. Moreover, the C-MAPSS dataset is based on 21 sensors, likely encapsulating more relevant information for RUL estimation compared to FEMTO features, which stem from only two physical quantities (vibration readings in two directions). This is also supported by Figure 6-23, which shows that most derived features of the FEMTO dataset are mutually correlated. Introduction of additional features and tuning of pre-processing parameters (such as a window size beyond 1/10s) could provide a more informative dataset for RUL prediction.

## 6.4 Conclusions

This paper introduced a methodology for RUL prediction utilising a limited number of run-to-failure sequences, as well as binary health and fault condition data. The approach can be considered a feature reduction and data fusion method, aimed at improving generalisation where few training sequences or limited computing resources are available.

Several configurations of the method were implemented and compared to the baseline LSTM method. Using the open C-MAPSS FD001 turbofan degradation dataset, it was shown that AE-based HI-generation provides a higher RUL prediction accuracy compared to MD-based HI generation, albeit at a substantially higher computing effort. Conversely, it was found that the MD-based approach is especially suited for conditions where quick model training is required, or computing power is limited. Using the full training set, the training time reduction by MD-SVR is substantial at 8.9% of the LSTM baseline method's training duration (Figure 6-19). When the number of training sequences is reduced to 5%, the training duration of both the baseline LSTM method and the proposed MD-LSTM is 47%-48%, while the MD-SVR training duration reduces further to 0.04%. This work therefore has implications on considerations for green AI [201], contributing to the development of more efficient and environmentally friendly algorithms. The choice between the application of the proposed method through either the AE or MD-based approach therefore depends on the prioritisation between prediction accuracy or computing time requirements. Nevertheless, the introduced MD-based LSTM prediction (MD-LSTM) was able to consistently outperform the baseline LSTM approach for training cases using under 20% of training sequences of the full training set (Figure 6-18). For example, when comparing the prediction RMSE at a reduction of the available number of training sequences to 5%, the greatest impact was seen on the C-MAPSS FD004 dataset, where the proposed method showed an average prediction

improvement by 19.2% relative to the baseline method. The proposed method therefore demonstrated an improved generalisation from a limited number of training sequences, addressing the research gap found in Subchapter 2.4.

A further RUL prediction approach based on LS regression was presented. This method is applicable when no training sequences are available and has the lowest computing demand. On the flipside, it assumes a polynomial (e.g., quadratic) progression of the HI and showed the highest prediction error among the compared methods.

An additional comparison of baseline LSTM and MD-LSTM on the FEMTO dataset of bearing degradation was less conclusive. The results showed largely similar prediction performance with greater variance in the MD-LSTM results but also partially improved prediction accuracy in favour of MD-LSTM. The reasons are likely related to characteristics of the dataset, such as its initially limited size and a high level of inconsistency between training sequences.

From the obtained findings and literature, the following areas are highlighted as current challenges and future work in the research of prognostics and condition monitoring for rotating machinery.

Due to the demonstrated potential of the MD-based HI generation, it is suggested to further develop this method to approach the performance of AE-based HI generation while retaining the computational efficiency of the MD-based method. This can be approached by an optimisation of MD features towards a consistent HI range in addition to a maximisation of MD separation. Conversely, AE-based HI generation offers the potential to encapsulate complex nonlinear relationships of the processed condition data and may be effective for data fusion of complex signal patterns. The reconstruction ability of AE for various signal types and signal properties (such as periodic and statistical characteristics) should be therefore further investigated. At the same time, techniques to maximise the reconstruction error for untrained data should be developed.

It was shown across all methods that the reduction of training sequences leads to a wider spread of prediction performance. In other words, after the random sampling of limited training sequences, part of the training runs resulted in a competitive model performance, whereas models from different samples of training sequences underperformed. Methods for advance assessment of training data (regarding data distribution and quality) should be therefore researched. The desired consequence is optimised training efficiency, leading to minimised data and energy consumption.

A segmentation of machine degradation into different sections has the potential to improve the prediction performance. In case of the polynomial LS regression method, this can be incorporated by fitting a suitable polynomial (in terms of polynomial order and constraints) to the identified degradation phase. A common but inflexible approach in NN-based prediction,

---

is to limit the training range of RUL values. Expanding on that, separate models for different prediction ranges (e.g., for long-term, mid-term and short-term predictions) should be considered. The presented HI-generation approach in combination with clustering can contribute to automatically identify relevant degradation phases for further development in this area.

## 7 Conclusions and future work

This chapter concludes the thesis by a summary of the main findings and contributions, reflecting on the foundation of the state of the art set out in Chapter 2. Finally, main directions of future work in the covered research area are recommended.

### 7.1 Conclusions

This thesis dealt with the structural-mechanical evaluation of rotating machinery under two perspectives. The first area of concern addressed in this thesis is OMA of rotating machinery. This domain is, on one hand, challenging due to characteristics of the unmeasured excitation force and, on the other hand, relevant due to the importance of operational modal parameters in the design, test, and validation of developed mechanical systems and components. The second main branch of rotating machinery evaluation targeted by this thesis is RUL prediction, which falls under the field of predictive condition monitoring. Current state-of-the-art ML methods show notable achievements in this field, which has great potential for reducing cost while increasing safety across the life span of rotating machinery by means such as early fault detection and optimised predictive maintenance procedures.

Subchapter 2.1 and Subchapter 2.2 provided the foundation for subsequent thesis contributions by evaluating the state of the art for OMA of rotating machinery based on existing literature. Subchapter 2.3 evaluated openly available vibration datasets with respect to their usability for OMA and OBMA applications. The summarised dataset characteristics facilitate the selection of most suitable datasets for future research. Finally, Subchapter 2.4 compared the current state of the art in condition monitoring utilising modal parameters on one hand and more generic data-driven approaches based on ML on the other hand.

The first open simulation dataset of rotating machinery vibration under acceleration conditions was introduced in Chapter 4. It addresses the lack of datasets suitable for OMA, and thus contributes to further research and development of OMA, OBMA, and other signal processing methods under acceleration/deceleration runs. The dataset offers itself as a foundation for benchmark and comparison studies of existing and future methods. This is additionally facilitated by publication of the simulation source code, allowing for adaptation and extension of the dataset for future research. The lack of research regarding the impact of different operating conditions on method performance is addressed by the introduced dataset with simulations of three varied and quantified parameters, providing a foundation for future parametric studies.

The parametric comparison study in Chapter 5 performed an evaluation of OMA, OBMA, and the proposed AOBMA method. A unique feature of this study is the systematic evaluation of variations in the excitation force in terms of relative harmonic and random force composition

(harmonic ratio), finding an impact of this parameter on the number of modes identified by OBMA and AOBMA. The study was the first to find that OBMA and AOBMA outperformed OMA in mode shape estimation by achieving significantly higher MACX and MPC values. In the comparison across 9 common identified modes, the average MACX value of AOBMA and OBMA exceeded 0.99, while the baseline OMA was limited to an average of 0.86.

The proposed AOBMA method presented in Chapter 5 addresses several limitations of OBMA, such as ambiguous results, which can vary substantially depending on the processed machine order. AOBMA addresses this limitation by detrending and weighted averaging of tracked machine orders, resulting in a single set of resulting modal parameters, which cover the combined range of the processed orders. This facilitates the analysis procedure and provides clearer results. This was shown in the parametric simulation study, where AOBMA was able to correctly identify the greatest number of modes at high harmonic ratios. At a harmonic ratio of 0.8, for example, it accurately identified an average of 11.9 modes per estimation, while OBMA and baseline OMA followed with 9.5 and 9 modes on average, respectively. AOBMA also reduces the amount of uncorrelated noise in the averaged order signals, leading to improved accuracy of modal estimates compared to OBMA. As a result, AOBMA showed a lower mean absolute relative error of 0.03 for damping ratio estimations across the compared modes of the simulation study while OBMA provided an error value of 0.32, depending on the processed order.

A novel data-efficient methodology for RUL prediction was presented in Chapter 6. A major limitation of current ML-based methods for RUL prediction is that a large number of run-to-failure sequences are typically required as training data. To address this issue, the proposed methodology incorporates data from discrete machine conditions (i.e., binary conditions of healthy and faulty states), which are more feasible to obtain compared to large amounts of progressive degradation data in the form of run-to-failure sequences. The proposed approach provides feature reduction and achieves improved generalisation. This is evidenced by lower prediction errors compared to the baseline method when the original number of run-to-failure training sequences are reduced below 20% of the original dataset. For example, a reduction of training sequences to 5% led to a prediction accuracy improvement by 11.4% compared to the baseline LSTM method. In addition, the potential for reducing computational time of individual methods depending on the reduction of training data was evaluated. The proposed MD-SVR method was proved to be particularly resource-saving with an average training duration of 8.9% compared to the baseline LSTM method when the full training set is utilised. These findings allow to prioritise methods based on available data as well as computational or energy resources. The latter factor has increasing relevance due to considerations for environmental impact and the emerging field of green AI.

## 7.2 Recommendations for future work

As the dataset proposed in Chapter 4 is suitable to serve as a foundation for benchmark and comparison studies of OMA methods, such future work is encouraged to promote reproducibility and comparability of research. The varied operational parameters included in the simulation dataset shall furthermore be used in future work to gain deeper insight into the performance of methods under a variety of operating conditions.

In this regard, the comparison study accompanying the proposed AOBMA method in Chapter 5 utilised one of the three varied simulation parameters from the dataset, namely the varied harmonic ratio of the excitation amplitude. Therefore, it would be beneficial to apply the remaining introduced parameters (i.e., varied measurement noise levels and machine acceleration rates) to the AOBMA method as well as other current and future methods. While AOBMA contributes to an improved performance and usability of OBMA, the limitation of overestimated damping ratios and the difficulty in identifying close modes compared to general OMA remains. Since this is due to the distorted order-spectra, future modal models accounting for these distortions and post-processing methods for correction of distorted order-spectra would address this issue and are suggested for future research.

Future research in RUL prediction (and condition monitoring in general) should consider contextual data to distinguish between actual fault information of the monitored component and independent external factors, such as potential changes in environmental conditions. OMA can be used to provide supplementary context information as it is suited to assess global structural changes, which are subject to operating and environmental influence, and large-scale degradation, in turn influencing the response of localised components. For future methods, it is suggested to combine modal parameters and ML approaches based on raw data to account for both global and the local machine conditions. This has the potential to increase the reliability and accuracy of the developed condition monitoring systems.



## References

- [1] M. L. Adams, *Rotating Machinery Vibration: From Vibration to Troubleshooting*, 2nd ed. CRC Press, 2009.
- [2] S.-K. Au, *Operational Modal Analysis: Modeling, Bayesian Inference, Uncertainty Laws*. Liverpool: Springer, 2017.
- [3] R. Brincker, C. Ventura, and P. Andersen, "Why output-only modal testing is a desirable tool for a wide range of practical applications," *Proceedings of the International Modal Analysis Conference (IMAC)*, vol. 265, 2003.
- [4] M. Batel, "Operational Modal Analysis - Another Way of Doing Modal Testing," *Sound & Vibration*, vol. 36, no. 8, pp. 22–27, 2002.
- [5] B. Peeters and G. De Roeck, "Stochastic System Identification for Operational Modal Analysis: A Review," *Journal of Dynamic Systems, Measurement, and Control*, vol. 123, no. 4, pp. 659–667, 2001.
- [6] G. Busca, A. Datteo, M. Paksoy, C. Pozzuoli, C. Segato, and M. Vanali, "Experimental vs Operational Modal Analysis: A Flyover Test Case," in *Proceedings of the 33rd IMAC: Dynamics of Civil Structures*, 2015, vol. 77, pp. 365–377.
- [7] N.-J. Jacobsen, "Separating Structural Modes and Harmonic Components in Operational Modal Analysis," in *Proceedings of the International Modal Analysis Conference (IMAC)*, 2006, vol. 5, pp. 2335–2342.
- [8] W. Weijtjens, R. Shirzadeh, G. De Sitter, and C. Devriendt, "Classifying resonant frequencies and damping values of an offshore wind turbine on a monopile foundation for different operational conditions," *IET Renewable Power Generation*, vol. 8, no. 4, pp. 433–441, 2014.
- [9] P. Mohanty and D. J. Rixen, "Operational modal analysis in the presence of harmonic excitation," *Journal of Sound and Vibration*, vol. 270, no. 1–2, pp. 93–109, Feb. 2004.
- [10] Rolls-Royce Holdings plc, "Rolls-Royce in final build phase for world's largest aero-engine technology demonstrator," *Rolls-Royce press releases*, 2022. [Online]. Available: <https://www.rolls-royce.com/media/press-releases/2022/18-07-2022-rr-in-final-build-phase-for-worlds-largest-aero-engine-technology-demonstrator.aspx>. [Accessed: 29-Aug-2022].
- [11] J. W. Connolly, J. T. Csanky, and A. Chicatelliz, "Advanced control considerations for turbofan engine design," in *52nd AIAA/SAE/ASEE Joint Propulsion Conference*, 2016, pp. 1–18.
- [12] A. J. Volponi, "Gas turbine engine health management: Past, present, and future trends," *Journal of Engineering for Gas Turbines and Power*, vol. 136, no. 5, pp. 1–20,

- 2014.
- [13] IATA Maintenance Cost Technical Group, "Airline Maintenance Cost Executive Commentary, Edition 2019: An Exclusive Benchmark Analysis (FY2018 data)," 2019.
- [14] D. Budeanu and C. Markou, "From Aircraft Health Monitoring to Aircraft Health Management: White Paper on AHM," 2022.
- [15] G. Sternharz and T. Kalganova, "Current Methods for Operational Modal Analysis of Rotating Machinery and Prospects of Machine Learning," in *Proceedings of the 38th IMAC: Rotating Machinery, Optical Methods & Scanning LDV Methods, 2020*, vol. 6, pp. 155–163.
- [16] G. Sternharz, C. Mares, and T. Kalganova, "Performance of order-based modal analysis for operational rotating hardware considering excitations composed of various harmonic and random amplitudes," in *Proceedings of ISMA 2020 - International Conference on Noise and Vibration Engineering, 2020*, pp. 1465–1479.
- [17] G. Sternharz, T. Kalganova, C. Mares, and M. Meyeringh, "Comparative performance assessment of methods for operational modal analysis during transient order excitation," *Mechanical Systems and Signal Processing*, vol. 169, pp. 108719 (1–23), 2022.
- [18] G. Sternharz, T. Kalganova, and C. Mares, "Simulation Dataset for Signal Processing and Operational Modal Analysis of Rotating Machinery Vibration During Acceleration," *Computing in Science & Engineering*, pp. 1–10, 2022. (Submitted on 06/08/2022).
- [19] G. Sternharz, "Simulation Dataset for Signal Processing and Operational Modal Analysis of Rotating Machinery Vibration During Acceleration," *Mendeley Data*, 2022. [Online]. Available: <https://data.mendeley.com/datasets/8z2db4rswr/draft?a=9056040e-ab32-47bb-b1bc-9e331ec042be> (Submitted on 06/08/2022).
- [20] G. Sternharz, J. Skackauskas, A. Elhalwagy, A. J. Grichnik, T. Kalganova, and M. N. Huda, "Self-Protected Virtual Sensor Network for Microcontroller Fault Detection," *Sensors*, vol. 22, no. 2, pp. 454 (1–27), 2022.
- [21] G. Sternharz, A. Elhalwagy, and T. Kalganova, "Data-Efficient Estimation of Remaining Useful Life for Machinery with a Limited Number of Run-to-Failure Training Sequences," *IEEE Access*, vol. 10, pp. 129443–129464, 2022.
- [22] W. Yang, H. Li, S. J. Hu, and Y. Teng, "Stochastic Modal Identification in the Presence of Harmonic Excitations," *Proceedings of the 6th International Operational Modal Analysis Conference (IOMAC)*, 2015.
- [23] K. Motte, W. Weijtjens, C. Devriendt, and P. Guillaume, "Operational Modal Analysis in the Presence of Harmonic Excitations: A Review," *Proceedings of the 33rd IMAC:*

- 
- Dynamics of Civil Structures*, vol. 2, pp. 379–395, 2015.
- [24] P. Mohanty and D. J. Rixen, “Identifying mode shapes and modal frequencies by operational modal analysis in the presence of harmonic excitation,” *Experimental Mechanics*, vol. 45, no. 3, pp. 213–220, 2005.
- [25] G. Zhang, B. Tang, and G. Tang, “An improved stochastic subspace identification for operational modal analysis,” *Measurement: Journal of the International Measurement Confederation*, vol. 45, no. 5, pp. 1246–1256, 2012.
- [26] N. Møller, S. Gade, and H. Herlufsen, “Stochastic Subspace Identification Technique in Operational Modal Analysis,” *Proceedings of the 1st International Operational Modal Analysis Conference (IOMAC)*, 2005.
- [27] V. Delavaud, T. Gouache, B. Coulange, L. O. Gonidou, and S. Foucaud, “Performances assessment of OMA methods applied to altered vibration signals,” *Proceedings of the International Conference on Noise and Vibration Engineering (ISMA)*, pp. 3223–3235, 2014.
- [28] B. Peeters, B. Cornelis, K. Janssens, and H. Van der Auweraer, “Removing Disturbing Harmonics in Operational Modal Analysis,” *Proceedings of the 2nd International Operational Modal Analysis Conference (IOMAC)*, vol. 1, pp. 185–192, 2007.
- [29] M. W. Häckell and R. Rolfes, “Long-term monitoring of modal parameters for SHM at a 5 MW offshore wind turbine,” *Proceedings of the 9th International Workshop on Structural Health Monitoring (IWSHM)*, vol. 1, pp. 1310–1317, 2013.
- [30] M. Ghalishooyan, M. Abdelghani, and A. Shooshtari, “Modal Identification of Rotating Machinery using the INOPMA Algorithm,” *Proceedings of the 7th International Operational Modal Analysis Conference (IOMAC)*, pp. 1–4, 2017.
- [31] V. Delavaud, T. Gouache, B. Coulange, L. O. Gonidou, and S. Foucaud, “Modal Identification of Systems Subjected to Harmonic Excitation with Variable Frequency and Amplitude,” *Proceedings of the 6th International Operational Modal Analysis Conference (IOMAC)*, 2015.
- [32] J. Bienert, P. Andersen, and R. Aguirre, “A Harmonic Peak Reduction Technique for Operational Modal Analysis of Rotating Machinery,” *Proceedings of the 6th International Operational Modal Analysis Conference (IOMAC)*, 2015.
- [33] M. Abdelghani and D. J. Inman, “Modal Appropriation for Use with In-Operation Modal Analysis,” *Shock and Vibration*, vol. 2015, pp. 1–5, 2015.
- [34] E. Di Lorenzo, S. Manzato, B. Peeters, F. Marulo, and W. Desmet, “Operational Modal Analysis for Rotating Machines: Challenges and Solutions,” in *Proceedings of the 7th International Operational Modal Analysis Conference (IOMAC)*, 2017.
- [35] J. Dion, I. Tawfiq, and G. Chevallier, “Harmonic component detection: Optimized

- Spectral Kurtosis for operational modal analysis,” *Mechanical Systems and Signal Processing*, vol. 26, pp. 24–33, 2012.
- [36] A. Agneni, G. Coppotelli, and C. Grappasonni, “A method for the harmonic removal in operational modal analysis of rotating blades,” *Mechanical Systems and Signal Processing*, vol. 27, pp. 604–618, 2012.
- [37] N.-J. Jacobsen and P. Andersen, “Operational Modal Analysis on Structures With Rotating Parts,” *Proceedings of the International Conference on Noise and Vibration Engineering (ISMA)*, vol. 5, pp. 2491–2506, 2008.
- [38] G. Vachtsevanos, F. Lewis, M. Roemer, A. Hess, and B. Wu, *Intelligent Fault Diagnosis and Prognosis for Engineering Systems*. Hoboken, New Jersey: John Wiley & Sons, Inc., 2006.
- [39] E. Bechhoefer and M. Kingsley, “A review of time synchronous average algorithms,” in *Annual Conference of the Prognostics and Health Management Society, PHM 2009*, 2009, pp. 1–10.
- [40] S. Manzato, J. R. White, B. LeBlanc, B. Peeters, and K. Janssens, “Advanced Identification Techniques for Operational Wind Turbine Data,” *Proceedings of the 31st IMAC: Topics in Modal Analysis*, vol. 7, pp. 195–209, 2013.
- [41] R. B. Randall, M. D. Coats, and W. A. Smith, “Repressing the effects of variable speed harmonic orders in operational modal analysis,” *Mechanical Systems and Signal Processing*, vol. 79, pp. 3–15, 2016.
- [42] Z. Daher, E. Sekko, J. Antoni, C. Capdessus, and L. Allam, “Estimation of the synchronous average under varying rotating speed condition for vibration monitoring,” in *Proceedings of ISMA 2010 - International Conference on Noise and Vibration Engineering*, 2010, pp. 2779–2787.
- [43] D. Abboud, J. Antoni, S. Sieg-Zieba, and M. Eltabach, “Deterministic-random separation in nonstationary regime,” *Journal of Sound and Vibration*, vol. 362, pp. 305–326, 2016.
- [44] R. B. Randall, B. Peeters, J. Antoni, and S. Manzato, “New cepstral methods of signal pre-processing for operational modal analysis,” *Proceedings of the International Conference on Noise and Vibration Engineering (ISMA)*, pp. 755–764, 2012.
- [45] H. Vold and J. Leuridan, “High Resolution Order Tracking at Extreme Slew Rates Using Kalman Tracking Filters,” *Shock and Vibration*, vol. 2, pp. 507–516, 1995.
- [46] N.-J. Jacobsen, P. Andersen, and R. Brincker, “Using Enhanced Frequency Domain Decomposition as a Robust Technique to Harmonic Excitation in Operational Modal Analysis,” *Proceedings of the International Conference on Noise and Vibration Engineering (ISMA)*, vol. 6, pp. 3129–3140, 2006.

- 
- [47] N.-J. Jacobsen, P. Andersen, and R. Brincker, "Eliminating the Influence of Harmonic Components in Operational Modal Analysis," *Proceedings of the International Modal Analysis Conference (IMAC)*, vol. 1, pp. 152–162, 2007.
- [48] P. J. Daems, C. Peeters, P. Guillaume, and J. Helsen, "Removal of non-stationary harmonics for operational modal analysis in time and frequency domain," *Mechanical Systems and Signal Processing*, vol. 165, no. January 2021, p. 108329, 2022.
- [49] P. Mohanty and D. J. Rixen, "A modified Ibrahim time domain algorithm for operational modal analysis including harmonic excitation," *Journal of Sound and Vibration*, vol. 275, no. 1–2, pp. 375–390, Aug. 2004.
- [50] P. Mohanty and D. J. Rixen, "Modified ERA method for operational modal analysis in the presence of harmonic excitations," *Mechanical Systems and Signal Processing*, vol. 20, no. 1, pp. 114–130, Jan. 2006.
- [51] W. Weijtjens, J. Lataire, C. Devriendt, and P. Guillaume, "Dealing with periodical loads and harmonics in operational modal analysis using time-varying transmissibility functions," *Mechanical Systems and Signal Processing*, vol. 49, no. 1–2, pp. 154–164, 2014.
- [52] W. Weijtjens, G. De Sitter, C. Devriendt, and P. Guillaume, "Operational modal parameter estimation of MIMO systems using transmissibility functions," *Automatica*, vol. 50, no. 2, pp. 559–564, 2014.
- [53] E. Di Lorenzo *et al.*, "Dynamic characterization of wind turbine gearboxes using Order-Based Modal Analysis," in *Proceedings of the International Conference on Noise and Vibration Engineering (ISMA)*, 2014, pp. 4349–4362.
- [54] K. Janssens, Z. Kollar, B. Peeters, S. Pauwels, and H. Van der Auweraer, "Order-based resonance identification using operational PolyMAX," in *Proceedings of the International Modal Analysis Conference (IMAC)*, 2006, vol. 2, pp. 566–575.
- [55] E. Di Lorenzo, S. Manzato, B. Peeters, F. Marulo, and W. Desmet, "Best Practices for Using Order-Based Modal Analysis for Industrial Applications," in *Proceedings of the 35th IMAC: Topics in Modal Analysis & Testing*, 2017, vol. 10, pp. 69–84.
- [56] A. Mbarek *et al.*, "Comparison of experimental and operational modal analysis on a back to back planetary gear," *Mechanism and Machine Theory*, vol. 124, pp. 226–247, Jun. 2018.
- [57] E. Di Lorenzo, S. Manzato, B. Peeters, F. Vanhollebeke, W. Desmet, and F. Marulo, "Order-Based Modal Analysis: A modal parameter estimation technique for rotating machineries," in *Proceedings of the 6th International Operational Modal Analysis Conference (IOMAC)*, 2015.
- [58] X. Zhang and L. Yue, "Order Based Modal Analysis Using Vold-Kalman Filter,"

- Prognostics and System Health Management Conference*, 2019.
- [59] B. Peeters, P. Gajdatsy, P. Aarnoutse, K. Janssens, and W. Desmet, “Vibro-acoustic operational modal analysis using engine run-up data,” in *Proceedings of the 3rd International Operational Modal Analysis Conference (IOMAC)*, 2009, vol. 2, pp. 447–455.
- [60] S. Gres, P. Andersen, and L. Damkilde, “Operational Modal Analysis of Rotating Machinery,” *Proceedings of the 36th IMAC: Rotating Machinery, Vibro-Acoustics & Laser Vibrometry*, vol. 7, pp. 67–75, 2018.
- [61] A. A. Fenerci, K. A. Kvåle, Ø. W. Petersen, A. Rønnquist, and O. Øiseth, “Wind and Acceleration Data from the Hardanger Bridge,” *Norges teknisk-naturvitenskapelige universitet*, 2020. [Online]. Available: <https://doi.org/10.21400/5ng8980s>. [Accessed: 20-Feb-2022].
- [62] K. Maes and G. Lombaert, “Monitoring data for railway bridge KW51 in Leuven, Belgium, before, during, and after retrofitting,” *KU Leuven*, 2020. [Online]. Available: <https://doi.org/10.5281/zenodo.3745914>. [Accessed: 20-Feb-2022].
- [63] C.-W. Kim, F. Zhang, K.-C. Chang, P. McGetrick, and Y. Goi, “Ambient and Vehicle-Induced Vibration Data of a Steel Truss Bridge Subject to Artificial Damage,” *Mendeley Data*, 2021. [Online]. Available: <https://data.mendeley.com/datasets/sc8whx4pvm/2>. [Accessed: 20-Feb-2022].
- [64] A. Whittaker, “Full-Scale Seismically Isolated Bridge Testing (NEES-2010-0976),” *State University of New York at Buffalo*, 2017. [Online]. Available: <https://datacenterhub.org/deedsdv/publications/view/310>. [Accessed: 20-Feb-2022].
- [65] KU Leuven, “Z24 Bridge Benchmark.” [Online]. Available: <https://bwk.kuleuven.be/bwm/z24>. [Accessed: 20-Feb-2022].
- [66] D. Lurcock, D. Thompson, and O. G. Bewes, “Dataset for Groundborne Railway Noise and Vibration in Buildings: Results of a Structural and Acoustic Parametric Study,” *University of Southampton*, 2018. [Online]. Available: <http://dx.doi.org/10.5258/SOTON/396986>. [Accessed: 20-Feb-2022].
- [67] J. Wallace and E. Taciroglu, “Field Testing of a Non-ductile Reinforced Concrete Building in Turkey (NEES-2010-0929),” *University of California, Los Angeles*, 2017. [Online]. Available: <https://datacenterhub.org/deedsdv/publications/view/382>. [Accessed: 20-Feb-2022].
- [68] S.-K. Au, “BAYOMA book datasets,” *Harvard Dataverse*, 2020. [Online]. Available: <https://doi.org/10.7910/DVN/7EVTXG>. [Accessed: 20-Feb-2022].
- [69] S. Dyke, S. Krishnan, and Z. Sun, “144 DOF Dynamic Measurement from a 50’ Full Scale Highway Sign Support Truss (NEES-2011-1013),” *Purdue University at West*

- Lafayette*, 2017. [Online]. Available: <https://datacenterhub.org/deedsdv/publications/view/378>. [Accessed: 20-Feb-2022].
- [70] O. Avci, O. Abdeljaber, S. Kiranyaz, M. Hussein, M. Gabbouj, and D. Inman, "A New Benchmark Problem for Structural Damage Detection: Bolt Loosening Tests on a Large-Scale Laboratory Structure," in *Proceedings of the 39th IMAC, Dynamics of Civil Structures, Volume 2*, 2021, pp. 15–22.
- [71] J. Bodtke *et al.*, "Ambient Vibration Modal Analysis of Natural Rock Towers and Fins," *University of Utah*, 2021. [Online]. Available: <https://doi.org/10.7278/S50D-N12Q-SA1Z>. [Accessed: 20-Feb-2022].
- [72] R. R. Stefan Wernitz, Benedikt Hofmeister, Clemens Jonscher, Tanja Griebmann, "LUMO - Leibniz University Test Structure for Monitoring," *Leibniz Universität Hannover*, 2021. [Online]. Available: <https://doi.org/10.25835/0027803>. [Accessed: 20-Feb-2022].
- [73] University of California San Diego, "Data from mechanical rectilinear systems obtained in the UGCL." [Online]. Available: <http://mechatronics.ucsd.edu/data/ugcl/rectilinear/>. [Accessed: 20-Feb-2022].
- [74] J. Kullaa, "Benchmark Data for Structural Health Monitoring," *7th European Workshop on Structural Health Monitoring EWSHM*, 2014. [Online]. Available: <https://www.ndt.net/search/docs.php3?id=17050>.
- [75] Los Alamos National Laboratory, "SHMTools - SHM Data Sets and Software." [Online]. Available: <https://www.lanl.gov/projects/national-security-education-center/engineering/software/shm-data-sets-and-software.php>. [Accessed: 20-Feb-2022].
- [76] Case Western Reserve University, "Bearing Data Center - Seeded Fault Test Data." [Online]. Available: <https://engineering.case.edu/bearingdatacenter>. [Accessed: 19-Feb-2022].
- [77] A. Agogino and K. Goebel, "Milling Data Set," *BEST lab, UC Berkeley*, 2007. [Online]. Available: <https://ti.arc.nasa.gov/tech/dash/groups/pcoe/prognostic-data-repository/#milling>. [Accessed: 21-Feb-2022].
- [78] J. Lee, H. Qiu, G. Yu, J. Lin, and Rexnord Technical Services, "Bearing Data Set," *Center for Intelligent Maintenance Systems (IMS), University of Cincinnati*, 2007. [Online]. Available: <https://ti.arc.nasa.gov/tech/dash/groups/pcoe/prognostic-data-repository/#bearing>. [Accessed: 21-Feb-2022].
- [79] The Prognostics and Health Management Society, "2009 PHM Challenge Competition Data Set," 2009. [Online]. Available: <https://phmsociety.org/public-data-sets/>. [Accessed: 20-Feb-2022].

- [80] P. Nectoux *et al.*, “FEMTO Bearing Data Set,” *FEMTO-ST Institute*, 2012. [Online]. Available: <https://ti.arc.nasa.gov/tech/dash/groups/pcoe/prognostic-data-repository/#femto>. [Accessed: 20-Feb-2022].
- [81] E. Bechhoefer, “Condition Based Maintenance Fault Database for Testing of Diagnostic and Prognostics Algorithms,” *MFPT*. [Online]. Available: <https://www.mfpt.org/fault-data-sets/>. [Accessed: 20-Feb-2022].
- [82] H. Huang and N. Baddour, “Bearing Vibration Data under Time-varying Rotational Speed Conditions,” *Mendeley Data*, 2019. [Online]. Available: <https://data.mendeley.com/datasets/v43hmbwxpm/2>. [Accessed: 20-Apr-2022].
- [83] Y. Liang, “The motor fault diagnosis experiment dataset,” *Zenodo*, 2019. [Online]. Available: <https://doi.org/10.5281/zenodo.3553755>. [Accessed: 17-Apr-2022].
- [84] Y. Liang, B. Li, and B. Jiao, “A deep learning method for motor fault diagnosis based on a capsule network with gate-structure dilated convolutions,” *Neural Computing and Applications*, vol. 33, no. 5, pp. 1401–1418, 2021.
- [85] A. E. Treml, R. A. Flauzino, M. Suetake, and A. N. R. Maciejewski, “Experimental database for detecting and diagnosing rotor broken bar in a three-phase induction motor,” *IEEE DataPort*, 2020. [Online]. Available: <https://dx.doi.org/10.21227/fmnm-bn95>. [Accessed: 17-Apr-2022].
- [86] A. E. Treml, R. A. Flauzino, R. A. Ramos, and G. C. Brito, “Broken Rotor Bar Fault Detection in Asynchronous Machines Using Vibration Analysis,” in *IEEE Power and Energy Society General Meeting (PESGM)*, 2019.
- [87] O. Mey, W. Neudeck, A. Schneider, and O. Enge-Rosenblatt, “Unbalance Detection of a Rotating Shaft Using Vibration Data,” *Kaggle*, 2020. [Online]. Available: <https://www.kaggle.com/datasets/jishnukoliyadan/vibration-analysis-on-rotating-shaft>. [Accessed: 20-Apr-2022].
- [88] R. Viitala, J. Miettinen, T. Tiainen, and R. Viitala, “Rotor & bearing vibration dataset,” *Mendeley Data*, 2020. [Online]. Available: <https://data.mendeley.com/datasets/pdrxyfprfk/1>. [Accessed: 20-Apr-2022].
- [89] Universidade Federal do Rio de Janeiro COPPE/Poli/UFRJ, “MAFAULDA Machinery Fault Database,” 2021. [Online]. Available: [http://www02.smt.ufrj.br/~offshore/mfs/page\\_01.html](http://www02.smt.ufrj.br/~offshore/mfs/page_01.html). [Accessed: 19-Feb-2022].
- [90] R. Brincker and C. E. Ventura, *Introduction to Operational Modal Analysis*. Chichester, UK: John Wiley & Sons, Ltd, 2015.
- [91] C. Rainieri and G. Fabbrocino, *Operational Modal Analysis of Civil Engineering Structures: An Introduction and Guide for Applications*. Springer, 2014.
- [92] S. Manzato, E. Di Lorenzo, A. Medici, F. Vanhollebeke, B. Peeters, and W. Desmet,



- “Order Based Modal Analysis Versus Standard Techniques to Extract Modal Parameters of Operational Wind Turbine Gearboxes,” *Proceedings of the 33rd IMAC: Topics in Modal Analysis*, vol. 10, pp. 115–122, 2015.
- [93] A. K. S. Jardine, D. Lin, and D. Banjevic, “A review on machinery diagnostics and prognostics implementing condition-based maintenance,” *Mechanical Systems and Signal Processing*, vol. 20, no. 7, pp. 1483–1510, 2006.
- [94] S. Wang and M. Xu, “Modal Strain Energy-based Structural Damage Identification: A Review and Comparative Study,” *Structural Engineering International*, vol. 29, no. 2, pp. 234–248, 2019.
- [95] A. Rytter, “Vibrational Based Inspection of Civil Engineering Structures,” Aalborg University, 1993.
- [96] T. Brotherton, G. Jahns, J. Jacobs, and D. Wroblewski, “Prognosis of faults in gas turbine engines,” *IEEE Aerospace Conference Proceedings*, vol. 6, pp. 163–172, 2000.
- [97] Y. Lei, N. Li, L. Guo, N. Li, T. Yan, and J. Lin, “Machinery health prognostics: A systematic review from data acquisition to RUL prediction,” *Mechanical Systems and Signal Processing*, vol. 104, pp. 799–834, 2018.
- [98] R. Zhao, R. Yan, Z. Chen, K. Mao, P. Wang, and R. X. Gao, “Deep learning and its applications to machine health monitoring,” *Mechanical Systems and Signal Processing*, vol. 115, pp. 213–237, 2019.
- [99] N. B. Jones and Y. H. Li, “A review of condition monitoring and fault diagnosis for diesel engines,” *Tribotest*, vol. 6, no. 3, pp. 267–291, 2000.
- [100] Y. Wang, Y. Zhao, and S. Addepalli, “Remaining useful life prediction using deep learning approaches: A review,” *Procedia Manufacturing*, vol. 49, no. 2019, pp. 81–88, 2020.
- [101] O. Abdeljaber, O. Avci, S. Kiranyaz, M. Gabbouj, and D. J. Inman, “Real-time vibration-based structural damage detection using one-dimensional convolutional neural networks,” *Journal of Sound and Vibration*, vol. 388, pp. 154–170, 2017.
- [102] B. C. Wen, M. Q. Xiao, X. Q. Wang, X. Zhao, J. F. Li, and X. Chen, “Data-driven remaining useful life prediction based on domain adaptation,” *PeerJ Computer Science*, vol. 7, pp. 1–25, 2021.
- [103] C. Li, R. V. Sánchez, G. Zurita, M. Cerrada, and D. Cabrera, “Fault diagnosis for rotating machinery using vibration measurement deep statistical feature learning,” *Sensors*, vol. 16, no. 6, 2016.
- [104] M. Radzieński, M. Krawczuk, and M. Palacz, “Improvement of damage detection methods based on experimental modal parameters,” *Mechanical Systems and Signal*

- Processing*, vol. 25, no. 6, pp. 2169–2190, 2011.
- [105] N. Stubbs, J. T. Kim, and C. R. Farrar, “Field verification of a nondestructive damage localization and severity estimation algorithm,” in *Proceedings of the International Society for Optical Engineering (SPIE)*, 1995, vol. 182, pp. 210–218.
- [106] S. Park, N. Stubbs, R. Bolton, S. Choi, and C. Sikorsky, “Field verification of the damage index method in a concrete box-girder bridge via visual inspection,” *Computer-Aided Civil and Infrastructure Engineering*, vol. 16, no. 1, pp. 58–70, 2001.
- [107] S. M. H. Pooya and A. Massumi, “A novel and efficient method for damage detection in beam-like structures solely based on damaged structure data and using mode shape curvature estimation,” *Applied Mathematical Modelling*, vol. 91, pp. 670–694, 2021.
- [108] G. F. Gomes and R. S. Giovani, “An efficient two-step damage identification method using sunflower optimization algorithm and mode shape curvature (MSDBI–SFO),” *Engineering with Computers*, vol. 38, no. 2, pp. 1711–1730, 2022.
- [109] L. Dolinski and M. Krawczuk, “Analysis of modal parameters using a statistical approach for condition monitoring of the wind turbine blade,” *Applied Sciences*, vol. 10, no. 17, pp. 1–17, 2020.
- [110] A. Khatir, M. Tehami, S. Khatir, and M. Abdel Wahab, “Multiple damage detection and localization in beam-like and complex structures using co-ordinate modal assurance criterion combined with firefly and genetic algorithms,” *Journal of Vibroengineering*, vol. 18, no. 8, pp. 5063–5073, Dec. 2016.
- [111] L. Balsamo, S. Mukhopadhyay, R. Betti, and H. Lus, “Damage Detection Using Flexibility Proportional Coordinate Modal Assurance Criterion,” in *Proceedings of the 31st IMAC: Topics in Modal Analysis*, 2013, pp. 1–8.
- [112] S. Patil and D. Mallikarjuna Reddy, “Damage Identification in Hemp Fiber (*Cannabis sativa*) Reinforced Composite Plates Using MAC and COMAC Correlation Methods: Experimental Study,” *Journal of Natural Fibers*, vol. 19, no. 4, pp. 1249–1264, Apr. 2022.
- [113] P. Jia, Y. Rong, and Y. Huang, “Condition monitoring of the feed drive system of a machine tool based on long-term operational modal analysis,” *International Journal of Machine Tools and Manufacture*, vol. 146, p. 103454, 2019.
- [114] Y. Shokrani, V. K. Dertimanis, E. N. Chatzi, and M. N. Savoia, “On the use of mode shape curvatures for damage localization under varying environmental conditions,” *Structural Control and Health Monitoring*, vol. 25, no. 4, 2018.
- [115] E. Di Lorenzo, “Operational Modal Analysis for Rotating Machines: Challenges and Solutions,” Università degli Studi di Napoli Federico II, 2017.

- 
- [116] K. Fischer and D. Coronado, "Condition Monitoring of Wind Turbines: State of the Art, User Experience and Recommendations," *VBG PowerTech*, no. VGB Research Project 383, pp. 51–56, 2015.
- [117] N. A. J. Lieven, "Neural Networks for Modal Analysis," in *Modal Analysis and Testing*, Dordrecht: Springer, 1999, pp. 507–528.
- [118] J. Carroll, S. Koukoura, A. McDonald, A. Charalambous, S. Weiss, and S. McArthur, "Wind turbine gearbox failure and remaining useful life prediction using machine learning techniques," *Wind Energy*, vol. 22, no. 3, pp. 360–375, 2019.
- [119] J. Qu, F. Liu, Y. Ma, and J. Fan, "A Neural-Network-Based Method for RUL Prediction and SOH Monitoring of Lithium-Ion Battery," *IEEE Access*, vol. 7, pp. 87178–87191, 2019.
- [120] Z. Kang, C. Catal, and B. Tekinerdogan, "Remaining Useful Life (RUL) Prediction of Equipment in Production Lines Using Artificial Neural Networks," *Sensors*, vol. 21, no. 3, pp. 1-20 (932), 2021.
- [121] L. Guo, N. Li, F. Jia, Y. Lei, and J. Lin, "A recurrent neural network based health indicator for remaining useful life prediction of bearings," *Neurocomputing*, vol. 240, pp. 98–109, 2017.
- [122] S. Hochreiter, "Recurrent neural net learning and vanishing gradient," *International Journal of Uncertainty, Fuzziness and Knowledge-Based Systems*, vol. 6, no. 2, pp. 107–116, 1998.
- [123] R. Pascanu, T. Mikolov, and Y. Bengio, "On the difficulty of training recurrent neural networks," in *ICML'13: Proceedings of the 30th International Conference on Machine Learning*, 2013, vol. 28, pp. 1310–1318.
- [124] S. Hochreiter and J. Schmidhuber, "Long Short-Term Memory," *Neural Computation*, vol. 9, no. 8, pp. 1735–1780, 1997.
- [125] K. Cho, B. Van Merriënboer, D. Bahdanau, and Y. Bengio, "On the Properties of Neural Machine Translation: Encoder–Decoder Approaches," in *Proceedings of SSST-8, Eighth Workshop on Syntax, Semantics and Structure in Statistical Translation*, 2014, pp. 103–111.
- [126] H. Zhang, Q. Zhang, S. Shao, T. Niu, and X. Yang, "Attention-Based LSTM Network for Rotatory Machine Remaining Useful Life Prediction," *IEEE Access*, vol. 8, pp. 132188–132199, 2020.
- [127] X. Li, Q. Ding, and J. Q. Sun, "Remaining useful life estimation in prognostics using deep convolution neural networks," *Reliability Engineering and System Safety*, vol. 172, no. November 2017, pp. 1–11, 2018.
- [128] B. Yang, R. Liu, and E. Zio, "Remaining Useful Life Prediction Based on a Double-

- Convolutional Neural Network Architecture,” *IEEE Transactions on Industrial Electronics*, vol. 66, no. 12, pp. 9521–9530, 2019.
- [129] S. Ren, K. He, R. Girshick, and J. Sun, “Faster R-CNN: Towards Real-Time Object Detection with Region Proposal Networks,” in *Advances in Neural Information Processing Systems*, 2015.
- [130] B. Zhao, H. Lu, S. Chen, J. Liu, and D. Wu, “Convolutional neural networks for time series classification,” *Journal of Systems Engineering and Electronics*, vol. 28, no. 1, pp. 162–169, 2017.
- [131] Y. Liu, X. Hu, and W. Zhang, “Remaining useful life prediction based on health index similarity,” *Reliability Engineering and System Safety*, vol. 185, pp. 502–510, May 2019.
- [132] M. M. Manjurul Islam, A. E. Prosvirin, and J.-M. Kim, “Data-driven prognostic scheme for rolling-element bearings using a new health index and variants of least-square support vector machines,” *Mechanical Systems and Signal Processing*, vol. 160, Nov. 2021.
- [133] F. Yang, M. S. Habibullah, T. Zhang, Z. Xu, P. Lim, and S. Nadarajan, “Health index-based prognostics for remaining useful life predictions in electrical machines,” *IEEE Transactions on Industrial Electronics*, vol. 63, no. 4, pp. 2633–2644, Apr. 2016.
- [134] Y. Wei, D. Wu, and J. Terpenney, “Learning the health index of complex systems using dynamic conditional variational autoencoders,” *Reliability Engineering and System Safety*, vol. 216, Dec. 2021.
- [135] Y. Fan, S. Nowaczyk, and T. Rögnvaldsson, “Transfer learning for remaining useful life prediction based on consensus self-organizing models,” *Reliability Engineering and System Safety*, vol. 203, no. September 2019, p. 107098, 2020.
- [136] C. Sun, M. Ma, Z. Zhao, S. Tian, R. Yan, and X. Chen, “Deep Transfer Learning Based on Sparse Autoencoder for Remaining Useful Life Prediction of Tool in Manufacturing,” *IEEE Transactions on Industrial Informatics*, vol. 15, no. 4, pp. 2416–2425, 2019.
- [137] J. Zhu, N. Chen, and C. Shen, “A new data-driven transferable remaining useful life prediction approach for bearing under different working conditions,” *Mechanical Systems and Signal Processing*, vol. 139, p. 106602, 2020.
- [138] A. Listou Ellefsen, E. Bjørlykhaug, V. Æsøy, S. Ushakov, and H. Zhang, “Remaining useful life predictions for turbofan engine degradation using semi-supervised deep architecture,” *Reliability Engineering and System Safety*, vol. 183, no. November 2018, pp. 240–251, 2019.
- [139] H. Li, W. Wang, Z. Li, L. Dong, and Q. Li, “A novel approach for predicting tool

- remaining useful life using limited data,” *Mechanical Systems and Signal Processing*, vol. 143, p. 106832, 2020.
- [140] H. Takeyama and R. Murata, “Basic Investigation of Tool Wear,” *Journal of Engineering for Industry*, vol. 85, no. 1, pp. 33–37, Feb. 1963.
- [141] E. Usui, T. Shirakashi, and T. Kitagawa, “Analytical prediction of cutting tool wear,” *Wear*, vol. 100, no. 1–3, pp. 129–151, Dec. 1984.
- [142] X. Fang, R. Zhou, and N. Gebraeel, “An adaptive functional regression-based prognostic model for applications with missing data,” *Reliability Engineering and System Safety*, vol. 133, pp. 266–274, 2015.
- [143] N. Gebraeel, A. Elwany, and J. Pan, “Residual life predictions in the absence of prior degradation knowledge,” *IEEE Transactions on Reliability*, vol. 58, no. 1, pp. 106–117, 2009.
- [144] J. Wang, Y. Liang, Y. Zheng, R. X. Gao, and F. Zhang, “An integrated fault diagnosis and prognosis approach for predictive maintenance of wind turbine bearing with limited samples,” *Renewable Energy*, vol. 145, pp. 642–650, 2020.
- [145] B. Merainani, S. Laddada, E. Bechhoefer, M. A. A. Chikh, and D. Benazzouz, “An integrated methodology for estimating the remaining useful life of high-speed wind turbine shaft bearings with limited samples,” *Renewable Energy*, vol. 182, pp. 1141–1151, 2022.
- [146] A. Widodo and B. S. Yang, “Machine health prognostics using survival probability and support vector machine,” *Expert Systems with Applications*, vol. 38, no. 7, pp. 8430–8437, 2011.
- [147] V. T. Tran and B. S. Yang, “An intelligent condition-based maintenance platform for rotating machinery,” *Expert Systems with Applications*, vol. 39, no. 3, pp. 2977–2988, 2012.
- [148] G. Sternharz, “Development and Evaluation of a Bi-axial Mechanical Fan Blade Testing Rig Model Utilising Finite Element Method,” Technische Universität Berlin, 2018.
- [149] P. Avitabile, *Modal Testing: A Practitioner’s Guide*. Wiley, 2017.
- [150] O. C. Zienkiewicz, R. L. Taylor, and J. Z. Zhu, *The Finite Element Method: Its Basis and Fundamentals*, 6th ed. Elsevier, 2005.
- [151] R. Gasch, K. Knothe, and R. Liebich, *Strukturdynamik: Diskrete Systeme und Kontinua*, 2nd ed. Berlin, Heidelberg: Springer Berlin Heidelberg, 2012.
- [152] C. Lanczos, “An Iteration Method for the Solution of the Eigenvalue Problem of Linear Differential and Integral Operators,” *Journal of Research of the National Bureau of Standards*, vol. 45, no. 4, pp. 255–282, Oct. 1950.

- [153] J. G. F. Francis, "The QR Transformation - A Unitary Analogue to the LR Transformation - Part 1," *The Computer Journal*, vol. 4, no. 3, pp. 265–271, Mar. 1961.
- [154] A. Czekanski, N. El-Abbasi, and S. A. Meguid, "Optimal time integration parameters for elastodynamic contact problems," *Communications in Numerical Methods in Engineering*, vol. 17, no. 6, pp. 379–384, 2001.
- [155] S. Carstens, "Modellbildung und numerische Mechanik tensegrer Strukturen Dissertation," Universität Kassel, 2013.
- [156] K. H. Huebner, D. L. Dewhirst, D. E. Smith, and T. G. Byrom, *The Finite Element Method for Engineers*, 4th ed. Wiley, 2001.
- [157] E. Reynders, "System Identification Methods for (Operational) Modal Analysis: Review and Comparison," *Archives of Computational Methods in Engineering*, vol. 19, no. 1, pp. 51–124, 2012.
- [158] C. D. Meyer, *Matrix Analysis and Applied Linear Algebra*. Philadelphia, PA: Society for Industrial and Applied Mathematics (SIAM), 2000.
- [159] M. López-Aenlle, R. Brincker, F. Pelayo, and A. F. Canteli, "On exact and approximated formulations for scaling-mode shapes in operational modal analysis by mass and stiffness change," *Journal of Sound and Vibration*, vol. 331, no. 3, pp. 622–637, Jan. 2012.
- [160] M. L. Aenlle and R. Brincker, "Modal scaling in operational modal analysis using a finite element model," *International Journal of Mechanical Sciences*, vol. 76, pp. 86–101, Nov. 2013.
- [161] D. J. Ewins, *Modal Testing: Theory, Practice and Application*, 2nd ed. Baldock, Hertfordshire, England: Research Studies Press Ltd., 2000.
- [162] S. T. Bailie, W. F. Ng, and W. W. Copenhaver, "Experimental Reduction of Transonic Fan Forced Response by Inlet Guide Vane Flow Control," *Journal of Turbomachinery*, vol. 132, no. 2, pp. 021003 1–8, 2010.
- [163] C. Manu, "Dynamic analysis of structures with closely spaced modes using the response spectrum method," *Computers and Structures*, vol. 22, no. 3, pp. 405–412, 1986.
- [164] U. Fuellekrug, M. Boeswald, D. Goege, and Y. Govers, "Measurement of FRFs and modal identification in case of correlated multi-point excitation," *Shock and Vibration*, vol. 15, no. 3–4, pp. 435–445, 2008.
- [165] P. Lubrina, S. Giclais, C. Stephan, M. Boeswald, Y. Govers, and N. Botargues, "AIRBUS A350 XWB GVT: State-of-the-Art Techniques to Perform a Faster and Better GVT Campaign," *Proceedings of the 32nd IMAC, Topics in Modal Analysis II*, vol. 8, pp. 243–256, 2014.

- 
- [166] R. J. Allemang, "The modal assurance criterion - Twenty years of use and abuse," *Sound & Vibration*, vol. 37, no. 8, pp. 14–21, 2003.
- [167] P. Vacher, B. Jacquier, and A. Bucharles, "Extensions of the MAC criterion to complex modes," in *Proceedings of ISMA 2010 - International Conference on Noise and Vibration Engineering*, 2010, pp. 2713–2725.
- [168] R. N. Bracewell, *The Fourier Transform and its Applications*, 3rd ed. Singapore: McGraw-Hill, 2000.
- [169] W. L. Briggs and V. E. Henson, *The DFT: An Owners' Manual for the Discrete Fourier Transform*. Philadelphia: Society for Industrial and Applied Mathematics, 1995.
- [170] I. Amidror, *Mastering the Discrete Fourier Transform in One, Two or Several Dimensions: Pitfalls and Artifacts*, vol. 43. London: Springer, 2013.
- [171] J. R. Blough, "Improving the Analysis of Operating Data on Rotating Automotive Components," University of Cincinnati, 1998.
- [172] T. Hastie, R. Tibshirani, and J. Friedman, *The Elements of Statistical Learning: Data Mining, Inference, and Prediction*. Springer, 2009.
- [173] P. C. Mahalanobis, "On generalized distance in statistics," in *Proceedings of the National Institute of Sciences of India*, 1936, vol. 2, no. 1, pp. 49–55.
- [174] H. Drucker, C. J. C. Burges, L. Kaufman, A. Smola, and V. Vapnik, "Support Vector Regression Machines," *Advances in Neural Information Processing Systems*, vol. 1, pp. 155–161, 1997.
- [175] B. E. Boser, I. M. Guyon, and V. N. Vapnik, "A Training Algorithm for Optimal Margin Classifiers," in *Proceedings of the 5th Annual Workshop on Computational Learning Theory*, 1992, pp. 144–152.
- [176] G. E. Hinton and R. R. Salakhutdinov, "Reducing the Dimensionality of Data with Neural Networks," *Science*, vol. 313, no. 5786, pp. 504–507, Jul. 2006.
- [177] R. Markert and M. Seidler, "Analytically based estimation of the maximum amplitude during passage through resonance," *International Journal of Solids and Structures*, vol. 38, no. 10–13, pp. 1975–1992, 2001.
- [178] H. P. Hackenberg and A. Hartung, "An Approach for Estimating the Effect of Transient Sweep Through a Resonance," *Journal of Engineering for Gas Turbines and Power*, vol. 138, no. 8, pp. 1–12, 2016.
- [179] G. Gloth and M. Sinapius, "Analysis of swept-sine runs during modal identification," *Mechanical Systems and Signal Processing*, vol. 18, no. 6, pp. 1421–1441, 2004.
- [180] Q. Dollon, J. Antoni, A. Tahan, M. Gagnon, and C. Monette, "Operational Modal Analysis of hydroelectric turbines using an order based likelihood approach," *Renewable Energy*, vol. 165, pp. 799–811, 2021.

- [181] A. Brandt, "ABRAVIBE - A toolbox for teaching and learning vibration analysis," *Sound and Vibration*, vol. 47, no. 11, pp. 12–17, 2013.
- [182] D. F. Aldridge, "Mathematics of Linear Sweeps," *Canadian Journal of Exploration of Geophysics*, vol. 28, no. June, pp. 62–68, 1992.
- [183] Dassault Systèmes Simulia Corp., "Abaqus Analysis User's Guide." Abaqus v2016, Providence, RI, 2015.
- [184] M. Geradin and D. J. Rixen, *Mechanical Vibrations: Theory and Application to Structural Dynamics*, 3rd ed. John Wiley & Sons, Ltd, 2015.
- [185] ANSYS, "ANSYS Explicit Dynamics Analysis Guide." ANSYS, Inc., Canonsburg, PA, p. 394, 2020.
- [186] ANSYS, "ANSYS Theory Reference." ANSYS, Inc., Canonsburg, PA, p. 1286, 2020.
- [187] ANSYS, "ANSYS Structural Analysis Guide." ANSYS, Inc., Canonsburg, PA, p. 484, 2020.
- [188] Universal Analytics Inc., "UAI/NASTRAN User's Guide." Universal Analytics Inc., Torrance, CA, 1999.
- [189] K. Worden and G. R. Tomlinson, *Nonlinearity in structural dynamics: Detection, identification and modelling*. Bristol: Institute of Physics Publishing, 2001.
- [190] Uwe Dorka, "Hybrid experimental-numerical simulation of vibrating structures," in *Proceedings of the International Workshop WAVE*, 2002, pp. 183–191.
- [191] H. Vold, K. Napolitano, D. Hensley, and M. Richardson, "Aliasing in modal parameter estimation," *Sound & Vibration*, pp. 12–17, 2008.
- [192] W. Fladung and H. Vold, "An orthogonal view of the polyreference least-squares complex frequency modal parameter estimation algorithm," in *Proceedings of the 33rd IMAC: Topics in Modal Analysis*, 2015, vol. 10, pp. 171–182.
- [193] M. H. Richardson and D. L. Formenti, "Parameter estimation from frequency response measurements using rational fraction polynomials," in *Proceedings of the International Modal Analysis Conference (IMAC)*, 1982, pp. 167–181.
- [194] H. I. Vold, "Methods and apparatus for modal parameter estimation," US 2009/0204355 A1, 2009.
- [195] D. A. Bies, C. H. Hansen, and C. Q. Howard, *Engineering Noise Control: Theory and Practice, Fourth Edition*, 5th ed. CRC Press, 2018.
- [196] K. Shin and J. K. Hammond, *Fundamentals of Signal Processing for Sound and Vibration Engineers*. Wiley, 2008.
- [197] O. Matsushita, M. Tanaka, H. Kanki, M. Kobayashi, and P. Keogh, *Vibrations of Rotating Machinery*, vol. 16. Tokyo: Springer Japan, 2017.
- [198] A. Cattaneo, S. Manzoni, and M. Vanali, "Frequency resolution and number of



- averages effects on the accuracy and dispersion of operational modal analysis results,” in *4th International Operational Modal Analysis Conference (IOMAC)*, 2011, no. 2008, pp. 462–472.
- [199] E. Strubell, A. Ganesh, and A. McCallum, “Energy and policy considerations for modern deep learning research,” *AAAI 2020 - 34th AAAI Conference on Artificial Intelligence*, pp. 1393–13696, 2020.
- [200] P. Dhar, “The carbon impact of artificial intelligence,” *Nature Machine Intelligence*, vol. 2, no. 8, pp. 423–425, 2020.
- [201] R. Schwartz, J. Dodge, N. A. Smith, and O. Etzioni, “Green AI,” *Communications of the ACM*, vol. 63, no. 12, pp. 54–63, 2020.
- [202] N. Srivastava, E. Mansimov, and R. Salakhutdinov, “Unsupervised Learning of Video Representations using LSTMs,” in *32nd International Conference on Machine Learning (ICML)*, 2015, vol. 1, pp. 843–852.
- [203] N. Costa and L. Sánchez, “Variational encoding approach for interpretable assessment of remaining useful life estimation,” *Reliability Engineering and System Safety*, vol. 222, no. January, p. 108353, 2022.
- [204] F. O. Heimes, “Recurrent neural networks for remaining useful life estimation,” in *2008 International Conference on Prognostics and Health Management*, 2008, pp. 1–6.
- [205] J. Zhang, P. Wang, R. Yan, and R. X. Gao, “Long short-term memory for machine remaining life prediction,” *Journal of Manufacturing Systems*, vol. 48, no. May, pp. 78–86, 2018.
- [206] S. Zheng, K. Ristovski, A. Farahat, and C. Gupta, “Long Short-Term Memory Network for Remaining Useful Life estimation,” in *IEEE International Conference on Prognostics and Health Management (ICPHM)*, 2017, pp. 88–95.
- [207] A. Saxena, K. Goebel, D. Simon, and N. Eklund, “Damage propagation modeling for aircraft engine run-to-failure simulation,” in *International Conference on Prognostics and Health Management, PHM 2008*, 2008.
- [208] S. Zhao, Y. Zhang, S. Wang, B. Zhou, and C. Cheng, “A recurrent neural network approach for remaining useful life prediction utilizing a novel trend features construction method,” *Measurement: Journal of the International Measurement Confederation*, vol. 146, pp. 279–288, 2019.
- [209] W. Caesarendra and T. Tjahjowidodo, “A review of feature extraction methods in vibration-based condition monitoring and its application for degradation trend estimation of low-speed slew bearing,” *Machines*, vol. 5, no. 4, 2017.
- [210] B. Peeters, H. Van der Auweraer, P. Guillaume, and J. Leuridan, “The PolyMAX Frequency-Domain Method: A New Standard for Modal Parameter Estimation?,”

- Shock and Vibration*, vol. 11, pp. 395–409, 2004.
- [211] B. Peeters, H. Van Der Auweraer, F. Vanhollebeke, and P. Guillaume, “Operational modal analysis for estimating the dynamic properties of a stadium structure during a football game,” *Shock and Vibration*, vol. 14, no. 4, pp. 283–303, 2007.
- [212] P. Guillaume, P. Verboven, S. Vanlanduit, H. Van Der Auweraer, and B. Peeters, “A poly-reference implementation of the least-squares complex frequency-domain estimator,” in *Proceedings of the 21st IMAC*, 2003.
- [213] R. A. Horn and C. R. Johnson, *Matrix analysis*. Cambridge: Cambridge University Press, 1990.
- [214] T. Nestorović, M. Trajkov, and M. Patalong, “Identification of modal parameters for complex structures by experimental modal analysis approach,” *Advances in Mechanical Engineering*, vol. 8, no. 5, pp. 1–16, 2016.
- [215] B. Cauberghe, “Applied frequency-domain system identification in the field of experimental and operational modal analysis,” Vrije Universiteit Brussel, 2004.
- [216] W. Fladung and H. Vold, “An improved implementation of the orthogonal polynomial modal parameter estimation algorithm using the orthogonal complement,” in *Proceedings of the 33rd IMAC: Topics in Modal Analysis*, 2015, vol. 10, pp. 157–170.
- [217] P. Verboven, “Frequency-domain system identification,” Vrije Universiteit Brussel, 2002.
- [218] B. Cauberghe, P. Guillaume, P. Verboven, S. Vanlanduit, and E. Parloo, “On the influence of the parameter constraint on the stability of the poles and the discrimination capabilities of the stabilisation diagrams,” *Mechanical Systems and Signal Processing*, vol. 19, no. 5, pp. 989–1014, 2005.
- [219] P. Verboven, “Frequency-Domain System Identification for Modal Analysis,” Vrije Universiteit Brussel, 2002.
- [220] T. Kailath, *Linear Systems*. Prentice-Hall, 1980.
- [221] B. Peeters, P. Guillaume, H. Van Der Auweraer, B. Cauberghe, P. Verboven, and J. Leuridan, “Automotive and aerospace applications of the PolyMAX modal parameter estimation method,” in *Proceedings of the 22nd IMAC*, 2004.
- [222] B. Peeters, G. Lowet, H. Van der Auweraer, and J. Leuridan, “A New Procedure for Modal Parameter Estimation,” *Sound and Vibration*, vol. 38, no. 1, pp. 24–28, 2004.
- [223] M. El-Kafafy and P. Guillaume, “Model parameter estimation of structures with overdamped poles,” in *Proceedings of ISMA 2010 - International Conference on Noise and Vibration Engineering*, 2010, pp. 3373–3389.
- [224] L. Mulder, “Applied Frequency-Domain System Identification in the Field of Experimental Modal Analysis,” University of Twente, 2017.

- 
- [225] Z. Jiao and A. U. Mange, "Poly-X, the Poly-Reference LSCF Implementation and Experiment." Crystal Instruments, pp. 1–4, 2019.
- [226] C. S. Lin, "Frequency-domain approach for the parametric identification of structures with modal interference," *Journal of Mechanical Science and Technology*, vol. 33, no. 9, pp. 4081–4091, 2019.
- [227] J. Slavič, M. Mršnik, M. Česnik, J. Javh, and M. Boltežar, *Vibration Fatigue by Spectral Methods: From Structural Dynamics to Fatigue Damage - Theory and Experiments*. Elsevier, 2020.

## Appendix A OMA case study of an aluminium plate under harmonic excitation

The described experiment was conducted by Jacobsen et al. [46] and the acquired vibration measurements were used for further analysis work below, performed by the author of this thesis. The authors of the original experiment present techniques for harmonic identification and propose a method for reduction of identified harmonics based on the EFDD method. In contrast to that, this appendix uses the experimental data to determine and compare the general performance of several available OMA methods. The raw measurements are sourced from the examples package of the OMA software Artemis Modal. This appendix forms a part of a publication [15] by the thesis author.

An aluminium plate (Figure A-1a) was instrumented with 16 unidirectional accelerometers measuring vibration response normal to its surface. Random tapping on the plate was combined with a harmonic input load from a shaker to resemble an influence of rotating components. The measurement data has a sampling frequency of 4096 Hz and a duration of 60 s.

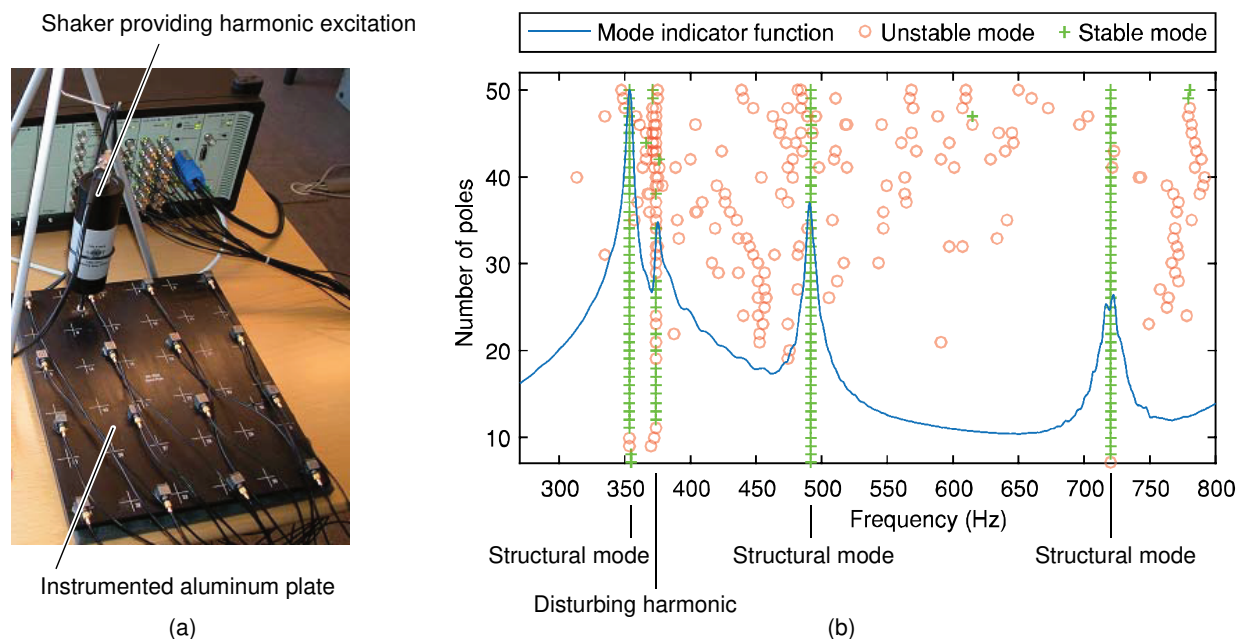


**Figure A-1: Experimental setup of the instrumented plate [46] (a), stabilization diagram of the plate by the ITD OMA method (b)**

The measured accelerations were analysed by 6 different OMA methods: Enhanced Frequency-Domain Decomposition (EFDD), Curve-fit Frequency-Domain Decomposition (CFDD), SSI Principal Components (SSI-PC), SSI Unweighted Principal Components (SSI-UPC), SSI Canonical Variate Analysis (SSI-CVA), multireference Ibrahim Time-Domain (ITD) method. As introduced in Subchapter 2.1, EFDD and CFDD are frequency-domain methods;

SSI-PC, SSI-UPC and SSI-CVA can be attributed to SSI-DATA methods; finally, ITD is an algorithm closely related to SSI-COV.

The ITD stabilization diagram in Figure A-1b clearly shows the first three structural modes. The detrimental impact of the input harmonic is also visible as it is identified as a stable mode. However, this is not necessarily problematic as long as the analyst is aware of this.

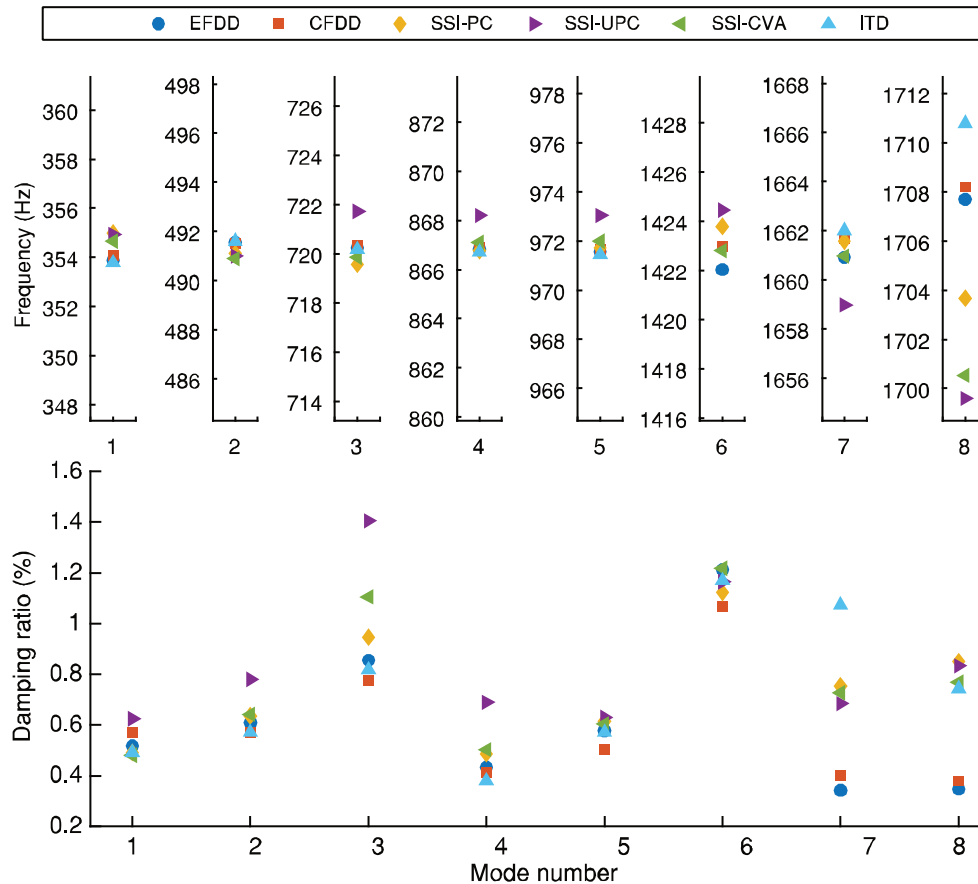


**Figure A-2: Eigenfrequencies (top) and damping ratios (bottom) of the plate estimated by 6 different OMA methods**

Modal parameters of 8 plate modes are estimated by all 6 OMA methods and illustrated in Figure A-2. It is visible that each method reports different values for the eigenfrequency and damping ratio, although the same structure and dataset were used for each OMA method. Analysing the structural response without harmonic excitation leads to the respective eigenfrequency and damping ratio of 354 Hz and 0.65 % for the first mode when using EFDD [46]. The estimated modal values presented in Figure A-2 do not significantly differ from these numbers. Therefore, it can be concluded that the estimation of the first mode is not disturbed by the harmonic excitation in neither of the compared OMA methods. This is due to the setup with a single harmonic, which has a low amplitude relative to the response of the neighbouring first mode as shown by Figure A-1b.

Nevertheless, the estimated modal parameters differ overall. The maximum relative deviations of the methods per mode are limited to 0.7% in eigenfrequencies (at mode 8) but reach 213% for the damping ratios (at mode 7).

## Appendix B Polyreference Least Squares Complex Frequency Domain (pLSCF) method for OMA

The Polyreference Least Squares Complex Frequency Domain (pLSCF/PolyMax) OMA method extends the LSCF method to consider multiple references, thereby increasing the method's theoretical performance to identify closely spaced modes. In contrast to LSCF, the method also does not require a Singular Value Decomposition (SVD) step, which not only adds computational effort but also results in a worse fit of the data to the modal model [210].

A detailed theoretical description of the pLSCF EMA method is given in [210]. It operates on FRFs as the primary input data. The OMA version of pLSCF is described in [211] and requires spectra from operational response measurements instead. On this foundation, this appendix describes the main steps of the operational pLSCF algorithm. The content from Appendix B.1 was published by the author of this thesis in [16].

### B.1 Spectrum estimation for data input

To calculate spectral estimations from the measurements, first the correlation function  $R$  is determined over the time lags  $i$  from the measurement samples  $y$ :

$$R_{yy,i} = \frac{1}{N} \sum_{k=0}^{N-1} y_{k+i} y_k^T \quad (\text{B.1})$$

When the correlation functions of positive time lags  $i$  are multiplied by a window weighting function  $w$  (to reduce frequency-domain leakage) and the DFT is applied, so-called half-spectra  $S_{yy}^+$  are obtained as shown in Equation (B.2) [211].  $L$  specifies the maximum time lag, which is typically much smaller than the total number of measurement samples  $N$  to avoid high variance that occurs at high time lags in correlation functions.

$$S^+(\omega) = \frac{w_0 R_0}{2} + \sum_{k=1}^L w_k R_{YY,k} \exp(-j\omega k \Delta t) \quad (\text{B.2})$$

In the same way, the cross spectra between all  $l$  outputs and a (smaller) set of  $m$  reference outputs are computed and assembled into an  $l \times m$  half spectrum matrix.

Due to the symmetry of full spectra, all information on the system dynamics is retained by the half spectra and a modal decomposition from the matrix of half spectra can be obtained as shown in Equation (B.3) [211]. Here,  $\{v_i\}$  are the mode shape vectors and  $\langle g_i \rangle$  are the operational reference factors, which are related to the modal participation factors known from EMA.

$$[S^+(\omega)] = \sum_{i=1}^n \frac{\{v_i\}\langle g_i \rangle}{j\omega - \lambda_i} + \frac{\{v_i^*\}\langle g_i^* \rangle}{j\omega - \lambda_i^*} \quad (\text{B.3})$$

There are different methods to calculate spectra and the previously described spectrum estimation is known as the weighted correlogram. An alternative is the modified Welch's periodogram, which estimates spectra directly from the DFT of window-weighted measurements without the need of correlation functions. The benefit of the weighted correlogram, however, is that an exponential window can be applied to reduce leakage, while the modified Welch's periodogram typically requires a Hann window, leading to a bias of modal damping estimates [211]. On the other hand, it has been also observed that spectrum estimations by the weighted correlogram method can result in decreased accuracy of the identified mode shapes [91], so it can be useful to apply both methods and compare the results considering these characteristics.

## B.2 Fitting of the model coefficients and determination of the poles

The matrix of spectrum estimations (using either half-spectra  $[S^+(\omega)] \in \mathbb{C}^{N_o \times N_r}$  or one-sided spectra  $[S(\omega)] \in \mathbb{C}^{N_o \times N_r}$  [91]) is used to fit a Right Matrix-Fraction Description (RMFD) model:

$$[S(\omega_f)] = [B(\omega_f)] \cdot [A(\omega_f)]^{-1} \quad (\text{B.4})$$

The RMFD model consists of a numerator matrix  $[B] \in \mathbb{C}^{N_o \times N_r}$  and a denominator matrix  $[A] \in \mathbb{C}^{N_r \times N_r}$  of the same dimensions.  $[B]$  and  $[A]$  are defined as polynomials with the basis functions  $\Omega^i(\omega)$  (also called the generalized transform variable), with the respective polynomial coefficients  $[\beta_i]$  and  $[\alpha_i]$  for increasing degrees  $i$  ( $i=1, \dots, N_p$ ) and with the polynomial order  $N_p$  as shown in Equation (B.5). For discrete frequency lines  $\omega_f$  ( $f=1, \dots, N_f$ ) the basis functions are written as  $\Omega_f^i$ , defined in Equation (B.6).

$$[B(\omega)] = \sum_{i=0}^{N_p} \Omega^i(\omega_f) [\beta_i], \quad [A(\omega)] = \sum_{i=0}^{N_p} \Omega^i(\omega_f) [\alpha_i] \quad (\text{B.5})$$

$$\Omega^i(\omega_f) = \Omega_f^i = e^{(j\omega_f \Delta t)i} \quad (\text{B.6})$$

Considering individual outputs  $o$  ( $o=1, \dots, N_o$ ), i.e. rows, of the GSD matrix  $\langle S_o(\omega) \rangle \in \mathbb{C}^{1 \times N_r}$ , Equation (B.4) can be formulated for individual rows of the numerator matrix  $\langle B_o \rangle \in \mathbb{C}^{1 \times N_r}$  with the common denominator matrix  $[A]$ :

$$\langle S_o(\omega_f) \rangle = \langle B_o(\omega_f) \rangle \cdot [A(\omega_f)]^{-1} \quad (\text{B.7})$$



$$\langle B_o(\omega_f) \rangle = \sum_{i=0}^{N_p} \Omega^i(\omega_f) \langle \beta_{o,i} \rangle \quad (\text{B.8})$$

The coefficients for increasing polynomial term degrees  $i$  are composed into the coefficient matrices  $[\beta_o] \in \mathbb{R}^{N_p+1 \times N_r}$  and  $[\alpha] \in \mathbb{R}^{N_r(N_p+1) \times N_r}$  as follows and are further combined into the coefficient matrix  $[\theta] \in \mathbb{R}^{(N_o+N_r)(N_p+1) \times N_r}$ :

$$[\beta_o] = \begin{bmatrix} \langle \beta_{o0} \rangle \\ \langle \beta_{o1} \rangle \\ \vdots \\ \langle \beta_{oN_p} \rangle \end{bmatrix}, \quad [\alpha] = \begin{bmatrix} [\alpha_0] \\ [\alpha_1] \\ \vdots \\ [\alpha_{N_p}] \end{bmatrix}, \quad [\theta] = \begin{bmatrix} [\beta_o] \\ [\beta_1] \\ \vdots \\ [\beta_{N_o}] \\ [\alpha] \end{bmatrix} \quad (\text{B.9})$$

Since the goal is to estimate the model coefficients  $[\theta]$ , the CSDs  $\langle S_o(\omega_f, \theta) \rangle$  modelled by the RMFD are written as a function of these coefficients. The error  $\langle \epsilon_o^{\text{NL}}(\omega_f, \theta) \rangle$  between the RMFD fit  $\langle S_o(\omega_f, \theta) \rangle$  and the CSD estimates from measured data  $\langle \hat{S}_o(\omega_f) \rangle$  is defined as:

$$\begin{aligned} \langle \epsilon_o^{\text{NL}}(\omega_f, \theta) \rangle &= w_o(\omega_f) (\langle S_o(\omega_f, \theta) \rangle - \langle \hat{S}_o(\omega_f) \rangle) \\ &= w_o(\omega_f) (\langle B_o(\omega_f, \beta_o) \rangle \cdot [A(\omega_f, \alpha)]^{-1} - \langle \hat{S}_o(\omega_f) \rangle) \end{aligned} \quad (\text{B.10})$$

Here, a scalar weighting function  $w_o(\omega_f) \in \mathbb{R}$  is introduced, which leads to a weighted least squares problem and allows frequency-dependent weighting of individual output channels in case of varying measurement noise or variance.

However, this error function has a nonlinear dependency on the coefficients  $[\theta]$  (denoted by the superscript “NL”) due to the matrix multiplication between  $\langle B_o \rangle$  and  $[A]^{-1}$  and their contained coefficients. It is therefore approximated into an linear error function  $\langle \epsilon_o^{\text{L}}(\omega_f, \theta) \rangle \in \mathbb{C}^{1 \times N_r}$  by multiplying the nonlinear error function with  $[A]$  [210]:

$$\begin{aligned} \langle \epsilon_o^{\text{L}}(\omega_f, \theta) \rangle &= \langle \epsilon_o^{\text{NL}}(\omega_f, \theta) \rangle \cdot [A(\omega_f, \alpha)] \\ &= w_o(\omega_f) (\langle B_o(\omega_f, \beta_o) \rangle - \langle \hat{S}_o(\omega_f) \rangle \cdot [A(\omega_f, \alpha)]) \\ &= w_o(\omega_f) \sum_{i=0}^{N_p} (\Omega_f^i \langle \beta_{o,i} \rangle - \Omega_f^i \langle \hat{S}_o(\omega_f) \rangle [\alpha_i]) \end{aligned} \quad (\text{B.11})$$

The linear error functions are then written in a matrix  $[E_o(\theta)] \in \mathbb{C}^{N_f \times N_r}$  with individual rows used for all frequency lines  $\omega_f$  [210]:

$$[E_o(\theta)] = \begin{bmatrix} \langle \epsilon_o^{\text{L}}(\omega_1, \theta) \rangle \\ \langle \epsilon_o^{\text{L}}(\omega_2, \theta) \rangle \\ \vdots \\ \langle \epsilon_o^{\text{L}}(\omega_{N_f}, \theta) \rangle \end{bmatrix} = \begin{bmatrix} [X_o] & [Y_o] \end{bmatrix} \begin{bmatrix} [\beta_o] \\ [\alpha] \end{bmatrix} \quad (\text{B.12})$$

The submatrices  $[X_o] \in \mathbb{C}^{N_f \times N_p + 1}$  and  $[Y_o] \in \mathbb{C}^{N_f \times N_r(N_p + 1)}$ , where the operator  $\otimes$  is used for the Kronecker product, are defined as:

$$[X_o] = \begin{bmatrix} w_o(\omega_1) \langle \Omega_1^0 & \Omega_1^1 & \cdots & \Omega_1^{N_p} \rangle \\ w_o(\omega_2) \langle \Omega_2^0 & \Omega_2^1 & \cdots & \Omega_2^{N_p} \rangle \\ \vdots \\ w_o(\omega_{N_f}) \langle \Omega_{N_f}^0 & \Omega_{N_f}^1 & \cdots & \Omega_{N_f}^{N_p} \rangle \end{bmatrix} \quad (\text{B.13})$$

$$[Y_o] = \begin{bmatrix} -w_o(\omega_1) \langle \Omega_1^0 & \Omega_1^1 & \cdots & \Omega_1^{N_p} \rangle \otimes \langle \hat{S}_o(\omega_1) \rangle \\ -w_o(\omega_2) \langle \Omega_2^0 & \Omega_2^1 & \cdots & \Omega_2^{N_p} \rangle \otimes \langle \hat{S}_o(\omega_2) \rangle \\ \vdots \\ -w_o(\omega_{N_f}) \langle \Omega_{N_f}^0 & \Omega_{N_f}^1 & \cdots & \Omega_{N_f}^{N_p} \rangle \otimes \langle \hat{S}_o(\omega_{N_f}) \rangle \end{bmatrix} \quad (\text{B.14})$$

To derive a (weighted) linear least squares equation, the loss function  $l_f$  is defined utilising the matrix trace (sum of the matrix entries on the main diagonal) denoted by  $\text{tr}(\bullet)$ :

$$\begin{aligned} l_f(\theta) &= \sum_{o=1}^{N_o} \text{tr}([E_o(\theta)]^H \cdot [E_o(\theta)]) \\ &= \sum_{o=1}^{N_o} \text{tr} \left( \begin{bmatrix} [\beta_o]^H & [\alpha]^H \end{bmatrix} \cdot \begin{bmatrix} [X_o]^H \\ [Y_o]^H \end{bmatrix} \cdot \begin{bmatrix} [X_o] & [Y_o] \end{bmatrix} \cdot \begin{bmatrix} [\beta_o] \\ [\alpha] \end{bmatrix} \right) \\ &= \sum_{o=1}^{N_o} \text{tr} \left( \begin{bmatrix} [\beta_o]^H & [\alpha]^H \end{bmatrix} \cdot \begin{bmatrix} [R_o] & [P_o] \\ [P_o]^T & [T_o] \end{bmatrix} \cdot \begin{bmatrix} [\beta_o] \\ [\alpha] \end{bmatrix} \right) \end{aligned} \quad (\text{B.15})$$

Here, the model coefficients  $[\theta]$  are assumed to be real-valued, which is enforced by taking the real parts for the calculation of the matrix components  $[R_o] \in \mathbb{R}^{N_p + 1 \times N_p + 1}$ ,  $[P_o] \in \mathbb{R}^{N_p + 1 \times N_r(N_p + 1)}$  and  $[T_o] \in \mathbb{R}^{N_r(N_p + 1) \times N_r(N_p + 1)}$ , as specified below:

$$\begin{aligned} [R_o] &= \text{Re}([X_o]^H \cdot [X_o]) \\ [P_o] &= \text{Re}([X_o]^H \cdot [Y_o]) \\ [T_o] &= \text{Re}([Y_o]^H \cdot [Y_o]) \end{aligned} \quad (\text{B.16})$$

To find the minimum of the loss function  $l(\theta)$ , Equation (B.15), its partial derivatives with respect to  $[\beta_o]$  and  $[\alpha]$  are set to zero:

$$\frac{\partial l(\theta)}{\partial \beta_o} = 2([R_o][\beta_o] + [P_o][\alpha]) = [0], \quad \forall o = 1, \dots, N_o \quad (\text{B.17})$$

$$\Rightarrow [\beta_o] = -[R_o]^{-1}[P_o][\alpha]$$

$$\frac{\partial l(\theta)}{\partial \alpha} = 2 \sum_{o=1}^{N_o} ([P_o]^T[\beta_o] + [T_o][\alpha]) = [0] \quad (\text{B.18})$$

The expression for  $[\beta_o]$  from Equation (B.17) is substituted into Equation (B.18), which eliminates the  $\beta$  coefficients and reduces the number of equations to be solved. This provides the so-called reduced normal equations with the matrix  $[M] \in \mathbb{R}^{N_r(N_p+1) \times N_r(N_p+1)}$ :

$$\underbrace{\left[ 2 \sum_{o=1}^{N_o} ([T_o] - [P_o]^T [R_o]^{-1} [P_o]) \right]}_{=[M]} [\alpha] = [M][\alpha] = [0] \quad (\text{B.19})$$

A constraint is introduced to the denominator coefficients  $[\alpha]$  to avoid the trivial solution of  $[\alpha] = [0]$ . This also resolves the parameter redundancy of the RMFD model, where different solutions of  $[\alpha]$  satisfy Equation (B.4) [210], [212]. For this purpose, the denominator coefficient matrix  $[\alpha_i]$  of the lowest polynomial order term is constrained to the  $(N_r \times N_r)$  identity matrix  $[I_{N_r}]$ , i.e.  $[\alpha_0] = [I_{N_r}]$ . As shown in Equation (B.20), by considering the submatrices of  $[M]$  and  $[\alpha]$ , the submatrix  $[\alpha_s]$  is obtained, which provides the least squares estimate for coefficient matrices of the remaining polynomial terms [157].

$$\begin{aligned} [M][\alpha] &= \begin{bmatrix} [M_{s11}] & [M_{s12}] \\ [M_{s21}] & [M_{s22}] \end{bmatrix} \begin{bmatrix} [I_{N_r}] \\ [\alpha_s] \end{bmatrix} = [0] \\ &\Rightarrow \\ &[\alpha_s] = -[M_{s22}]^{-1} [M_{s21}] \end{aligned} \quad (\text{B.20})$$

The full matrix  $[\alpha]$ , containing coefficient matrices of all orders, is then reconstructed as [91]:

$$[\alpha] = \begin{bmatrix} [I_{N_r}] \\ [\alpha_s] \end{bmatrix} = \begin{bmatrix} [I_{N_r}] \\ -[M_{s22}]^{-1} [M_{s21}] \end{bmatrix}, \quad (\text{B.21})$$

where

$$[M_{s22}] = \left[ M_{(N_r+1:(N_p+1)N_r, N_r+1:(N_p+1)N_r)} \right],$$

$$[M_{s21}] = \left[ M_{(N_r+1:(N_p+1)N_r, 1:N_r)} \right]$$

Here, the submatrices of  $[M]$  are written with the subscript notation  $[M_{(R_1:R_n, C_1:C_n)}]$ , where  $R_1$  and  $R_n$  denote the first and last row (with intermediate rows) taken from  $[M]$  into the submatrix, respectively, and similarly  $C_1$  and  $C_n$  specify the first and last column number included into the submatrix.

A common approach to determine the roots of a polynomial is to solve the eigenvalue problem of the polynomial's companion matrix [213]. With this technique, the companion matrix  $[A_C] \in \mathbb{R}^{N_r N_p \times N_r N_p}$  in Equation (B.22) is constructed from the denominator matrix coefficients of the pLSCF model [192].

$$[A_C] = \begin{bmatrix} -[\alpha_1] & -[\alpha_2] & \cdots & -[\alpha_{N_p-1}] & -[\alpha_{N_p}] \\ [I_{N_r}] & [0] & \cdots & [0] & [0] \\ [0] & [I_{N_r}] & \cdots & [0] & [0] \\ \vdots & \vdots & \ddots & \vdots & \vdots \\ [0] & [0] & \cdots & [I_{N_r}] & [0] \end{bmatrix} \quad (\text{B.22})$$

Solving the standard eigenvalue problem of the companion matrix  $[A_C]$  in Equation (B.22) provides  $N_p N_o$  poles  $z_{i_\lambda}$  of the RMFD model [210].

$$([A_C] - z_{i_\lambda}[I])\{V_{i_\lambda}\} = \{0\} \quad (\text{B.23})$$

Corresponding to the used basis functions as per Equation (B.6), the poles derived from the eigensolution are likewise in z-domain and are transformed into the Laplace domain with the following relation [91], [192].

$$z_{i_\lambda} = e^{\lambda_{i_\lambda} \Delta t} \Rightarrow \lambda_{i_\lambda} = \frac{\ln(z_{i_\lambda})}{\Delta t} \quad (\text{B.24})$$

Thereafter, the eigenfrequencies and damping ratios of the estimated dynamic system can be derived from poles  $\lambda_{i_\lambda}$  as shown earlier using Equations (3.10)-(3.12). The corresponding eigenvector  $\{V_{i_\lambda}\}$  of the companion matrix is related to the operational reference vector  $\langle g_{i_\lambda} \rangle \in \mathbb{C}^{1 \times N_r}$  as shown in Equation (B.25) [192], [214]. As a result, the operational reference vector for the mode  $i_\lambda$  is obtained from the last  $N_r$  rows of  $\{V_{i_\lambda}\}$ .

$$\{V_{i_\lambda}\} = \begin{Bmatrix} z_{i_\lambda}^{N_p-1} \{g_{i_\lambda}^T\} \\ \vdots \\ z_{i_\lambda} \{g_{i_\lambda}^T\} \\ \{g_{i_\lambda}^T\} \end{Bmatrix} \quad (\text{B.25})$$

The mode shapes can be derived from the RMFD model directly, which requires to restore the numerator coefficient matrices  $[\beta_o]$  from the estimated  $[\alpha]$  coefficients using the relationship in Equation (B.17). However, a more common approach is to apply a second LS-based calculation to determine the residues and mode shapes from the measured CSD with the Least Squares Frequency Domain (LSFD) method. This approach is preferred as it leads to a more consistent modal model with greater mode shape estimation accuracy [215]. As such, the LSFD method is described in detail in Appendix C.

## B.3 Implementation variants of pLSCF

### B.3.1 Basis functions in the Laplace or z domain

Originally, the LSCF method (the single-reference predecessor method to pLSCF) was formulated in the Laplace domain with basis functions defined as:

$$\Omega^i(\omega_f) = \Omega_f^i = (j\omega_f)^i \quad (\text{B.26})$$

Since then, however, the use of the z domain (Equation (B.6)) is typically preferred to the Laplace domain (Equation (B.26)) because of its favourable numerical conditioning [91]. The reason is that, in the z domain, the polynomials are orthogonal and the frequencies  $\omega_f$  are wrapped around the unit circle in the complex plane, as seen from Equation (B.6). Although the frequency wrapping bears the danger of aliasing of out-of-band modes [191], the benefit is that values of the basis function remain bounded to the magnitude of 1. In contrast to that, the standard power polynomials in the Laplace domain in Equation (B.26) grow exponentially with  $i$ , severely limiting the usable model order  $i$  and analysed frequency bandwidth (i.e.,  $\omega_f$ ). The unbounded growth of the basis functions can be avoided by a normalisation of the frequencies to  $\omega_f \in [-1,1]$ . However, as a result, the basis functions tend to zero at high model orders  $i$ , also leading to ill-conditioning. A more stable alternative is the use of orthogonal polynomials [216].

### B.3.2 Real or complex-valued polynomial coefficients

In the presented implementation, real-valued coefficients [ $\theta$ ] are assumed and enforced with Equation (B.16). A discussion on the choice of real or complex polynomial coefficients in the LSCF method is given in [217]. The author describes that complex-valued coefficients are preferred because, in that case, the polynomial order can be halved to estimate the same number of modes compared to the use of real-valued coefficients.

In own observations of the pLSCF implementation with complex-valued coefficients, the first poles are indeed estimated at lower orders, as shown in Figure B-1 (right). At the same time, however, with the complex-valued implementation, the stabilisation of modes can suffer (assuming the same stabilisation criteria) and the stabilisation diagrams become less clear with more computational poles. Furthermore, higher model orders are less critical when the z domain implementation is used, as explained in the previous paragraph. These reasons also likely explain why the majority of published pLSCF descriptions appears to implement real-valued coefficients as shown in Table B-1.

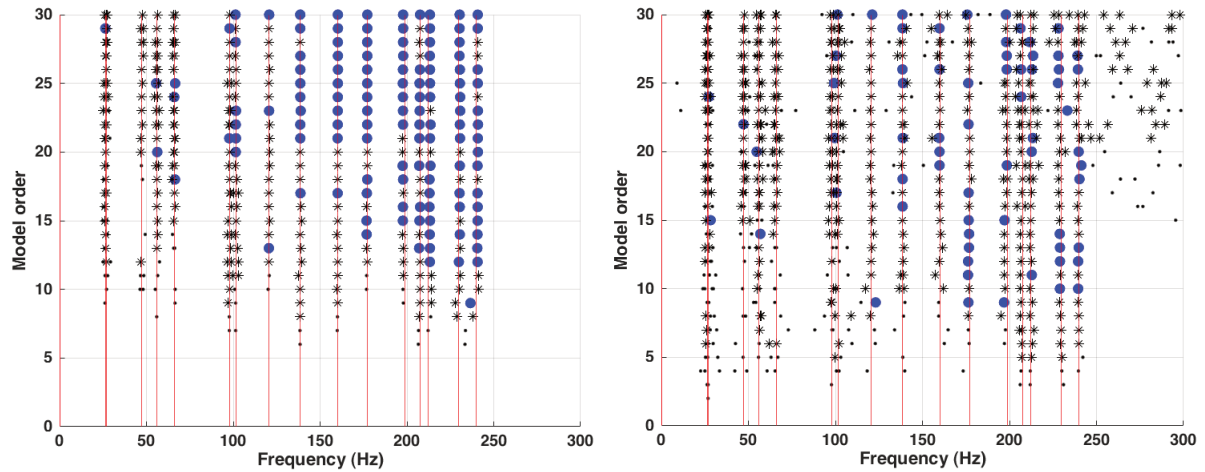


**Figure B-1: Stabilisation diagrams of pLSCF implementations with real-valued (left) and complex-valued (right) polynomial coefficients (unstable poles: \*, stabilised frequency: \*, stabilised frequency and damping: ●, target frequencies: red vertical lines)**

### B.3.3 Order of the constrained coefficient and sign of the basis function power

While in Equation (B.21) a least squares solution is provided for the case where the coefficient matrix  $[\alpha_0]$  of the lowest order is constrained, alternatively, the following equation is formulated when the coefficient matrix  $[\alpha_{N_p}]$  of the highest order  $N_p$  is constrained [91]:

$$[\alpha] = \begin{bmatrix} -[M_{(1:N_p N_r, 1:N_p N_r)}]^{-1} [M_{(1:N_p N_r, N_p N_r + 1:(N_p + 1)N_r)}] \\ [I_{N_r}] \end{bmatrix} \quad (\text{B.27})$$

In [218] it is shown that, depending on the chosen order (highest or lowest) of the constrained coefficient, a solution of the system is found containing either only stable or only unstable poles with both solutions being mathematically valid. It is also shown that this change of the constrained coefficient is equivalent to a change of the basis functions between  $\Omega_f^i$  and  $\Omega_f^{-i}$ . This results in a pair-wise combination for which the desired solution of only stable physical poles is obtained:

- Basis function  $\Omega_f^i$  with a constrained coefficient matrix of the lowest order (as described in Appendix B.2)
- Basis function  $\Omega_f^{-i}$  with a constrained coefficient matrix of the highest order (as described in this section)

In the latter case, the corresponding companion matrix (previously Equation (B.22)) for the extraction of poles and operational reference vectors adapts the following form [214]:

$$[A_C] = \begin{bmatrix} -[\alpha_{N_p-1}] & -[\alpha_{N_p-2}] & \cdots & -[\alpha_1] & -[\alpha_0] \\ [I_{N_r}] & [0] & \cdots & [0] & [0] \\ [0] & [I_{N_r}] & \cdots & [0] & [0] \\ \vdots & \vdots & \ddots & \vdots & \vdots \\ [0] & [0] & \cdots & [I_{N_r}] & [0] \end{bmatrix} \quad (\text{B.28})$$

To conclude this appendix, Table B-1 gives an overview of different implementation variants of pLSCF found in literature in chronological order. Further evaluations on the sign of the basis function exponent (positive or negative) and on the order used for the identity parameter constraint can be found in [218]. Verboven [219] discussed the solving of the coefficient matrix and the differences resulting from a complex or real coefficient matrix.

**Table B-1: Overview of pLSCF implementation variants in literature**

Reference, year	Basis function exponent	Parameter identity constraint of which order	Weighted	Companion matrix (types according to [220])	Toeplitz matrices real or imaginary
[212], 2003	Negative	Highest	Yes	N/A	Real
[210], 2004	Positive	N/A	Yes	N/A	Real
[221], 2004	Negative	Highest	Yes	N/A	Real
[222], 2004	Negative	N/A	N/A	Bottom, increasing	N/A
[211], 2007	Positive	N/A	N/A	N/A	N/A
[223], 2010	Negative	Highest	Yes	Top, decreasing	Complex
[157], 2012	Positive	Highest	No	N/A	Complex
[91], 2014	Positive	Highest	No	Top, decreasing	Complex
[91], 2014	Negative	Lowest	N/A	Top, decreasing	N/A
[216], 2015	Positive	Lowest	N/A	Top, increasing	N/A
[192], 2015	N/A	Highest	N/A	Bottom, increasing	N/A
[214], 2016	Negative	N/A	N/A	Top, decreasing	N/A
[224], 2017	Positive	Highest	Yes	Top, decreasing	Complex
[225], 2019	Negative	Highest	Yes	Bottom, increasing	Real
[226], 2019	Negative	Highest	No	Bottom, increasing	Real

N/A: not available, i.e., not specified

## Appendix C Least Squares Frequency Domain (LSFD) method for the determination of mode shapes and residues

This appendix describes the LSFD method, which is a common approach to fit mode shapes or residue matrices to measured CSD data once estimations of the system poles (i.e. eigenfrequencies and damping ratios) are available. The required pole estimations can stem from the pLSCF method described in the previous appendix or other OMA algorithms. Although the LSFD method is widely applied in several configurations, there appears to be a lack of accessible literature to cover the method and its variations in a comprehensive and generalised way (in terms of independent number of references and outputs). This shortcoming is addressed by this appendix. For example, the single-reference and multi-reference formulations of LSFD for the determination of residue matrices are given in [91]. However, residual factors, used to model the influence of out-of-band modes are not estimated and the multi-reference estimation is only presented for square residue matrices. The references [214] and [227] incorporate the estimation of upper and lower out-of-band residuals but are limited to a single-reference estimation of residue matrices. The estimation of residue matrices (instead of mode shapes) described by the listed references neglects one of the major benefits of pLSCF compared to LSCF [210]. That is, operational reference vectors (in case of OMA) or modal participation vectors in case of EMA) are estimated from pLSCF, which allows to estimate mode shapes directly, without residue estimation and SVD, as will be explained further below.

The LSFD method estimates the pole-residue modal model (also known as the partial fraction description) shown in Equation (B.3). The model is expanded below to include residual factors in matrices  $[LR] \in \mathbb{R}^{N_o \times N_r}$  and  $[UR] \in \mathbb{R}^{N_o \times N_r}$ .  $[LR]$  models the contribution, that the lower frequency range of modes at frequencies exceeding the analysis band have. Similarly, the purpose of  $[UR]$  is to express the effect of the upper frequency range of modes, which fall below the analysed frequency range. Individual elements of these matrices correspond to the respective matrix elements (i.e. CSDs) in  $[S(\omega)] \in \mathbb{C}^{N_o \times N_r}$  and can be considered as slope factors of the spectral contributions of out-of-band modes. The proportionality in relation to the frequency axis or value  $j\omega$  depends on the foundational physical quantity of the spectra (displacement, velocity, or acceleration) [149] and type of spectra (FRF, full or half spectra) [211]. Corresponding to the case of full acceleration spectra [211], the model equation below describes  $[LR]$  with proportionality to 1 (constant value function) and  $[UR]$  as the slope of the frequency to the power of four.



$$[S(\omega)] = \sum_{i_\lambda=1}^{N_\lambda} \left( \frac{\{v_{i_\lambda}\}\langle g_{i_\lambda} \rangle}{j\omega - \lambda_{i_\lambda}} + \frac{\{v_{i_\lambda}^*\}\langle g_{i_\lambda}^* \rangle}{j\omega - \lambda_{i_\lambda}^*} \right) + [LR] + (j\omega)^4 [UR] \quad (C.1)$$

The outer product of the mode shape vector  $\{v\}$  and operational reference vector  $\langle g \rangle$  results in the residue matrix  $[R] \in \mathbb{C}^{N_o \times N_r}$ . As seen in Equation (C.2), each column of  $[R]$  contains the mode shape vector  $\{v\}$  scaled by an entry of  $\langle g \rangle$ .

$$[R_{i_\lambda}] = \{v_{i_\lambda}\}\langle g_{i_\lambda} \rangle = \begin{Bmatrix} v_1 \\ v_2 \\ \vdots \\ v_{N_o} \end{Bmatrix}_{i_\lambda} \langle g_1 \ g_2 \ \cdots \ g_{N_r} \rangle_{i_\lambda} = \begin{bmatrix} v_1 g_1 & \cdots & v_1 g_{N_r} \\ \vdots & \ddots & \vdots \\ v_{N_o} g_1 & \cdots & v_{N_o} g_{N_r} \end{bmatrix}_{i_\lambda} \quad (C.2)$$

The pole-residue model can be resembled by the algebraic linear Equation (C.3):

$$[A][\bar{R}] = [\bar{S}] \quad (C.3)$$

In case of the single-reference estimation of residue matrix components, the Equation (C.3) consists of the matrices  $[A] \in \mathbb{C}^{N_f \times 2N_\lambda + 2}$ ,  $[\bar{R}] \in \mathbb{C}^{2N_\lambda + 2 \times N_o}$ , and  $[\bar{S}] \in \mathbb{C}^{N_f \times N_o}$  given below. The unknown parameters (i.e. elements of the residuals  $[LR]$ ,  $[UR]$  and residue matrices  $[R_{i_r}]$  for a single reference  $i_r$  and all  $N_\lambda$  modes) are separated in the matrix  $[\bar{R}]$ .

$$[A] = \begin{bmatrix} \frac{1}{j\omega_1 - \lambda_1} & \frac{1}{j\omega_1 - \lambda_1^*} & \cdots & \frac{1}{j\omega_1 - \lambda_{N_\lambda}} & \frac{1}{j\omega_1 - \lambda_{N_\lambda}^*} & 1 & (j\omega_1)^4 \\ \vdots & \vdots & \ddots & \vdots & \vdots & \vdots & \vdots \\ 1 & 1 & \cdots & 1 & 1 & 1 & (j\omega_{N_f})^4 \\ \frac{1}{j\omega_{N_f} - \lambda_1} & \frac{1}{j\omega_{N_f} - \lambda_1^*} & \cdots & \frac{1}{j\omega_{N_f} - \lambda_{N_\lambda}} & \frac{1}{j\omega_{N_f} - \lambda_{N_\lambda}^*} & 1 & (j\omega_{N_f})^4 \end{bmatrix} \quad (C.4)$$

$$[\bar{R}] = \begin{bmatrix} \langle v_1 g_{i_r} \rangle \cdots \langle v_{N_o} g_{i_r} \rangle_1 \\ \langle v_1 g_{i_r} \rangle \cdots \langle v_{N_o} g_{i_r} \rangle_1^* \\ \vdots \\ \langle v_1 g_{i_r} \rangle \cdots \langle v_{N_o} g_{i_r} \rangle_{N_\lambda} \\ \langle v_1 g_{i_r} \rangle \cdots \langle v_{N_o} g_{i_r} \rangle_{N_\lambda}^* \\ \langle LR_{(:,i_r)}^T \rangle \\ \langle UR_{i_r} \rangle \end{bmatrix} \quad (C.5)$$

$$[\bar{S}] = \begin{bmatrix} \langle S_{(:,i_r)}^T(\omega_1) \rangle \\ \vdots \\ \langle S_{(:,i_r)}^T(\omega_{N_f}) \rangle \end{bmatrix} \quad (C.6)$$

An approximation  $[\bar{R}_{LS}]$  is found for the parameters in matrix  $[\bar{R}]$  using the least squares method by taking the pseudo inverse  $[A^\dagger]$  of  $[A]$  as shown in (C.7). This is equivalent to the minimisation of the squared difference between the modelled and measured spectrum function matrix  $[S(\omega)]$  for reference  $i_r$ .

$$[\bar{R}_{LS}] = \underbrace{([A^H][A])^{-1}[A^H]}_{[A^\dagger]} [\bar{S}] \quad (C.7)$$

Single vectors for each residue matrix  $[R_{i_\lambda}]$  are obtained in Equation (C.5) because a single reference  $i_r$  is used. Comparing the matrix elements from Equation (C.2) and (C.5) shows that row vectors in  $[\bar{R}]$  correspond to transposed column vectors in  $[R_{i_\lambda}]$ . As explained with Equation (C.2), these vectors can be readily used as mode shape estimations.

The structure of the pole-residue model in Equation (C.1) with terms in conjugate pairs is also reflected by the conjugate pair entries in  $[A]$  and unknown parameter matrix  $[\bar{R}]$ . However, the LS approximation does not mathematically enforce that the resulting parameters in  $[\bar{R}]$  are actual complex conjugates. This eases the restrictions to the solution compared to the modal model and thus negatively impacts the model consistency. To address this issue, an alternative formulation of the pole-residue model can be used as shown in Equation (C.8). It is based on the assumption of hysteresis damping with coefficients  $\eta \approx 2\xi$  and is often more realistic compared to the common assumption of viscous damping [214].

$$[S(\omega)] = \sum_{i_\lambda=1}^{N_\lambda} \left( \frac{\{v_{i_\lambda}\}\{g_{i_\lambda}\}}{\omega_{i_\lambda}^2 - \omega^2 + j\eta_{i_\lambda}\omega^2} \right) + [LR] + (j\omega)^4 [UR] \quad (C.8)$$

For conciseness, in the following the denominators of the modal model from Equation (C.8) are denoted in a short form:

$$d_{i_f, i_\lambda} = \omega_{i_\lambda}^2 - \omega_{i_f}^2 + j\eta_{i_\lambda}\omega_{i_f}^2 \quad (C.9)$$

By constructing Equation (C.8) in the matrix form of Equation (C.3), the matrices  $[A]$  and  $[\bar{R}]$  are reduced in size and change as follows:

$$\underbrace{\begin{bmatrix} 1 & \dots & 1 & 1 & (j\omega_1)^4 \\ d_{1,1} & \dots & d_{1,N_\lambda} & \vdots & \vdots \\ \vdots & \ddots & \vdots & \vdots & \vdots \\ 1 & \dots & 1 & 1 & (j\omega_{N_f})^4 \\ d_{N_f,1} & \dots & d_{N_f,N_\lambda} & \vdots & \vdots \end{bmatrix}}_{[A] \in \mathbb{C}^{N_f \times N_\lambda + 2}} \underbrace{\begin{bmatrix} \langle v_1 g_{i_r} \rangle \dots \langle v_{N_o} g_{i_r} \rangle_1 \\ \vdots \\ \langle v_1 g_{i_r} \rangle \dots \langle v_{N_o} g_{i_r} \rangle_{N_\lambda} \\ \langle LR_{(:,i_r)}^T \rangle \\ \langle LR_{(:,i_r)}^T \rangle \end{bmatrix}}_{[\bar{R}] \in \mathbb{C}^{N_\lambda + 2 \times N_o}} = \underbrace{\begin{bmatrix} \langle S_{(:,i_r)}^T(\omega_1) \rangle \\ \vdots \\ \langle S_{(:,i_r)}^T(\omega_{N_f}) \rangle \end{bmatrix}}_{[\bar{S}] \in \mathbb{C}^{N_f \times N_o}} \quad (C.10)$$

To consider  $N_r$  references in the LS fit, the equation matrices are extended to a multi-reference formulation as follows:

$$\underbrace{\begin{bmatrix} [I_{N_r}] & \dots & [I_{N_r}] & [I_{N_r}] & (j\omega_1)^4 [I_{N_r}] \\ d_{1,1} & \dots & d_{1,N_\lambda} & \vdots & \vdots \\ \vdots & \ddots & \vdots & \vdots & \vdots \\ [I_{N_r}] & \dots & [I_{N_r}] & [I_{N_r}] & (j\omega_{N_f})^4 [I_{N_r}] \\ d_{N_f,1} & \dots & d_{N_f,N_\lambda} & \vdots & \vdots \end{bmatrix}}_{[A] \in \mathbb{C}^{N_r N_f \times N_r(N_\lambda + 2)}} \underbrace{\begin{bmatrix} [R_{i_1}]^T \\ \vdots \\ [R_{N_\lambda}]^T \\ [LR]^T \\ [UR]^T \end{bmatrix}}_{[\bar{R}] \in \mathbb{C}^{N_r(N_\lambda + 2) \times N_o}} = \underbrace{\begin{bmatrix} [S(\omega_1)]^T \\ \vdots \\ [S(\omega_{N_f})]^T \end{bmatrix}}_{[\bar{S}] \in \mathbb{C}^{N_r N_f \times N_o}} \quad (C.11)$$

From modal analysis theory it follows that  $\text{rank}([R_{i_\lambda}]) = 1$ , which is visible in the definition of the residue matrix in Equation (C.2). That is, there is one linearly independent vector in the row and column space of  $[R_{i_\lambda}]$ . Following this assumption, the first column of the left-singular vector matrix  $[U]$  from the SVD of  $[R_{i_\lambda}]$  in Equation (C.12) represents the estimated mode shape  $\{v_{i_\lambda}\}$  [91].

$$[R_{i_\lambda}] = [U][\Sigma][V]^T \quad (\text{C.12})$$

However, the least squares solution of Equation (C.11) does not enforce that the estimated parameters in  $[\bar{R}]$  adhere to the assumption of  $\text{rank}([R_{i_\lambda}]) = 1$ . This first improves the fit with inconsistent residue matrices but subsequently worsens the same, once the mode shapes for the modal model are determined through SVD [91], [211]. Moreover, the assumption also does not hold in case of mode multiplicity [212].

This issue is resolved with pLSCF because it determines the operational reference vectors in addition to system poles as shown with Equation (B.25). The SVD step then avoided by adapting the LSFD to utilise the operational reference vectors and to determine mode shapes estimates directly. This approach is illustrated below.

The single reference adaptation of the LSFD method to derive mode shapes directly results from Equation (C.10) by placing the operational reference factors  $g_{i_r, i_\lambda}$  from  $[\bar{R}]$  into  $[A]$  as shown below:

$$\underbrace{\begin{bmatrix} \frac{g_{i_r,1}}{d_{1,1}} & \dots & \frac{g_{i_r, N_\lambda}}{d_{1, N_\lambda}} & 1 & (j\omega_1)^4 \\ \vdots & \ddots & \vdots & \vdots & \vdots \\ \frac{g_{i_r,1}}{d_{N_f,1}} & \dots & \frac{g_{i_r, N_\lambda}}{d_{N_f, N_\lambda}} & 1 & (j\omega_{N_f})^4 \end{bmatrix}}_{[A] \in \mathbb{C}^{N_f \times N_\lambda + 2}} \underbrace{\begin{bmatrix} \langle v_1 \dots v_{N_o} \rangle_1 \\ \vdots \\ \langle v_1 \dots v_{N_o} \rangle_{N_\lambda} \\ \langle LR_{(:, i_r)}^T \rangle \\ \langle LR_{(:, i_r)}^T \rangle \end{bmatrix}}_{[\bar{R}] \in \mathbb{C}^{N_\lambda + 2 \times N_o}} = \underbrace{\begin{bmatrix} \langle S_{(:, i_r)}^T(\omega_1) \rangle \\ \vdots \\ \langle S_{(:, i_r)}^T(\omega_{N_f}) \rangle \end{bmatrix}}_{[S] \in \mathbb{C}^{N_f \times N_o}} \quad (\text{C.13})$$

The multi-reference implementation is based on the expansion below. It reduces to the single-reference variant from Equation (C.13) for  $N_r=1$ .

$$\underbrace{\begin{bmatrix} \left[ \begin{array}{ccc} \frac{g_{1,1}}{d_{i_f,1}} & \dots & \frac{g_{1, N_\lambda}}{d_{i_f, N_\lambda}} \\ \vdots & \ddots & \vdots \\ \frac{g_{N_r,1}}{d_{i_f,1}} & \dots & \frac{g_{N_r, N_\lambda}}{d_{i_f, N_\lambda}} \end{array} \right] & \begin{bmatrix} I_{N_r} \\ \vdots \\ I_{N_r} \end{bmatrix} & (j\omega_{i_f})^4 \begin{bmatrix} I_{N_r} \\ \vdots \\ I_{N_r} \end{bmatrix} \\ \dots & \dots & \dots \\ \dots & \dots & \dots \end{bmatrix}}_{[A] \in \mathbb{C}^{N_r N_f \times N_\lambda + 2 N_r}} \underbrace{\begin{bmatrix} \langle v_1 \dots v_{N_o} \rangle_1 \\ \vdots \\ \langle v_1 \dots v_{N_o} \rangle_{N_\lambda} \\ [LR]^T \\ [UR]^T \end{bmatrix}}_{[\bar{R}] \in \mathbb{C}^{N_\lambda + 2 N_r \times N_o}} = \underbrace{\begin{bmatrix} [S(\omega_1)]^T \\ \vdots \\ [S(\omega_{N_f})]^T \end{bmatrix}}_{[S] \in \mathbb{C}^{N_r N_f \times N_o}} \quad (\text{C.14})$$

## Appendix D Supplementary dataset information

This document describes the file structure of the dataset proposed in Chapter 4 and the usage of the open-source code to generate additional simulated time response. The open source dataset as well as the content of this appendix are submitted to a data repository [19] and are currently under peer review along with the corresponding journal paper submission [18].

### D.1 Dataset file structure

The simulation time responses are provided as arrays stored as MATLAB (.mat) files. The folder structure and file contents are given in Table D-2. The data files are subdivided into subfolders depending on the varied simulation parameter:

**Table D-1: Simulation parameters with corresponding dataset subfolder names and program code variables**

Varied parameter	Dataset subfolder	Variable name in “ExpParametricSim.m”
Run-up duration	VarDur	t_dur
Harmonic amplitude ratio	VarHarm	exc_harm_rat_loop
Measurement noise ratio	VarNoise	meas_noise_perc_loop

For illustration and visual verification purposes, each of the subfolders contains a subfolder “plots” with a power spectral density and a spectrogram plot generated from each data file.

**Table D-2: Dataset folder and file structure**

Dataset		
VarDur	VarHarm	VarNoise
714_10_4000_0.8_1.mat	714_100_4000_0.0_1.mat	714_100_4000_0.6_1_0.mat
714_10_rpm.mat	714_100_4000_0.2_1.mat	714_100_4000_0.6_1_0.5.mat
714_10_t.mat	714_100_4000_0.4_1.mat	714_100_4000_0.6_1_1.mat
714_20_4000_0.8_1.mat	714_100_4000_0.6_1.mat	714_100_4000_0.6_1_2.mat
714_20_rpm.mat	714_100_4000_0.8_1.mat	714_100_4000_0.6_1_4.mat
714_20_t.mat	714_100_4000_1.0_1.mat	714_100_4000_0.6_1_8.mat
714_40_4000_0.8_1.mat	714_100_rpm.mat	714_100_4000_0.6_1_16.mat
714_40_rpm.mat	714_100_t.mat	714_100_rpm.mat
714_40_t.mat	plots	714_100_t.mat
714_80_4000_0.8_1.mat		plots
714_80_rpm.mat		
714_80_t.mat		
714_160_4000_0.8_1.mat		
714_160_rpm.mat		
714_160_t.mat		
714_320_4000_0.8_1.mat		
714_320_rpm.mat		
714_320_t.mat		
plots		

The file names of the model response arrays adhere to the following labelling pattern:

<approx. sampling frequency (Hz)>\_<run duration (s)>\_<Excitation RMS sum  $\Sigma_{i2}$  at end of run (N)>\_<harmonic ratio  $h_{rat}$ >\_<random sample>\_<measurement noise (%)>

“Random sample” refers to the repetition number of the simulation run with another generated sample of the random excitation signal. As a foundation, a single run per parameter variation is provided in the published dataset. However, an arbitrary number of repetitions can be readily generated with the provided source code in “ExpParametricSim.m” by increasing the integer value of the variable “exc\_rand\_samples”, which can be useful for Monte Carlo studies.

Files storing the simulated model response contain 2D arrays, where each row represents a time step, and each column represents the model DOF number. Data values are accelerations in  $m/s^2$ . Model DOF numbers in X and Y direction are related to the model node numbers  $i_{node}$  as follows:

$$\begin{aligned} DOF_X &= 2 i_{node} - 1 \\ DOF_Y &= 2 i_{node} \end{aligned} \quad (D.1)$$

Additional data files ending with “\_t.mat” and “\_rpm.mat” contain 1D arrays of the time (s) and rpm values per sample, respectively.

## D.2 Program code for data generation

The folder “SourceCode” contains two further subfolders “Matlab” and “Abaqus”. These subfolders contain program code for the respective software environment (MATLAB and Abaqus), which can be used for replication, adaptation, and expansion of the provided simulation dataset.

The following sections give an introduction on the utilisation of these files.

### D.2.1 MATLAB

The main program routine of the subfolder “Matlab” is in the MATLAB script file “ExpParametricSim.m”. The beginning of the file contains user-specified program settings, such as the simulation time step frequency (variable “fs\_sim”) and target downsampled output frequency (variable “fs\_target”). Values for the presented simulation parameters of the dataset are provided as lists into the variables listed in Table D-1. On execution of “ExpParametricSim.m”, simulated time responses, time and rpm vectors are generated and stored per default inside the subfolder “sim\_output”.

The remaining files in the “Matlab” subfolder are dependencies of the main routine and provide the system matrices (“SysMatrices.mat”) and functions such as labelling (“MapToStr.m”), time integration (“NewmarkResp.m”), and output signal downsampling (“FilterDownsample.m”).

## D.2.2 Abaqus

For the present dataset, the MATLAB routine (described in the previous section) is recommended over the Abaqus-based simulation routine described below. The reason is that more execution steps and a longer simulation duration are required for an equivalent output. Nevertheless, the program code and description for the Abaqus-based approach are provided as an alternative to MATLAB and to share an adaptable procedure for other parametric simulations with higher complexity, which can require the Abaqus platform.

The main program routine of the subfolder “Abaqus” is in the Python script file “GenerateAbqInps.py”. The beginning of the file contains user-specified program settings, which are similar but not equal to the functionality of the previously described MATLAB-based code. For example, the simulation time step interval is set by the variable “t\_incr”, but downsampling would require a separate post-processing step after simulating with Abaqus and reading in the simulated response data.

On execution of “GenerateAbqInps.py”, the script generates a series of excitation signals based on the user-set parameters, fills them into a prepared Abaqus input file (“\_template.inp” from the subfolder “generated\_abq\_inps”), and saves it as a separate Abaqus input file for each parameter variation. For this purpose, the template file “\_template.inp” contains the following placeholder tags, which are automatically replaced by script-generated data:

```
{job_name}, {fx_name}, {fy_name}, {f_interval}, {max_sim_incr}, {sim_duration},  
{fx_sequence}, {fy_sequence}
```

Per default, “GenerateAbqInps.py” saves the filled Abaqus input files into the subfolder “generated\_abq\_inps” along with a single Windows batch (.bat) file, containing commands to execute Abaqus simulation jobs on each of the created Abaqus input files.

Execution of the batch file starts the Abaqus simulations, each of which generates an Abaqus output database (.odb) file with simulation results. An Abaqus script (“AbqOdbXYExport.py”) is provided to batch extract the DOF acceleration time response from the Abaqus-proprietary .obd files into text-formatted report (.rpt) files. For correct usage of “AbqOdbXYExport.py”, please refer to the notes within the file.

The described procedure is summarised under steps 2-5 in Table D-3. It can be adapted to generate parametric simulations of arbitrary user-defined setups starting from the definition of a desired simulation case as an Abaqus project and input file (step 1).

**Table D-3: Execution steps for the conducted parametric simulations with Abaqus**

<b>Step</b>	<b>Description</b>	<b>Execution environment</b>	<b>Corresponding file</b>
1	Creation of an Abaqus project and .inp file containing the base definitions for geometry, element types and properties, force locations, boundary conditions, nodal output requests, simulation parameters	Abaqus CAE	N/A
2	Preparation of a template .inp file with placeholder tags for parametrised values	Text editor	_template.inp
3	Batch generation of input force functions with all variations of the parametric variables and generation of individual .inp files containing each specific variation	External Python script	GenerateAbqInps.py
4	Sequential or parallel batch execution of Abaqus simulations/jobs defined by the .inp files, each resulting in a corresponding .odb (output database) file	OS command prompt	abq_job_8-cpus.bat
5	Batch extraction of DOF outputs from all .odb files into .rpt (report) text files	Abaqus Python script	AbqOdbXYExport.py